

Characterization of Inorganic Polyphosphate in Mammalian Cells

by

Lihan Xie

A dissertation submitted in partial fulfillment
of the requirements for the degree of
Doctor of Philosophy
(Molecular, Cellular, and Developmental Biology)
in The University of Michigan
2020

Doctoral Committee:

Professor Ursula H. Jakob, Chair
Professor Kenneth M. Cadigan
Professor Robert S. Fuller
Professor Yanzhuang Wang
Professor Haoxing Xu

Lihan Xie

lihanx@umich.edu

ORCID iD: 0000-0003-0760-5806

© Lihan Xie 2020

Dedication

To the memories of my grandma and my uncle, who taught me about love, courage and perseverance.

Acknowledgements

I would like to thank my advisor, Dr. Ursula Jakob, for taking me on an incredible journey of scientific training and personal growth. As a mentor, she always led by example and nurtured the qualities of a good scientist in me. As much as she inspired me to strive for excellence, she supported me to overcome every challenge. I am truly grateful to Ursula for being valued not only as a student but also as a colleague. I believe that it was HER trust and confidence that made me into a stronger person. Thank you, Ursula!

I also appreciate the intellectual and emotional support from my other committee members: Dr. Kenneth Cadigan, Dr. Yanzhuang Wang, Dr. Haoxing Xu and Dr. Robert Fuller, for they always offered me constructive feedback on the project as well as valuable career advice.

Furthermore, I owe my sincere thanks to all the past and present members of the Jakob and Bardwell Labs, who were the most passionate, knowledgeable, creative and collaborative colleagues, and more importantly, the most caring, supportive and inspirational friends. In particular, I would like to thank Daniela Knoefler Koniczek, Justine Lempart, Ellen Quarles, Daphne Bazopoulou, Jan Dahl, Francois Beaufay, Kathrin Ulrich, Bryndon Oleson, Akash Rai, Janakraj Bhattraai and Philipp Huettemann from the Jakob Lab, and Veronika Sachsenhauser, Hyun-hee Kim, Changan Lee, Xiexiong Deng, Kevin Wu, Ben Meinen, Mark Dulchavsky and Rishav Mitra from the Bardwell Lab. Their companionship had been a great gift. Specially, I would like to thank Maria E. Solesio Torregrosa, my collaborator and long-time friend, for her passionate support and encouragement. I would also like to thank Asavari Rajpurkar and Benjamin Sliwinski for their great work as undergraduate students. Lastly, I would like to thank Dr. Michael Gray for supervising my rotation project, Dr. Nicolas Santoro from the Center of Chemical Genomics for assisting with part of my thesis work and Christopher Sinkler for helping with data transfer to facilitate the writing process.

Over the last six years, I was very fortunate to share many memorable moments with my dear friends. There are too many to acknowledge, but here, I would like to thank Mingxue Gu, Daniela Knoefler Koniczek, Veronika Sachsenhauser, May Tsoi, I-Uen (Yvonne) Hsu, Wenjia Wang, Xin

Wen, Filipa Teixeira, Denise de Castro Fernandes and Anke Kaufmann for making Ann Arbor my second home.

Lastly, I would like to express deep gratitude to my parents for their unconditional love and support. Throughout my life, they have inspired me to become a better person by serving as role models. Without them, I would not have been who I am today. And to make them proud is my greatest wish and motivation.

Table of Contents

Dedication.....	ii
Acknowledgements.....	iii
List of Tables.....	x
List of Figures.....	xi
Abstract.....	xiv
Chapter 1 The Subcellular Localizations, Functions and Regulation of Inorganic Polyphosphate.....	1
1.1 PolyP biosynthesis and regulation in bacteria.....	2
1.2 PolyP localizations and functions in eukaryotic cells.....	3
1.2.1 Nucleus	4
1.2.2 Plasma membrane and inner mitochondrial membrane.....	5
1.2.3 Mitochondrial matrix	6
1.2.4 Lysosome	7
1.2.5 Cytoplasmic vesicle	7
1.2.6 Matrix vesicle.....	8
1.2.7 Regulation of polyP levels and chain lengths	9
1.2.8 A proposed mechanism for the versatile functions of polyP	10
1.3 PolyP kinase – in the past and on the horizon.....	11
1.3.1 <i>E. coli</i> PPK1.....	12
1.3.2 <i>P. aeruginosa</i> PPK2	12

1.3.3	<i>D. discoideum</i> PPK2	13
1.3.4	<i>S. cerevisiae</i> Vtc4.....	13
1.3.5	Are mitochondria the origin of polyP?	13
1.3.6	The conjunction of polyP and inositol pyrophosphate (PP-IP) synthesis.....	14
1.3.7	PolyP-consuming enzymes.....	15
Chapter 2 Accumulation of Inorganic Polyphosphate Is a Cellular Response to Cisplatin-Induced Apoptosis.....		
2.1	Introduction.....	16
2.2	Materials and methods	17
2.2.1	Reagents, plasmids, and proteins	17
2.2.2	Cell lines	18
2.2.3	Cisplatin treatment.....	18
2.2.4	Proliferation and cell death assays.....	18
2.2.5	Flow cytometry	20
2.2.6	Immunofluorescence staining.....	20
2.2.7	Uptake of fluorescently labeled polyP	21
2.2.8	Image quantification	22
2.2.9	Generation of stable <i>ScPPX</i> -expressing cells	22
2.2.10	<i>Ex vivo ScPPX</i> activity assay.....	23
2.2.11	Statistics	23
2.3	Results.....	24
2.3.1	Cisplatin treatment triggers polyP accumulation in cancer cells	24
2.3.2	Cisplatin treatment leads to nucleolar polyP foci formation.....	26
2.3.3	Cisplatin-induced polyP response positively correlates with cellular toxicity .	27

2.3.4	Exogenous polyP administration increases cisplatin sensitivity of selected cancer cells.....	29
2.4	Discussion	31
2.5	Supplemental information.....	35
Chapter 3	The Dynamic Rearrangement of Nucleolar Inorganic Polyphosphate Is Inflicted by Ribosome RNA Synthesis Stress	41
3.1	Introduction.....	41
3.2	Materials and methods	44
3.2.1	Reagents.....	44
3.2.2	Cell lines and treatments.....	45
3.2.3	Cytotoxicity assays	45
3.2.4	Immunofluorescence labeling.....	46
3.2.5	Plasmid transfection.....	47
3.2.6	Fluorescence recovery after photobleaching (FRAP).....	48
3.3	Results.....	48
3.3.1	Cisplatin-induced polyP foci form at the light nucleolar cap, Cajal body, and fibrillar cap.....	48
3.3.2	Formation of polyP foci in the nucleoli and Cajal bodies is a result of RNA pol I inhibition.....	52
3.3.3	IP6K1 is a novel component of the light nucleolar cap	54
3.3.4	Light nucleolar caps are highly dynamic structures	56
3.3.5	Nucleolar polyP is sensitive to the inhibition of rRNA processing	58
3.4	Discussion	60
3.4.1	PolyP partitions to light nucleolar caps, fibrillar caps and Cajal bodies in response to rRNA transcription inhibition	60

3.4.2	Potential roles of polyP in the regulation of RNA Pol I.....	62
3.4.3	PolyP might also respond to the inhibition of rRNA processing	64
3.4.4	IP6K1 is a novel component of the light nucleolar cap	64
3.4.5	The role of polyP in the phase separation of the nucleolus	65
3.5	Outlook	66
3.6	Supplemental information.....	68
Chapter 4	Identification of Polyphosphate Regulatory Genes in Mammalian Cells.....	75
4.1	Introduction.....	75
4.2	Materials and methods	77
4.2.1	Reagents.....	77
4.2.2	Nutrient shift treatment of <i>E. coli</i>	78
4.2.3	Immunofluorescence labeling and visualization of polyP in <i>E. coli</i>	78
4.2.4	High throughput siRNA screens for polyP regulatory genes.....	79
4.2.5	Quantitative reverse transcription polymerase chain reaction (qRT-PCR).....	82
4.2.6	Western blotting.....	84
4.2.7	Immunofluorescence labeling and confocal microscopy.....	85
4.3	Results.....	86
4.3.1	Visualization of polyP accumulation in nutrient shifted bacteria using the mCherry- <i>EcPPX_c</i> probe	86
4.3.2	A genome-wide siRNA screen for polyP regulators in the human genome.....	87
4.3.3	Validation of <i>PPK</i> candidate genes using ON-TARGETplus SMARTpool® siRNAs.....	95
4.3.4	Explorations of <i>ATP5F1E</i> and <i>PANK4</i> siRNAs.....	98
4.3.5	Validation of <i>PPK</i> candidate genes with individual siGENOME siRNAs.....	101
4.3.6	Potential candidates for genes that downregulate polyP.....	103

4.3.7	Potential candidates for the regulation of cisplatin sensitivity in HeLa cells .	105
4.4	Discussion	109
4.4.1	An siRNA screen designed for identifying human <i>PPK</i> genes.....	109
4.4.2	Validation of the potential candidates for human <i>PPK</i> genes.....	110
4.4.3	Evaluation of the candidates for human <i>PPK</i> genes.....	111
4.4.4	Potential candidates for the downregulation of polyP	114
4.4.5	Potential mechanisms for the regulation of cisplatin sensitivity	115
4.5	Outlook	116
4.6	Supplemental information.....	117
	Bibliography	122

List of Tables

Chapter 1

Table 1.1 The subcellular localizations and physiological functions of polyP in different species 9

Chapter 4

Table 4.1 Candidates for genes upregulating polyP levels in HeLa cells upon cisplatin treatment 90

Table 4.2 Percentage of cisplatin responding cells in selected candidates transfected with ON-TARGETplus SMARTpool® siRNAs 96

Table 4.3 PolyP content before and after cisplatin treatment and the respective fold change in selected candidates targeted by ON-TARGETplus SMARTpool® siRNAs 97

Table 4.4 Potential candidates for genes responsible for polyP downregulation..... 103

Table 4.5 Potential candidates for the regulation of cisplatin toxicity..... 106

Supplementary Table 4.1 Candidates for genes upregulating polyP levels based on the average fluorescence intensities of mCherry-*EcPPXc* in the nucleus117

List of Figures

Chapter 1

Figure 1.1 PolyP, a simple, universal, and multifunctional polyanion. 2

Figure 1.2 Subcellular localizations of polyP in the eukaryotic cell. 5

Chapter 2

Figure 2.1 Cytotoxic cisplatin treatment triggers formation of nuclear polyP foci. 26

Figure 2.2 Cisplatin-induced polyP foci are adjacent to RNA Pol I in the nucleolus..... 27

Figure 2.3 Correlation between cisplatin-induced polyP accumulation and cellular toxicity..... 28

Figure 2.4 Exogenous polyP increases cisplatin-induced cellular toxicity..... 31

Supplementary Figure 2.1 Cytotoxic cisplatin treatment causes polyP foci formation in cancer cells.
..... 36

Supplementary Figure 2.2 Cellular localization of polyP and cleaved caspase-3 after cisplatin
treatment. 37

Supplementary Figure 2.3 Dose- and time-dependence of cisplatin-induced polyP response in
ovarian cancer cells..... 38

Supplementary Figure 2.4 Manipulation of intracellular polyP levels and distribution in HeLa cells.
..... 40

Chapter 3

Figure 3.1 Structural organization of the nucleolus..... 43

Figure 3.2 Cisplatin-triggered polyP foci colocalize with markers for light nucleolar caps, Cajal
bodies, and fibrillar caps. 51

Figure 3.3 PolyP foci appear at light nucleolar caps, Cajal bodies, and fibrillar caps upon ActD
treatment. 54

Figure 3.4 IP6K1 accumulates in the light nucleolar cap structures upon rRNA transcription inhibition.....	56
Figure 3.5 Nopp140 is a dynamic member of the light nucleolar caps and other nuclear bodies.	57
Figure 3.6 A distinct type of nucleolar polyP foci occur upon the disruption of late rRNA processing but not the formation of nucleolar aggresomes or cytoplasmic stress granules.	59
Supplementary Figure 3.1 Cisplatin-induced polyP foci are distinct from dark nucleolar caps, central bodies, and PML bodies.....	69
Supplementary Figure 3.2 Colocalization analysis of polyP and nuclear markers in cisplatin-treated cells with fluorescence intensity plots.	70
Supplementary Figure 3.3 PolyP foci are not a direct readout of DNA damage or cell death.	71
Supplementary Figure 3.4 Colocalization analysis of polyP and nuclear markers in ActD-treated cells using fluorescence intensity plots.....	72
Supplementary Figure 3.5 PolyP foci formed upon ActD treatment are excluded from dark nucleolar caps and central bodies.	73
Supplementary Figure 3.6 Fibrillarin-GFP is highly dynamic in the light nucleolar cap and communicates with the surrounding environment.....	74
 Chapter 4	
Figure 4.1 Immunofluorescence labeling of polyP by mCherry- <i>EcPPX_c</i> in nutrient shifted <i>E. coli</i> cells.	87
Figure 4.2 Workflow of a genome-wide siRNA screen for mammalian <i>PPK</i> genes in cisplatin-treated HeLa cells using mCherry- <i>EcPPX_c</i> immunofluorescence labeling.....	88
Figure 4.3 Distributions of three major parameters of the primary screen.....	93
Figure 4.4 Frequency distribution analysis of basal polyP levels and fold increase of polyP concentrations upon cisplatin treatment in the candidates of the primary screen.....	94
Figure 4.5 Validation of <i>ATP5F1E</i> with individual siRNAs from the siGENOME and the ON-TARGETplus libraries.	100
Figure 4.6 PANK4 upregulation in cisplatin-treated cells.....	101

Figure 4.7 Effects of individual siGENOME siRNAs on the polyP content of selected candidates after cisplatin treatment.....	103
Figure 4.8 Biological processes overrepresented by the potential candidates that downregulate polyP.....	105
Figure 4.9 A gene ontology enrichment analysis of targets involved in the regulation of cisplatin sensitivity.	108
Supplementary Figure 4.1 Assessment of the knockdown efficiencies of siGENOME and ON-TARGETplus SMARTpool [®] siRNAs by qRT-PCR and Western blotting analyses.	121

Abstract

Inorganic polyphosphate (polyP) is a linear chain of three to around one thousand orthophosphates linked by phosphoanhydride bonds. Not only is polyP considered as a “molecular fossil” that existed on the primordial earth, but it is also universally found in all living species tested so far. Yet, unlike many other conserved molecules in biology, the pathways by which polyP is metabolized are not conserved, and the polyP synthesizing and degrading machineries in mammalian cells are still completely unknown. This lack in knowledge substantially hampers progress in polyP research since it renders reverse genetics powerless in deciphering the physiological functions of polyP in these species. Moreover, it raises two very important questions in the field: 1) why did evolution give rise to vastly different mechanisms to generate such a conserved molecule, and 2) what are the roles of this ancient polymer in modern species and time?

In my thesis work, I used a multipronged approach to address these questions. First of all, I detected an enrichment of polyP in the nucleolus of HeLa cells using an immunofluorescence probe derived from the polyP-binding domain of *Escherichia coli* exopolyphosphatase. This fraction of polyP is highly dynamic to environmental stress – it rapidly accumulates and relocates to distinct foci in the nucleolus during cisplatin-mediated apoptosis. The extent of polyP accumulation in such foci positively correlates with the intrinsic susceptibility of different ovarian cancer cells to cisplatin. And indeed, when we supplemented HeLa cells and ovarian cancer cells with exogenous polyP, they became significantly albeit slightly sensitized to the chemotherapeutic drug.

To take this one step further, I revealed the identities of cisplatin-triggered polyP foci with fluorescence colocalization analysis and reported polyP in the light nucleolar cap, fibrillar cap and Cajal body. Formation of these polyP-rich compartments is inflicted by impaired ribosome RNA synthesis, which underlies cisplatin toxicity. Intriguingly, I also discovered inositol hexakisphosphate kinase, a polyP-related protein, as a novel component of the light nucleolar cap. These results prompted me to hypothesize that polyP, a highly negatively charged polymer, might play a role in regulating the structural dynamics of this phase-separated compartment.

However, to illustrate the molecular mechanisms of polyP functions relies on the identification of

polyP metabolizing enzymes, in particular, polyphosphate kinase in mammalian cells. Therefore, I conducted a whole genome siRNA screen for genes involved in the up- and down-regulation of polyP, using cisplatin-induced polyP accumulation as a reporter. I proposed several promising candidates, *GRIN3B*, *P2RY1*, *ATP5F1E*, *PANK4* and *AP3MI*, which might be responsible for signaling polyP synthesis or catalyzing the reaction itself. Furthermore, I discovered a potential connection between inositol phosphate metabolism and polyP regulation. Meanwhile, I also uncovered genes involved in the following pathways: nucleotide excision repair, the ubiquitin-proteasome system, and cell cycle progression, to be essential regulators of cisplatin toxicity and potential targets for optimizing the current platinum-based therapeutic interventions.

In summary, my work has revealed an important aspect of polyP function in nucleolar stress response and begun to explore the molecular mechanisms of this phenomenon. Moreover, I have laid the foundation for future work aimed at characterizing the polyP regulatory network in mammalian cells, especially the long-sought polyphosphate kinase.

Chapter 1 The Subcellular Localizations, Functions and Regulation of Inorganic Polyphosphate

This chapter is partially adapted from the following review article: “Inorganic polyphosphate, a multifunctional polyanionic protein scaffold” (1) written as part of my thesis work.

Inorganic polyphosphate (polyP) consists of minimally three and maximally up to one thousand phosphates, connected via high-energy phosphoanhydride bonds (Fig. 1.1). Originally emerged during volcanic eruptions, polyP is thought to be one of the first energy-rich molecules on earth (2). Early work revealed that some microorganisms accumulate polyP in dense metachromatic granules that can be visualized with methylene blue staining (3). However, few studies reported the potential physiological role(s) of polyP in bacteria or any other organism, causing the polyP field to lie dormant for much of the 20th century. This situation changed, however, once polyP caught the attention of Sylvvy Kornberg and later that of her husband Arthur Kornberg, who spent the last 15 years of his career investigating the “forgotten polymer” (4). Kornberg and his team developed many of the currently available polyP detection and quantification methods (5,6), and, most importantly, identified the enzymes responsible for polyP synthesis in bacteria (7,8). This breakthrough discovery enabled them, for the first time, to genetically manipulate polyP synthesis in a living organism and hence systematically evaluate the physiological consequences of polyP depletion. As it turns out, polyP fulfills a number of different functions in bacteria; polyP production was found to increase stress resistance, motility, and biofilm formation as well as contribute to sporulation, quorum sensing, and virulence (6,9-14). In eukaryotes, polyP appears to play an equally large number of diverse roles, ranging from stimulating blood clotting through the activation of factor XII to chelating calcium for bone mineralization, stabilizing mTOR, and triggering apoptosis (15-18). This amalgam of seemingly unrelated functions (Fig. 1.1) poses new and even more intriguing questions as to how such a simple polyanion like polyP can fulfill all these different roles (Table 1.1). Furthermore, the field urges the discovery of the polyP biosynthetic pathways in the mammalian species, which not only possesses a far-reaching impact on the physiological activities of the organisms but may also be exploited to regulate the

progression of pathological conditions.

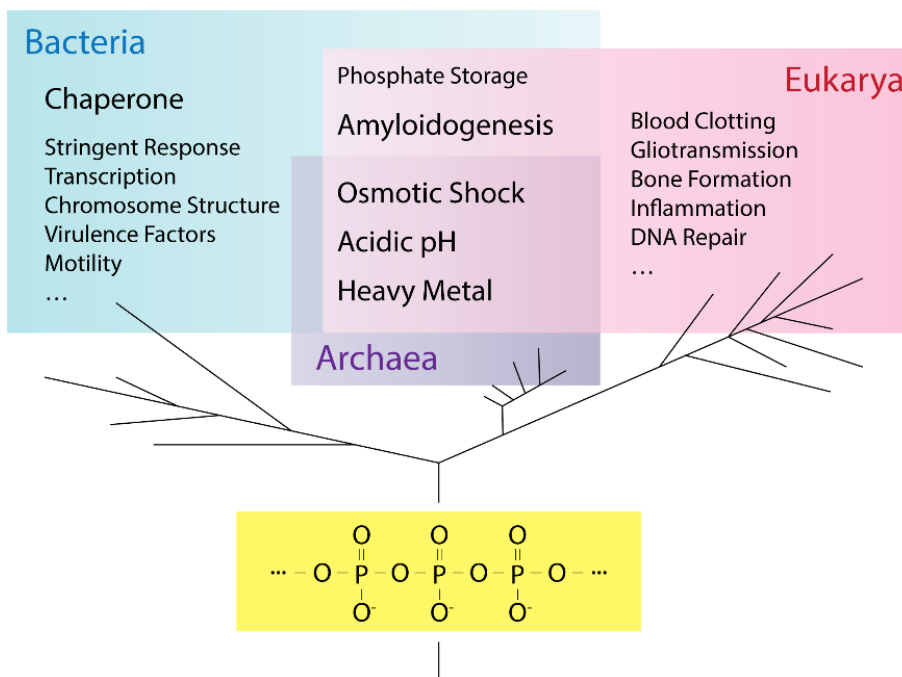


Figure 1.1 PolyP, a simple, universal, and multifunctional polyanion. The linear polyP chain consists of minimally three and maximally up to about 1,000 orthophosphates linked by high-energy phosphoanhydride bonds. PolyP has been identified in all the organisms tested so far, where it fulfills an astonishing array of different functions. This figure was adapted from the review article “Inorganic polyphosphate, a multifunctional polyanionic protein scaffold” (1).

1.1 PolyP biosynthesis and regulation in bacteria

Many bacteria, including numerous pathogens, encode the non-essential enzyme polyphosphate kinase (PPK1), which catalyzes the reversible transfer of the terminal γ -phosphate of ATP to polyP (the *in vivo* starting molecule is not yet known) (7). In addition to PPK1, some microorganisms encode a second, structurally unrelated kinase, PPK2, which catalyzes the transfer of terminal P_i from polyP to GDP to form GTP (8,19,20). Most if not all of these bacteria also encode the exopolyphosphatase PPX, which hydrolyzes polyP into individual phosphates, thereby indirectly utilizing the cellular ATP pool to maintain phosphate homeostasis (21).

Steady state concentrations of polyP in the bacterial cytosol are typically in the low micromolar range, even in the mutant strains that lack the polyphosphatase PPX (22). These results suggest that the levels and/or activity of PPK must be tightly regulated, a conclusion that makes energetic sense given that polyP synthesis draws from the cellular ATP pool. Yet, upon nutrient shift (5,23) or exposure to osmotic changes (5), acidic pH (24), oxidants such as hypochlorous acid (25) or very high temperatures (26), bacteria rapidly accumulate high levels of polyP. In fact, under some

of these stress conditions, bacteria have been shown to convert millimolar amounts of ATP into extremely long chains of polyP (>1,000 Pi), decreasing their cellular ATP pool by up to 30-50% in the process (25). Not surprisingly, preventing bacteria from synthesizing polyP (i.e., by deleting *ppk1*) makes them exquisitely sensitive to nutrient deprivation, oxidants or high temperature (25-29). In addition, deletion of the *ppk1* gene has been shown to decrease bacterial pathogenicity in a comprehensive manner, i.e., by reducing motility, colonization, virulence factor production and biofilm formation (28,30) (Table 1.1).

Much of Kornberg's research focused on how bacterial polyP synthesis is regulated and which potential transcriptional regulators might control *ppk1* gene expression (5,6,23). These studies revealed that the *ppk1* gene is a direct target of sigma³⁸, the master transcriptional regulator for late stationary phase genes (31). PolyP, in turn, induces transcription of *rpoS* (the gene encoding sigma³⁸) and further amplifies its own synthesis (23,28,32). While these results nicely explained the increased PPK1 and polyP levels in the bacteria during the stationary growth phase, they failed to reveal how polyP synthesis is regulated during *rpoS*-independent stress conditions, such as oxidative or heat stress. As it turns out, in contrast to many stress-induced transcriptional responses, polyP-synthesis appears to be primarily regulated on a posttranscriptional and/or posttranslational level. In *Pseudomonas fluorescens*, for instance, mRNA transcripts of the *ppk1* gene have been shown to be targeted by antisense RNA, which finetunes PPK1 synthesis and hence regulates polyP abundance (33). Our study in HOCl-treated *Escherichia coli* cells revealed that polyP accumulation is, at least in part, mediated by the reversible inactivation of PPX. In this case, reversible oxidation of a critical cysteine, located in the polyP binding site, directly inactivates PPX until reducing conditions are restored (25). Despite these insights, it is clear that inactivation of PPX is only part of the polyP accumulation story. Since *ppx* deletion strains do not accumulate polyP in the absence of stress and PPK1 levels do not seem to significantly increase upon nutrient shift or other stress conditions in *E. coli* (22,34,35), it is highly likely for PPK1 to be post-translationally regulated, either directly or through stress-sensitive regulators. Once PPK1 is activated and polyP is synthesized, however, transient inactivation of PPX will guarantee that polyP levels remain high until non-stress conditions are restored.

1.2 PolyP localizations and functions in eukaryotic cells

The earliest studies on the distribution of polyP in mammalian cells used subcellular fractionation

and biochemical quantification assays. They reported that polyP is present in the nucleus, plasma membrane, cytoplasm and intracellular organelles (36). Recently developed polyP-specific probes, including DAPI (whose excitation and emission spectra shift significantly when bound to polyP instead of DNA) (37), *EcPPX_c* fusion proteins (38,39) or JC-D7 and JC-D8 (40) supported these results, but they also demonstrated that polyP is particularly enriched in the nucleolus, acidocalcisomes (a conserved organelle rich in protons, calcium and phosphorous) and mitochondria. Moreover, polyP was found to be secreted from astrocytes and subsequently taken up by neurons, suggesting that it is present both inside and outside of the cell (41,42) (Fig. 1.2).

1.2.1 Nucleus

The proximity of polyP and nucleic acids has been first reported in prokaryotic species and yeast. Traditionally, PolyP-RNA complexes, held together by divalent cations, such as Mg²⁺ and Ca²⁺, were purified (43,44). Later on, studies in *E. coli* postulated that polyP-RNA interactions might be crucial to control RNA stability *in vivo*, as PPK1 was identified as a component of the RNA degradation machinery (i.e., the degradosome) (45). In cyanobacteria, on the other hand, polyP granules were predominantly observed around the nucleoid (46), where ribosomes are enriched under normal growth conditions. Hence, despite the fact that polyP and nucleic acids are both negatively charged, polyP might be associated with DNA and/or RNA, not only physically but also functionally.

Contrary to the primitive nucleoid, which largely contains naked DNA, the nucleus of eukaryotic organisms has a highly compact organization of genetic information and a sophisticated compartmentalization of biochemical reactions. Therefore, it is not surprising that polyP exhibits a more precise arrangement in the nucleus. Notably, several lines of evidence established that polyP resides in the nucleolus (38,47-49), a prominent membraneless structure and the birthplace of ribosomes. *In situ* labeling of polyP with an immunofluorescence probe pinpointed polyP to the dense fibrillar component and the fibrillar center, but not the granular component of the nucleolus (38) (Fig. 1.2). To this date, the molecular details of nucleolar polyP await further characterization. Yet, a novel posttranslational (non-enzymatic) modification, namely polyphosphorylation, which involves the covalent attachment of polyP chains to the lysine residues of selected nucleolar and glycosomal proteins (47,48,50), could in part explain the specific targeting of polyP to the nucleolus.

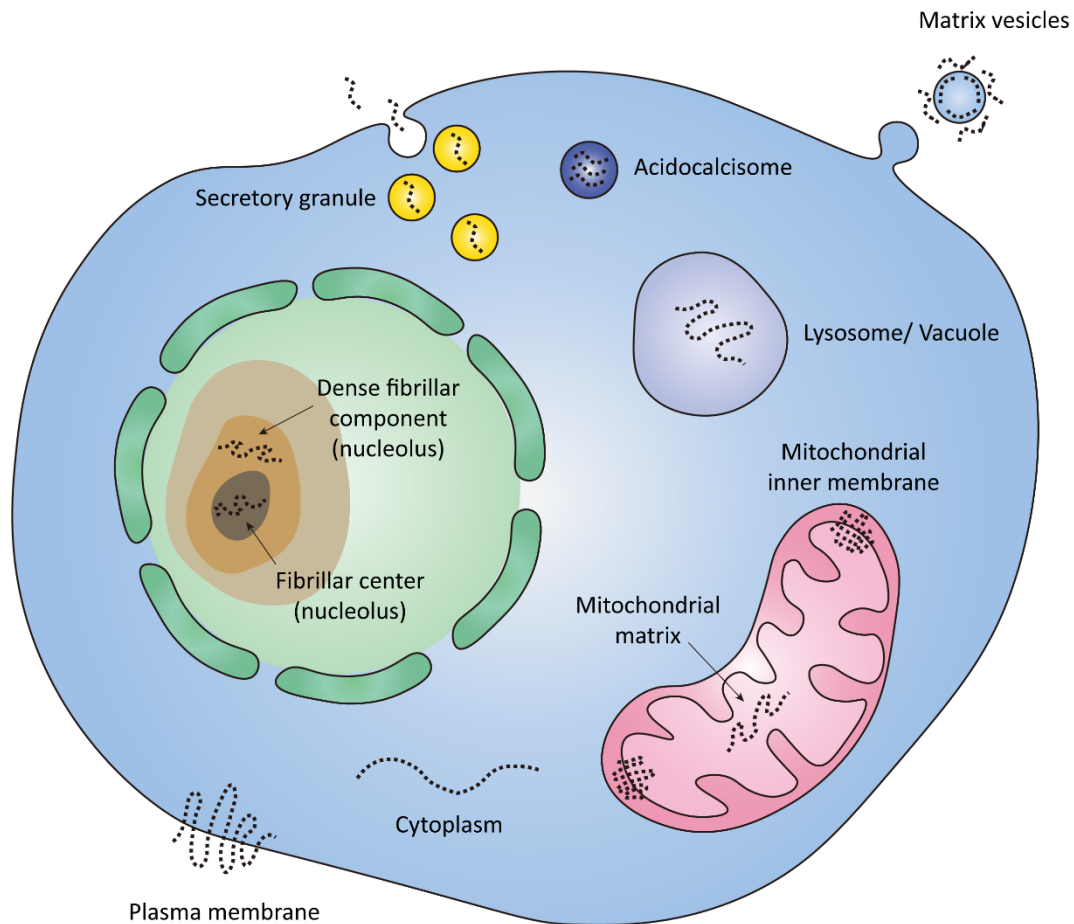


Figure 1.2 Subcellular localizations of polyP in the eukaryotic cell. PolyP (represented by a dashed line) was found in the nucleus (specifically, in the fibrillar center and dense fibrillar component of the nucleolus), on the plasma membrane and inner mitochondrial membrane, in the mitochondrial matrix, lysosome or vacuole lumen, cytoplasmic vesicles (including acidocalcisomes and secretory vesicles) and on the outer and inner surfaces of matrix vesicles. Organelles in which polyP have not been detected are omitted, and the sizes of different organelles are not drawn to scale.

1.2.2 Plasma membrane and inner mitochondrial membrane

Mammalian cells have evolved a robust membranous system. Embedded within the plasma membrane and the inner mitochondrial membrane are various channels made up of polyP, Ca^{2+} , and a second biopolymer, polyhydroxybutyrate (PHB) (Fig. 1.2). PHB- Ca^{2+} -polyP complexes were first observed in the plasma membrane of *E. coli*, where they were proposed to serve as an entrance channel for foreign DNA during transformation (51). The architecture of the PHB- Ca^{2+} -polyP complex has been deduced from the biochemical features of the three constituents (51). In this model, the periphery of the channel is lined with PHB, whose methyl group extends outwards and anchors the macromolecule in the surrounding lipid bilayer. Meanwhile, the ester oxygen of PHB is posed to the interior of the channel, where it is bridged to the phosphoryl oxygen of polyP by a calcium ion. Altogether, PHB, Ca^{2+} , and polyP form a channel of 2.4 nm diameter (externally)

with an approximate molar ratio of 1: 0.5: 1. However, both the gating mechanism and the selectivity of the PHB-Ca²⁺-polyP complex remain elusive thus far.

Intriguingly, as evolution takes place, the PHB-Ca²⁺-polyP unit is incorporated into a number of proteinaceous assemblies which dwell in a variety of intracellular compartments and hence impose a multifaceted impact on the cell.

One category of such complexes includes, but is not limited to, the K⁺ channel of streptomyces A (KcsA) in *Streptomyces Lividans* (52), the cold-sensing transient receptor potential melastatin 8 (TRPM8) channel (53) in the peripheral neurons, and the Ca²⁺-ATPase in erythrocytes (54). The functional roles of these assemblies are far from clear. Whereas removal of polyP by exopolyphosphatase greatly alters the voltage-gating properties of TRPM8 (53), the erythrocyte calcium pump is postulated to catalyze polyP synthesis and degradation (54). Taken together, these observations suggest that polyP is not only a structural scaffold but also a dynamic regulator that governs the functional states of these ion-conducting complexes.

A less well-characterized PHB-Ca²⁺-polyP assembly was identified in the inner mitochondrial membrane as part of the mitochondrial permeability transition pore (mPTP) (55,56). In spite of the critical roles that are played by mPTP in energy homeostasis and cell death, the molecular composition of this channel is still enigmatic. In addition to PHB, Ca²⁺, and polyP, subunits of the F₀F₁-ATPase are compelling candidates for configuring mPTP (57-59), albeit with conceivable differences from the classic ATP-producing engine. In accordance with this idea, an F₀F₁-ATPase dimer resembles mPTP in the electrophysiological properties (59). In addition, the transmembrane and pore-forming element of the F₀ rotor, namely the c subunit was found to interact with the PHB-Ca²⁺-polyP complex (57,58). Hence, it is plausible that mitochondria, regarded as the powerhouse of the cell, engage cognate machineries to coordinate energy production, stress response, and cell survival. Being an energetic biopolymer itself, polyP could be a direct or indirect product of the ensemble, an ingenious switch between the two facets of F₀F₁-ATPase activities, or both.

1.2.3 Mitochondrial matrix

In contrast to the membrane-bound polyP fractions, the mitochondrial matrix contains an alternative polyP reserve, which adopts a ‘free’ form (Fig. 1.2). There, the negatively charged polymer made up of 15 to 25 phosphates is likely to interact with Ca²⁺ (60), a crucial messenger for metabolic and proapoptotic stimuli. PolyP depletion by an ectopic expression of yeast

exopolyphosphatase in the mitochondrial matrix profoundly impacts the metabolomic landscape of the cell, shifting the major source of ATP production from oxidative phosphorylation to glycolysis (61). Given the reliance of tumor cells on glycolysis for sustained proliferation, it is plausible that free mitochondrial polyP may play a role during tumorigenesis and the progression of cancer.

1.2.4 Lysosome

The unicellular eukaryotic species *Saccharomyces cerevisiae* differs from the vast majority of other eukaryotes in that it contains a known polyphosphate kinase – the vacuolar transporter chaperone 4 (Vtc4) (62). Vtc4 is part of an elaborate ring-like structure, which couples polyP synthesis with its translocation into the vacuole where polyP is stored (63) (Fig. 1.2). Vacuolar polyP is a central player in the phosphate homeostasis. The vacuole appears to sequester phosphate when cells are actively growing (62) and releases it to supply the building blocks for DNA replication during the S phase (64). Moreover, vacuolar polyP chelates heavy metals, such as manganese and cadmium, to prevent cellular damage caused by toxic environmental pollutants (65,66). In addition, polyP increases nitrogen storage by complexing arginine without disturbing the osmolarity of the cell (67). For these reasons, it is crucial to synchronize polyP production and its translocation to the vacuolar lumen. Otherwise, excess polyP in the cytoplasm will not only distort the morphology of the cell but also interfere with the growth rate of this organism (68).

Compared to a wealth of knowledge about vacuolar polyP in yeast, little is known about lysosomal polyP in mammalian cells. This is largely due to the fact that lysosomes do not contain Vtc4, or any other functional equivalent known to date. Only a few studies have addressed the presence of polyP in the lysosome, using human fibroblasts and cultured mouse astrocytes (41,42,69) At a minimum, part of the lysosomal polyP in astrocytes can be mobilized by an exocytic signal and contributes to gliotransmission and neuronal firing (41,42).

1.2.5 Cytoplasmic vesicle

The most prominent polyP deposit in mammalian cells is the acidocalcisome (39,70-72) (Fig. 1.2), an acidic, calcium-rich organelle, which is conserved from bacteria to humans (73). Historically, acidocalcisomes were first identified in the unicellular parasites, i.e., *Trypanosoma* (74). Yet, more detailed molecular analysis rendered this structure analogous to ancient volutin granules in bacteria (75) as well as to electron-dense granules in human platelets, mast cells, and basophils (39,71).

The commonality of volutin granules, acidocalcisomes, and platelet dense granules is that they all contain an extraordinary amount of polyP. In platelets, for example, the intragranular polyP concentration can reach levels of up to 130 mM (in phosphate unit) (71), nearly 1000-fold more than the average polyP level in other mammalian cells and tissues (36). This unique feature makes physiologic sense as acidocalcisome polyP is readily secreted and executes extracellular tasks in the organism, including acting in the blood clotting cascade and eliciting proinflammatory responses (16,39,76-79).

PolyP secretion and uptake have also been documented in the brain, despite the fact that neurons and other nerve cells do not contain acidocalcisomes. The most prominent polyP storage appears to be in the synaptic vesicles in neurons and the postulated ATP-containing vesicles in astrocytes (41,80) (Fig. 1.2). Both structures are responsive towards environmental cues. Neuronal polyP is released upon membrane depolarization (80), and polyP vesicles in astrocytes are released upon elevated cytoplasmic Ca^{2+} levels, which are characteristic of many physiological and pathological conditions (41,42). Once secreted, polyP exerts at least two functions on nearby cells: 1) polyP substantially enhances the firing rate of neurons via a direct modulation of the voltage-gated sodium, potassium, and calcium channels (80) and 2) polyP functions as a gliotransmitter by activating the purinergic receptor P2Y1 found in astrocytes (42). Intriguingly, the G protein-coupled receptor P2Y1 incurs a Ca^{2+} release from the ER, setting into motion a subsequent polyP-induced polyP release (42), which serves to amplify the signal via a feed forward mechanism. PolyP signaling is prevalent among all astrocytes and selected neurons (42). Furthermore, it is endowed with a critical role in overseeing the autonomic behaviors in mice (42).

1.2.6 Matrix vesicle

An alternative polyP-rich vesicle, namely the matrix vesicle buds from the apical membrane of osteoblast, creating a platform for calcium and phosphate condensation into hydroxyapatite (81), the basic material of cartilage, bone, and teeth. As its name suggests, matrix vesicle floats in the extracellular environment and exhibits an opposite membrane topology to the aforementioned cytoplasmic polyP enclosures. Electron microscopy revealed that polyP populates the outer and inner surfaces of the vesicle, less so the lumen (81) (Fig. 1.2). Once hydrolyzed, for example, by the alkaline phosphatase on the plasma membrane of osteoblast, polyP is converted to phosphate and shifts the equilibrium towards hydroxyapatite formation (17,82). Hence, mobilization of polyP

on the matrix vesicle is programmed to support the continuous development of the skeleton.

Table 1.1 The subcellular localizations and physiological functions of polyP in different species

Species	Subcellular localization (if described)	Function	Reference
<i>E. coli</i>		Stringent response	(5,6)
		Stationary phase survival	(10,27)
		Stress resistance (heat, oxidants, osmotic shock, acidic pH, and heavy metal)	(10,25-28,83)
		Biofilm formation	(28,84)
		Persistence	(28,85)
		Transcription	(23,28,32)
	Ribosome	Translation	(86)
	Plasma membrane	DNA entry	(87)
<i>P. aeruginosa</i>		Cellular structures (nucleoid and cell envelope)	(30)
		Motility	(11,12,30)
		Stress resistance (oxidants and desiccation)	(29,30)
		Biofilm formation	(13,30)
		Virulence	(13)
		Quorum sensing	(13)
		Colonization	(28)
<i>S. cerevisiae</i>	Nucleoplasm, nucleolus	Posttranslational modification	(47,48,50)
	Vacuole	Phosphate homeostasis	(62,64)
	Vacuole	Arginine sequestration	(67)
	Cytoplasm	Stress resistance (heavy metal)	(65,66)
<i>Dictyostelium discoideum</i>		DNA synthesis and repair	(64,88)
		Development and germination	(89,90)
		Predation	(90)
		Cytokinesis	(91)
<i>T. brucei</i> and <i>T. cruzi</i>	Nucleolus, glycosome	Posttranslational modification	(50)
		Stress resistance (osmotic shock)	(92-94)
		Cytokinesis	(92)
		Infection	(93,95)
<i>Homo sapiens</i>	Plasma membrane, cytoplasm	Ion channel activation	(53,96)
	Plasma membrane, cytoplasm	Signaling (mTOR, FGF2, and integrin @1)	(18,97,98)
	Mitochondria	Mitochondrial activity (mPTP opening, Ca ²⁺ homeostasis, and energy metabolism)	(15,60)
	Nucleolus	rRNA transcription	(38,48)
		DNA repair	(88)
	Acidocalcisome	Blood clotting and inflammation	(16,39,71,76-79)
	Synaptic vesicles, putative ATP-containing vesicles, lysosomes	Neurotransmission and gliotransmission	(41,42,80)
	Matrix vesicles	Bone mineralization	(17,81)

1.2.7 Regulation of polyP levels and chain lengths

Due to a lack of feasible tools for polyP detection, it is very challenging even nowadays to monitor polyP dynamics *in situ* and in real time. Nonetheless, an immense knowledge has accumulated in the past two decades when discrete, static snapshots of polyP were spliced to reflect the differential regulation and constant mobilization of this molecule by intra- and extracellular signals.

Apart from certain cell types such as thrombocytes, mast cells, and basophils, which store up to 130 mM polyP (in P_i unit) in the form of medium-sized polyP chains in the dense granules (71), eukaryotic polyP levels are generally in the micromolar range, and their chain lengths vary between 50 and 800 P_i (36). Based on tissue-wide studies in rats and mice, the heart and the brain appear to contain the highest amounts of polyP ($\sim 100 \mu\text{M}$), followed by the lung, the kidney and the liver (36,99). On the organellar level, nucleus accommodates almost twice as much polyP as the plasma membrane, overtaking the cytoplasm and the mitochondrion by several folds (36). Taken together, these observations evince a convoluted program of polyP localization and abundance possibly determined by the developmental cues of an organism.

So far, no conditions have been reported in mammalian cells that would cause such a massive increase in polyP levels as what has been observed in nutrient-shifted or oxidatively-stressed bacteria. That being said, substantial polyP fluctuations accompany a handful of physiological and pathological processes in the eukaryotic species. For instance, brain polyP levels seem to decline with age and Alzheimer's disease state (84,100), alluding to the role of polyP in amyloidogenesis not only *in vitro* but also *in vivo*. Furthermore, at the onset of apoptosis, human leukemia cell line HL60 exploits an ingenious design that the quantity of polyP levels off while the proportion of long vs. short chain polyP markedly reduces (100). Hence, polyP level and chain length might represent two independent tiers of a seemingly multi-dimensional network for polyP regulation. As the field continues to search for conditions which allow polyP accumulation, it will shed light on the conundrum whether mammalian cells have inherited the capacity to upregulate polyP in the face of stress from their bacterial ancestors. And if so, is it conducted by transcriptional, translational or post-translational changes? Undoubtedly, this endeavor will gain momentum once the long-sought mammalian polyphosphate kinase(s) and polyphosphatase(s) are unearthed, or vice versa.

1.2.8 A proposed mechanism for the versatile functions of polyP

Based on the previous description, polyP is an unfathomable biopolymer whose primordial origin and simplistic structure clearly defy its sophisticated arrangements and diverse functions in the eukaryotic cell (Figure 1.1, Fig. 1.2 and Table 1.1). Ample evidence corroborates the roles of polyP in a wide range of biological processes, which include stress response, apoptosis, neurodegeneration, inflammation, blood clotting, and so on (101-105). Conceivably, this amalgam

of polyP activities directly reflects and results from the intricate local environment where polyP is effective. Although it is plausible that the phosphate- and energy-rich nature of polyP is due to alter organismal physiology in certain aspects, it is the interaction between polyP and those molecules located to the same subcellular compartments that is mostly likely to underpin the versatility of polyP functions.

In full agreement with this view, polyP acts as a promiscuous protein scaffold with a broad spectrum of clients (25,26,84,106,107). Essentially, this negatively-charged polymer is capable of discerning a folding intermediate and remodeling it to an amyloid-like, β -sheet-rich structure (25,26,84). Such conformational rearrangement is the staple of all polyP-client complexes studied to date. However, in stark contrast, the physiological outcome of polyP-client interaction is utterly dependent on the intrinsic property of the client. For non-amyloidogenic proteins, such as luciferase and citrate synthase, association with polyP shields the client from aggregation under proteotoxic stress and primes it for refolding once a permissive environment is restored (25,26). And for the amyloidogenic counterparts, exemplified by A β , α -synuclein, and tau, polyP accelerates fibril formation and alters fibril morphology so profoundly as to modify the stability and hence the seeding capacity of these macromolecules (84,106,107). Overall, research from our lab infers that polyP is a cytoprotective agent whose fundamental working mechanism(s) involve dictating the folding pathways of its clients (25,26,28,29,84) and furthermore orchestrating the downstream cellular responses in a physiological or pathological setting.

1.3 PolyP kinase – in the past and on the horizon

The biggest remaining puzzle in the field is the question how polyP is synthesized in mammalian species. Unlike many other conserved molecules that are known in biology, polyP is not synthesized via the same conserved pathway but derived from seemingly unrelated ATP-fueled engines that show no sequence homology and have no homologues in higher eukaryotes. Even if one focuses only on the prokaryotic branch of the phylogenetic tree, clear homologues of *E. coli* PPK1 are absent in a large number of polyP-synthesizing species (108). Therefore, in lieu of a homology-based quest for mammalian PPK, divergent paths are taken to 1) deepen our understanding of the known polyP kinases in other organisms in an attempt to seek undercover connections to their mammalian parallels; 2) scrutinize the proteomes of endogenous polyP-rich organelles; and 3) resolve the conjunction of polyP and inositol pyrophosphates, whose regulation

and perhaps even biosynthesis are evidently entwined.

1.3.1 *E. coli* PPK1

In the early 1990s, the biggest breakthrough in the polyP field came as the Kornberg group successfully purified *E. coli* PPK1 and cloned its gene (*ppk1*) (7,109), marking the transition from a descriptive observation of polyP to a mechanistic investigation of its activities. In-depth bioinformatic analyses failed to recognize any homologues of *ppk1* in 40 % of all taxa in the prokaryotic kingdoms (110). Furthermore, this gene was adopted by only a few eukaryotic species, such as *Caenorhabditis remanei*, *Candida humicola* and *Dictyostelium discoideum* through horizontal gene transfer (91,105,111). An unexpected structural similarity manifests in the catalytic domains of PPK1 and phospholipase D (PLD), which lack any perceptible sequence homology or functional overlap (112). As a lipid phosphatase, PLD hydrolyzes phosphatidylcholine to phosphatidic acid and choline, thereby remodeling the lipid composition of the plasma membrane and partaking in signal transduction (113). Due to the fundamental differences of the reactions that PPK and PLD catalyze, perturbation of PLD has not been studied specifically in the context of polyP. Yet, with PPK being the predominant source of polyP biosynthesis in bacteria, it might be fruitful to inspect the obscure connections between the structures, activities and evolution of these two enzymes.

1.3.2 *P. aeruginosa* PPK2

As researchers readily expanded polyP research to a pathogenic bacterium *P. aeruginosa*, they unveiled a parallel pathway for polyP generation and utilization centered on a nucleoside diphosphate kinase called PPK2 (8,19). In line with the fact that *P. aeruginosa* PPK1 (a close homologue of *E. coli* PPK1) and PPK2 are not related, there are rudimentary disparities pertaining to the substrates, metal cofactors, velocities and chain length preferences of the two enzymes (8). Most strikingly, PPK2 exhibits a 75-fold higher specific activity for replenishing GTP with polyP and GDP than building polyP chains via the reverse reaction (8,19). Essentially, 80 % of polyP in *P. aeruginosa* is synthesized by PPK1 (8), turning PPK2 into an auxiliary mechanism for maintaining polyP levels in this organism. Mapping *ppk2* in the phylogenetic tree evinced a coexistence of *ppk1* and *ppk2* genes in around 90 % of all species with *ppk2* (110). This finding strengthens the idea that the energetically-favored ATP pathway is more prominent for making polyP in bacteria and archaea. Still, the discovery of *P. aeruginosa* PPK2 is instrumental. Not only

did it reveal an unexplored avenue in bacterial activities, but it also enlightened the field on a form of polyP-consuming enzyme(s) which may harness the energy of nucleoside triphosphates and give rise to polyP chains in a designated environment.

1.3.3 *D. discoideum* PPK2

The perhaps most disputable polyP kinase, *D. discoideum* PPK2, is thought to consist of three actin-related proteins: ERpA, ArpD, and ACT28 (114). This tripartite protein complex was purified (with highly-enriched specific activity) from the *ppk1* null strain of *D. discoideum* and considered to be a backup polyP kinase until recent evidence *in vivo* raised doubt on this claim. The leading argument was made by the Saiardi group who observed a complete depletion of polyP by solely knocking out *ppk1* (89). This result challenged the disposition that actin-related proteins might take charge of manufacturing polyP in an enormous number of species where no other polyP kinases have been discovered (110).

1.3.4 *S. cerevisiae* Vtc4

The feasibility of doing high throughput genomic screenings led to the unanticipated discovery of yeast polyP kinase – Vtc4, which traverses the vacuolar membrane (62). The cytoplasmic domain of Vtc4, which contains the catalytic site, entrains the γ -phosphate of ATP into a growing polyP chain (63). The newly synthesized polymer is simultaneously deposited to the vacuolar lumen through a membrane channel formed by the VTC complex and presumably driven by an established electrochemical gradient across the vacuolar membrane (68).

While the mammalian lysosome is reminiscent of the yeast vacuole, no Vtc4 homologues have been identified in the mammalian structure. Nonetheless, fluorescence labeling of polyP traces it in the lysosomes of glial cells in mice (41,42), opening up questions whether *de novo* synthesis of polyP takes place in the lysosome or whether polyP is merely a cargo of the vesicular transport system. The former conjecture is supported by the observation that isolated lysosomes from human fibroblasts actively incorporate [32 P]Pi into long-chain [32 P]polyP (69). This finding brings about an exciting opportunity to isolate the polyP synthesizing enzyme(s) from the lysosome proteome.

1.3.5 Are mitochondria the origin of polyP?

Emerging evidence now proposes mitochondria as the most promising location of mammalian polyP kinase(s). The rationale appears to be several-fold. From an endosymbiotic perspective,

mitochondria arose from engulfed bacteria which possibly enveloped the oldest polyP-related enzymes on earth. While immense adaptations ensued to define the traits of a eukaryotic cell, mitochondria remain one of the hotspots for polyP deposit and function even after two billion years. More importantly, abrogation of mitochondrial membrane potential by either drugs or membrane permeabilization diminishes polyP signal in this compartment (115), which signifies the action of proton motive force in sustaining normal polyP levels. To take this one step further, Baev et al. reported what seems to be a polyP synthesis event in isolated mitochondria, namely an increase of mitochondrial polyP signal with the addition of substrates for the electron transport chain, but not ATP itself, and a prompt inhibition of this activity by oligomycin, a widely-used toxin for F₀F₁-ATPase (116). Surely, this finding raises an intriguing question whether the ATP-producing engine is designated to making another extremely energetic molecule in mammalian cells.

1.3.6 The conjunction of polyP and inositol pyrophosphate (PP-IP) synthesis

Apart from polyP, there is another class of energy-rich molecules, PP-IP, which bear phosphoanhydride bond-linked diphosphate groups at one or more positions of the six-carbon inositol ring. The first steps of PP-IP synthesis can be executed by two families of enzymes, inositol hexakisphosphate kinases (IP6Ks) and inositol hexakisphosphate and diphosphoinositol pentakisphosphate kinases (PPIP5Ks). IP6K1 and PPIP5K recognize specific forms of IP₅ and IP₆ and convert them to IP₇, or even IP₈, by phosphorylating selected phosphate groups attached to inositol (117,118). Genetic manipulation of *IP6K1* or *PPIP5K* interferes with numerous biological processes, including haemostasis, carcinogenesis, inflammation, cell migration, signaling, and etc. (119). Notably, the activities of PP-IP largely overlap with those of polyP – an expected outcome based on the fact that polyP synthesis itself is superintended by PP-IP. Ample evidence in yeast, *Trypanosoma* and mice corroborates an abrupt decrease of polyP when PP-IP production is impeded by knocking out *Ip6k1* or *KCS1* (the gene that encodes yeast IP6K1), *VIP1* (the gene that encodes yeast PPIP5K) or other critical genes in the inositol phosphate and PP-IP pathways (120-123). Mechanistically, IP₆, IP₇, and IP₈ (which contains two pyrophosphate groups instead of a triphosphate chain) potentiate polyP synthesis with increasing efficacies by directly binding to the SPX domain of the VTC complex (124,125). Since the levels of PP-IP fluctuate with that of phosphate (125), PP-IP might therefore serve as a messenger between phosphate profusion in the cytoplasm and polyP accumulation in the vacuole. On a slightly different tangent, IP₈ in the form of triphosphoinositol pentakisphosphate (PPP-IP₅) is a genuine product of IP6K1 *in vitro* and *in*

vivo (117), which ratifies an underappreciated role of IP6K in assembling short phosphate chains. Hitherto, it is unclear whether there are any limits on the length of phosphate stretches emanating from the inositol core and to which enzymes these decisions are delegated. However, it is certainly appealing to conceptualize a model for polyP synthesis where PP-IP acts as the root for alternating polyP elongation and release.

1.3.7 PolyP-consuming enzymes

In the search for novel polyP-synthesizing machineries, a few enzymes were recognized for their ability to use polyP as a phosphate donor. Such examples include glucokinase, NAD kinase, dolichyl diphosphate-polyphosphate phosphotransferase, and so on (108,126). Although their reactions may be reversed by excess substrates, it is unknown whether such conditions can ever be reached *in vivo*.

In summary, polyP biosynthetic pathways have diverged so profoundly that homology-based approaches can hardly connect the “dots” (i.e., known polyP kinases in a few model organisms) and restore the full evolutionary picture of this activity. The fact that polyP itself is so well-conserved while its metabolism is so versatile suggests an irreplaceable yet highly adaptive role of polyP in the cell. Focusing on the mammalian species, there are two outstanding features of this polymer: 1) the scarcity of polyP under normal growth condition as well as stress conditions tested so far and 2) the complexity of polyP localizations and functions. On one hand, these characteristics imply that polyP is tightly regulated *in vivo*; on the other hand, they set the bottleneck towards identifying the key players of the polyP regulatory network. Therefore, both conceptual and technical innovations are urged to overcome these barriers. After all, finding the enzyme(s) that synthesize and regulate polyP synthesis in mammals is key – once this is achieved, many of the remaining doors will open and hopefully reveal how this ancient biomolecule works today.

Chapter 2 Accumulation of Inorganic Polyphosphate Is a Cellular Response to Cisplatin-Induced Apoptosis

This work has been published as a research article (127) in the journal *Frontiers in Oncology*. I designed and performed the following experiments: 1) visualization of time- and dose-dependent polyP accumulation in the nucleoli of HeLa cells and ovarian cancer cells after cisplatin treatment; 2) colocalization analysis of polyP and cleaved caspase-3; 3) assessment of ovarian cancer cell proliferation in response to cisplatin challenge; and 4) establishment and characterization of a stable HeLa cell line which overexpressed yeast exopolyphosphatase in the nucleus. I wrote part of the draft and revised the full manuscript. Other coauthors, Daniela Knoefler, Asavari Rajpurkar, Nicole Taube, Akash S. Rai, Jake Erba, Benjamin Sliwinski and Moses Markowitz acquired and analyzed data for the rest of the experiments, and Ellen Quarles contributed to data analysis. Daniela Knoefler and Ellen Quarles performed the statistical analysis. Daniela Knoefler wrote the first draft of the manuscript, and Ellen Quarles wrote sections of it.

2.1 Introduction

About 1,600 patients die of cancer each day, making cancer the disease with the second highest mortality rate in the United States (128). Platinum-containing drugs such as cisplatin, one of the oldest approved chemotherapeutic agents, are used in about 50% of chemotherapies administered to cancer patients (129). Nevertheless, treatment with cisplatin is associated with significant problems. As a DNA-damaging agent, cisplatin kills not only cancer cells but also healthy cells. Off-target effects can be irreversible and include hearing loss and neuropathy (130). Moreover, while cisplatin treatment has been shown to be effective in reducing the mortality of testicular, bladder, cervical, and head and neck cancer, other tumors such as lung cancer are innately resistant towards cisplatin (131,132). Finally, many cancer types have been reported to develop cisplatin resistance coinciding with long term treatment. For example, ovarian cancer cells may respond well during initial chemotherapy treatment but commonly become resistant when the cancer reoccurs (131). Thus, the non-specific toxicity of cisplatin and the resistance of some cancers restrict the therapeutic use of the drug. To increase the treatment options for cancer patients, it is

therefore of crucial importance to understand how mammalian cells respond to cisplatin-mediated toxicity and hence identify targets that might increase cisplatin sensitivity specifically in cancer cells.

The toxicity of cisplatin is attributed primarily to its interaction with DNA and the cisplatin-induced formation of DNA adducts and double strand breaks (133,134). This DNA damage, if not properly mended by the cellular DNA repair machinery, blocks cell cycle progression and induces apoptosis (135). However, induction of apoptosis has also been observed in cells lacking a nucleus (136), implying that cisplatin might target other cellular components in addition to nuclear DNA. Based on recent work which showed that cisplatin also interacts with mitochondrial DNA, proteins, and small molecules such as glutathione (137-140), it was proposed that mitochondrial dysfunction and/or oxidative stress contribute to cisplatin toxicity. These unexpected results emphasize the need to further elucidate the mechanism of cisplatin action.

Our lab has recently discovered that bacteria respond to oxidative stress treatment with the accumulation of large amounts of inorganic polyphosphates (polyP), linear chains of phosphoanhydride bond-linked phosphates, which serve to protect proteins and cells against irreversible oxidative damage (25). Mammalian cells also synthesize polyP, but functional studies focused primarily on its roles in cell proliferation, apoptosis, angiogenesis, metastasis, blood clotting, and inflammation (18,77,79,98,141-143). Here we set out to test whether polyP plays a role during cisplatin-induced stress in mammalian cells. Our studies revealed that several cancer cell lines respond to cisplatin treatment with a robust upregulation and redistribution of endogenous polyP, leading to the formation of distinct nucleolar polyP foci. Instead of the expected cytoprotective function of polyP, however, we discovered that the levels of endogenous polyP directly correlate with the levels of caspase-mediated apoptosis induction, suggesting that polyP plays a role in cisplatin-mediated apoptosis. Indeed, by administering exogenous polyP, we were able to increase cisplatin-induced toxicity, suggesting that altering cellular polyP levels might represent a potential novel mechanism to modulate the therapeutic efficacy of cisplatin.

2.2 Materials and methods

2.2.1 Reagents, plasmids, and proteins

Polyphosphates with chain lengths of 14, 60, 130 and 300 P_i were kindly provided by T. Shiba (Regenetiss, Japan) and aliquoted in smaller volumes to avoid repeated freeze-thaw cycles. A cis-

Diammineplatinum(II) dichloride (Sigma-Aldrich) stock solution (3 mM) was prepared in double distilled water. The plasmid pETM41-*EcPPXc*, which encodes the Maltose Binding Protein (MBP)-*EcPPXc* was a kind gift from Florian Freimoser (Addgene plasmid #38329; <http://n2t.net/addgene:38329>; RRID:Addgene_38329) (144). To generate the mCherry-*EcPPXc* fusion protein, *EcPPXc* was cloned into the mCherry-containing pTEV5 vector between BamHI and NotI sites. To generate the alternative GFP-*EcPPXc* probe, GFP was amplified from the pEGFP-N2 vector with flanking regions containing NdeI and BamHI recognition sequences and inserted to replace mCherry in the mCherry-*EcPPXc* construct. The purification of His-tagged mCherry-*EcPPXc*, GFP-*EcPPXc*, and their respective His-tagged control proteins, mCherry and GFP, was done using a Ni-NTA column (Qiagen, Hilden, Germany). All reagents were purchased from Thermo Fisher Scientific (Waltham, MA, USA), Sigma-Aldrich (St. Louis, MO, USA) or New England Biolabs (Ipswich, MA, USA) unless specified otherwise.

2.2.2 Cell lines

HeLa EM2-11ht cell line (145) was a generous gift of Dr. J. Nandakumar, University of Michigan. HeLa EM2-11ht and HeLa (ATCC[®] CCL-2[™], ATTC, Manassas, VA, USA) cells were grown in DMEM (#11995065, Thermo Fisher Scientific). The ovarian cancer cell lines OVCAR3 and OVCAR8 (a generous gift of Dr. K. McLean, University of Michigan) were cultured in DMEM (ATCC[®] 30-2002[™]) from ATTC (Manassas, VA, USA). All media were supplemented with 10% Fetal Bovine Serum (#F4135, Sigma-Aldrich) and 1% Penicillin-Streptomycin (#15140122, Thermo Fisher Scientific). Cells were grown at 37°C with 5% CO₂.

2.2.3 Cisplatin treatment

Cells grown to ~ 80% confluence were detached from the flask using 0.25% Trypsin-EDTA (#25200056, Thermo Fisher Scientific). 1.2×10^5 cells were seeded in each well of a 24-well plate and 10^4 cells were plated in each well of a 96-well plate. After the cells were allowed to attach overnight, they were treated with a range of cisplatin concentrations for the indicated period of time.

2.2.4 Proliferation and cell death assays

All microplate reader-based assays were performed in 96-well cell culture plates (#3596, Corning, Inc., Corning, NY, USA). The WST-1 Cell Proliferation Assay Kit (#10008883, Cayman Chemical,

Ann Arbor, Michigan, USA) was used to assess proliferation. Briefly, medium containing cisplatin was removed from the 96-well plate, and the mixture of the WST-1 Developer Reagent and the Electron Mediator Solution was first diluted in fresh medium to the working concentration and then added to the treated cells. Absorbance was measured in a BMG FLUOstar Omega microplate reader (Ortenberg, Germany) at a wavelength of 450 nm. Using the average of three technical replicates, the absorbance readings of the treated samples were normalized to those of the untreated cells.

To determine the fraction of cells with compromised cell membranes as a readout for cell death, the SYTOXTM Green Nucleic Acid Stain (#S7020, Thermo Fisher Scientific) was used (146). All cisplatin treatments were set up in duplicates in a 96-well plate. Following the treatment, one set of samples were permeabilized with 120 μ M Digitonin (#D141, Sigma-Aldrich) while the other remained unperturbed. Then, 5 μ M SYTOXTM Green Nucleic Acid Stain was added to all the wells, and the samples were incubated for 30 minutes at 37°C. The fluorescence of incorporated SYTOXTM Green Nucleic Acid Stain was measured in a Tecan Infinite M1000 microplate reader (Männedorf, Switzerland) using an excitation wavelength of 504 nm and an emission wavelength of 523 nm. With the fluorescence from the digitonin-treated samples serving as the readout for total cell number, the percentage of dead cells was calculated by normalizing the fluorescence of the unperturbed wells to the fluorescence of the corresponding digitonin-treated wells.

The percentage of dead cells was also determined using Trypan Blue, which stains cells with disrupted membranes. Treated cells were detached from the wells using 0.25% Trypsin-EDTA, and an aliquot of cells was mixed and incubated shortly with Trypan Blue Solution (#15250061, Thermo Fisher Scientific). Stained (i.e., dead) cells and unstained (i.e., live) cells were counted in a light microscope and the percentage of dead cells was calculated.

To determine the extent of apoptosis induction, a luminescence-based activity assay for the executioner caspases, caspase-3 and caspase-7, was utilized. Cells were seeded at a density of 10^4 cells per well in a white 96-well plate with clear bottom (#CLS3610, Corning, Inc.). The Caspase-Glo[®] 3/7 assay (#G8090, Promega Corporation, Madison, WI, USA) was used to measure the activity of caspase-3 and caspase-7. The manufacturer's instructions were followed with the exception that only 70 μ l of the Caspase-Glo 3/7 Reagent was added to 70 μ l of fresh medium to each well. After incubating the plate for 30 minutes at room temperature, luminescence was

measured at 23°C in a BMG FLUOstar Omega microplate reader (Ortenberg, Germany). Each treatment was performed with three technical replicates and the average was calculated.

2.2.5 Flow cytometry

Following cisplatin treatment, cells were detached using 0.25% Trypsin-EDTA and combined with the supernatant, which contained dead, floating cells. Then, all cells were spun down at 300 g at room temperature for 5 minutes, and the pellet was washed with Cell Staining Buffer (#420201, BioLegend, San Diego, CA, USA). For the labeling of apoptotic and necrotic cells, the FITC Annexin V Apoptosis Detection Kit with PI (#640914, BioLegend, San Diego, CA, USA) was used, following the manufacturer's protocol. In short, the cell pellet was resuspended in Annexin V Binding Buffer. Then, Annexin V and Propidium iodide (PI) were added to the cell suspension. The percentage of Annexin V- and PI-positive cells (i.e., late apoptotic or necrotic cells) was measured in an Attune NxT Flow Cytometer (Thermo Fisher Scientific, Waltham, MA, USA; courtesy of the Buttita Lab, University of Michigan, Ann Arbor, MI, USA). Annexin V was measured in the BL1 channel while PI was measured in the BL3 channel. Gating was done using Annexin V-single stained cells, PI-single stained cells, and a double positive control.

2.2.6 Immunofluorescence staining

For fluorescence microscopy, cells were seeded onto 12 mm cover slips (#CLS-1760-012, Chemglass Life Sciences, Inc., Vineland, NJ, USA) placed in a 24-well plate (#3526, Corning, Inc.). Following cisplatin treatment, cells were fixed in 4% v/v freshly prepared paraformaldehyde (#1578100, Electron Microscopy Sciences, Hatfield, PA, USA) at room temperature for 15 minutes, washed with PBS and permeabilized in 0.3% Triton X-100 (#0219485480, MP Biomedicals, Solon, OH, USA) for 10 minutes. Triton X-100 was prepared in blocking solution, which contained 1% bovine serum albumin (#A3059, Sigma-Aldrich) in PBS. After a brief wash, cells were incubated in blocking solution for 1 h at room temperature. For the visualization of endogenous polyP, mCherry-*EcPPXc* or GFP-*EcPPXc*, and the respective control protein mCherry or GFP, were used at a concentration of 10 µg/ml in blocking solution and incubated overnight at 4°C, protected from light. For the staining of apoptotic cells, a rabbit cleaved caspase-3 (Asp175) monoclonal antibody (#MAB835, R&D Systems, Minneapolis, MN, USA) was used at a concentration of 8 µg/ml in blocking solution. For the staining of p53, a mouse p53 antibody (#DO-1, Santa Cruz Biotechnology, Dallas, TX, USA) was used at a concentration of 4 µg/ml. To stain RNA

polymerase I, a rabbit anti-PAF49 IHC antibody (#IHC-00474, Bethyl Laboratories, Montgomery, TX, USA) was used at a concentration of 8 $\mu\text{g}/\text{ml}$. To label nucleophosmin (NPM1), an anti-NPM1 antibody (#32-5200, Thermo Fisher Scientific) was used at a concentration of 2 $\mu\text{g}/\text{ml}$. Incubation of these primary antibodies was performed overnight at 4 °C together with polyP staining. The next day, cells were washed with PBS and then incubated with the respective secondary antibody for 1 h at room temperature, protected from light. Secondary antibodies used in this study were obtained from Abcam, Cambridge, United Kingdom and included goat anti-rabbit IgG-Alexa Fluor[®] 488 (#ab150077), donkey anti-mouse IgG-Alexa Fluor[®] 488 (#ab150105), and goat anti-rabbit IgG-Alexa Fluor[®] 647 (#ab150079). After washing with PBS, cells were incubated with DAPI (#D1306, Thermo Fisher Scientific) at a concentration of 2.5 $\mu\text{g}/\text{ml}$ for 10 minutes at room temperature to stain the nucleus. Cells were washed five times with PBS before the coverslips were mounted on microscope objective slides using Citifluor AF1 mounting medium (#19470, Ted Pella, Inc., Redding, CA, USA).

Fluorescence images for mCherry-*EcPPXc* staining were acquired with a 40 \times objective on an Olympus BX61 upright microscope (Olympus, Center Valley, PA, USA) equipped with a Photometrics Coolsnap HQ2 cooled CCD camera and a quad filter set (DAPI/ FITC/ TRITC/ CY-5). A closed feedback loop was enabled to keep the illumination of the X-Cite[®] exacte mercury lamp consistent. GFP-*EcPPXc* labeling and colocalization analysis of polyP, RNA polymerase I, and NPM1 were performed with a Leica SP8 laser scanning confocal microscope (Leica GmbH, Mannheim Germany) on a DMI8 microscope base using LAS X software, 100 \times oil objective (#11506378, Leica GmbH) and a 405 nm diode laser, in addition to a multi-line white light laser, set to 488, 594, and 647 nm excitation wavelengths. Spectral detection using a PMT from 410 to 480 nm was utilized for DAPI, a HyD detector from 493 to 560 nm for GFP and Alexa Fluor[®] 488, and a HyD detector from 653 to 800 nm for Alexa Fluor[®] 647.

2.2.7 Uptake of fluorescently labeled polyP

PolyP₃₀₀ was end-labeled with Alexa Fluor[™] 647 Cadaverine (#A30679, Thermo Fisher Scientific, Waltham, MA, USA) as described in (84). A labeling efficiency of 10-15% was obtained. HeLa cells were seeded on coverslips as described above. After washing the cells with PBS, they were incubated with 200 μM labeled polyP (in Pi units) overnight in the absence or presence of 25 μM cisplatin. Staining for endogenous polyP was performed as described above using the GFP-

EcPPXc probe.

2.2.8 Image quantification

Immunofluorescence images of DAPI and mCherry-*EcPPXc* (or GFP-*EcPPXc*) were used to define the puncta regions and quantify their signals using Fiji (ImageJ) software. Briefly, nuclear regions of interest (ROIs) were defined in the DAPI channel, using *Thresholded Blur*, *Make Binary*, and *Fill Holes* followed by hand segmentation to ensure accurate ROIs, and applied to the mCherry-*EcPPXc* (or GFP-*EcPPXc*) channel. Total nuclear signal was measured. Then the nuclear ROIs were separated into distinct files, and each nuclear ROI was used to define puncta ROIs. Puncta ROIs were found by applying several ImageJ plugins in order: *Median* and *Thresholded Blur* to reduce background noise and maintain puncta edges, *Subtract Background* with a rolling ball radius of 5 pixels to define areas that are brighter than nucleoplasm signal, and finally *Make Binary*, *Fill Holes*, and *Watershed* to define the puncta ROIs. These puncta ROIs were then applied to the original mCherry-*EcPPXc* (or GFP-*EcPPXc*) channel to record size and pixel intensity information. Finally, nucleoplasm signal was measured by defining a nucleoplasm ROI: Nuclear ROI with holes for all the puncta ROIs found in that nucleus. This was measured as for the puncta ROIs. Image background signal was determined by defining five non-cellular ROIs per image and averaging the pixel intensity. This background was subtracted from all ROI data. R Studio was used to analyze puncta data and produce the dot plot in Figure 2.1 and the histograms and dot plot in Supplementary Figure 2.1. (<https://www.rstudio.com>).

2.2.9 Generation of stable *ScPPX*-expressing cells

ScPPX, with an N terminal Nuclear Localization Sequence (NLS) followed by three FLAG tags, was cloned into pBI-4 vector using NotI and SalI and subsequently inserted into pBI-F3 vector using SarI and StuI. HeLa EM2-11ht cells were seeded in a 6-well plate with the density of 3×10^5 cells/ well and transfected the next day with 1 μg pCAGGS-IRES-Puro plasmid and 1 μg NLS-3 \times FLAG-*ScPPX* plasmid using Lipofectamine™ 3000 (#L3000008, Thermo Fisher Scientific), following the manufacturer's protocol. After 12 hours of incubation with the transfection mix, cells were transferred to a 10 mm culture dish and grown in the presence of 5 $\mu\text{g}/\text{ml}$ puromycin dihydrochloride (#P8833, Sigma-Aldrich). After 36 hours, puromycin was removed, cells were rinsed with PBS and then grown in medium supplemented with 40 μM ganciclovir (#G2536, Sigma-Aldrich) for 8 to 10 days until single colonies appeared. Single colonies were picked and

grown in the absence or presence of 200 ng/ ml doxycycline hyclate (#D9891, Sigma-Aldrich) to induce *ScPPX* protein expression. The expression of NLS-3× FLAG-*ScPPX* was verified with Western Blotting using a mouse anti-FLAG M2 antibody (#F3165, Sigma-Aldrich). All vectors were kind gifts of Dr. J. Nandakumar, University of Michigan.

2.2.10 *Ex vivo ScPPX activity assay*

NLS-3× FLAG-*ScPPX* transgenic HeLa EM2-11ht cells were seeded in a 6-well plate at the density of 1.5×10^5 cells/ well. The next day, expression of *ScPPX* was induced with 200 ng/ ml doxycycline for 48 hours, after which 25 μ M cisplatin was added, and cells were incubated for another 24 hours. Cells were detached using 0.25% Trypsin-EDTA, collected with PBS and spun down at 300 g at room temperature for 5 minutes. The pellet was washed once with 100 μ l lysis buffer: 20 mM Tris-HCl pH 7.5, 50 mM NaCl, 2 mM EDTA, 1% IGEPAL[®] CA-630 (#I8896, Sigma-Aldrich), cOmplete[™], EDTA-free Protease Inhibitor Cocktail (#5056489001, Sigma-Aldrich), 12.5 units/ ml Pierce[™] Universal Nuclease for Cell Lysis (#88702, Thermo Scientific) and spun down at 300 g at 4°C for 5 minutes. The pellet was resuspended in 100 μ l lysis buffer, and cells were lysed by sonication at 4°C. The activity of *ScPPX* was measured using the EnzChek[®] Phosphate assay kit (#E6646, Thermo Fisher Scientific) following the manufacturer's instructions. As substrate for *ScPPX*, 150 μ M polyP₁₃₀ was added to the reaction mix, and the release of phosphate was monitored by absorbance reading in a Synergy HTX multi-mode microplate reader (BioTek, Winooski, VT, USA). For the normalization of input, the protein amount of each sample was measured using the DC[™] protein assay (#5000112, Bio-Rad Laboratories, Hercules, CA, USA) following the manufacturer's instructions, and absorbance was determined at 700 nm in a BMG FLUOstar Omega microplate reader (Ortenberg, Germany). The specific activity of *ScPPX* was calculated from the initial rate of polyP₁₃₀ degradation and the protein concentration of the cell lysate.

2.2.11 Statistics

If not noted otherwise, the average of $N > 3$ biological replicates and the s.e.m. are plotted. Graphing and statistics were performed using GraphPad Prism 7 (San Diego, CA, USA). Number of replicates and significance level are found in each figure legend.

2.3 Results

2.3.1 Cisplatin treatment triggers polyP accumulation in cancer cells

To study the effects of cisplatin treatment on the levels and distribution of polyP in cancer cells, we treated the cervical cancer cell line HeLa EM2-11ht (from here on referred to as HeLa) with 0, 5, 15, and 25 μM cisplatin for 12 and 24 hours, and visualized endogenous polyP using the specific probe GFP-*EcPPXc*. This fusion protein consists of the C-terminal polyP-binding domain of *Escherichia coli* exopolyphosphatase (*EcPPXc*) (144,147) and the fluorescent protein GFP. Staining of fixed cells with GFP lacking the *EcPPXc* domain revealed a negligible background signal in both untreated and cisplatin-treated cells (Fig. S2.1A). In contrast, however, staining with the polyP-specific probe GFP-*EcPPXc* revealed polyP signals in the nucleus of unstressed HeLa cells (Fig. 2.1A). These signals dramatically increased upon cisplatin treatment in a dose- and time-dependent manner and presented themselves as distinct and bright nuclear foci (Fig. 2.1A). The apparent cisplatin-induced accumulation of endogenous polyP was significant and consistent across experiments (Fig. 2.1B) as well as in another HeLa clone obtained from the American Type Culture Collection (Fig. S2.1B). In-depth quantification of the distribution and intensity of nuclear polyP puncta of four experiments revealed that following cisplatin stress (red symbols and bars) the number of polyP puncta per cell drastically decreased (Fig. S2.1C, top panel) while the size of the puncta (Fig. S2.1C, middle panel) and their fluorescence intensity (Fig. S2.1C, bottom panel) significantly increased. These results indicate that the cellular polyP pool not only increases but significantly rearranges its subcellular localization upon cisplatin exposure.

To characterize the viability of the cells following the treatment, we focused on treatment conditions which led to the most profound changes in cellular polyP in HeLa cells, that is, 25 μM cisplatin treatment for 24 hours. We observed that this treatment was sufficient to significantly impair the proliferation of HeLa cells, causing a 60% reduction in cell numbers compared to the untreated control (Fig. 2.1C). Cisplatin-treated cells also displayed, on average, a 5-fold induction of cell death as measured by the percentage of Annexin V and Propidium Iodide-positive cells (Fig. 2.1D) as well as Trypan Blue-positive cells (Fig. S2.1D). Moreover, treatment with cisplatin caused a 3-fold increase in both caspase-3 and caspase-7 activities (Fig. 2.1E), doubled the amount of cleaved caspase-3 (Fig. S2.1E), and elevated the levels of the tumor suppressor p53 when compared to the untreated control (Fig. 2.1F). Based on these results, we concluded that the

cisplatin treatment we used to trigger a robust polyP response concomitantly inhibits proliferation and induces cell death through caspase activation and p53 stabilization in HeLa cells.

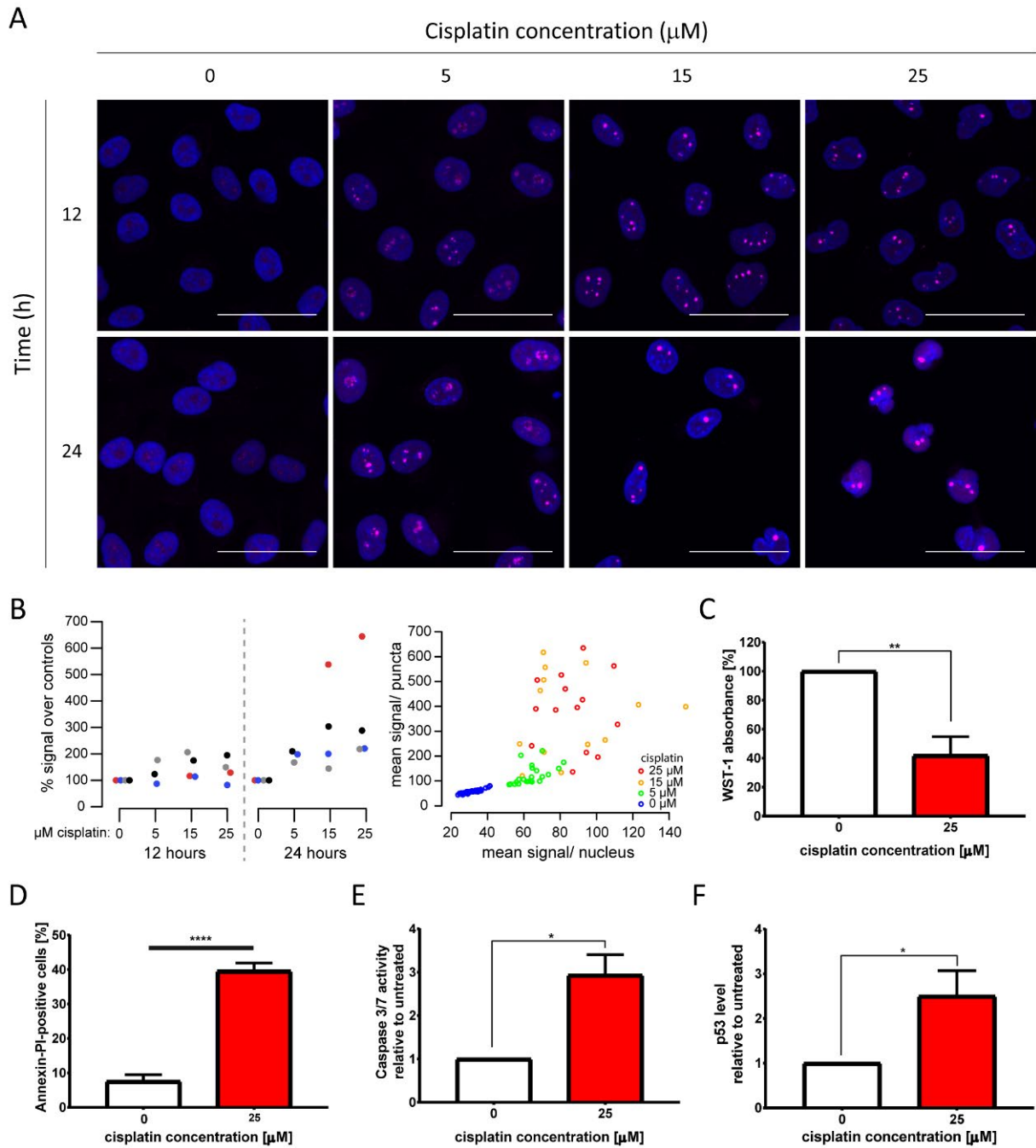


Figure 2.1 Cytotoxic cisplatin treatment triggers formation of nuclear polyP foci. (A) Visualization of endogenous polyP levels and distribution in HeLa cells treated with 0, 5, 15, and 25 μM cisplatin for 12 and 24 hours, respectively. The overlay of GFP-*EcPPXc* signal (magenta) and DAPI signal (blue) reveals the nuclear localization of polyP. Representative images of projected z series are displayed. Scale bar: 50 μm . (B) Quantification of polyP levels following the same cisplatin treatments as those described in (A). Left: Four replicate experiments are shown, color coded by experiment. (Mean GFP-*EcPPXc* signal increased as [cisplatin] increased: $p = 0.0367$ at 24 hours by repeated measures ANOVA. Measurements at 12 hours were not significantly different. Right: From one representative experiment, the mean GFP-*EcPPXc* signal of the puncta regions is plotted against the mean value of the non-puncta regions of each nucleus. (C-F) Evaluations of cell viability after 25 μM cisplatin treatment for 24 hours (red bars). (C) Proliferation was determined by WST-1 assay (N= 6, mean + s.e.m., unpaired t-test, **: $p=0.0011$). (D) Percentage of Annexin V and PI-positive cells was measured by flow cytometry (N= 4, mean + s.e.m., unpaired t-test, ****: $p<0.0001$). Apoptosis induction was monitored by (E) activity of caspases 3 and 7 (N=3, mean + s.e.m., unpaired t-test, *: $p=0.0147$), and (F) p53 level (N= 6, mean + s.e.m., unpaired t-test, *: $p=0.0241$).

2.3.2 Cisplatin treatment leads to nucleolar polyP foci formation

By using the nuclear DNA stain DAPI as reference, we found that cisplatin-induced polyP foci mainly localized to the nucleoli of HeLa cells (Fig. 2.1A). To further investigate the subcellular localization of polyP following cisplatin treatment, we co-stained control and cisplatin-treated HeLa cells with GFP-*EcPPXc* and an antibody against nucleophosmin (NPM1), a protein localized to the granular component of the nucleoli (148). In untreated HeLa cells, we did not observe any significant overlap of GFP-*EcPPXc* fluorescence with NPM1 antibody signal (Fig. 2.2A, left panel, and Fig. S2.2A for controls). Upon cisplatin exposure, NPM1 re-localizes within the nucleus, like polyP. However, in contrast to polyP, NPM1 diffuses into the nucleoplasm and hence does not co-localize with polyP (Fig. 2.2A, right panel). These results excluded the possibility that polyP is enriched in the granular component of the nucleoli. To test whether polyP localizes to the fibrillar center or dense fibrillar component, sub-compartments of the nucleolus in which rDNA transcription and early processing take place (148), we conducted similar co-staining experiments but used an antibody against RNA polymerase I (Pol I), a component of the fibrillary center of nucleoli instead (149). As shown in Fig. 2.2B (and Fig. S2.2B for controls), we found a significant, albeit partial overlap between polyP (magenta) and RNA Pol I (cyan) fluorescence upon cisplatin treatment. These results were consistent with previous studies which showed co-localization of polyP and RNA Pol I in myeloma cells (38). Interestingly, the authors also observed a direct inhibition of RNA Pol I activity by polyP *in vitro*. Given that cisplatin is known to halt rRNA transcription in the concentration range of 25 to 100 μM *in vivo* (150), our finding that polyP and RNA Pol I are in close proximity after cisplatin treatment suggests that polyP and RNA Pol I might be physically interacting and/or functionally related. Yet, more vigorous biochemical analyses are needed to test this hypothesis.

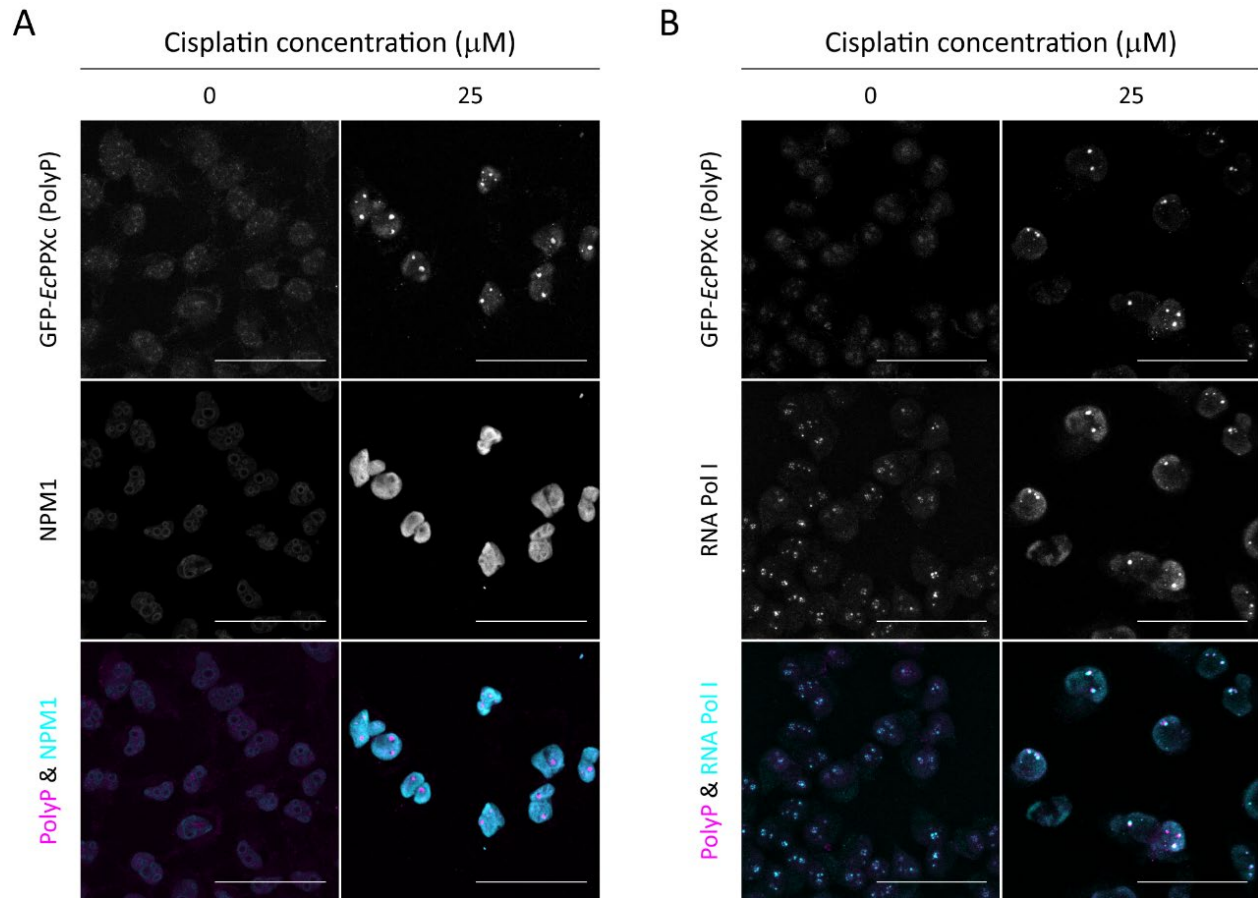


Figure 2.2 Cisplatin-induced polyP foci are adjacent to RNA Pol I in the nucleolus. Co-staining of untreated and cisplatin-treated HeLa cells with GFP-*EcPPXc* and (A) an NPM1 antibody or (B) an RNA Pol I antibody. The overlay of polyP (magenta) and the respective nucleolar marker (cyan) is shown to illustrate the localization of polyP foci in the nucleolus. Representative images of projected z series are displayed. Scale bar: 50 μm . The corresponding control images labeled with GFP and the fluorescent secondary antibodies are shown in Fig. S2.2, A and B.

2.3.3 Cisplatin-induced polyP response positively correlates with cellular toxicity

Microscopic analysis of cisplatin-treated cells revealed a significant cell-to-cell variation in polyP staining after treatment with 25 μM cisplatin for 24 hours. Intriguingly, we also observed significant cell-to-cell variation in the cleaved caspase-3 signal, suggesting a potential correlation between polyP levels and cleaved caspase-3 signal (and hence initiation of apoptosis). To investigate whether a correlation between polyP levels and cleaved caspase-3 levels exists, we determined the amount of cleaved caspase-3 signal and that of mCherry-*EcPPXc* signal after cisplatin treatment in four independent experiments using between 12 and 46 individual cells per experiment. These measurements revealed that, on average, cells with higher polyP levels have increased levels of cleaved caspase-3 (Fig. 2.3A). It is of note that cisplatin-induced cleaved caspase-3 and polyP do not co-localize to the same cellular compartment after 24 hours of cisplatin

exposure (Fig. S2.2C), rendering a direct interaction between the two molecules very unlikely.

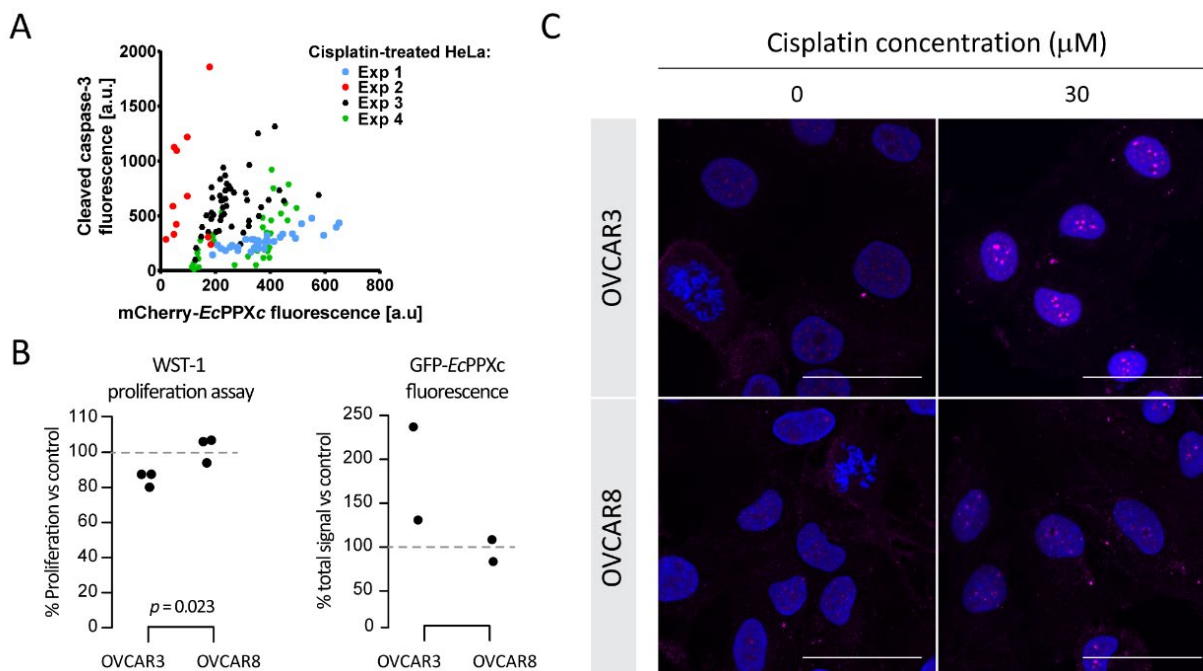


Figure 2.3 Correlation between cisplatin-induced polyP accumulation and cellular toxicity. (A) Correlation of polyP levels and cleaved caspase-3 levels in individual HeLa cells treated with 25 μM cisplatin for 24 hours. Four different experiments were conducted, and symbols of the same color represent cells from the same experiment. (B) A positive correlation between nuclear polyP levels and cisplatin-triggered proliferation inhibition in ovarian cancer cells. Cisplatin-sensitive cell line OVCAR3 and cisplatin-resistant cell line OVCAR8 were treated with 30 μM cisplatin for 8 hours. Cisplatin toxicity was indicated by reduced viability of cisplatin-treated cells with the WST-1 assay (left panel). P-values were derived from two-tailed T-tests. And average nuclear polyP levels, normalized to untreated controls, were measured by GFP-EcPPXc fluorescence intensity (right panel). (C) Visualization of endogenous polyP in ovarian cancer cells with varying degrees of cisplatin sensitivity. OVCAR3 and OVCAR8 cells were subject to the same treatment as that in (B). Images from a representative experiment are shown to demonstrate the distinct polyP responses of OVCAR3 and OVCAR8 cells to cisplatin, revealed by the different intensities and distribution of GFP-EcPPXc signals (magenta). Nuclear DNA was labeled with DAPI. Representative images of projected z series are displayed. Scale bar: 50 μm .

The observed positive correlation between cisplatin-mediated polyP accumulation and apoptosis initiation in HeLa cells prompted us to explore other cancer cells with intrinsically different sensitivities to cisplatin and compare their polyP responses after the drug treatment. Based on IC_{50} values reported in the literature, ovarian cancer cell line OVCAR3 is 1.4 to 2-fold more susceptible to cisplatin than the ovarian cancer cell line OVCAR8 (151,152). We confirmed these results with WST-1 proliferation assays, which showed that OVCAR8 cells are indeed more resistant to cisplatin treatment compared to OVCAR3 cells (Fig. 2.3B, left panel). Similar to HeLa cells, both ovarian cancer cell lines responded to cisplatin treatment with a dose- and time-dependent increase in nuclear polyP levels as well as the formation of distinct nucleolar polyP foci (Fig. S2.3, A and B). However, and in agreement with our previous results, the extent to which OVCAR8 cells responded to cisplatin treatment with the upregulation and redistribution of polyP was much less

pronounced compared to OVCAR3 cells (Fig. 2.3B, right panel and Fig. 2.3C). In fact, at least twice the amount of cisplatin was necessary to trigger a response in OVCAR8 cells that was comparable to what we observed in OVCAR3 cells (Fig. S2.3, A and B). These results supported our previous conclusion that cisplatin-mediated polyP accumulation and rearrangement positively correlate with the level of apoptosis induction and hence cisplatin sensitivity. Although the underlying mechanism remains elusive, the dynamic changes of nuclear polyP appear to be a bona fide response to cisplatin-induced toxicity in various carcinomas and related to the susceptibilities of cancer cells to the chemotherapeutic agent.

2.3.4 Exogenous polyP administration increases cisplatin sensitivity of selected cancer cells

Based on our observation that the accumulation of endogenous polyP correlates with the induction of apoptosis upon cisplatin exposure (Fig. 2.3), we investigated whether manipulating cellular polyP levels would alter cisplatin sensitivity. Unfortunately, the genetic manipulation of *in vivo* polyP levels in mammalian systems is hampered by the fact that the polyP producing and decomposing enzyme(s) are still unknown (1). In an attempt to decrease endogenous polyP levels, we expressed the *S. cerevisiae* exopolyphosphatase (*ScPPX*) under a doxycycline-inducible promoter (145) specifically in the nucleus of HeLa cells. Similar strategies to decrease cellular polyP have been used previously albeit with variable success (18,48,50). We confirmed the doxycycline-induced expression of *ScPPX* in the stable cell clones (Fig. S2.4A), and subsequently, we measured the enzymatic activity of *ScPPX* in cell lysates by monitoring the degradation of chemically synthesized polyP. Comparing *ScPPX* specific activity in cell lysates of untreated cells ($370 \text{ mmol Pi} \cdot \text{min}^{-1} \cdot \text{g}^{-1}$) versus cisplatin-treated cells ($449 \text{ mmol Pi} \cdot \text{min}^{-1} \cdot \text{g}^{-1}$) revealed that the yeast enzyme was fully functional in the presence of cisplatin. However, we failed to observe a greater than 10% reduction in the amount of polyP that accumulated in the *ScPPX*-expressing cells following cisplatin treatment (Fig. S2.4B). As a result, there was no significant difference in the cisplatin-induced proliferation deficiency between the *ScPPX*-expressing cells and their parent cells either (Fig. S2.4C).

Being unable to significantly decrease endogenous polyP levels, we employed the opposite approach and determined whether increasing endogenous polyP levels might alter the cisplatin sensitivity of HeLa cells. We and others have previously shown that mammalian cells readily take up exogenous polyP (Fig. S2.4D) (42). We therefore exposed HeLa cells simultaneously to

cisplatin and exogenous polyP and determined whether polyP supplementation affects the sensitivity of cells toward cisplatin. Indeed, HeLa cells treated with 5 μ M cisplatin in combination with either 200 μ M polyP₁₃₀ or polyP₃₀₀ showed a more severe growth defect compared to those treated with cisplatin alone (Fig. 2.4A). Cytotoxicity assays confirmed these results and showed that the presence of physiologically relevant chain lengths of polyP, that is, polyP₁₃₀ and polyP₃₀₀ significantly increased the efficacy of a higher cisplatin dose, i.e., 25 μ M, in triggering apoptosis and eventually cell death (Fig. 2.4, B and C). Notably, we did not observe any effect when we supplemented cisplatin treatment with shorter polyP chains (polyP₁₄ and polyP₆₀), a finding that was fully consistent with previous reports that physiological chain lengths of polyP (>60 Pi units) are disproportionally more effective than short polyP chains in a variety of polyP functional assays (84). Moreover, we excluded that incubation of cells with polyP in the absence of cisplatin affects cell growth or survival (Fig. 2.4, A-C). To test whether polyP enhances cisplatin efficacy also in other cell lines, we co-treated OVCAR3 cells with both polyP and cisplatin (Fig. 2.4D). Again, we observed a significantly increased toxicity of cisplatin when the treatment was combined with polyP. These results strongly suggest that non-toxic, physiologically relevant polyP levels and chain lengths are able to synergistically increase the cytotoxicity of cisplatin in cancer cells.

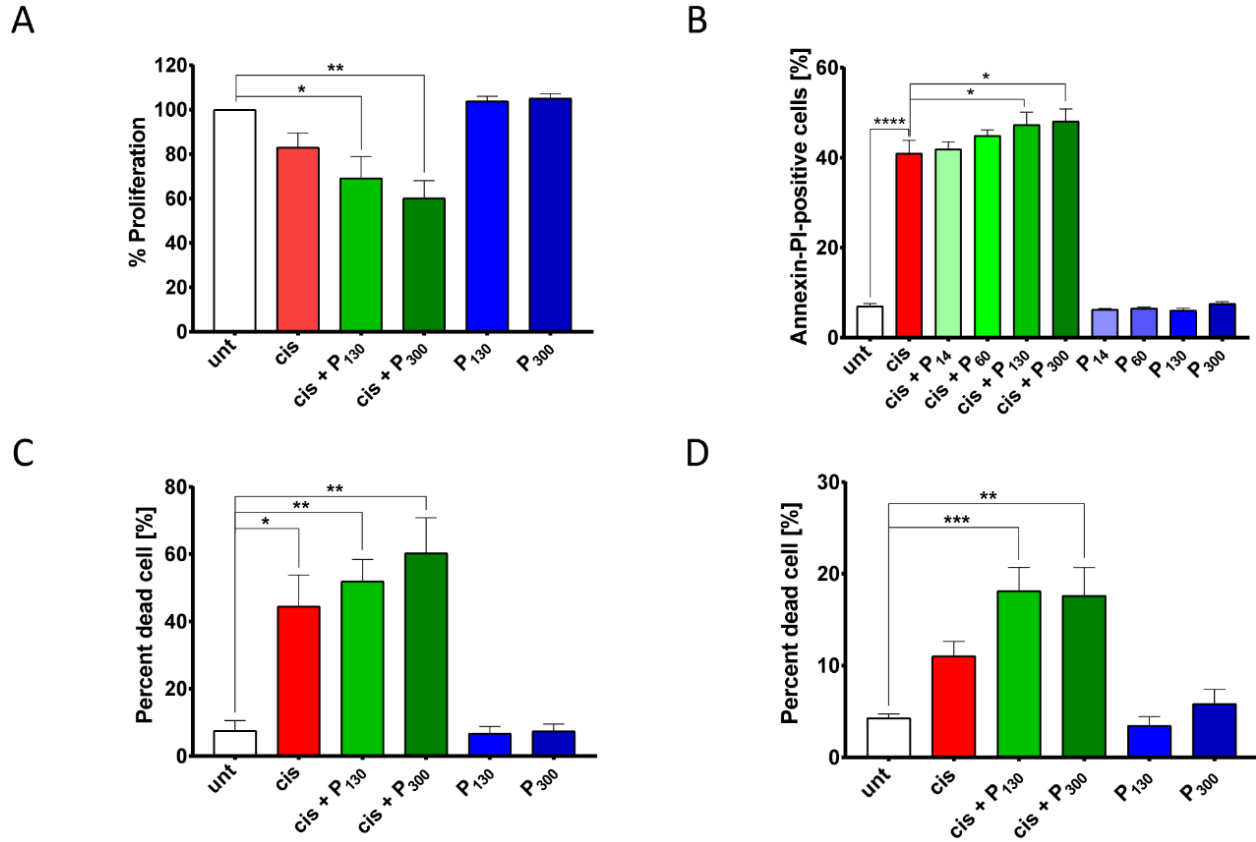


Figure 2.4 Exogenous polyP increases cisplatin-induced cellular toxicity. (A) Proliferation of HeLa cells treated with 5 μ M cisplatin in the absence (red bars) or presence of polyP (green bars) or exposed to 200 μ M polyP₁₃₀ or polyP₃₀₀ only (blue bars) (N = 5, mean + s.e.m). A one-way ANOVA followed by a Tukey multiple comparison test was performed (*: p<0.05; **: p<0.01). (B) Percentage of Annexin V and PI-positive HeLa cells following the combined treatment of 25 μ M cisplatin and 200 μ M exogenous polyP₁₄₋₃₀₀ (shades of green) compared to cisplatin only treatment (red bar) and polyP alone control (blue bars) (N=7, mean + s.e.m., one-way ANOVA with Dunnett's multiple comparison, *: p<0.05; ****: p<0.0001). (C) Percentage of SYTOX Green-permeable (i.e., dead) HeLa cells simultaneously treated with 25 μ M cisplatin and 200 μ M polyP₁₃₀ or polyP₃₀₀ (green bars). Treatment with 25 μ M cisplatin alone is shown in red and the polyP only control is shown in blue (N = 3; mean + s.e.m.). A one-way ANOVA followed by a Tukey multiple comparison test was performed (*: p<0.05; **: p<0.01). (D) Percentage of SYTOX Green-permeable (i.e., dead) ovarian cancer cell line OVCAR3 simultaneously treated with 25 μ M cisplatin and 200 μ M polyP₁₃₀ or polyP₃₀₀ (green bars), or exposed to either 25 μ M cisplatin (red bar) or polyP only (blue bars) (N = 3; mean + s.e.m.). A one-way ANOVA followed by a Tukey multiple comparison test was performed (**: p<0.01; ***: p<0.001).

2.4 Discussion

In this study we discovered that several different cancer cell lines respond to cisplatin treatment with the accumulation of endogenous polyP (Fig. 2.1 and Fig. S2.3), whose relative cellular levels appeared to directly correlate with apoptosis induction and cell death. Cisplatin treatment seemed to trigger both new polyP synthesis as well as subcellular reorganization of polyP pools into distinct nucleolar foci, coinciding with a general cisplatin-induced reorganization of the nucleoli. These membraneless compartments, which are the birthplace of the ribosomes, have previously been shown to be sensitive to perturbations in metabolic rates, cellular stress, and DNA damage (148,153). Here, we report the identification of cisplatin-induced polyP foci primarily in the

fibrillar center and dense fibrillar component, the regions of rDNA transcription and early processing (148). These results suggested that polyP might be involved in the process and/or regulation of ribosomal RNA synthesis, a conclusion that was further supported by our findings that polyP partially co-localizes with RNA Pol I upon cisplatin stress (Fig. 2.2). Intriguingly, previous unrelated studies showed 1) that polyP directly inhibits RNA Pol I activity *in vitro* (38) and 2) that cisplatin treatment inhibits the activity of RNA Pol I *in vivo* (154). Based on our results and the finding that cisplatin-induced polyP levels and apoptosis induction are directly linked, it is now tempting to speculate that cisplatin-induced polyP accumulation affects the activity of RNA Pol I, thereby activating the apoptotic program. It is of note that reduction of RNA Pol I-mediated transcription triggers p53-mediated apoptosis in lymphoma cells but not in non-tumor cells (155). This specificity raises the intriguing possibility that polyP might affect RNA Pol I activity and enhance cisplatin toxicity specifically in cancer cells. In support of this notion, a recent report found that the administration of polyP triggered apoptosis in human colon cancer but failed to induce apoptosis in primary cultures of murine small intestinal epithelial cells (156).

In support of our hypothesis that polyP plays a role in inducing and/or regulating the progression of apoptosis following cisplatin stress, we found that cells with higher levels of endogenous polyP had, on average, higher levels of apoptosis (Fig. 2.3). Cleaved caspase-3 and cisplatin-induced polyP puncta, however, do not localize to the same compartment (Fig. S2.2C), raising the question whether polyP acts on other steps in this pathway. The nucleolus has long been implicated to partake in the execution of apoptosis (157). Intriguingly, many nucleolar proteins, including topoisomerase I (Top1), a potential substrate of caspase-3 (158,159), have recently been found to be polyphosphorylated, a novel post-translational modification characterized by the addition of polyP chains to lysines (47). Functioning as a molecular switch, polyphosphorylation not only appears to mediate the translocation of substrates in and out of the nucleolus but also governs their functional activities. Hence it will be of interest to determine whether accumulation of polyphosphorylated components lead to the observed puncta formation and contribute to the mechanism by which polyP modulates the course of apoptosis.

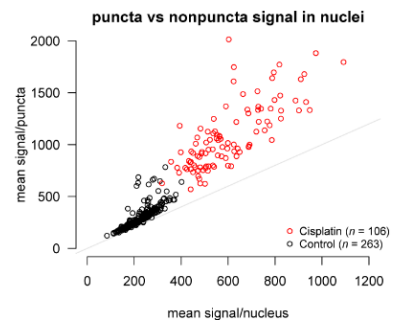
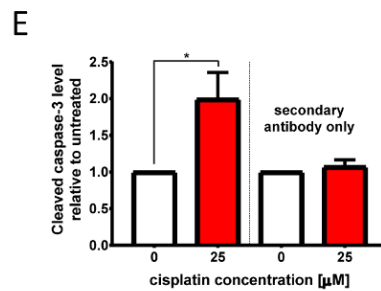
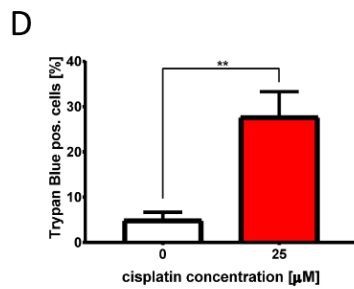
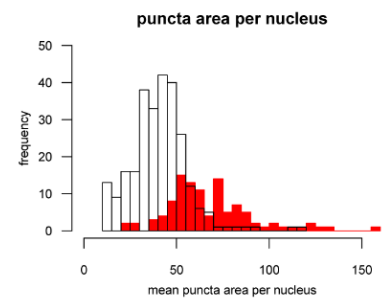
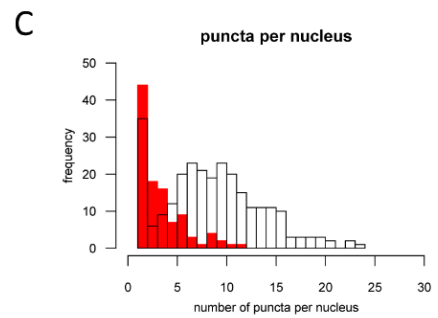
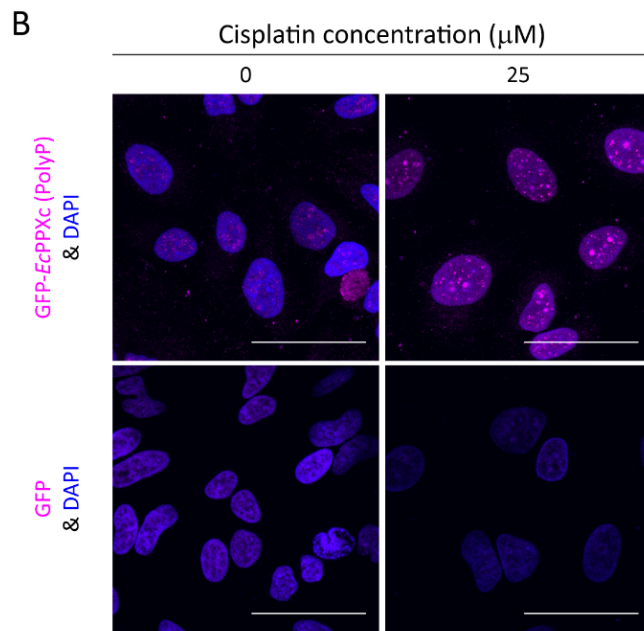
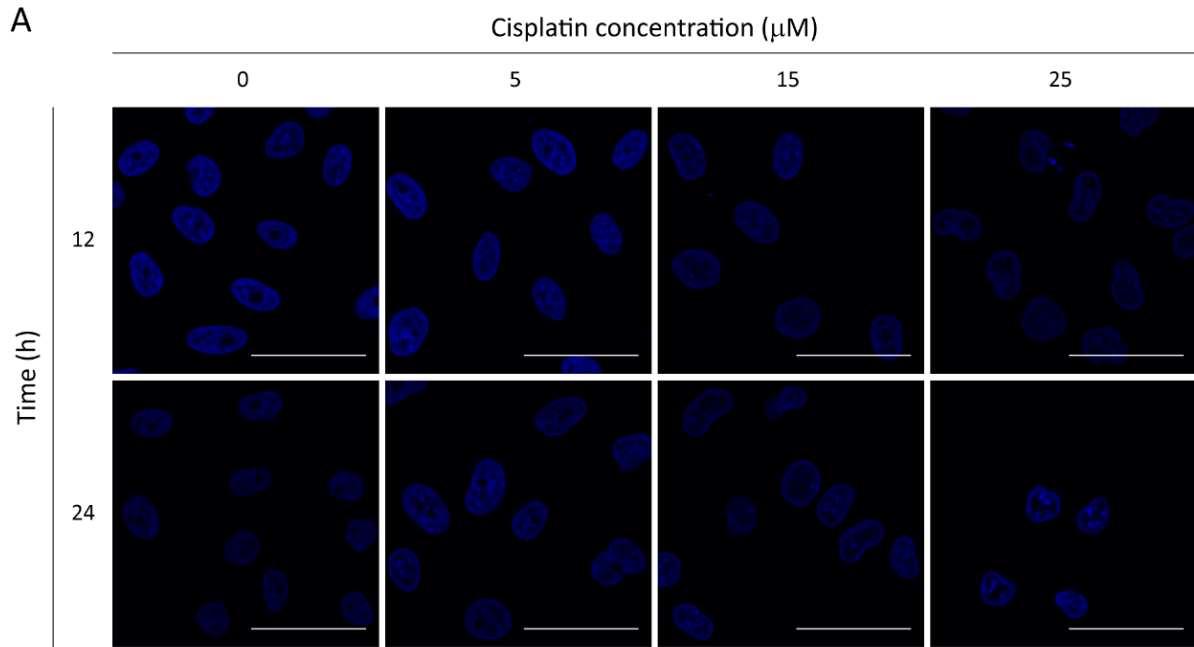
Our observation that cleaved caspase-3 and endogenous polyP levels positively correlate now raises the fundamental question whether cells that innately generate more polyP are more sensitive to cisplatin (i.e., polyP being a mediator of apoptosis), or whether cells that are more sensitive to cisplatin accumulate more polyP (i.e., polyP being a “by-product” of apoptosis induction). A key

experiment that would help to answer this question is to test the cisplatin sensitivity of polyP-depleted cells. However, the process of how polyP is generated in mammalian cells has yet to be discovered (1). Unable to manipulate the mammalian players of polyP synthesis, we therefore attempted to modulate endogenous polyP by expressing a polyP-degrading enzyme from yeast (18). This approach, however, was unsuccessful in reducing endogenous polyP levels or affecting cisplatin sensitivity in our study (Fig. S2.4). Since the inability to reduce cellular polyP levels was not due to potential inhibitory effects of cisplatin on the enzymatic activity of *ScPPX*, we now speculate that cisplatin-induced polyP might either not be accessible to exopolyphosphatases *in vivo* (160), or that the spatial confinement of polyP in the interior of the nucleolus might protect polyP from *ScPPX* (50). Indeed, when we probed the subcellular localization of polyP and *ScPPX*, we found that the two molecules did not partition to the same region in the nucleus. While endogenous polyP was highly enriched in the nucleolus, *ScPPX* was most abundant in the cytosol and nucleoplasm (Fig. S2.4E). Furthermore, we cannot rule out the possibility that the polyP-degrading enzyme, *ScPPX*, and the polyP-binding probe, *EcPPXc*, recognize different fractions of polyP in the cells. The former might be capable of scavenging soluble polyP (exemplified by polyP in the mitochondrial matrix) (15), whereas the latter might selectively bind complexed polyP retained in the protein network after paraformaldehyde fixation.

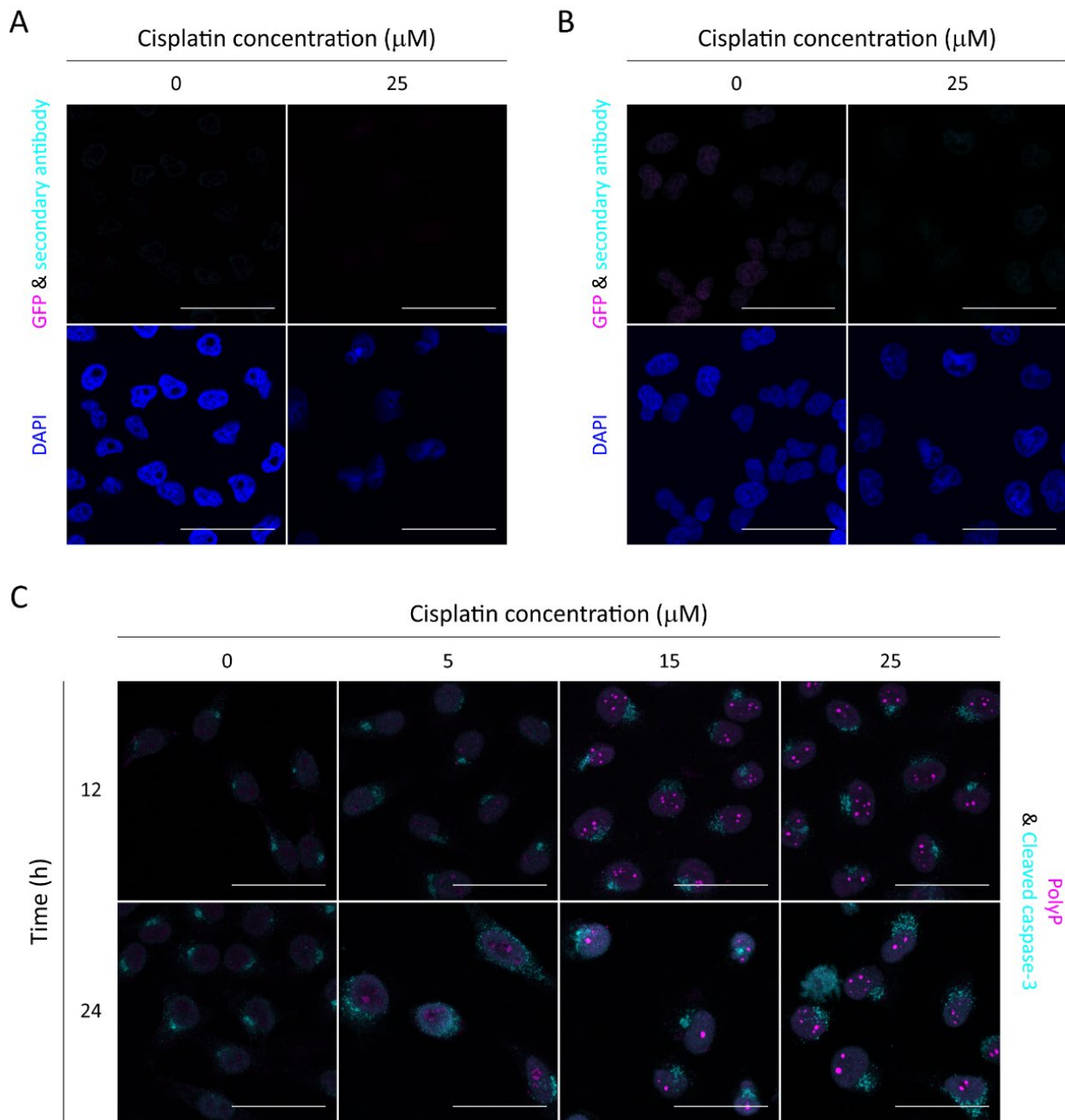
We then took the opposite approach and increased polyP levels by incubating cells with exogenous polyP chains, which are routinely taken up by mammalian cells. These experiments revealed that increasing the levels of polyP in cells did indeed increase cisplatin-mediated toxicity in a chain length-dependent manner (Fig. 2.4). While the polyP-mediated augmentation of cisplatin toxicity was highly reproducible and significant, the relative increase in cytotoxicity was considered modest and ranged between 5-10%. However, we would like to emphasize that supplementation of exogenous, synthetic polyP is an imperfect approach to modify intracellular polyP distribution and/or abundance. In fact, when we monitored the subcellular localization of fluorescently labeled polyP₃₀₀ chains, it was evident that they did not fully recapitulate the nucleolar localization of endogenous polyP fractions (Fig. S2.4D). Hence, we expect much more pronounced enhancement of cisplatin potency by polyP once we will be able to genetically manipulate endogenous polyP levels. Nevertheless, our results are supported by published reports, which showed that supplementation of lung cancer cells with exogenous polyP increased radiation-induced DNA double strand breaks and decreased cell survival (161). Moreover, the pro-metastatic protein h-

Prune, whose expression correlates with lung cancer progression, has been shown to be a short-chain exopolyphosphatase *in vitro* (143,162). Taken together, these findings suggest that mammalian cancer cells might have acquired mechanisms to regulate their cellular polyP levels and hence their drug resistance. Therefore, a strategy to increase polyP levels might be a promising avenue in the attempt to sensitize cancer cells to cisplatin treatment. This, however, requires the ultimate breakthrough in polyP research, namely the discovery of the mammalian polyP regulatory machineries and the development of pharmacological tools to target them efficiently and specifically.

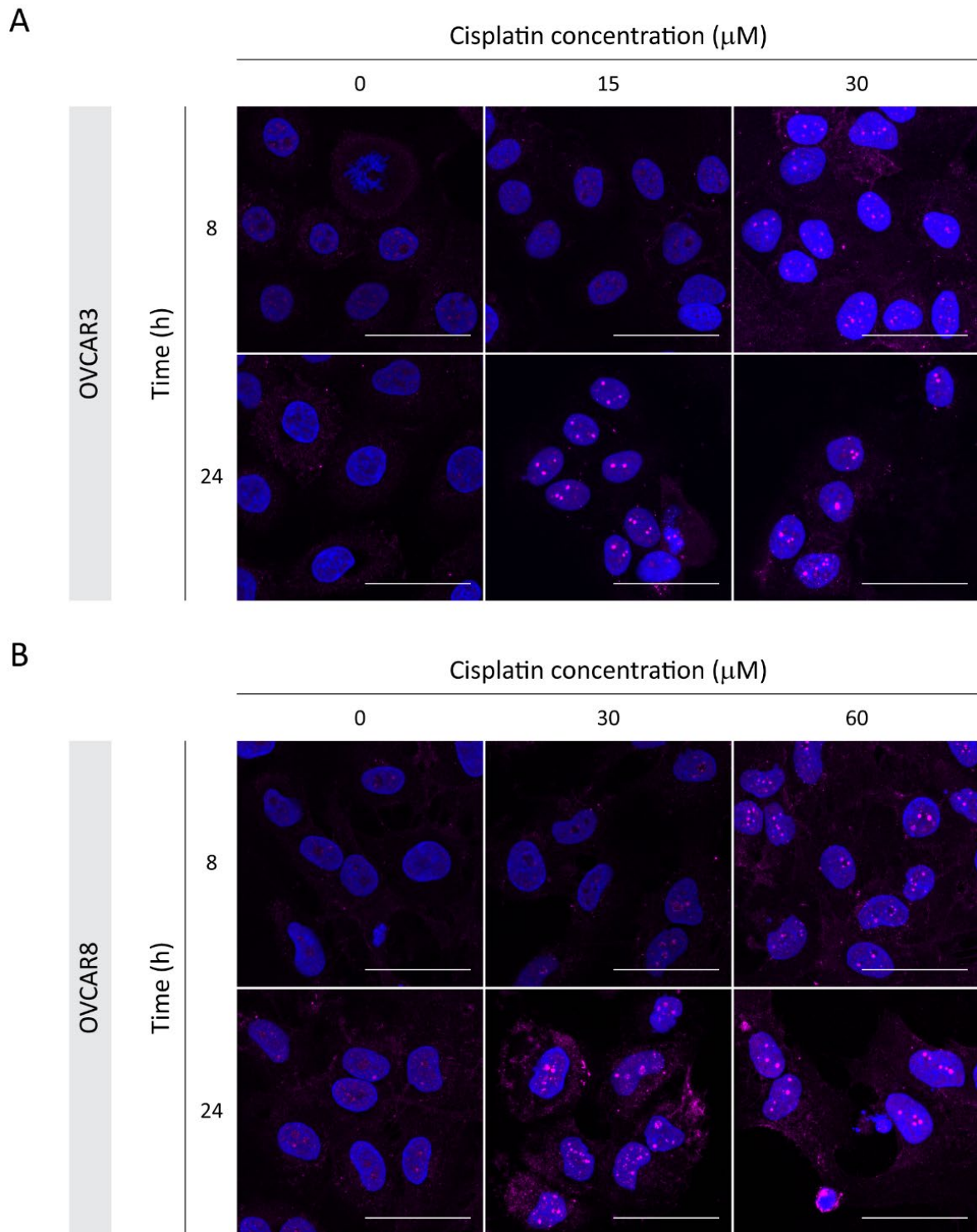
2.5 Supplemental information



Supplementary Figure 2.1 Cytotoxic cisplatin treatment causes polyP foci formation in cancer cells. (A) Control images of HeLa cells labeled with GFP, instead of GFP-*EcPPXc*, after various cisplatin treatments. Signal in the GFP channel (magenta) was negligible, indicating a very low level of unspecific binding of the GFP-*EcPPXc* probe. DAPI (blue) was used to locate the cell nuclei. Representative images of projected z series are displayed. Scale bar: 50 μm . (B) PolyP accumulation and foci formation in HeLa-ATCC cells following cisplatin treatment. An overlay of GFP-*EcPPXc* (magenta) and DAPI (blue) signals revealed the newly formed polyP foci in the nucleus of cisplatin-treated cells. This phenomenon is polyP-specific, as no such changes were observed with GFP labeling. Representative images of projected z series are displayed. Scale bar: 50 μm . (C) Quantification of polyP foci in untreated HeLa cells (white bars and symbols) and cells treated with 25 μM cisplatin for 24 hours (red bars and symbols). There is a change in the number (top panel), area (middle panel), and fluorescence intensity (bottom panel) of polyP foci upon cisplatin exposure. A representative analysis is shown. Welch Two Sample t-tests were performed, and the FDR-adjusted p-values for the representative experiment are displayed. (D) Cisplatin-induced cell death measured by Trypan blue staining. (N = 7, mean + s.e.m., unpaired t-test, **: p=0.0021). (E) Apoptosis induction monitored by the increased levels of cleaved caspase-3 immunofluorescence. (N= 9, mean + s.e.m., unpaired t-test, *: p=0.0148). No significant changes were observed in the unspecific binding of the fluorescent secondary antibody alone.

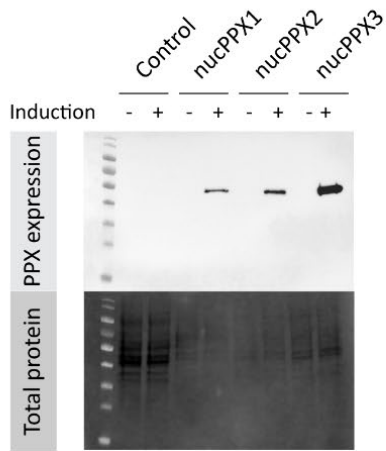


Supplementary Figure 2.2 Cellular localization of polyP and cleaved caspase-3 after cisplatin treatment. (A and B) HeLa cells, untreated or treated with 25 μM cisplatin for 24 hours, were labeled with GFP and the corresponding fluorescent secondary antibodies for (A) NPM1 and (B) RNA Pol I stainings. An overlay of GFP (magenta) and the secondary antibody signal (cyan) is shown to assess the levels of unspecific binding. Nuclear DNA, illustrated by DAPI fluorescence, was used to locate the cells. Representative images of projected z series are displayed. Scale bar: 50 μm . (C) Co-staining using GFP-*EcPPXc* (magenta) and a cleaved caspase-3 antibody (cyan) depicted the dose- and time-dependence of apoptosis induction in HeLa cells triggered by cisplatin and revealed distinct localization of polyP and cleaved caspase-3 in the cells. Representative images of projected z series are displayed. Scale bar: 50 μm .

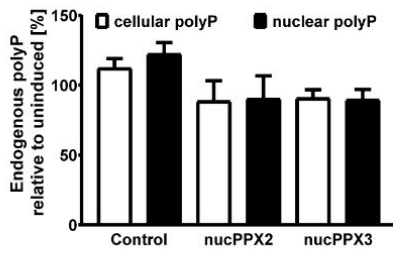


Supplementary Figure 2.3 Dose- and time-dependence of cisplatin-induced polyP response in ovarian cancer cells. (A) Cisplatin-sensitive ovarian cancer cell line OVCAR3 and (B) cisplatin-resistant ovarian cancer cell line OVCAR8 were treated with increasing concentrations of cisplatin for 8 and 24 hours and labeled with GFP-*EcPPXc* (magenta) to monitor the changes in polyP levels and distribution. Nuclear DNA was revealed by DAPI fluorescence (blue). Representative images of projected z series are displayed. Scale bar: 50 μm .

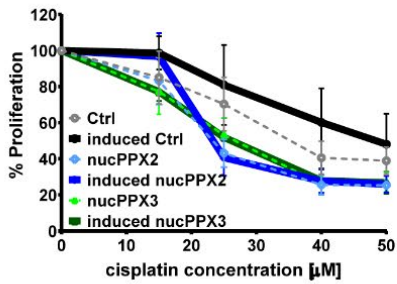
A



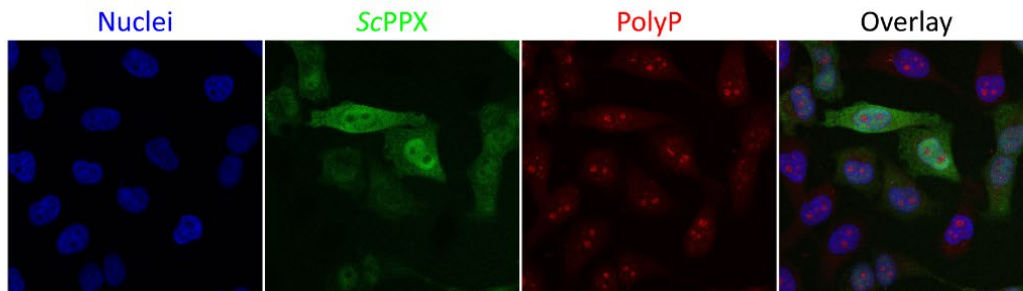
B



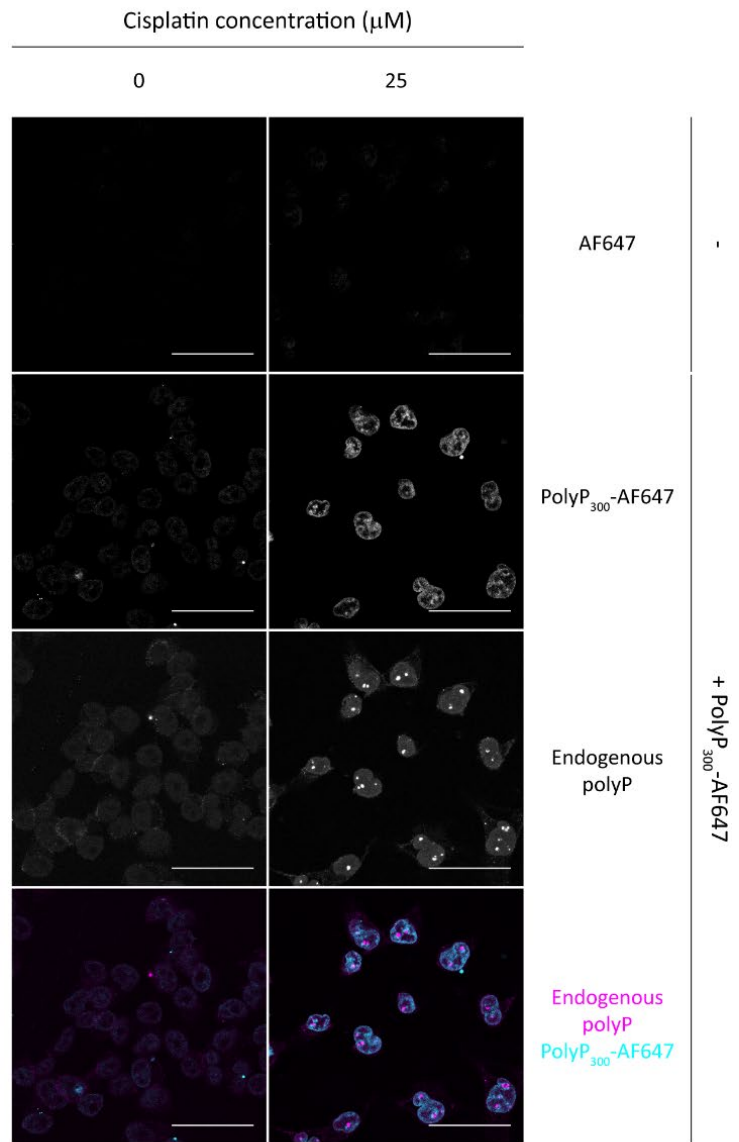
C



E



D



Supplementary Figure 2.4 Manipulation of intracellular polyP levels and distribution in HeLa cells. (A) Western Blotting analysis of doxycycline-induced FLAG-tagged *ScPPX* expression in the nucleus of normal HeLa cells (Control) and three independent clones of stably transfected HeLa cells with FLAG-tagged *ScPPX* (nucPPX1-3). The signal of anti-FLAG antibody is shown in the top panel. The Bio-Rad Mini-PROTEAN® TGX Stain-Free™ protein gel allowed visualization of the amount of cell lysates run on the gel (bottom panel). (B) Quantification of endogenous polyP levels in the total cell (white bar) and in the nucleus (black bars) following the induction of *ScPPX* expression. PolyP levels were normalized to the corresponding non-induced samples. The average and s.e.m. of 3 experiments for the wildtype control and two stable clones are shown. (The nucPPX1 clone did not show any effect in two biological replicates). (C) Proliferation of normal HeLa cells (black and gray) and *ScPPX* stable clones (blue and green) upon cisplatin exposure. *ScPPX* expression was induced by doxycycline (solid lines) and compared to the non-induced samples (dashed lines). The average of 4 experiments and the s.e.m. are displayed (The nucPPX1 clone has been tested twice and showed similar results). (D) Uptake and redistribution of fluorescently labeled polyP in parallel to cisplatin treatment. 200 μ M Alexa Fluor 647-labeled polyP₃₀₀ was supplemented to HeLa cells in the absence or presence of 25 μ M cisplatin for 24 hours. The cellular localization of endogenous polyP (labeled with GFP-*EcPPXc*, magenta) and that of exogenous polyP (Alexa Fluor 647-labeled, cyan) seemed to be different. (E) Subcellular localization of polyP and transiently expressed *ScPPX* in HeLa cells. An overlay of the fluorescence signal of anti-FLAG antibody (green), mCherry-*EcPPXc* (red), and DAPI (blue) showed distinct compartmentalization of polyP and FLAG-tagged *ScPPX* in the nucleus of HeLa cells.

Chapter 3 The Dynamic Rearrangement of Nucleolar Inorganic Polyphosphate Is Inflicted by Ribosome RNA Synthesis Stress

3.1 Introduction

Previous work from our lab revealed that endogenous polyphosphate (polyP) accumulates at distinct foci in the nucleolus of various cancer cells upon treatment with the anticancer drug cisplatin (127). Moreover, the extent of polyP accumulation positively correlates with the intrinsic cisplatin sensitivity of the cell. This earlier work also showed that upon uptake of exogenous polyP, selected tumor cells become sensitized to the cisplatin treatment. Taken together, these findings suggest that polyP is a downstream effector of cisplatin, and that alterations in polyP levels might be a novel strategy for cancer interventions. Yet, to explore this idea, we must first understand the mechanistic details as well as the physiological impact of the cisplatin-mediated polyP response in the mammalian cells.

As potent chemotherapeutic agents, platinum-derived drugs, including cisplatin, inflict irreversible damage to the DNA, proteins, and small molecules of proliferating cells (137,139,140,163-165). Then, they activate apoptotic signaling pathways and incur a non-inflammatory type of cell death (129).

Among the list of known cisplatin toxicities, inhibition of rRNA synthesis might be the most promising mechanism to engage polyP (150,154). Based on our and other's results, a portion of polyP and RNA polymerase I (Pol I), the principal source of rRNA, are held in the fibrillar center (FC) of the nucleolus in untreated cells (38). Moreover, we found that upon cisplatin intake, both molecules relocate to the same nucleolar foci where they remain in the vicinity of each other (127). Notably, the cisplatin concentrations needed to mobilize this pair of molecules also coincide with those known to stall rDNA transcription (150,154). Hence, it is now tempting to speculate that polyP and RNA pol I physically and perhaps functionally converge in response to cisplatin stress.

The nucleolus is a multiplex, highly dynamic assembly of over seven hundred proteins and two hundred RNAs (166,167). These molecules are compacted into three independent yet collaborative moieties: the aforementioned fibrillar component (FC), the dense fibrillar component (DFC), and

the granular component (GC) (148). Each of the three regions undertakes a specific task in ribosomal biogenesis: rDNA is transcribed at the border of FC and DFC, and the premature rRNA is processed throughout DFC and GC prior to entering the nucleoplasm (148). In an interphase nucleolus, DFC is sandwiched between FC at the interior core and GC in the outmost layer (Fig. 3.1A). Remarkably, the boundary of each nucleolar compartment is demarcated not by a lipid bilayer but by the incompatible phase properties of itself and its adjacent environment (168). Phase separation is amenable to changes in protein concentration, ionic strength, pH, temperature, and so on (169). Thus, it not only allows free communications between different nucleolar compartments but also enables a prompt structural rearrangement of the nucleolus in reply to various stress stimuli.

So far, at least three types of unconventional nucleolar morphologies have been observed (170). Low doses of actinomycin D (ActD), which arrest rDNA transcription, lead to the formation of a variety of cap structures that line up the periphery of the nucleolus (171) (Fig. 3.1B). Based on their constituents and appearances in the electron microscope, these cap structures are further categorized into dark nucleolar caps, light nucleolar caps, and fibrillar caps. More than a decade ago, the compositions of dark and light nucleolar caps have been elucidated with immunofluorescence labeling (171). As it turns out, dark nucleolar caps are dominated by nucleoplasmic proteins, such as fused in sarcoma (FUS) and PTB-associated splicing factor (PSF), while light nucleolar caps recruit a number of DFC members, including Nopp140 and fibrillarin, which are in charge of premature rRNA processing. The core machineries of rDNA transcription, represented by RNA pol I, upstream binding factor (UBF), TBP-associated factors (TAFs), and DNA topoisomerase I (TOP1) are temporarily stored in the fibrillar caps adjacent to the light nucleolar caps. Notably, this is by no means an exhaustive list of nucleolar segregates formed after ActD treatment. Another protein, coilin, which is a classic Cajal body marker, moves onto the nucleolar surface and occupies what overlaps extensively but not completely with the light nucleolar caps (171,172). Whether coilin belongs to a new type of nucleolar cap structure remains an open question. Yet, this observation signifies an unprecedentedly finetuned structure of the nucleolus, which remains to be fully explored. All the aforementioned caps surround the so-called central body originated from GC and reconfigure the nucleolus in an effort to cope with stalled rRNA gene transcription.

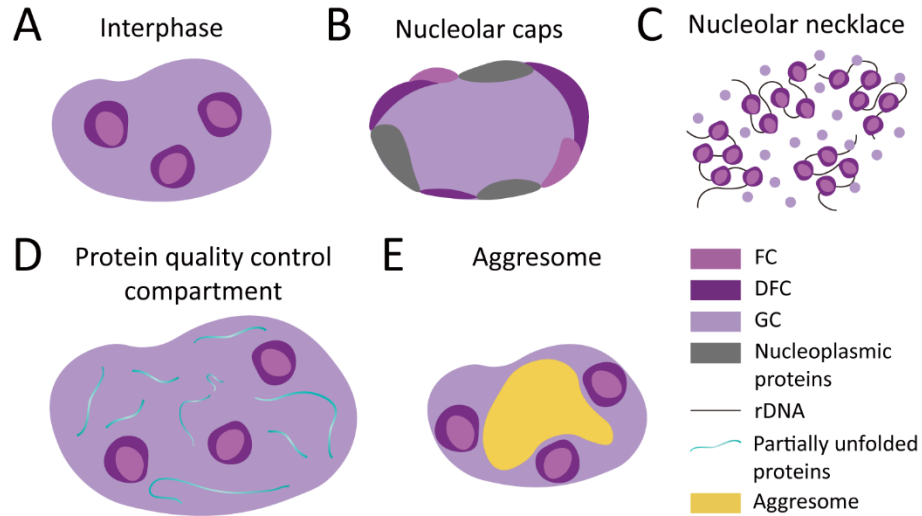


Figure 3.1 Structural organization of the nucleolus. Nucleolus is a multicomponent, phase-separated entity with versatile structural patterns adopted in different cellular environments. **(A)** In an interphase nucleolus, FC, DFC and GC are compacted into three independent layers, with FC at the innermost core and GC on the outer surface. **(B)** Upon RNA pol I inhibition, not only nucleolar proteins but also nucleoplasmic components are recruited to a series of cap structures surrounding the periphery of the nucleolus. Among them, dark nucleolar caps (mainly consisting of nucleoplasmic proteins), light nucleolar caps (made up of DFC members), and fibrillar caps (derived from FC) are the most well characterized examples. **(C)** When late rRNA processing is abolished, the intact nucleolus disappears due to a complete dissipation of GC. Consequently, FC and DFC manifest themselves as interspersed “beads” on a “string” of extended rDNA – a structure denoted as nucleolar necklace. **(D)** In the case of a mild heat shock, which leads to substantial protein unfolding in the nucleoplasm, nearly two hundred aggregation-prone proteins are shuttled to the GC compartment where they will be sorted for either refolding or degradation. Notably, the volume of the nucleolus is enlarged due to an enormous capacity of GC for the arriving folding intermediates. **(E)** Proteasome inhibition causes a different subset of proteins, largely substrates of ubiquitin ligases, to be deposited at the center of the nucleolus, or the so-called aggresomes. Rarely are nucleolar markers found in these segregates, which differs them from the structure formed by GC for the partially unfolded proteins described in (D).

An alternative nucleolar conformation denoted as nucleolar necklace occurs upon inhibition of rRNA processing (173) (Fig. 3.1C). In this scenario, the architectures of FC and DFC appear normal, allowing for an unperturbed yield of premature rRNA. However, the shell-like GC region, which encompasses the late rRNA processing machineries dissolves. This lifts the spatial confinement imposed by GC on the other two compartments, and consequently, an extended piece of rDNA becomes decorated with interspersed FC and DFC granules just like a string running through a cluster of beads. The appearance of the nucleolar necklace is typically observed in cells treated with 5,6-Dichloro-1- β -D-ribofuranosylbenzimidazole (DRB) (173). But it is important to note that, as an adenosine analog, DRB has more than one cellular target, such as P-TEFb and casein kinase 2 (174,175), both of which are critical for RNA pol II transcription rather than rRNA processing.

Most recently, the nucleolus has been identified as a reservoir for metastable proteins when cells are challenged with proteotoxic stress conditions, such as heat shock (176,177), proteasome inhibition (178) or viral infection (due to an overload of newly synthesized proteins) (179). Upon

heat shock, roughly two hundred partially unfolded proteins are accommodated by the GC compartment in a conformation that is fully competent for either Hsp70-mediated refolding or ubiquitination and subsequent degradation (176,177) (Fig. 3.1D). Although it is plausible that uncharacterized ATP-independent chaperones exist in the GC, it is more likely that the intrinsic folding environment of this phase-separated domain is sufficient to confer the chaperone activities that are necessary for this wide spectrum of clients (177). Treatment with the proteasome inhibitor MG132, on the other hand, leads to a massive accumulation of substrates in the so-called nucleolar aggresome (178,180) (Fig. 3.1E). Such inclusions appear to be devoid of nucleolar markers (178), clearly indicating that different types of proteotoxic insults trigger different responses in the nucleolus. How detrimental signals of protein quality are transmitted to the nucleolus remains an open question awaiting further investigation.

In summary, the nucleolus takes advantage of phase separation to obtain the structural versatility required for a prompt response to diverse environmental cues. In this study, we investigated how nucleolar polyP responds to different stress treatments and characterized the nature of cisplatin-induced polyP foci. Our studies showed that polyP might serve as an important signal for rRNA regulation, and this finding deepened our understanding about the physiological functions of nucleolar polyP.

3.2 Materials and methods

3.2.1 Reagents

Cis-Diammineplatinum(II) dichloride (#P4394, Sigma-Aldrich) was dissolved in double distilled water at a stock concentration of 3 mM. Actinomycin D (ActD) (#11421, Cayman Chemical, Ann Arbor, MI, USA) was prepared in DMSO at a stock concentration of 5 mM. 5,6-dichloro-1- β -D-ribofuranosylbenzimidazole (DRB) (#D1916, Sigma-Aldrich) was dissolved in DMSO at 40 mg/ml. And MG132 (#474790, Millipore Sigma) was also solubilized by DMSO to yield a 2.5 mM stock solution. Recombinant human TNF- α in liquid form (#PHC3015L) was purchased from Thermo Fisher Scientific. BV6, an IAP antagonist (#5339650001, Sigma-Aldrich), was dissolved in DMSO to a stock concentration of 10 mM. Z-VAD(OMe)-FMK (#sc311561, Santa Cruz Biotechnology, Dallas, TX, USA), a caspase inhibitor, was reconstituted in DMSO at 20 mM. All the reagents except cisplatin were aliquoted and stored at -20 °C.

A vector containing GFP-*EcPPX_c* was generated in three steps. First, an *EcPPX_c* fragment was

amplified from the pETM41-*EcPPXc* plasmid, which encodes the Maltose Binding Protein (MBP)-*EcPPXc* (kindly provided by Florian Freimoser; Addgene plasmid #38329; <http://n2t.net/addgene:38329>; RRID:Addgene_38329) (144). Then, *EcPPXc* was cloned into a pTEV5 vector between BamHI and NotI restriction sites downstream of mCherry. Finally, mCherry sequence was swapped by GFP gene cloned from pEGFP-N2 plasmid with flanking NdeI and BamHI sites. GFP-*EcPPXc* and the respective control probe, GFP, were purified as His-tagged proteins with Ni-NTA columns (Qiagen, Hilden, Germany).

All reagents were obtained from Thermo Fisher Scientific (Waltham, MA, USA), Sigma-Aldrich (St. Louis, MO, USA), and New England Biolabs (Ipswich, MA, USA) unless stated otherwise.

3.2.2 Cell lines and treatments

HeLa (ATCC[®] CCL-2[™], ATTC, Manassas, VA, USA) cells and mouse embryonic fibroblasts (kindly provided by Dr. Miriam Greenberg at Wayne State University) were grown in DMEM (#11995065, Thermo Fisher Scientific). HeLa Kyoto cells which stably overexpress FUS-GFP (a generous gift from Dr. S. Alberti, Dresden University of Technology) (181) were cultured in DMEM (#10569010, Invitrogen). All media were supplemented with 10% Fetal Bovine Serum (#F4135, Sigma-Aldrich) and 1% Penicillin-Streptomycin (#15140122, Thermo Fisher Scientific). Cells were grown in a humidified incubator at 37°C with 5% CO₂.

An approximately 80% confluent cell monolayer was detached from the flask with 0.05% Trypsin-EDTA (#25300054, Thermo Fisher Scientific). For cytotoxicity assays, cells were plated in a 96-well tissue culture plate (#3596, Corning, Inc., Corning, NY, USA) with 10⁴ cells/ well. For immunofluorescence experiments, cells were seeded at a density of 5×10⁴ cells/ well in a 24-well plate (#3526, Corning, Inc.) containing a piece of coverslip (#CLS-1760-012, Chemglass Life Sciences, Inc., Vineland, NJ, USA) at the bottom of each well. On the next day, spent medium was removed and the fully attached cells were treated with cisplatin, ActD, DRB, MG132, or a combination of TNF- α , BV6, and Z-VAD-FMK (TSZ) with the designated conditions.

3.2.3 Cytotoxicity assays

Cell viability was quantified with the WST-1 Cell Proliferation Assay Kit (#10008883, Cayman Chemical, Ann Arbor, Michigan, USA) with slight modifications of the manufacturer's protocol. Briefly, the WST-1 Developer Reagent and the Electron Mediator Solution were first diluted to

their working concentrations in fresh medium. This mixture was then added to the cells after the supernatant was removed. Samples were incubated at 37 °C for 2 h to develop a stable absorbance signal at 450 nm wavelength which could be read by a BMG FLUOstar Omega Microplate Reader (Ortenberg, Germany). The average absorbance measurements of the drug treated samples were normalized to those of the untreated cells.

SYTOX™ Green Nucleic Acid Stain (#S7020, Thermo Fisher Scientific) was used to assess the extent of cell death. Following the protocol published in (146), two identical sets of samples were prepared. One of them was permeabilized with 120 µM Digitonin (#D141, Sigma-Aldrich) after drug treatment, while the other was undisturbed. Then, 5 µM SYTOX™ Green Nucleic Acid Stain was added to both sets of samples and kept at 37°C for 30 min. The fluorescence of stably incorporated SYTOX™ Green Nucleic Acid Stain only in the membrane compromised cells was measured by a Tecan Infinite M1000 Microplate Reader (Männedorf, Switzerland) set to 504 nm excitation wavelength and 523 nm emission wavelength. The signal intensity of digitonin-treated samples signified the total number of cells. Therefore, the percentage of dead cells in each condition was represented by the ratio of the fluorescence measurement of the unpermeabilized replicate over that of the corresponding digitonin-treated sample.

3.2.4 Immunofluorescence labeling

Control and drug treated cells were fixed with freshly made 4% (v/v) Paraformaldehyde (#1578100, Electron Microscopy Sciences, Hatfield, PA, USA) at room temperature for 20 minutes. After three washes with PBS, they were permeabilized with 0.3% (v/v) Triton X-100 (#0219485480, MP Biomedicals, Solon, OH, USA) for 10 minutes. Triton X-100 was dissolved in blocking buffer, containing 1% (w/v) Bovine Serum Albumin (#A3059, Sigma-Aldrich) in PBS. After three more washes with PBS, cells were incubated in blocking buffer for at least 1 h to prevent nonspecific binding. Endogenous polyP was labeled with GFP-*EcPPXc* (or the respective control probe, GFP) at a concentration of 10 µg/ ml in blocking solution. To label nuclear proteins of interest, the following mouse monoclonal antibodies from Santa Cruz were used – Nopp140 (E-7) (#sc-374033), coilin (F-7) (#sc-55594), UBF (F-9) (#sc-13125), p14 (F-12) (#sc-1661), PML (PG-M3) (#sc-966), and p-Histone H2A.X (Ser-139) (#sc-517348) antibodies. All these antibodies were used at a final concentration of 0.8 µg/ ml in blocking buffer. A rabbit polyclonal antibody for IP6K1 (#HPA040825, Sigma-Aldrich) was applied at 1.4 µg/ ml. A mouse anti-human G3BP

antibody (#611127, BD Biosciences, San Jose, CA; a generous gift from the Barmada Lab at University of Michigan) was used at 1 $\mu\text{g}/\text{ml}$. Samples were double labeled with GFP-*EcPPX_c* and a specific antibody for the protein of interest at 4 °C overnight in the dark. After that, they were rinsed three times with PBS and stained with compatible secondary antibodies for 2 h at room temperature, protected from light. Secondary antibodies from Abcam, Cambridge, United Kingdom, including donkey anti-mouse IgG-Alexa Fluor[®] 488 (#ab150105), donkey anti-mouse IgG-Alexa Fluor[®] 647 (#ab150107), and goat anti-rabbit IgG-Alexa Fluor[®] 647 (#ab150079) were used at a final concentration of 1 $\mu\text{g}/\text{ml}$. Following three washes with PBS, cells were labeled with a counter stain, i.e., 1 $\mu\text{g}/\text{ml}$ DAPI (#D1306, Thermo Fisher Scientific) for 10 min. Finally, cells were washed with PBS three more times and mounted in Citifluor AF1 mounting medium (#19470, Ted Pella, Inc., Redding, CA, USA) on a microscope objective slide.

Fluorescence imaging was performed with a Leica SP8 laser scanning confocal microscope (Leica GmbH, Mannheim, Germany) built on a DMI8 microscope base and via LAS X software (Leica GmbH). This microscope was equipped with a 100 \times oil objective (#11506378, Leica GmbH), a 405 nm diode laser, and a multi-line white light laser, whose excitation wavelengths were set to 488, 594 and 647 nm. To detect fluorescence emissions, a PMT was used for DAPI (410 to 480 nm), and a HyD detector was used for GFP (493 to 560 nm), Alexa Fluor[®] 488 (493 to 560 nm), and Alexa Fluor[®] 647 (653 to 800 nm).

3.2.5 Plasmid transfection

To monitor the dynamics of fibrillarin and Nopp140, HeLa cells were seeded at a density of 1.5×10^4 cells/ well on an 8-well Nunc[™] LabTek[™] II Chambered Coverglass (#155409PK, Thermo Fisher Scientific). Twenty-four hours later, cells were transfected with a plasmid encoding either fibrillarin-GFP or Nopp140-GFP (generous gifts from Dr. Y. Shav-Tal, Bar-Ilan University). Lipofectamine 2000[™] (#11668027, Thermo Fisher Scientific) was used to transfect the plasmids per the manufacturer's instructions with only slight modifications. The amount of plasmid, Lipofectamine[™] 2000, and Opti-MEM[™] Reduced Serum Medium (#31985062, Thermo Fisher Scientific) was designated for a single transfection event. Briefly, 0.75 μl Lipofectamine[™] 2000 reagent and 0.3 μg plasmid was each dissolved in 37.5 μl Opti-MEM[™] and incubated at room temperature for 5 min. Once combined, the reagents were mixed gently and incubated for another 20 min to allow plasmid packaging onto the liposome. Shortly before adding the transfection

mixture in a dropwise manner to the cells grown on coverglass, spent medium was removed and replaced with 150 μ l fresh medium in each well. Then, the cells were incubated at 37 °C for 4 h to take up the plasmid, followed by another medium change to get rid of superfluous copies of the plasmid. Overexpressed proteins were studied on the next day.

3.2.6 Fluorescence recovery after photobleaching (FRAP)

FRAP experiments were performed on a Leica SP8 laser scanning confocal microscope equipped with a 100 \times oil objective (with 3-fold digital zoom in), a Tokai Hit stage top incubator maintained at 37 °C, a 405 nm diode laser, a multi-line white light laser set to 488 nm excitation wavelength, and a HyD detector capturing GFP fluorescence emission from 493 to 560 nm. A FRAP protocol was developed in the LAS X software (Leica GmbH) as described below. The region to be photobleached was defined manually using the ROI tool. To deplete the fluorescence signal as rapidly as possible, the power of the 405 nm diode laser (i.e., the bleaching laser) was set to 100%. Image acquisition rate was adjusted to 0.865 s/ frame. Each time course consisted of two frames taken before photobleaching, (two frames during photobleaching which were not shown in the final dataset), and 18 frames acquired during fluorescence recovery.

3.3 Results

3.3.1 Cisplatin-induced polyP foci form at the light nucleolar cap, Cajal body, and fibrillar cap

To detail the molecular composition of cisplatin-induced polyP foci, we performed (immuno)fluorescence labeling of polyP and a list of nuclear body markers, including fused in sarcoma (FUS), Nopp140, UBF, p14, coilin, and promyelocytic leukemia (PML) in untreated HeLa cells and those treated with 40 μ M cisplatin for 24 h. The distribution and the relative abundance of polyP were visualized with GFP-*Ec*PPX_c, a recombinant fluorescent probe that interacts with polyP specifically via the substrate-binding domain of *Escherichia coli* exopolyphosphatase (147). It was evident that cisplatin treatment not only reproducibly increased GFP-*Ec*PPX_c intensity but also caused polyP relocation to prominent foci, which had different sizes and shapes and appeared in different regions within the nucleus (Fig. 3.2, Fig. S3.1, and Fig. S3.2). Merging the signals of polyP and each of the protein markers that we used and analyzing their fluorescence intensity profiles in designated cellular regions, we observed three categories of polyP foci based on their colocalizations. PolyP colocalized 1) with Nopp140 in the light nucleolar

caps (Fig. 3.2A and Fig. S3.2A); 2) with coilin in the Cajal bodies (Fig. 3.2B and Fig. S3.2B); and 3) with UBF in the fibrillar caps (Fig. 3.2C and Fig. S3.2C), respectively.

Even in untreated cells, Nopp140 and polyP exhibited similar patterns of DFC staining, albeit with relatively low signal intensities (Fig. 3.2A and Fig. S3.2A). In comparison, when cisplatin was administered, Nopp140 readily segregated into bright, crescent-shaped foci (Fig. 3.2A, arrows, and Fig. S3.2A) characteristic of the light nucleolar caps formed upon rDNA transcription inhibition. Notably, the responses of polyP to cisplatin resembled those of Nopp140, and polyP appeared to localize to the same structures (Fig. 3.2A, arrows, and Fig. S3.2A). Therefore, we propose that polyP is a previously unrecognized member of the light nucleolar caps.

This conclusion was further corroborated by the overlap of polyP and coilin, a Cajal body marker, which is known to accumulate at least partially in the light nucleolar caps upon cisplatin treatment (171,172). Indeed, while coilin was almost exclusively detected in the Cajal bodies in the nucleoplasm of untreated cells, it appeared as crescent-like puncta at the periphery of the nucleolus in cisplatin-treated samples (Fig. 3.2B, arrows, and Fig. S3.2B). Again, GFP-*EcPPXc* fluorescence increased in these structures (Fig. 3.2B, arrows, and Fig. S3.2B), consistent with the idea that polyP accumulates in the light nucleolar caps upon cisplatin treatment.

Cajal bodies, which are small, dotted and coilin-rich granules, did not seem to contain polyP unless the cells were stressed with cisplatin (Fig. 3.2B, arrowheads, and Fig. S3.2B). Interestingly, a subset of Nopp140-positive foci with similar numbers and morphology to Cajal bodies emerged in the nucleoplasm following cisplatin treatment (Fig. 3.2A, arrowheads, and Fig. S3.2A). Indeed, Nopp140 has been proposed to serve as the link between light nucleolar caps and Cajal bodies by physically interacting with coilin (182). Therefore, we postulate that Nopp140 together with polyP colocalize to Cajal bodies upon cisplatin treatment.

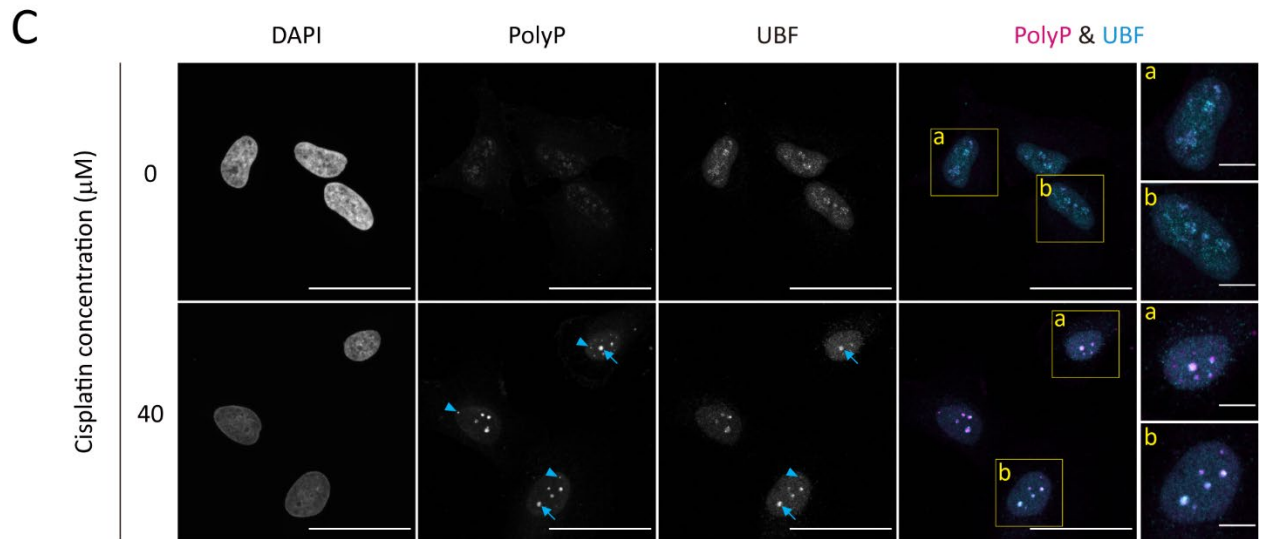
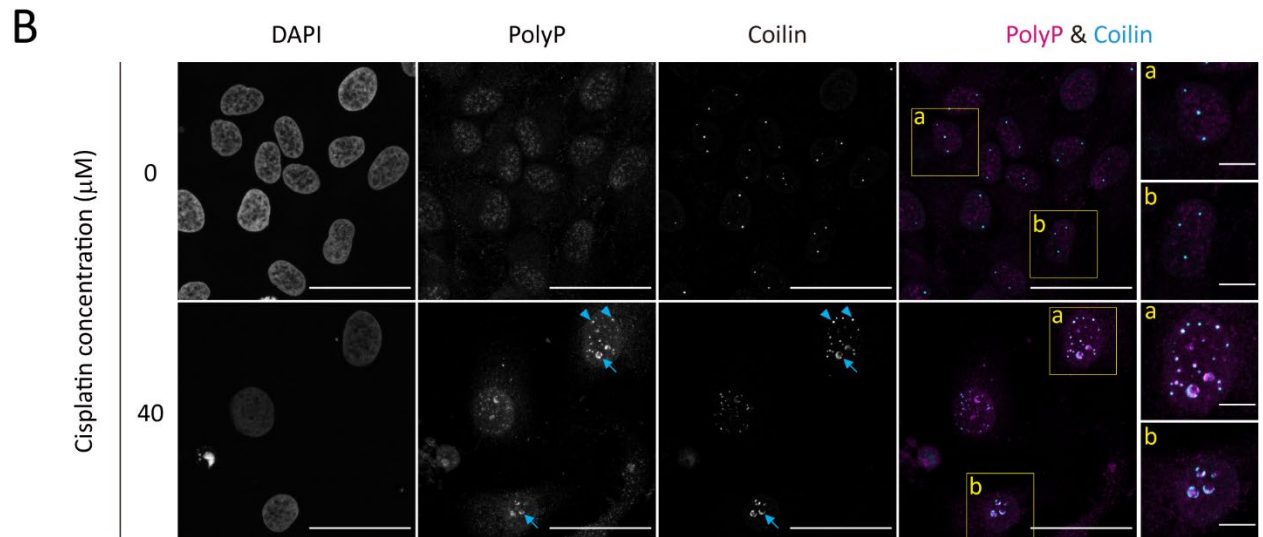
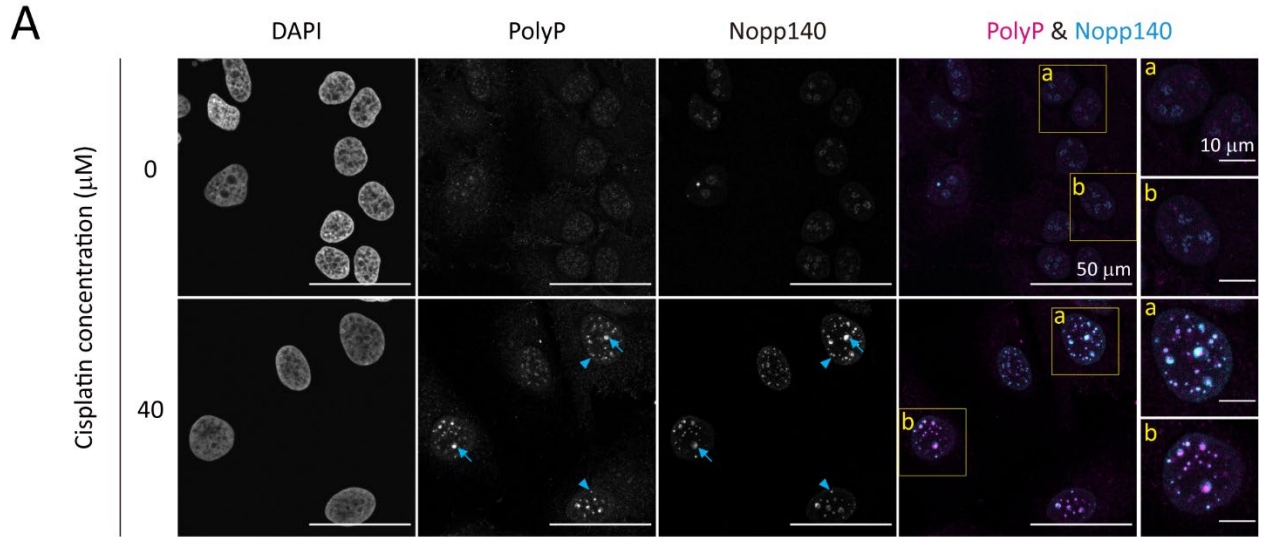


Figure 3.2 Cisplatin-triggered polyP foci colocalize with markers for light nucleolar caps, Cajal bodies, and fibrillar caps. Colocalization of polyP and (A) Nopp140, a light nucleolar cap marker, (B) coilin, a Cajal body marker, and (C) UBF, a fibrillar cap marker was assessed by immunofluorescence in either untreated HeLa cells (top row) or cells treated with 40 μ M cisplatin for 24 h (bottom row). Gray scale images from left to right depict the distribution of DNA (labeled with DAPI), polyP (labeled with GFP-*EcPPX_c*) and (A) Nopp140, (B) coilin or (C) UBF (labeled with the specific primary and secondary antibodies). In cisplatin-treated cells, typical light nucleolar caps (arrows) and Cajal bodies (arrowheads) are highlighted. An overlay of polyP (pseudo color: magenta) and the respective protein marker (pseudo color: cyan) is displayed in the rightmost panel with two regions (a and b) enlarged for more details. The corresponding fluorescence intensity plots for polyP and each protein marker can be found in Fig. S3.2. Representative images of projected z series are shown. Scale bar information is denoted in panel (A).

Prompted by the finding that a minor portion of polyP resides in the FC compartment of the nucleolus in untreated cells (38), we set out to analyze the spatial correlation between polyP and UBF, a fibrillar cap marker, in the context of cisplatin stress. As it turns out, cisplatin treatment led to significant changes in the shapes and fluorescence intensities of UBF puncta, consistent with the formation of fibrillar caps (Fig. 3.2C and Fig. S3.2C). These alterations were accompanied by an increase of GFP-*EcPPX_c* signal in the UBF-positive assemblies (Fig. 3.2C, arrows, and Fig. S3.2C). We thus concluded that cisplatin-induced polyP foci are also part of fibrillar cap structures. In stark contrast to Nopp140 and coilin, UBF was rarely drafted to nucleoplasmic foci, such as Cajal bodies (Fig. 3.2C, arrowheads, and Fig. S3.2C).

It is worthwhile mentioning that FC and DFC are tightly associated in an interphase nucleolus. Therefore, it is very likely that these compartments remain proximate to each other even when the nucleolus is reconfigured by cisplatin. This disposition reconciles our findings that polyP exhibits a substantial colocalization with both light nucleolar caps and fibrillar caps, marked by Nopp140 and UBF, respectively (Fig. 3.2, A and C; and Fig. S3.2, A and C).

On the contrary, we were unable to associate polyP accumulation with markers for dark nucleolar caps (demarcated by GFP-FUS) (Fig. S3.1A and Fig. S3.2D), central body (labeled with p14) (Fig. S3.1B and Fig. S3.2E), or PML bodies (Fig. S3.1C and Fig. S3.2F) either before or after cisplatin intake.

In summary, polyP, which is normally concentrated in the FC and DFC portions of the nucleolus, is selectively mobilized to the light nucleolar caps, Cajal bodies, and fibrillar caps after cisplatin treatment (Fig. 3.2 and Fig. S3.2). Notably, fibrillar caps and light nucleolar caps include rDNA transcription and processing machineries. Besides, light nucleolar cap protein Nopp140 and Cajal body marker coilin, which get shuffled bidirectionally in reply to cisplatin, not only coimmunoprecipitate with each other but also bind to RPA1, the catalytic core of RNA pol I, to suppress rRNA synthesis under certain stress conditions (172,183). Thereby, we propose that these

polyP hotspots may be genuine responses to cisplatin and/or strategies to combat this stress condition.

3.3.2 Formation of polyP foci in the nucleoli and Cajal bodies is a result of RNA pol I inhibition

Intrigued by the polyP deposits in nucleolar cap structures and Cajal bodies in cells challenged with cisplatin, we set out to unravel the molecular mechanisms underlying this phenotype. To begin with, we assessed the possibility that polyP was directly guided to DNA lesions. Using γ -H2AX as a readout for double stranded breaks (184), we confirmed the efficacy of our cisplatin treatment to reduce DNA stability with a massive upregulation of γ -H2AX immunofluorescence signal throughout the nucleus (Fig. S3.3A). However, we did not observe any consistent colocalization between γ -H2AX loci and polyP, suggesting that polyP was not directly associated with cisplatin-mediated DNA damage.

We then expanded the list of cytotoxic agents to determine how different types of cell death affect polyP abundance and localization. We tested a combined treatment with 10 ng/ml TNF- α , 10 nM BV6 (a SMAC mimetic), and 20 μ M Z-VAD-FMK (TSZ), which kills cells through necroptosis (185). However, this treatment did not recapitulate the polyP behavior observed upon cisplatin treatment despite an impairment of cell survival in embryonic mouse fibroblast (Fig. S3.3, B and C). Taken together, these results exclude the idea that polyP is merely a signature of dying cells. Instead, it appears that polyP might be actively and selectively involved in a designated cell death mechanism.

Cisplatin is well known to inhibit rDNA transcription when administered at the concentrations that we used in our experiments (150,154,172). To investigate whether stalling rRNA synthesis is sufficient to mobilize polyP, we investigated the effects of ActD, a specific inhibitor of RNA pol I activity when used at low concentrations (186). Indeed, treatment of HeLa cells with 10 ng/ml ActD for 4.5 h led to the formation of light nucleolar caps that were positive for both Nopp140 and polyP (Fig. 3.3A, arrows, and Fig. S3.4A) as well as coilin and polyP (Fig. 3.3B, arrows, and Fig. S3.4B). Moreover, the polyP signal was also prevalent in the regions designated as fibrillar caps where UBF accumulates in response to ActD (Fig. 3.3C, arrows, and Fig. S3.4C). In addition, we found a large number of Cajal bodies, featured by Nopp140 and coilin to contain polyP signals (Fig. 3.3, A and B, arrowheads; and Fig S3.4, A and B).

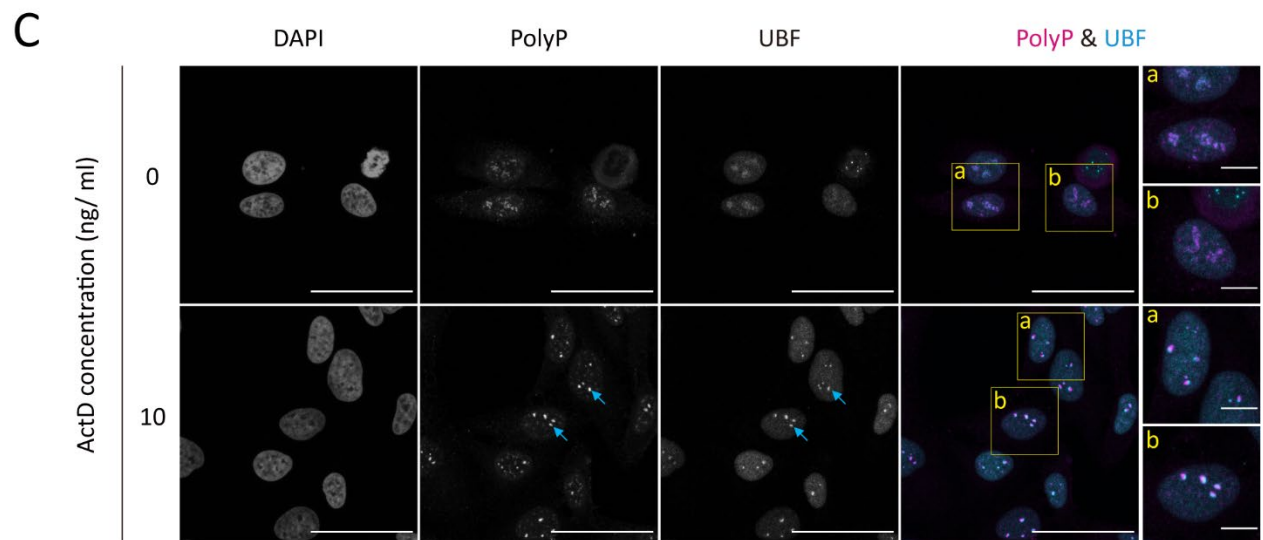
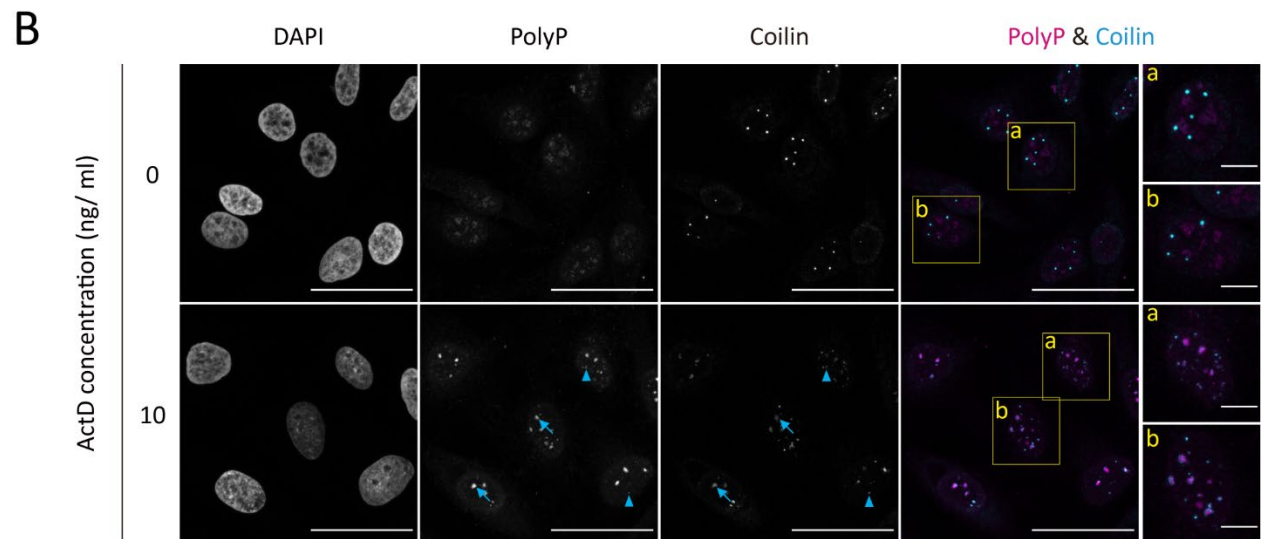
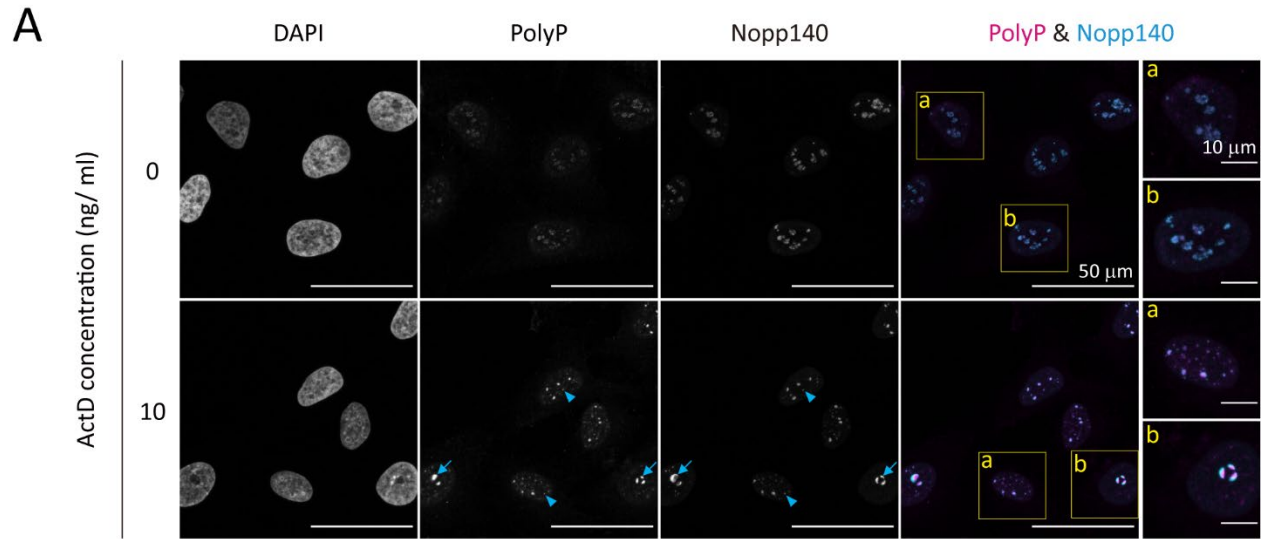


Figure 3.3 PolyP foci appear at light nucleolar caps, Cajal bodies, and fibrillar caps upon ActD treatment. Immunofluorescence experiments were performed to assess the colocalizations of polyP and (A) Nopp140, a light nucleolar marker, (B) coilin, a Cajal body marker, and (C) UBF, a fibrillar cap marker. HeLa cells were either untreated (top row) or treated with 10 ng/ml ActD for 4.5 h to block rRNA transcription. Gray scale images from left to right display the patterns of DNA (labeled with DAPI), polyP (labeled with GFP-*EcPPX_c*), and the respective protein marker (labeled with the specific primary and secondary antibodies). Typical light nucleolar caps are denoted with arrows and typical Cajal bodies are highlighted with arrowheads. Fluorescence images of PolyP (pseudo color: magenta) and the protein markers (pseudo color: cyan) are merged to illustrate the close proximity of these molecules. For each overlay, two regions (a and b) are enlarged for more details. The corresponding fluorescence intensity plots can be found in Fig. S3.4. Representative images of projected z series are shown. Scale bar information is included in panel (A).

On the contrary, neither dark nucleolar caps marked by FUS-GFP (Fig. S3.4D and Fig. S3.5A) nor central bodies labeled with p14 (Fig. S3.4E and Fig. S3.5B) showed a considerable amount of polyP.

In summary, by using ActD treatment, which allowed us to specifically inhibit RNA pol I activity, we observed a set of changes in the distribution and abundance of polyP identical to the ones observed with cisplatin treatment (Fig. 3.2, Fig. 3.3, Fig. S3.2, and Fig. S3.4). This result strongly suggests a correlation between disruption of rRNA synthesis and polyP mobilization.

3.3.3 IP6K1 is a novel component of the light nucleolar cap

With the advance of human protein atlas, the nucleolar proteome of HeLa cells has been documented in unprecedented details (<https://www.proteinatlas.org/>). Among the hundreds of nucleolar proteins, IP6K1 sparked our interest for being particularly enriched in FC and having been found to regulate polyP levels in yeast, *Trypanosoma*, and mice (120-123). Based on this premise, we investigated the spatial relationship between IP6K1 and polyP in the context of rRNA synthesis. As shown in Fig. 3.4A and Fig. 3.4B, a clear IP6K1 signal with irregular and diffuse pattern is visible in the nucleolus of untreated cells. Once we administered cisplatin or ActD, however, IP6K1 formed foci that colocalized partially with the highest levels of polyP (Fig. 3.4, A and B, arrows). Based on their count and morphology, we predicted that IP6K1 accumulated in light nucleolar caps. To test this idea, we conducted colocalization analysis of IP6K1 and Nopp140. IP6K1, which appeared to be enclosed in the Nopp140-positive DFC area under non stress conditions (as expected for a FC member) clearly segregated to the light nucleolar caps marked by Nopp140 upon ActD treatment (Fig. 3.4C). These results demonstrate that IP6K1 and polyP are found in close proximity in the nucleolus, and they are novel members of the light nucleolar caps under distinct rDNA stress conditions.

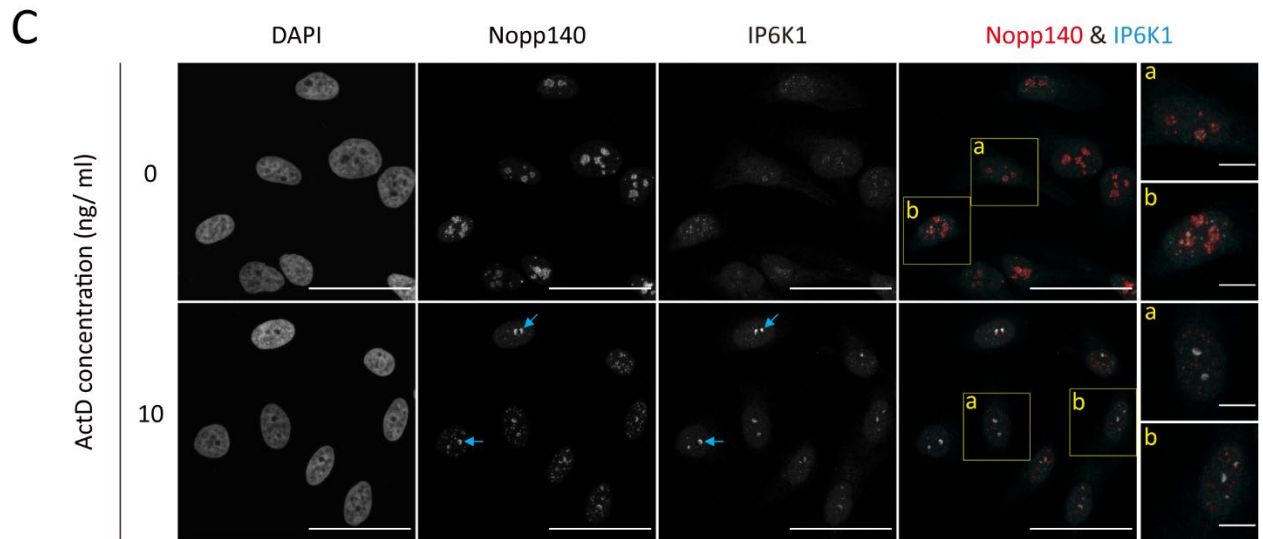
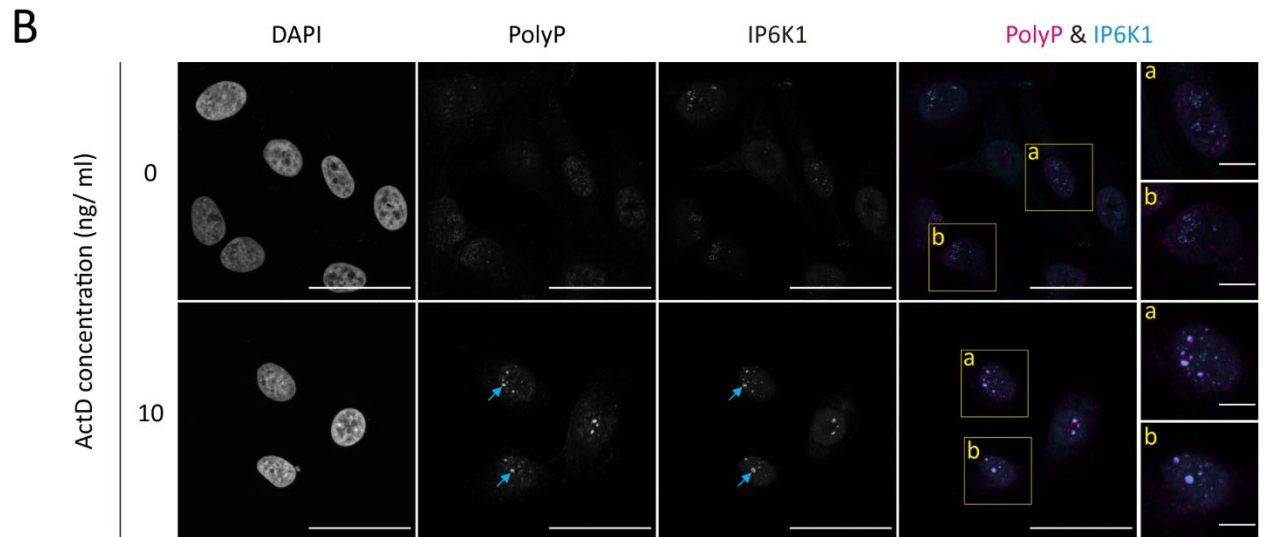
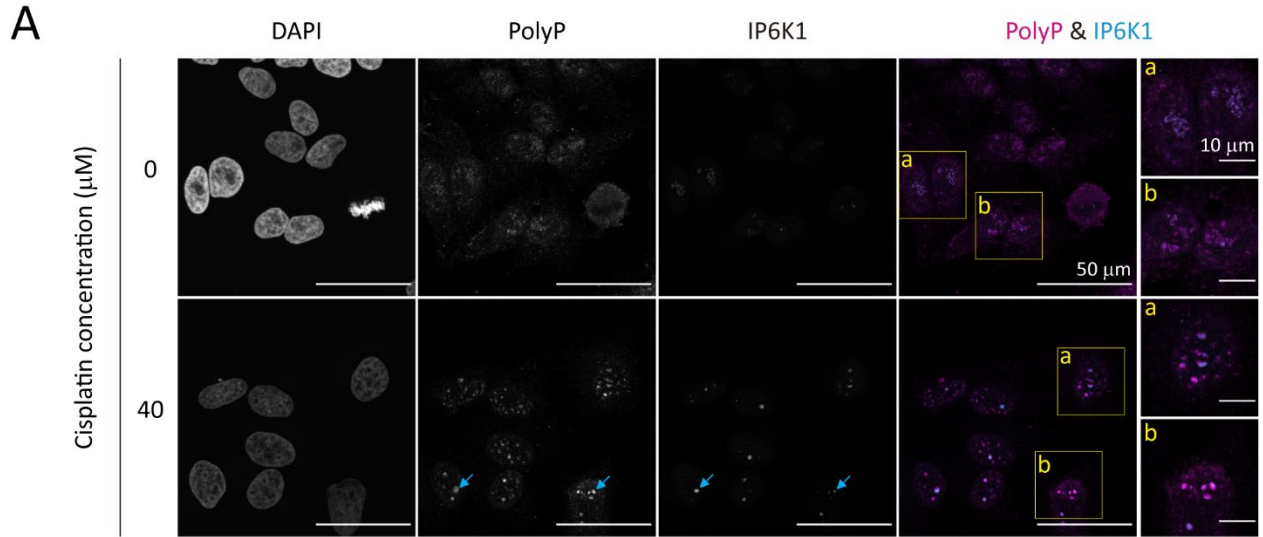


Figure 3.4 IP6K1 accumulates in the light nucleolar cap structures upon rRNA transcription inhibition. (A and B) Colocalization of polyP and IP6K1 was analyzed by immunofluorescence experiments in two conditions: (A) 40 μ M cisplatin treatment for 24 h and (B) 10 ng/ml ActD treatment for 4.5 h. Untreated HeLa cells (top rows) and treated cells (bottom rows) were labeled with DAPI (gray scale, left), GFP-*EcPPXc* (gray scale, middle), and specific primary and secondary antibodies for IP6K1 (gray scale, right). Typical nucleolar caps are highlighted with arrows. Fluorescence signals of polyP (pseudo color: magenta) and IP6K1 (pseudo color: cyan) are merged to exhibit the close proximity of the two molecules. Two regions (a and b) are enlarged for more details. (C) Colocalization of Nopp140, a light nucleolar cap marker, and IP6K1 was also examined by immunofluorescence. HeLa cells were stained with DAPI (gray scale, left), Nopp140 antibodies (gray scale, middle), and IP6K1 antibodies (gray scale, right) either before (top row) or after (bottom row) the same ActD treatment as that in (B). Classic light nucleolar cap structures are pointed out by arrows. An overlay of Nopp140 (pseudo color: red) and IP6K1 (pseudo color: cyan) fluorescence is displayed with two regions (a and b) enlarged for a magnified view. Representative images of projected z series are shown. Scale bar information is included in panel (A).

3.3.4 Light nucleolar caps are highly dynamic structures

Given the identification of components of the light nucleolar cap, we decided to test the structural dynamics of this compartment using fluorescence recovery after photobleaching (FRAP). This approach allows us to observe the diffusion of fluorescently labeled markers in real time and quantify the kinetics of this event. Originally, our goal was to visualize the dynamics of polyP in light nucleolar caps, however, this idea was limited by the lack of polyP probes suitable for live cell imaging. As an alternative, we took advantage of ectopically expressed Nopp140-GFP in HeLa cells as a representative of the overall phase properties of light nucleolar caps. Importantly, upon treatment with ActD, overexpressed Nopp140-GFP segregated to the periphery of the nucleolus and distinct nuclear bodies (presumably Cajal bodies) in the same way as its endogenous counterpart (Fig. 3.5, A, D and G). We then employed a photobleaching protocol and compared the mobility of Nopp140 in different parts of the nucleus. We chose to focus on three regions of interest: 1) a spot within the light nucleolar cap (Fig. 3.5, A-C), 2) the entire light nucleolar cap (Fig. 3.5, D-F); and 3) the entire nuclear body (Fig. 3.5, G-I). As shown by the fluorescence time-lapse images (Fig. 3.5, B, E and H), all three regions showed a recovery of signal intensity after photobleaching. When we plotted fluorescence intensity against time (Fig. 3.5, C, F and I), we observed a recovery rate on the timescale of seconds, consistent with earlier reports (171). Notably, fluorescence recovery within the nucleolar cap might be faster than the image acquisition rate (0.865 s/ frame), otherwise we would have observed a distinct “dark” region after photobleaching. Instead, it appeared that Nopp140-GFP diffusion had almost equilibrated by the time the first image was taken during fluorescence recovery (Fig. 3.5, B and C). This observation indicates a homogenous, liquid-like environment in this structure. On the contrary, recovery of Nopp140-GFP fluorescence across the boundaries between the light nucleolar cap and its adjacent environment, or between the nuclear body and the nucleoplasm was significantly slower (Fig. 3.5, E, F, H and I). This difference in the recovery rate likely reflects different phase properties of these sub-

organellar regions, which create an invisible barrier for the diffusion and exchange of highly localized molecules. Importantly, the dynamic behaviors of Nopp140 within the light nucleolar cap and across the border of this compartment were fully recapitulated by fibrillarlin, which was exclusively targeted to the light nucleolar cap upon ActD treatment (Fig. S3.6, A-F). These results strongly suggest that light nucleolar caps are overall highly dynamic. It is now tempting to speculate that polyP, a heavily negatively charged molecule just like a few known modulators of phase separation (187-190), might finetune the phase parameters so as to maintain a liquid-like state of the light nucleolar cap and nuclear bodies, preventing them from coalescing with other structures.

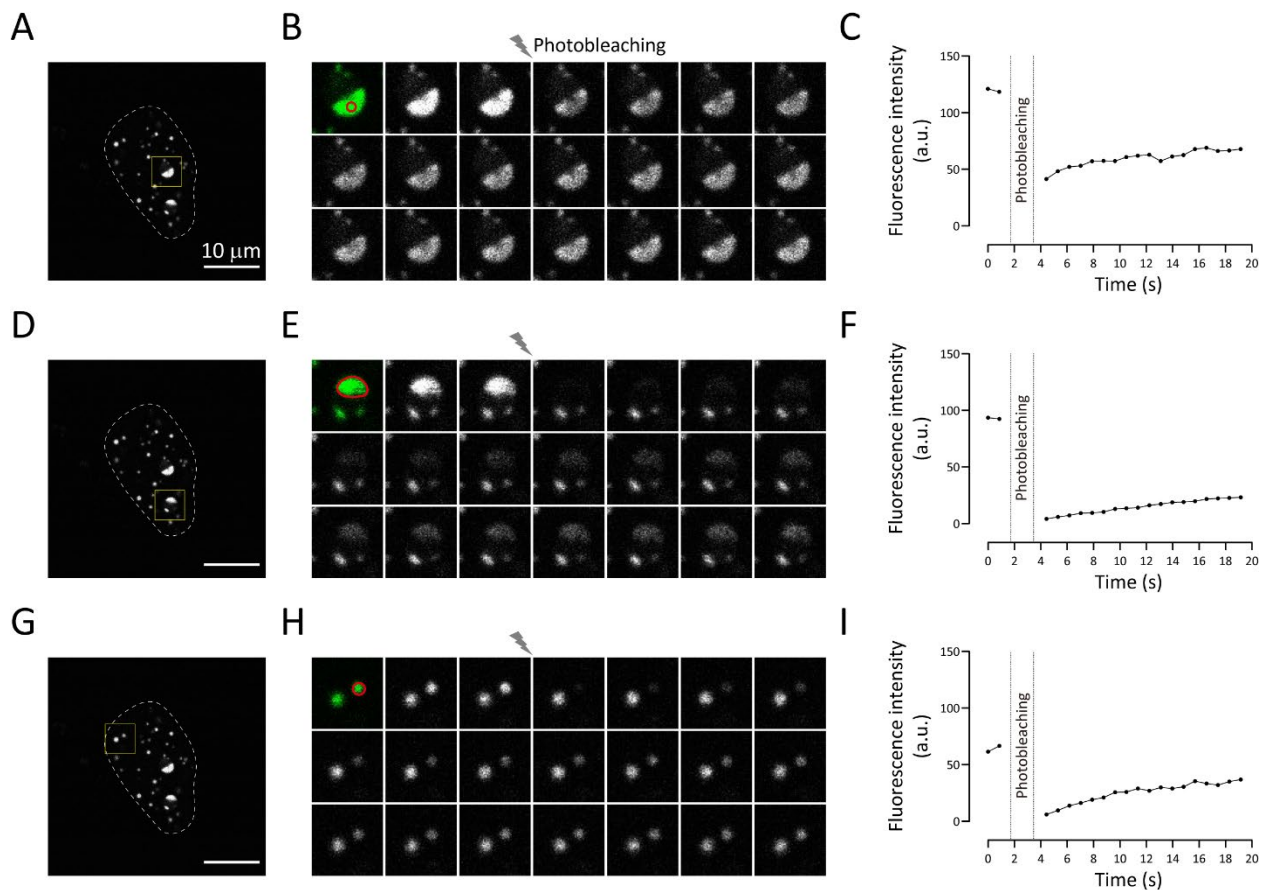


Figure 3.5 Nopp140 is a dynamic member of the light nucleolar caps and other nuclear bodies. (A-C) Nopp140 is diffusive in the light nucleolar cap. (A) Ectopically expressed Nopp140-GFP partitioned to light nucleolar caps and other nuclear bodies (presumably Cajal bodies) after ActD treatment. Nucleus was outlined by a white dashed line, and the nucleolus of interest was highlighted by a yellow square. Scale bar: 10 μm. (B) In the nucleolus highlighted in (A), photobleaching was directed to the region marked by a red circle. Time-lapse images of Nopp140-GFP were acquired before photobleaching and during fluorescence recovery. The time interval between each frame was 0.865 s. (C) Nopp140-GFP fluorescence in the photobleached region decreased sharply during photobleaching but rapidly recovered afterwards. Note that fluorescence measurements were unavailable during photobleaching. (D-F) Nopp140 is transported to light nucleolar caps from the adjacent environment. (D) A different nucleolus marked by the yellow square was studied. (E) Photobleaching was performed on the entire light nucleolar cap circled in red. Nopp140-GFP fluorescence signal was monitored before and after photobleaching. The interval between each frame of the time-

lapse images was 0.865 s. (F) Nopp140-GFP fluorescence in the marked region in (E) was largely depleted by photobleaching, but it slowly recovered post the exposure. (G-I) Nopp140-rich nuclear bodies are highly dynamic structures. (G) A smaller nuclear body highlighted by the yellow square was investigated for its crosstalk with the nucleoplasm. (H) An intact nuclear body, demarcated by a red circle, was subject to photobleaching. Time-lapse images of Nopp140-GFP fluorescence were taken before and after photobleaching with an interval of 0.865 s between each frame. (I) Nopp140-GFP fluorescence in the nuclear body was eliminated by photobleaching, whereas it gradually recovered after the treatment.

3.3.5 Nucleolar polyP is sensitive to the inhibition of rRNA processing

To test whether polyP redistributes also in the presence of other drugs that lead to structural rearrangements of the nucleolus, we treated HeLa cells with 10 μ M DRB for 2 h. DRB, an adenosine analog and kinase inhibitor, leads to the formation of the loose nucleolar necklace (173). Under these stress conditions, we observed the formation of both large and small polyP foci, which emerged in a prompt reaction towards the DRB treatment (Fig. 3.6A). Both types of polyP assemblies adopted a regular, round shape, which was in stark contrast to the crescent light nucleolar cap structures that formed upon cisplatin or ActD treatment. Interestingly, a number of the small polyP foci were found in patterns that resembled the nucleolar necklace (Fig. 3.6A, arrowheads). Some of the larger polyP foci were adjacent to but excluded from the nucleolus which typically had low DAPI signals (Fig. 3.6A, arrows). As of now, we are unable to trace the origins of these structures without further investigating the molecular compositions of these polyP assemblies. It is possible that they represent an intermediate state in the transition from an intact nucleolus to a nucleolar necklace or a result of the unspecific effects of DRB on RNA pol II.

On the contrary, we did not find any significant redistribution of polyP upon inactivation of the proteasome using MG132, which is known to deposit substrates of ubiquitin ligases at the center of the nucleolus denoted as “aggresome” (178,179). We tested a wide range of MG132 concentrations, i.e., 0 to 2.5 μ M, which neither triggered polyP accumulation nor relocation within the nucleolus (Fig. 3.6B), in spite of causing a clear defect in cell growth and survival (Fig. 3.6C). This result was consistent with the fact that MG132 does not interfere with the FC and DFC compartments (178), and it suggested that the polyP response is specific and not generally associated with nucleolar reorganization events.

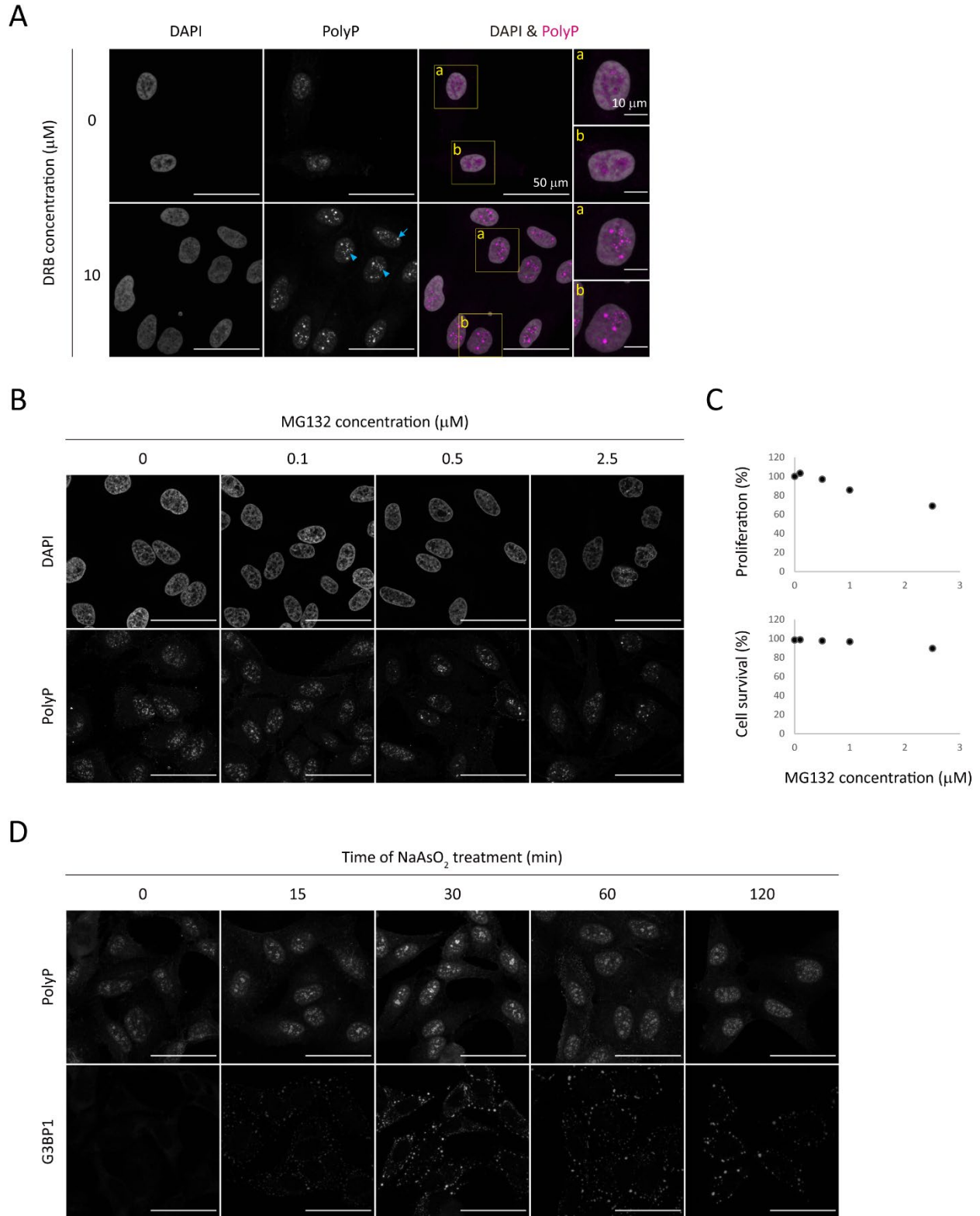


Figure 3.6 A distinct type of nucleolar polyP foci occur upon the disruption of late rRNA processing but not the formation of nucleolar aggresomes or cytoplasmic stress granules. (A) Immunofluorescence analysis of polyP localization and levels in untreated HeLa cells (top row) and cells treated with 10 μ M DRB for 2 h (bottom row) which inhibits late rRNA processing. DAPI fluorescence is an indicator for DNA and GFP-*Ec*PPX_c fluorescence is a readout for polyP. Two types of polyP foci are discernible:

large, round, isolated polyP foci are highlighted with arrows; and small, clustered polyP foci are pointed out by arrowheads. An overlay of DNA (pseudo color: gray) and polyP (pseudo color: magenta) signals is shown with two enlarged regions (a and b) for more details. **(B)** The patterns of endogenous polyP are delineated by immunofluorescence microscopy when HeLa cells were treated with 0, 0.1, 0.5, and 2.5 μM MG132 to block proteasomal activities. DAPI and GFP-*EcPPX_c* were used to label DNA and polyP respectively. **(C)** The cytotoxicity of MG132 was manifested in the growth defects (measured by WST-1 assay) (top) and cell death (quantified by SYTOX Green assay) (bottom) in HeLa cells. MG132 conditions were the same as those in (B). **(D)** The distribution of polyP in the process of stress granule formation was monitored by immunofluorescence techniques in HeLa cells. Cells treated with 0.5 mM NaAsO₂ for 0, 15, 30, 60, and 120 min were co-stained with GFP-*EcPPX_c* to reveal the abundance of polyP (top) and specific antibodies for G3BP1 (bottom), a stress granule marker, to monitor the extent of stress granule formation. Representative images of projected z series are shown. Scale bar information is included in panel (A).

Finally, we explored whether polyP incorporation is a universal character of phase-separated granules in mammalian cells. Here, we made use of G3BP1-positive stress granules in the cytoplasm (191). Whereas G3BP1 was expressed at very low levels in untreated HeLa cells, it formed heterogeneous, membraneless granules within 15 min of sodium arsenite (NaAsO₂) exposure (Fig. 3.6D). We did not detect any significant polyP signals even when we prolonged the NaAsO₂ incubation to 2 h (Fig. 3.6D). Instead, we observed a slight increase in the fluorescence intensity of nucleolar polyP that was concomitant with the increase in stress granules. Therefore, we conclude that polyP is not an essential scaffold for every phase separation-driven structure, although it might be influenced by the same environmental cues.

3.4 Discussion

3.4.1 PolyP partitions to light nucleolar caps, fibrillar caps and Cajal bodies in response to rRNA transcription inhibition

In this study, we explored the mechanistic details for our previous observation that polyP segregates to distinct nucleolar foci in cisplatin-treated cells. Using immunofluorescence analysis of polyP and a range of nuclear body markers, we identified polyP foci to localize at light nucleolar caps, fibrillar caps, and Cajal bodies (Fig. 3.2, Fig. 3.3, Fig. S3.2 and Fig. S3.4). These structures share structural and functional commonalities with each other. A number of light nucleolar cap proteins originate from the DFC and FC, which constitute active rDNA transcription sites (148). Moreover, light nucleolar cap structures reveal a dynamic crosstalk with Cajal bodies by exchanging their proteins and RNAs (172,182). Most importantly, however, both polyP-containing structures have previously been found to form once RNA pol I is inhibited and rRNA synthesis is stalled (150,172). This result suggests that polyP is functionally related to RNA pol I *in vivo*, and it is consistent with previous studies that showed polyP to inhibit RNA Pol I activity *in vitro* (38). Yet, it is unclear if and how polyP interacts with the other proteins in these cap structures, and what the functional significance of this colocalization is in the context of rRNA

synthesis stress.

We found that polyP associates with Nopp140, a light nucleolar cap marker. Previous work showed that Nopp140 is heavily phosphorylated, accounting for more than 25% of its apparent molecular weight and making it one of the most phosphorylated proteins in human cells (192). In fact, Nopp140 harbors ten serine-rich stretches with an average length of 15 residues (including sporadic glutamates and aspartates) joint by lysine- and proline-rich sequences (192). For a long time, serine was considered as the only target for phosphorylation in these segments. However, this paradigm has recently been shifted by the novel finding that poly acidic, serine and lysine-rich motifs (PASK), which are highly abundant in Nopp140, undergo polyphosphorylation events, i.e., the conjugation of polyP chains to lysine residues (47,48). Compared to serine/threonine phosphorylation, lysine polyphosphorylation is much more efficient in maximizing the phosphate content of Nopp140. This feature might be particularly beneficial to human Nopp140 since phosphorylation is pivotal for the structure and function of this protein. When phosphorylated, human Nopp140 adopts an intrinsically disordered conformation which is highly resistant to heat even at a boiling temperature (192,193). However, once phosphorylation is abolished at low ionic strength, namely 0.15 M salt, Nopp140 aggregates almost instantaneously (192). The drastic differences in the solubility of Nopp140 suggest that phosphorylation is a prerequisite for reducing the aggregation propensity of this protein and keeping it soluble. Intriguingly, polyP exerts robust chaperone activities on a variety of clients by shielding them from heat- and oxidation-induced misfolding (25,26,28,29). Hence, it is tempting to hypothesize that polyphosphorylation is exploited to increase the structural flexibility and solubility of Nopp140.

To test the idea that cisplatin or ActD treatment triggers the polyphosphorylation of Nopp140 *in vivo*, an established biochemical assay can be used to assess the molecular weight of Nopp140 in mammalian cell lysates before and after exopolyphosphatase treatment (47). In fact, SRP40, the yeast homologue of Nopp140, harbors two PASK-like motifs (48), consistent with the observation that SRP40 is phosphorylated *in vivo*, albeit to a much less extent than the rat and human counterparts (194). Therefore, it is also plausible that SRPP40 is polyphosphorylated. In this case, modulation of polyP levels in yeast by mutating *VTC4* (the yeast *PPK* gene) will provide a clear answer.

So far, the physiological functions of polyphosphorylation focus on the modification of subcellular

localization and/or enzymatic activity of the substrate (47). We wonder whether this portion of polyP could also exert chaperone function, a role that polyP plays in many bacteria (25,26,28,29). It is well-known that the nucleolar proteome faces major challenges in protein folding. On the one hand, the nucleolus is extremely densely packed with proteins and RNAs (166,167), on the other hand, a large number of nucleolar proteins are intrinsically disordered (195). In this regard, covalent attachment of polyP, a universal biopolymer and primordial chaperone (25), might become a promising strategy to increase the solubility of nucleolar proteins within this adverse folding environment. Coincidentally, coilin, another nucleolar and Cajal body marker proximal to polyP, also features two potential PASK motifs (48), which might account for the overlapping fluorescence of GFP-*EcPPX_c* and coilin antibodies (Fig. 3.2, Fig. 3.3, Fig. S3.2 and Fig. S3.4). Moreover, coilin like Nopp140 lacks a defined three-dimensional structure (196). It is unknown whether polyphosphorylation is essential to the structural dynamics of coilin yet. But if so, this finding will greatly strengthen the idea that polyP acts as a molecular chaperone across all kingdoms of life.

From a technical standpoint, colocalization of GFP-*EcPPX_c* fluorescence with Nopp140, coilin, and UBF (which contains a single PASK motif) suggests that *EcPPX_c*-derived probes might be genuine reporters of polyphosphorylation *in situ*. This claim is consistent with our previous proposal that immobilized, protein-bound polyP is favored over unbound, organellar polyP (in the mitochondria and secretory vesicles) by the immunofluorescence detection method. Based on the current knowledge of polyphosphorylation, it will be necessary to test the ability of *EcPPX_c* to bind polyphosphorylated and unphosphorylated forms of Nopp140, coilin, and other known targets of this modification (48). To take this one step further, polyphosphorylated proteins (as well as stable polyP binding partners) might coimmunoprecipitate with *EcPPX_c*-coated beads, and thus they could be identified by mass spectrometry. Once established, this approach will for the first time unveil the *in vivo* polyP-associated proteins in many eukaryotic organisms and provide a more comprehensive picture of polyP physiology.

3.4.2 Potential roles of polyP in the regulation of RNA Pol I

Our results suggested that the most likely trigger for polyP's partitioning to light nucleolar caps and Cajal bodies is the inhibition of RNA pol I. This finding was corroborated by a low-dose ActD treatment, which specifically stalls rDNA transcription and elicited the same redistribution of

polyP as previously observed with low concentrations of cisplatin (Fig 3.2, Fig. 3.3, Fig. S3.2 and Fig. S3.4). As antitumor remedies, both cisplatin and ActD intercalate into DNA double helix with a preference for GC-rich loci (197,198). This feature renders the promoter of 45S ribosomal gene a primary target for either drug even when they are administered at minimal concentrations (150,186). Given that nucleolar polyP is mobilized by the same regimens, it is very likely that polyP partakes in one or more downstream events in the rRNA synthesis pathway.

Prior to this study, the impact of polyP on the activity of RNA pol I has been determined *ex vivo* (38). When isolated nucleoli from myeloma cells were supplemented with physiological concentrations of exogenous polyP, the abrogation of transcriptional activity was observed (36). Therefore, it is conceivable that an inhibitory polyP concentration can be easily achieved in the segregated nucleolar compartments where polyP, RNA pol I, and other nucleolar proteins cluster in the presence of cisplatin or ActD (Fig. 3.2, Fig. 3.3, Fig. S3.2 and Fig. S3.4). To this date, neither the mechanism nor the physiological relevance of polyP-mediated inhibition of RNA pol I has been revealed. Here, we propose several mechanisms by which polyP may impair RNA pol I activities *in vivo*.

UBF, which colocalizes with polyP upon cisplatin and ActD treatment, is an essential transcription factor that stabilizes the pre-initiation complex containing TATA box-binding protein (TBP), TBP-associated factors (TAFs), and the RNA polymerase itself at the transcription start sites (199). Only when UBF is stably anchored at the upstream control element of rDNA will RNA pol I, which is usually in excess, be continuously recruited to the promoter region to sustain rRNA synthesis. Both bioinformatic predictions of PASK motifs and fluorescence colocalization of UBF and polyP suggest that UBF might be a target for polyphosphorylation (48). Furthermore, previous studies on Top1 and Nsr1, the first two polyphosphorylated proteins identified in the nucleolus of yeast, provided strong premises that polyphosphorylation is influential on protein localizations and functions (47). As such, it will be important to determine whether UBF is polyphosphorylated, and if so, how this modification affects the interaction between UBF and the upstream control element of rDNA.

In addition to UBF, Nopp140 and coilin are physiologically relevant binding partners and inhibitors of RPA1 (172,183), the largest subunit and catalytic core of RNA pol I. Whereas Nopp140 contains ten hypothetical PASK motifs, coilin contains two. The functional levels of

Nopp140 must be finetuned to maximize the yield of rRNA because once overexpressed, Nopp140 instigates a nucleolar segregation and an RNA pol I inactivation identical to those observed with ActD treatment (183). The same is true for an ectopic overexpression of coilin (172). Therefore, it will be curious to investigate the possibility that polyP interferes with rDNA transcription by modulating the levels of these proteins and/or their affinities for RPA1.

3.4.3 PolyP might also respond to the inhibition of rRNA processing

Our studies also showed that DRB, an adenosine analog which interferes with rRNA processing, triggers the polyP relocation to prominent nucleolar foci (Fig. 3.6A). However, in contrast to the distinct crescent shaped foci that form when rDNA transcription is halted, two different populations of round polyP assemblies appear following DRB treatment. Interestingly, several small polyP foci tend to cluster within a very short distance to each other, forming a pattern which recapitulates the so-called nucleolar necklace (173). Nucleolar necklaces are typically observed after DRB treatment since DRB effectively disengages the rRNA processing machinery in GC from the active transcription sites at the border of FC and DFC (173). Since polyP is an intrinsic component of FC and DFC, it is expected that the rearrangement of polyP phenocopies that of the nucleolar compartments. Yet, the most important evidence to support this idea would be the localization of FC/DFC markers to the small polyP granules, which can be monitored by immunofluorescence.

Equally enigmatic are the identities of the large polyP foci, some of which are clearly excluded from the nucleolus (Fig. 3.6A). This observation speaks against a connection between the large polyP foci and rRNA synthesis. Indeed, besides disrupting rRNA processing, DRB is recognized for inhibiting RNA pol II (174,175). Given a moderate conservation between RNA polymerases I and II (with 12 identical subunits) and the fact that mediator of RNA polymerase II transcription subunit 1 (MED1) is among the top candidates for polyphosphorylation (48), we postulate that RNA Pol II might also serve as a target of polyP.

3.4.4 IP6K1 is a novel component of the light nucleolar cap

IP6K1 is a key enzyme of the inositol phosphate pathway, taking charge of phosphorylating the most abundant form of inositol phosphate in human cells, namely IP₆, to form IP₇ and IP₈ (117). Both products belong to inositol polyphosphates, which not only resemble certain structural properties of polyP but also directly influence polyP synthesis. For instance, when *KCSI*, the yeast

homolog of *IP6K1*, is deleted, the cells become devoid of polyP, similar to the $\Delta vtc4$ strain lacking the polyP producing enzyme (123). Moreover, both IP₆ and IP₇ boost Vtc4 enzymatic activities, with IP₇ being a much more potent accelerator than IP₆ (124,125). Other species, including *Trypanosoma* and mice, also suffer from a decrease of polyP reserve when *Ip6k1* gene is knocked out (120-122). Although it is unlikely that IP6K1 is the mammalian PPK per se, as *Ip6k1*^{-/-} mice retain around 50% polyP in their platelets (122), it is evident that IP6K1 is involved in polyP synthesis at least tangentially.

From the Human Protein Atlas project, we became aware that IP6K1 is also located in the nucleolus, and we found the enzyme to colocalize with polyP under both non-stress and stress conditions (Fig. 3.4). Following ActD treatment, we observed the translocation of IP6K1 to the light nucleolar cap, coinciding with the relocation and accumulation of polyP in the same compartment. While we are unable to ascertain whether *de novo* polyP synthesis is responsible for this phenomenon, at a minimum, these results establish a spatial correlation between IP6K1 and polyP upregulation in the nucleolus. In a follow-up study, we plan to knockout/knockdown *IP6K1* in HeLa cells and compare their cisplatin- or ActD-mediated polyP response to that of the wildtype. This approach will provide a more straightforward answer to the question whether IP6K1 is responsible for polyP accumulation in the context of rRNA synthesis stress.

3.4.5 The role of polyP in the phase separation of the nucleolus

The nucleolus is an intricate, self-organized and phase-separated structure which retains very high protein motility within the same compartment and less so across the border of different compartments (Fig. 3.5 and Fig. S3.6). Characteristic of a phase-separated entity, the nucleolus is rich in charged and intrinsically disordered proteins (195). Many of them, such as fibrillarin and nucleolin, are capable of forming phase-separated droplets by themselves provided with the appropriate buffer conditions *in vitro* (168). Yet, to form an intact nucleolus in the cellular environment requires a multitude of regulations. By far, RNA and ATP are the most well-established regulators of phase separation (187-190). Their working mechanisms rely, at least partially, on their abundant negative charges, which interact with the positively charged residues enriched in the phase-separating nucleolar proteins. This notion leads us to propose that polyP, a similarly negatively charged and phosphate-rich molecule endogenous to the nucleolus, may contribute to the nucleolar phase separation process *in vivo*. An encouraging finding in *Citrobacter*

freundii supports this idea by showing that the phase separation behavior of an engineered substrate, +36GFP, was greatly affected by nutrient deprivation conditions, which are known to alter cellular polyP content (200). The same group reconstituted +36GFP coacervates *in vitro* and revealed a polyP chain length-dependent trait of this process (200), similar to other types of polyP protein interactions (25,26,84). It is intriguing whether this aspect of polyP activity has been preserved in the evolution of miscellaneous phase-separated compartments in the mammalian species. To answer this question, one must develop a feasible tool to either up- or down-regulate polyP levels (e.g., in the nucleolus) and analyze the corresponding kinetic parameters of local proteins using the FRAP technique. This proposal again alludes to the paramount importance of discovering the polyphosphate kinase(s) and polyphosphatases in mammalian cells.

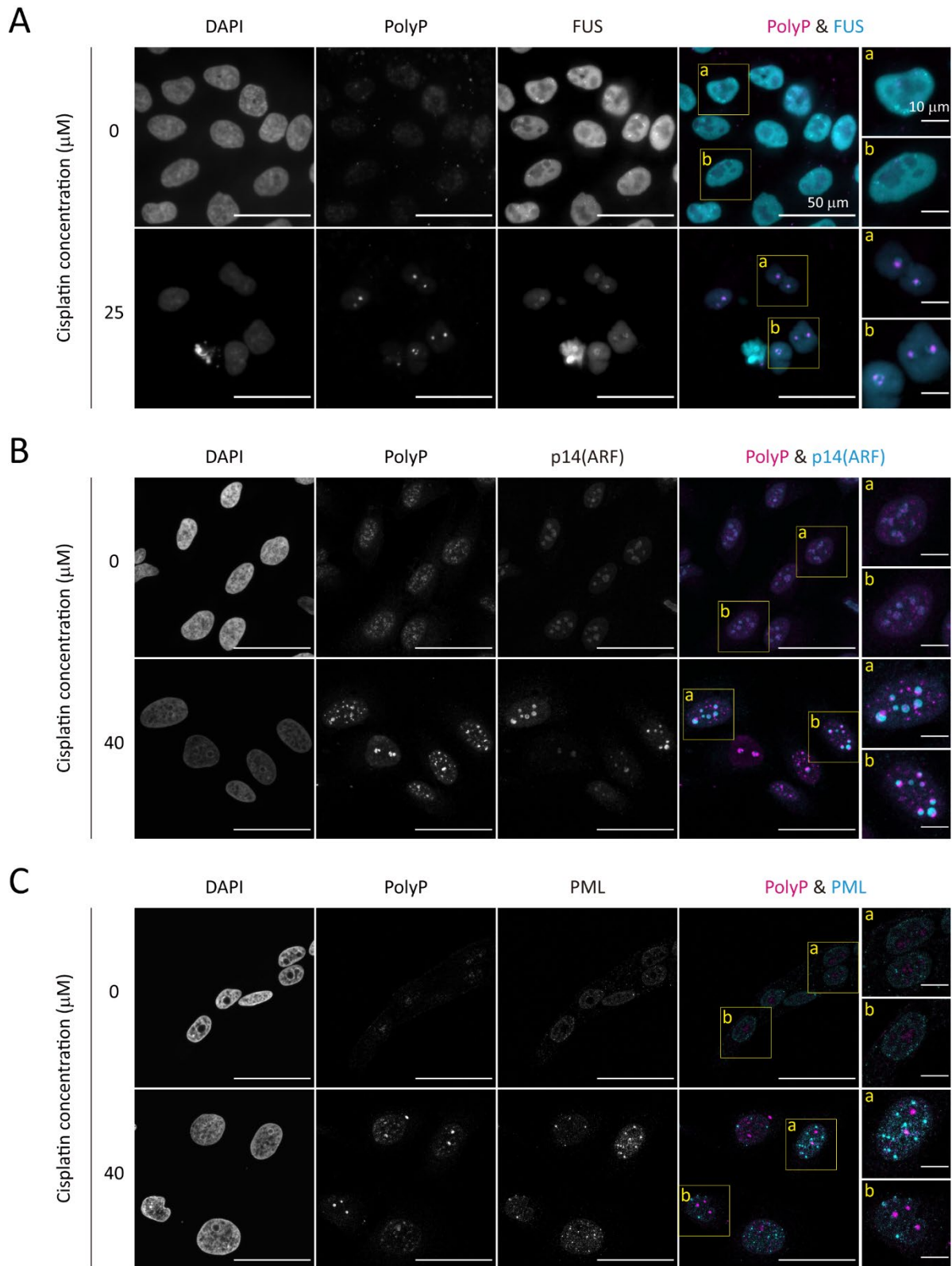
3.5 Outlook

We are confident that this study together with the abovementioned follow-up experiments will deepen our understanding of polyP and ribosome biogenesis. In addition to the emerging evidence which lays the foundation of polyphosphorylation in the late ribosome assembly (48), these experiments will reveal the role of polyP and polyphosphorylation in the *de novo* synthesis and processing of premature rRNA transcripts. By prioritizing Nopp140, coilin, and UBF among hundreds of candidates to be polyphosphorylated *in vivo*, we conceptualize novel mechanisms to leverage RNA pol I activities. Furthermore, we propose to engineer *EcPPX_c*-related tools to visualize and/or purify polyphosphorylated molecules from a cellular origin.

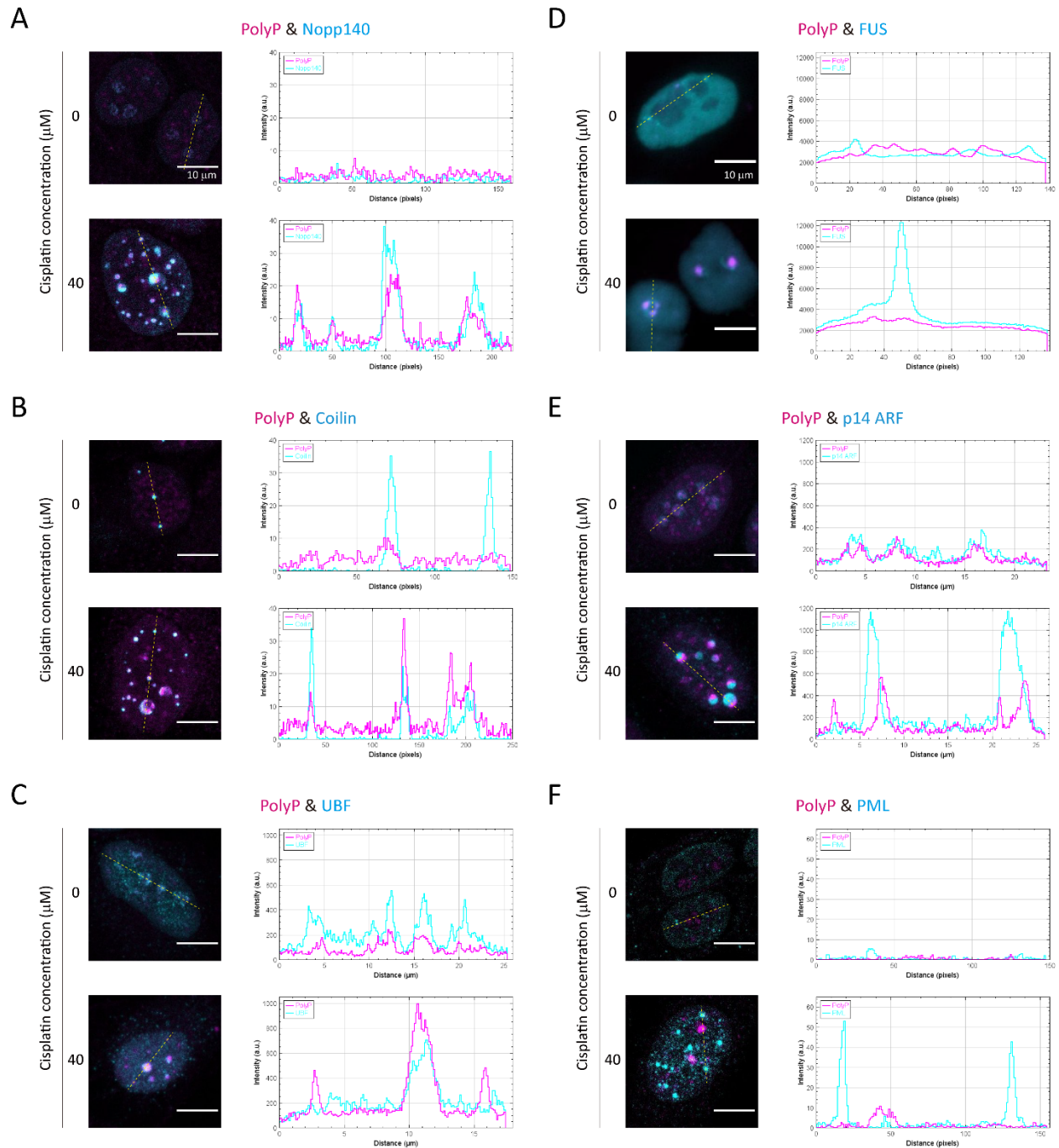
The ultimate transition from the description of polyP distributions in response to stress to the mechanistic understanding of polyP's role in the physiology of the eukaryotic cell, however, relies on the development of a robust and reliable polyP manipulation paradigm. Whereas this endeavor is greatly hindered by the unknown polyphosphate kinase(s) and polyphosphatase(s), it may be achieved by ectopically expressing *E. coli* or yeast polyP-metabolizing enzymes in an organelle/compartment of interest. Based on previous experiences from us and others, the success of this strategy seems to depend on the locations where these enzymes are targeted to (18,48,50,60). Alternatively, an endogenous nucleolar protein and potential polyP modifier, namely IP6K1, may be genetically ablated to indirectly affect polyP levels. However, the outcome of this approach will inevitably be confounded by inositol polyphosphates throughout the cell and therefore become hard to be interpreted. As far as we know, neither upregulation nor downregulation of polyP in the

nucleolus specifically has been reported so far. Therefore, this might be a niche for exploring polyP and ribosomal biogenesis through trial and error.

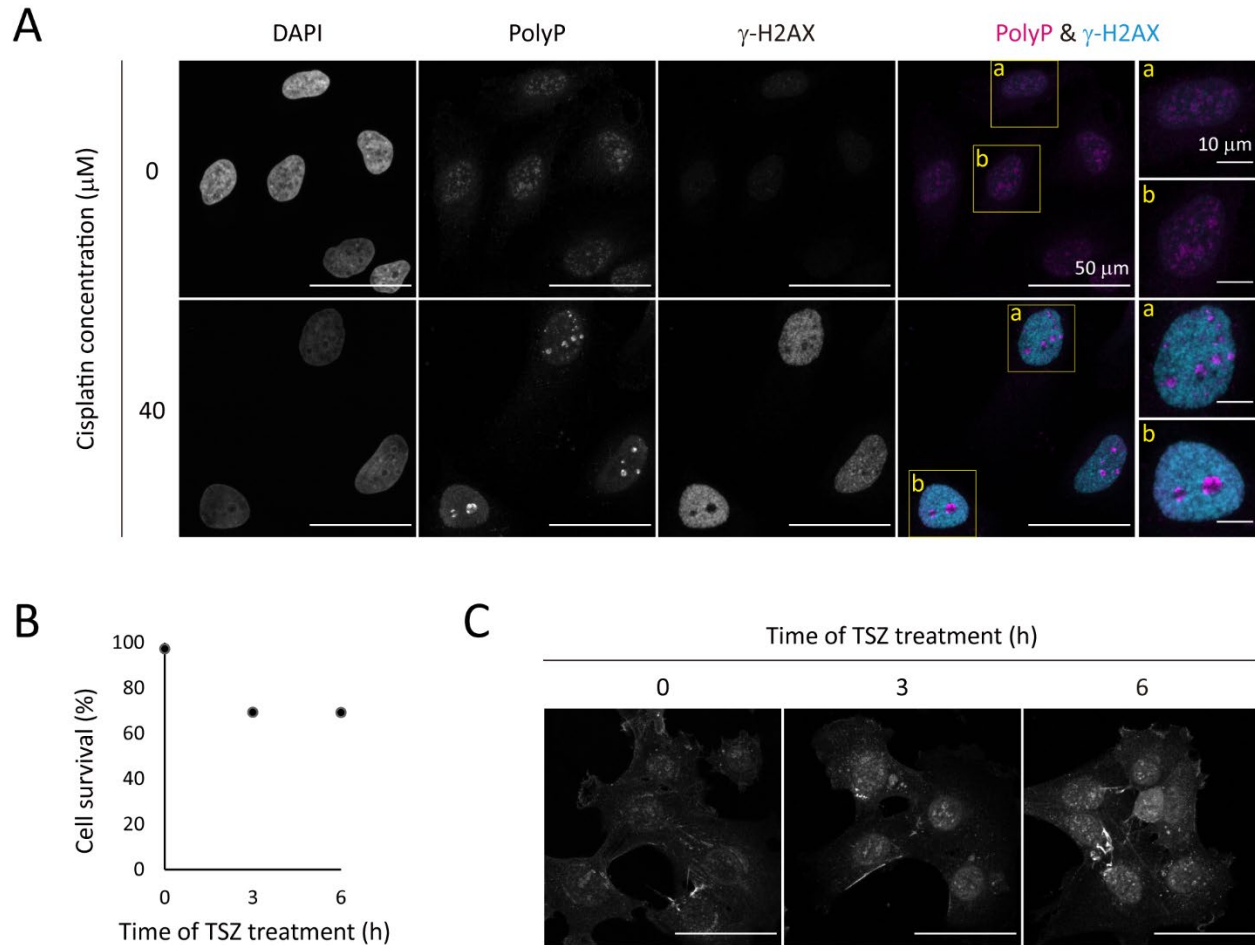
3.6 Supplemental information



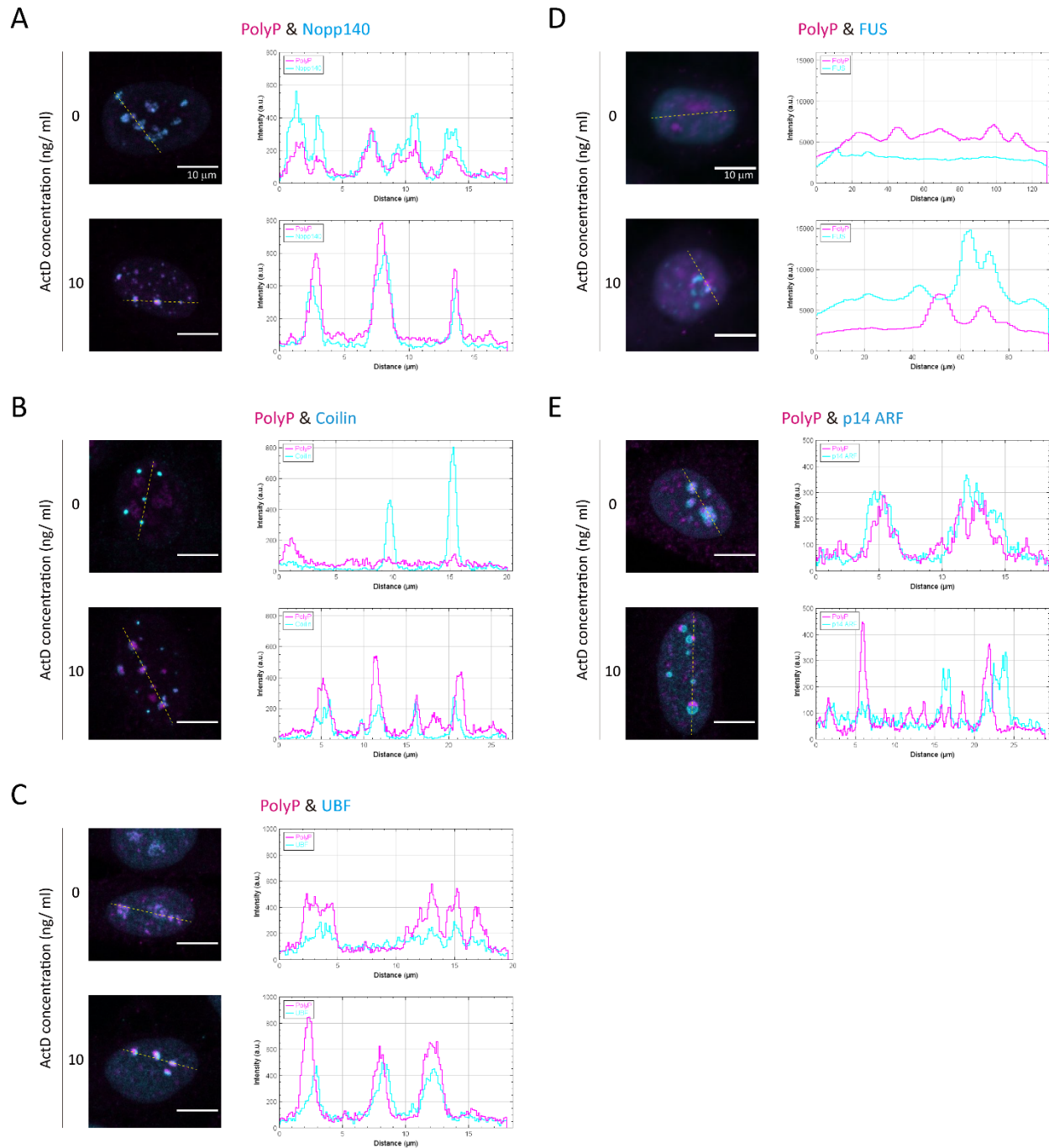
Supplementary Figure 3.1 Cisplatin-induced polyP foci are distinct from dark nucleolar caps, central bodies, and PML bodies. Colocalization of polyP and (A) FUS, a dark nucleolar cap marker, was monitored by labeling polyP with mCherry-*EcPPX_c* in a stable FUS-GFP-overexpressing HeLa Kyoto cell line. Partitioning of polyP and FUS was evident both before (top row) and after (bottom row) a 25 μ M cisplatin treatment for 24 h. From left to right are signals of DNA (revealed by DAPI), polyP (revealed by mCherry-*EcPPX_c*), and endogenously expressed FUS-GFP. PolyP (pseudo color: magenta) and FUS-GFP (pseudo color: cyan) fluorescence signals are merged and two regions (a and b) are enlarged for more details. Colocalizations of polyP and (B) the central body marker, p14(ARF) and (C) the PML body marker, PML were also examined by immunofluorescence. Untreated HeLa cells (top row) and cells treated with 40 μ M cisplatin for 24 h (bottom row) were labeled with GFP-*EcPPX_c* and the respective primary and secondary antibodies for the protein markers. DNA, polyP, and (B) p14(ARF) or (C) PML signals are shown from left to right. The rightmost image is an overlay of polyP (pseudo color: magenta) and the respective protein marker (pseudo color: cyan). Two regions (a and b) are enlarged for a detailed view. The corresponding fluorescence intensity plots can be found in Fig. S3.2. Representative images of projected z series are shown. Scale bar information is denoted in panel (A).



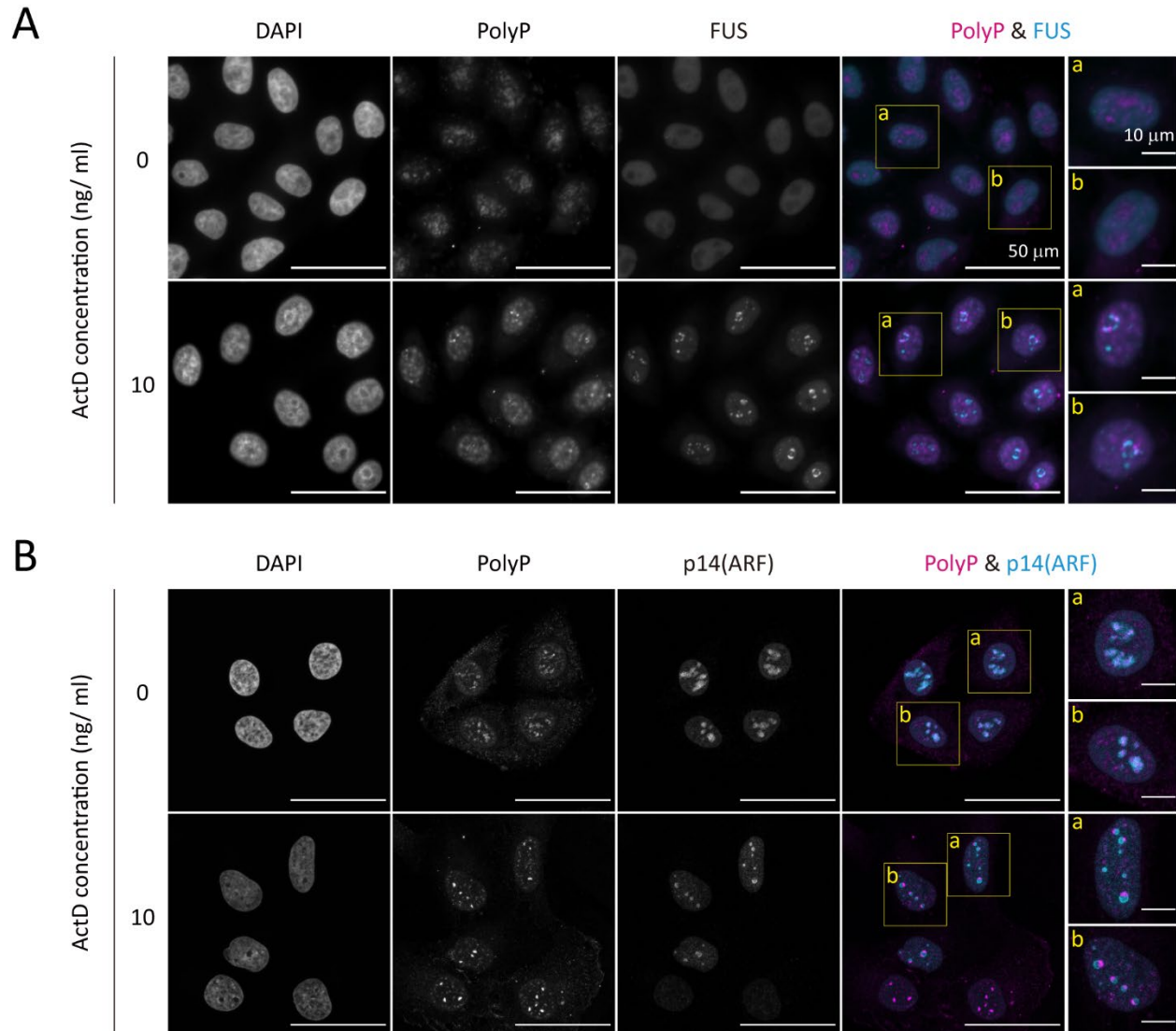
Supplementary Figure 3.2 Colocalization analysis of polyP and nuclear markers in cisplatin-treated cells with fluorescence intensity plots. The spatial correlation of polyP and (A) Nopp140, (B) coilin, (C) UBF, (D) FUS-GFP, (E) p14 or (F) PML was analyzed by measuring the fluorescence intensities of GFP-*EcPPX_c* (or mCherry-*EcPPX_c*) and the designated protein marker at the same positions in the nucleus. On the left of each panel, fluorescence images of untreated HeLa cells (top) and cells treated with 40 μM cisplatin for 24 h (bottom) are shown to visualize the distributions of polyP (pseudo color: magenta) and the respective nuclear marker (pseudo color: cyan). Positions of interest are defined by a yellow dashed line. On the right is the alignment of the fluorescence intensities of polyP (magenta) and the nuclear marker (cyan) at each position along the yellow dashed line (shown as the distance from the starting point). Each peak represents a punctum of polyP and/or the nuclear marker. The height of the peak is proportional to the signal intensity before and after cisplatin treatment, whereas the width of the peak indicates the size of the punctum. An overlapped peak is a signature of the colocalization of polyP and the corresponding nuclear marker.



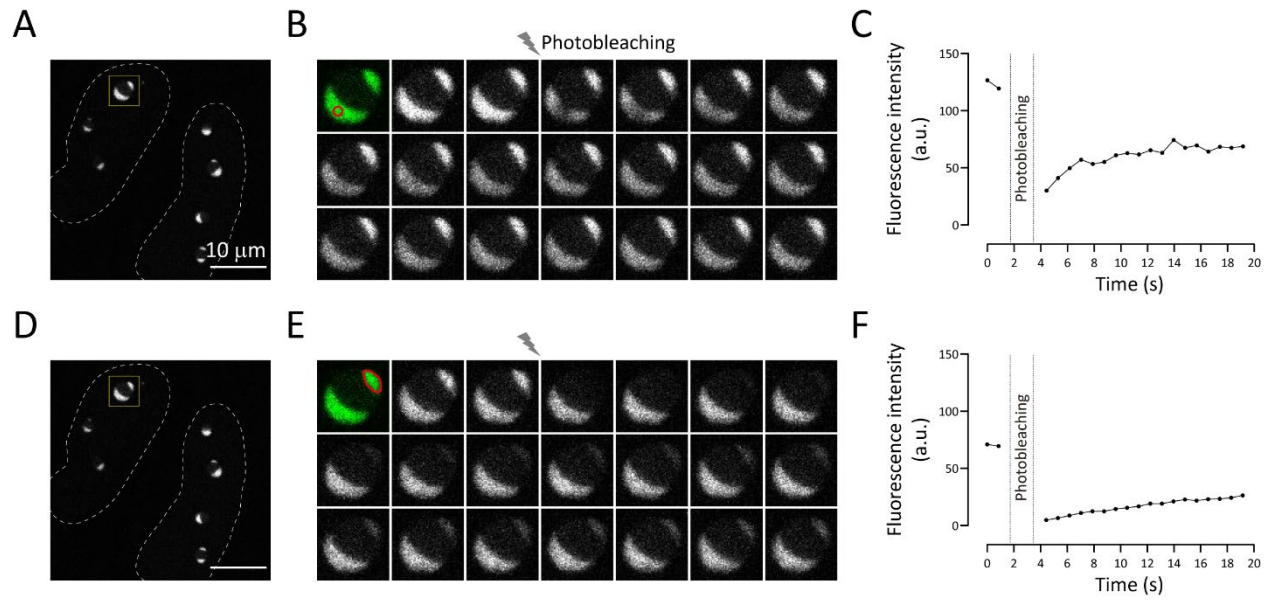
Supplementary Figure 3.3 PolyP foci are not a direct readout of DNA damage or cell death. (A) Immunofluorescence labeling of polyP and γ -H2AX, a reporter for DNA double stranded breaks, was performed in untreated HeLa cells (top row) and cells treated with 40 μ M cisplatin for 24 h (bottom row). The distributions of DNA (gray scale, left), polyP (gray scale, middle), and γ -H2AX (gray scale, right) were depicted by DAPI, GFP-*Ec*PPX_c, and specific primary and secondary antibodies for γ -H2AX. Overlaying polyP (pseudo color: magenta) and γ -H2AX (pseudo color: cyan) signals, it is evident that these two molecules belong to distinct nuclear compartments after cisplatin treatment. For each merged image, two regions (a and b) are enlarged for a more detailed view. Representative images of projected z series are shown. Scale bars are shown on the images. (B) Survival rates of mouse embryonic fibroblasts treated with 10 ng/ml TNF- α , 10 nM BV6 (a SMAC mimetic), and 20 μ M Z-VAD-FMK (denoted as TSZ) were measured by SYTOX Green assay. (C) The corresponding time lapse analysis of polyP levels and distributions after 0, 3, and 6 h TSZ treatment was conducted via fluorescence labeling of polyP with GFP-*Ec*PPX_c.



Supplementary Figure 3.4 Colocalization analysis of polyP and nuclear markers in ActD-treated cells using fluorescence intensity plots. The spatial correlation of polyP and (A) Nopp140, (B) coilin, (C) UBF, (D) FUS-GFP or (E) p14 was examined by plotting the fluorescence intensities of GFP-*EcPPX_c*/mCherry-*EcPPX_c* and the designated protein marker at the same positions in the nucleus. On the left side of each panel are fluorescence images of untreated HeLa cells (top) and cells treated with 10 ng/ml ActD for 4.5 h (bottom), showing the overlay of polyP (pseudo color: magenta) and nuclear marker (pseudo color: cyan) signals. A series of positions are selected by a yellow dashed line. On the right side are fluorescence intensity plots of polyP (magenta) and the nuclear marker (cyan) at different positions along the yellow dashed line (shown as their distances from the starting point). Each peak signifies a punctum of polyP and/or the nuclear marker. The height of the peak reflects the signal intensity before and after ActD treatment, and the width of the peak measures the size of the structure. Overlapped peaks are indications of the colocalizations of polyP and selected nuclear markers.



Supplementary Figure 3.5 PolyP foci formed upon ActD treatment are excluded from dark nucleolar caps and central bodies. (A) Colocalization study of polyP and FUS, a dark nucleolar cap marker, was conducted using immunofluorescence method. Untreated HeLa Kyoto cells (top row) and cells treated with 10 ng/ ml ActD for 4.5 h (bottom row) were labeled with DAPI (gray scale, left) and GFP-*EcPPX_c* (gray scale, middle). FUS-GFP (gray scale, right) was stably overexpressed in the cells. An overlay of polyP (pseudo color: magenta) and FUS-GFP (pseudo color: cyan) fluorescence is displayed with two regions (a and b) enlarged for a closer view. (B) Colocalization analysis of polyP and p14(ARF), a central body marker, was also examined in untreated HeLa cells (top row) and cells treated with the same ActD condition (bottom row). Gray scale images from left to right depict the patterns of DNA (stained with DAPI), polyP (stained with GFP-*EcPPX_c*), and p14(ARF) (stained with the specific primary and secondary antibodies). PolyP (pseudo color: magenta) and p14(ARF) (pseudo color: cyan) signals are merged to show the partition of the two molecules. Two regions (a and b) are enlarged for more details. The corresponding fluorescence intensity plots can be found in Fig. S3.4. Representative images of projected z series are shown. Scale bar information is included in panel (A)



Supplementary Figure 3.6 Fibrillarin-GFP is highly dynamic in the light nucleolar cap and communicates with the surrounding environment. (A-C) FRAP analysis of fibrillarin-GFP within the light nucleolar cap. (A) Overexpressed fibrillarin-GFP was targeted to light nucleolar caps upon ActD treatment in HeLa cells. Two nuclei were outlined by white dashed lines and the nucleolus of interest was highlighted by a yellow square. (B) In the same nucleolus as the one highlighted in (A), photobleaching was limited to the region with the red border, and time-lapse images of fibrillarin-GFP fluorescence were taken with a time interval of 0.865 s. The first two images were taken prior to photobleaching, and the following 18 images were taken during fluorescence recovery. (C) Fibrillarin-GFP fluorescence intensity in the photobleached area was plotted against time. Note that measurements were unavailable during photobleaching. (D-F) FRAP analysis of fibrillarin-GFP between light nucleolar caps and their adjacent environment. (D) The same cells (outlined by white dashed lines) and the same nucleolus (highlighted by the yellow square) were studied. (E) The entire nucleolar cap circled in red was subject to photobleaching, and time-lapse images of fibrillarin-GFP were acquired with a time interval of 0.865 s. Two images were taken before photobleaching, followed by 18 images taken after photobleaching. (F) Fibrillarin-GFP fluorescence intensity in the designated nucleolar cap decreased due to photobleaching and gradually recovered after photobleaching. Fluorescence intensity measurements were unavailable during photobleaching.

Chapter 4 Identification of Polyphosphate Regulatory Genes in Mammalian Cells

4.1 Introduction

Despite the high conservation of inorganic polyphosphate (polyP) (2), very little is known about the mechanisms by which it is synthesized and/or degraded in the vast majority of species. Ever since polyP aroused the attention of biologists in the 19th century, the field took the greatest leaps when the bona fide polyphosphate kinases (PPKs) were discovered, first in *Escherichia coli* (7) and later on in *Saccharomyces cerevisiae* (62). A lack of sequence homology between *E. coli ppk1*, yeast vacuolar transport chaperone 4 (*VTC4*), and any mammalian genes eliminates a bioinformatic approach to identify *PPK* genes in the human genome. Hence, coming up with alternative strategies is a prerequisite for solving the most intriguing puzzle in the field, namely how mammalian cells manage their polyP reserve.

By far the most successful attempts at identifying polyP synthesizing machineries utilized a combination of biochemical and genetic methods (7,62).

To isolate *E. coli* PPK1 from cell lysate, the Kornberg team combined a series of protein purification techniques with a highly sensitive, radioactivity-based PPK activity assay (7,201). This strategy allowed them to enrich PPK activity by nearly 60,000-fold with a concomitant 20,000-fold purification of the enzyme. Notably, a similar experimental setup led to the discovery of *D. discoideum* PPK2, whose *in vitro* polyP-synthesizing activity was corroborated by the same assay (114). However, the *in vivo* activity of this enzyme is still under debate (89). A commonality between *E. coli* PPK1 and *D. discoideum* PPK2 is their structural rigidity, which survived extensive purification procedures using sonication, detergents, salts, affinity binding, and etc. This feature together with a reliable specific activity assay are the core premises for uncovering an enzyme of interest with a biochemical approach. Undoubtedly, this path had been taken, in fact, as the first attempt to find the mammalian PPK (36,105). However, those early endeavors were futile as PPK activity was readily lost upon cell lysis. This dilemma brought about a prevalent view that mammalian PPK might reside in the lipid bilayers and/or utilize an electrochemical gradient across the membrane as an indispensable energy supply (202).

The identification of *Vtc4* was an unintended result of a genome-wide microarray analysis of phosphate metabolism genes in *S. cerevisiae* (62). Unlike *E. coli*, which accumulates polyP under oxidative stress with a less than two-fold upregulation of *ppk* transcripts (34), yeast elicits a similar response under phosphate limitation conditions yet with a surge of *VTC4* mRNA (62). In retrospect, *Vtc4* would not have been discovered had researchers not identified an environmental cue that triggered a change in polyP levels. Hence, conceptually, establishing an analogous scenario in other organisms whose genetic backgrounds are well documented and easily manipulated in a high throughput manner might pave the way to unveiling novel *PPK* genes, particularly those in mice and humans.

Another limiting factor in identifying the polyP machinery in mammalian systems is the quantitation of polyP levels. In a biochemical approach, three main steps, namely polyP extraction (with phenol chloroform), conversion to ATP (by *E. coli* PPK1), and ATP detection (with a luciferase assay) must be carefully executed to gauge the concentrations of intracellular polyP (203). Nonetheless, a few drawbacks are intrinsic to this workflow, including the preference of PPK1 for long chain polyP and the incomplete sample recovery rate. A second category of polyP detection tools are less quantitative yet uniquely suited to resolve the chain length distribution of polyP in a biological sample. This goal is achieved by combining gel electrophoresis with a negative staining of polyP with DAPI whose fluorescence signal gets rapidly photobleached under UV (204). However, a recent study challenges the specificity of this approach, especially for short chain polyP, by exhibiting an identical UV-sensitive feature of DAPI-IP₇ fluorescence (205). The same problem concerns *in situ* polyP visualization with DAPI staining because not only polyP but also inositol pyrophosphates and RNA induce a signature red-shift of the excitation and emission profile of the dye (37,206,207). Apart from DAPI, JC-D7 and JC-D8 are the only polyP reporters designed for live cell imaging (40). Both chemicals, albeit less promiscuous than DAPI, bind to polyP with much weaker affinity. This caveat might account for a limited application of these tools to engineered models where polyP is overrepresented (208).

In contrast, a wealth of knowledge on the subcellular localization of polyP was driven by the development of different variants of the inactive polyP binding domain of *E. coli* exopolyphosphatase (*EcPPX_c*), which revealed polyP in the vacuoles of yeast (147), cell walls of algae and fungi (144,209), acidocalcisome-like granules of animal eggs (210,211) and mast cells (39), and nucleoli of mammalian cells (38). The high sensitivity and specificity of *EcPPX_c* for

polyP was verified by competition assays (147) and follow-up studies using subcellular fractionation and biochemical quantification. Ideally, an enzymatic digestion of polyP in the samples prior to *EcPPX_c* labeling would provide the ultimate proof for the precision of this probe. However, this trial failed in practice possibly due to a tight association of polyP with other macromolecules, such as RNA (38), which appears to shield the polymer from being shortened at the ends. Thereby, alternative routes must be taken to corroborate the previous findings and uncover the full potential of *EcPPX_c*-related probes for characterizing the regulation of polyP in mammalian cells.

In this study, we assessed and confirmed the fidelity of *EcPPX_c* with *E. coli* strains undergoing nutrient starvation, a condition known to induce polyP accumulation in bacteria (5,212). We then conducted a genome-wide siRNA screen in HeLa cells treated with cisplatin and labeled with mCherry-*EcPPX_c* to search for genuine polyP regulators in the human genome. In the primary screen, we identified a list of 115 candidates for the human *PPK* genes, whose knockdowns resulted in more than 70% decrease in polyP levels after cisplatin treatment. We followed up on validating 36 of them and found a few potential polyP-related genes, i.e. *GRIN3B*, *P2RY1*, *ATP5F1E*, *PANK4*, and *AP3MI* to be of particular interest. Furthermore, we revealed a potential connection between inositol phosphate metabolism and polyP levels. Lastly, we discovered a subset of genes involved in DNA damage repair, the ubiquitin-proteasome system, and cell cycle progression to be essential for combating cisplatin stress in HeLa cells.

4.2 Materials and methods

4.2.1 Reagents

A vector containing mCherry-*EcPPX_c* was generated as previously reported (127). Briefly, we used the pETM41-*EcPPX_c* plasmid, which encodes the Maltose Binding Protein (MBP)-*EcPPX_c* (kindly provided by Florian Freimoser; Addgene plasmid #38329; <http://n2t.net/addgene:38329>; RRID:Addgene_38329) (144) as a template to amplify the *EcPPX_c* fragment by PCR. Next, this fragment was inserted between the BamHI and NotI recognition sites downstream of the mCherry-coding sequence in a pTEV5 vector. mCherry-*EcPPX_c* protein and the corresponding control, mCherry, were His-tagged and therefore could be purified with Ni-NTA columns (Qiagen, Hilden, Germany). All reagents used for cloning and protein purification were obtained from Thermo Fisher Scientific (Waltham, MA, USA), Sigma-Aldrich (St. Louis, MO, USA), and New England

Biolabs (Ipswich, MA, USA) unless mentioned otherwise.

4.2.2 Nutrient shift treatment of *E. coli*

The following amino acid and phosphate limitation protocol was adapted from (28). Briefly, *E. coli* strains with two different genetic backgrounds, wild-type (MG1655) and $\Delta ppk1\Delta ppx1$, were cultured in lysogeny broth (LB) at 37 °C overnight. Then, cells were diluted in potassium morpholinoprepanesulfonate (MOPS) buffer (#M2101, Teknova, Hollister, CA, USA) supplemented with 0.2% glucose, 100 μ M potassium phosphate, and 10 μ M thiamine to OD₆₀₀= 0.1 and cultured at 37 °C until mid-log phase (OD₆₀₀= 0.4 to 0.8). After that, cells were pelleted with centrifugation, and supernatant was discarded.

4.2.3 Immunofluorescence labeling and visualization of polyP in *E. coli*

Following nutrient downshift, the cell pellet was resuspended in freshly prepared 4% (v/v) Paraformaldehyde (#1578100, Electron Microscopy Sciences, Hatfield, PA, USA) and fixed for 20 min in a thermomixer set at room temperature, 500 rpm. Then, cells were spun down at 16,100 g for 1 min in a tabletop centrifuge, and paraformaldehyde was transferred to a hazardous waste container. Next, the cell pellet was rinsed with PBS for three times (by completely resuspending the cells and spinning them down). To penetrate the plasma membrane, cells were resuspended in a permeabilization buffer containing 0.3% Triton X-100 (#0219485480, MP Biomedicals, Solon, OH, USA) and 1% Bovine Serum Albumin (#A3059, Sigma-Aldrich) in PBS. Samples were incubated in the thermomixer using the same settings. Ten minutes later, cells were subject to another round of three PBS washes and subsequently blocked with 1% bovine serum albumin dissolved in PBS for 1 h. To label polyP, blocking buffer was replaced with 10 μ g/ ml mCherry-*EcPPX_c* solution, and cells were incubated at 4 °C, 500 rpm overnight. Hereon, samples should be shielded from light as much as possible. A final round of three PBS washes were performed to remove superfluous dye. Lastly, cell resuspension in PBS was mounted between a piece of coverslip and a microscope glass slide.

Differential interference contrast (DIC) images and mCherry fluorescence images were acquired immediately after sample preparation. The image acquisition platform was constructed with an Olympus BX61 upright microscope (Olympus, Center Valley, PA, USA) carrying a 40 \times objective, a Photometrics Coolsnap HQ2 cooled CCD camera equipped with a quad filter set (DAPI/ FITC/ TRITC/ CY-5), and an X-Cite[®] exacte mercury lamp whose illumination intensity was held

consistent with a feedback loop.

4.2.4 High throughput siRNA screens for polyP regulatory genes

4.2.4.1 Cell line

HeLa (ATCC[®] CCL-2[™], ATTC, Manassas, VA, USA) cells were grown in DMEM (#11995065, Thermo Fisher Scientific) supplemented with 10% Fetal Bovine Serum (#F4135, Sigma-Aldrich) and 1% Penicillin-Streptomycin (#15140122, Thermo Fisher Scientific). Cells were cultured at 37°C with 5% CO₂ until they reached ~ 80% confluent and were then detached from the flask using 0.05% Trypsin-EDTA (Thermo Fisher Scientific).

4.2.4.2 Genome-wide human siRNA libraries

The primary screen for human *PPK* genes was carried out using the Dharmacon siGENOME SMARTpool[®] human siRNA library (Dharmacon, Inc., Lafayette, CO, USA) purchased by and cataloged at the Life Science Institute, University of Michigan. In total, 18,110 genes and loci were targeted, each by a mixture of four siRNA duplexes to minimize the off-target effect. The lyophilized siRNAs were dissolved in siRNA buffer (#B002000UB100, Dharmacon, Inc.) to a concentration of 0.5 μM and stored at -80 °C in 384-well plates. In the primary screen, three out of sixty-seven siRNA stock plates were assayed at a time. Afterwards, all the hits were cherry-picked from the original siRNA stock plates, transferred to a new 384-well plate and retested in the same assay to generate a list of candidates.

Two validation screens for 36 promising candidates were performed with custom siRNA stock plates prepared with ON-TARGETplus SMARTpool[®] siRNAs and individual siGENOME siRNAs by Dharmacon, Inc.

To silence *ATP5F1E*, we used newly purchased siGENOME SMARTpool[®] siRNA (#M-012330-00), individual siGENOME siRNAs (#D-012330-01, #D-012330-02, #D-012330-03, and #D-012330-04), ON-TARGETplus SMARTpool[®] siRNA (#L-012330-02), and individual ON-TARGETplus SMARTpool[®] siRNAs (#J-012330-17, #J-012330-18, #J-012330-19, and #J-012330-20), all from Dharmacon, Inc. To knockdown *ATP5PB*, we used siGENOME SMARTpool[®] siRNA (#M-015956-01) and ON-TARGETplus SMARTpool[®] siRNA (#L-015956-01).

4.2.4.3 Reverse transfection of siRNA

The siRNA stock solutions were thawed at 4 °C overnight. A BioMek FX fluid handling robot (Beckman Coulter, Brea, CA, USA) equipped with sterile, RNase-free pipet tips (#B98224, Beckman Coulter) was utilized to transfer 2.4 µl (equivalent to 1.2 picomoles) siRNA from the siRNA stock plates to three identical 384-well black tissue culture plates with clear bottom (#6007460, PerkinElmer, Waltham, MA, USA). The transfection agent, Lipofectamine™ RNAiMax (#13778075, Thermo Fisher Scientific) was diluted in the Opti-MEM™ Reduced Serum Medium (#31985062, Thermo Fisher Scientific) at a ratio of 1: 110 and incubated at room temperature for 5 min. Then, a Multidrop Combi Dispenser (Thermo Fisher Scientific) with sterile tubing was employed to add 8 µl transfection mixture to each well. siRNAs and Lipofectamine™ RNAiMax were allowed to assemble at room temperature for 20 min. In the meantime, HeLa cells were trypsinized and resuspended in growth medium to a density of 6.7×10^4 cells/ml. After adding 30 µl cell suspension (or 2,000 cells) to each well with the Multidrop dispenser, the cells were grown for three days to allow for an efficient knockdown of the target gene or locus. In parallel, a non-targeting siRNA (#D0012061305, Dharmacon, Inc.), which lacks any matched sequences in the human transcriptome, was applied to the positive and negative controls.

4.2.4.4 Cisplatin treatment

Cis-Diammineplatinum(II) dichloride (#P4394, Sigma-Aldrich) was solubilized in double distilled water at a stock concentration of 3 mM. Following siRNA transfection and knockdown, spent medium was removed from the 384-well plates, and 0.4 mM cisplatin prepared in fresh growth medium was administered to the cells, with the only exception that one set of control (i.e., the positive control) was left untreated, mimicking the scenario where there was no polyP accumulation. Cisplatin treatment typically lasted for 24 h.

4.2.4.5 Immunofluorescence labeling

An adapted immunofluorescence protocol for high throughput screening was developed to visualize intracellular polyP levels. Briefly, cisplatin-containing medium was removed by covering the plates with thick, absorbent materials, inverting the plates and gently shaking them (so that any cisplatin contaminated materials could be disposed easily). Immediately afterwards, 30 µl freshly prepared 4% (v/v) paraformaldehyde was dispensed to each well by the Multidrop dispenser. The cells were fixed at room temperature in the dark for 20 min. Following a similar procedure as that

used for cisplatin, paraformaldehyde was removed from the plates, and the cells were rinsed three times with PBS using the Multidrop dispenser. Then, cellular membranes were penetrated with 30 μ l permeabilization buffer, which contained 0.3% Triton X-100 and 1% bovine serum albumin dissolved in PBS. After a 10 min incubation at room temperature, Triton X-100 was discarded and the cells were again rinsed with PBS for three times. To decrease the background noise caused by nonspecific binding, the cells were blocked with 1% bovine serum albumin in PBS (i.e., blocking buffer) for at least 1 h at room temperature. Later on, mCherry-*EcPPX_c* working solution was prepared at a concentration of 10 μ g/ ml in prechilled blocking buffer. Each well was filled with 50 μ l mCherry-*EcPPX_c* and kept at 4 °C overnight, protected from light. On the next day, after rinsing away mCherry-*EcPPX_c* with PBS for three times, the cells were incubated with 1 μ g/ ml DAPI (#D1306, Thermo Fisher Scientific) for 5 min in the dark, which served as a counter stain. As soon as three final rinses with PBS were completed, and each well was filled with 50 μ l PBS, the plates were sealed with black films and kept in the cold room, typically for 0 to 4.5 h, until the designated imaging sessions.

It is important to note that both cisplatin and paraformaldehyde were considered as hazardous chemicals. Therefore, all the reagents and materials that had been contaminated during sample preparation should be dealt with complying the local rules.

4.2.4.6 Image acquisition

A set of three plates, namely technical triplicates of the same siRNA transfection, were equilibrated to room temperature and loaded sequentially by the CRS Catalyst Express Robot Arm (Thermo Fisher Scientific) onto the automated ImageXpress Micro XLS Imager (Molecular Devices, San Jose, CA, USA). Fluorescence images were captured with the CFI Plan Fluor ELWD (extralong working distance) DM 20 \times C lens (Nikon, Minato City, Tokyo, Japan). Fluorophores were excited by the SOLA SE 2 Light Engine[®] (Lumencor, Inc., Beaverton, OR, USA). Specific excitation and emission wavelengths were set by a filter cube, which alternated between TxRed channel (for detecting mCherry-*EcPPX_c*) with 900 ms exposure time for cisplatin-treated samples and 1.5 s for untreated samples, and DAPI channel with 50 ms exposure time. In each well, five different positions were sampled to expand the number of cells and average out random noises. To obtain the best focus, manual adjustment for the post-laser offset was performed for each channel, followed by autofocus calibrated using the first three wells on the plate.

4.2.4.7 Image analysis

Fluorescence images were analyzed with the Multi-Wavelength Cell Scoring Application Module of the MetaXpress[®] Software (Molecular Devices). For the DAPI channel, a detection limit (i.e., fluorescence intensity above local background) and an estimated nucleus size were set to determine the number as well as the location of all the nuclei in the image. For the mCherry-*EcPPX_c* channel, a detection limit and an estimated cell size were defined to identify the cells. Then, mCherry-*EcPPX_c* fluorescence intensity was measured either for the entire cell or only for the nucleus (using the spatial information from the corresponding DAPI channel). A sorting criterion was created for the mCherry-*EcPPX_c* channel to highlight “cisplatin responsive cells” or cells accumulating 8.5 to 12 times as much polyP as the steady state level. The percentage of cisplatin responsive cells was calculated and served as the chief parameter for hit identification.

All the measurements, except cell count, were normalized to the internal controls on the same 384-well plate. The score of positive control was set to 0, and that of negative control was set to 100. Sample scores were calculated using the following formula: $100 \times [(sample\ value) - (positive\ control\ value)] / [(negative\ control\ value) - (positive\ control\ value)]$. Notably, normalized sample scores positively correlated with polyP content. Data storage, analysis, and hit identification were assisted by the MScreen platform (213) built in-house at the Center for Chemical Genomics, University of Michigan.

4.2.5 Quantitative reverse transcription polymerase chain reaction (qRT-PCR)

qRT-PCR analyses were performed to evaluate the knockdown efficiencies of *ATP5F1E* and *ATP5PB* siRNAs, with the non-targeting siRNA serving as the negative control.

For siRNA transfection, 4.8 picomoles of siRNA was added to a 96-well tissue culture plate (#3596, Corning, Inc., Corning, NY, USA). Then, we prepared transfection reagent by diluting Lipofectamine[™] RNAiMax in the Opti-MEM[™] reduced serum medium by 110-fold. After 5 min incubation at room temperature, 32 μ l transfection mixture was added to the siRNA, followed by another incubation for 20 min. Lastly, HeLa cells were seeded at a density of 8,000 cells/ well and incubated at 37 °C with 5% CO₂ for 72 h. To collect samples, spent medium was removed from the plate, and 20 μ l/ well TRIzol[™] reagent (#15596026, Thermo Fisher Scientific) was used to lyse the cells immediately. Usually, cell lysates from 8 identical wells transfected with the same siRNA were combined to scale up the amount of material. Samples could be stored at -80 °C if

necessary.

To extract total RNA from the cell lysate, we added 50 μ l chloroform (#C2432, Sigma-Aldrich) to 150 μ l cell lysate (thawed at room temperature). After a brief vortex for 30 s, we left the sample unperturbed until the aqueous phase and the organic phase started to reappear, which usually took 3 min. Then, a prolonged centrifugation was carried out at 12,000 rpm, 4 °C for 10 min to ensure a complete separation of the two phases. The aqueous layer was transferred to a clean, RNase-free Eppendorf tube and extracted with chloroform once more, following the same procedure described above. RNA concentration was measured with a NanoDrop™ 2000 spectrophotometer (Thermo Fisher Scientific).

cDNA was synthesized with the Radiant™ cDNA Synthesis Kit (#QC1125, Alkali Scientific, Inc., Lauderdale, FL, USA) per the manufacturer's instructions. Briefly, we set up two reactions in parallel: 1) a reverse transcription reaction with cDNA synthesis mix, reverse transcriptase, and total cellular RNA (4 pg to 4 μ g) and 2) a control reaction in which reverse transcriptase was substituted by DNase/RNase-free water (#10977015, Thermo Fisher Scientific). Both reactions were run at 42 °C for 30 min, prior to heat denaturation of the reverse transcriptase at 85 °C for 10 min.

The following primer sequences were designed for amplifying *ATP5F1E* cDNA: 5'-GTGGCCTACTGGAGACAGG-3' (forward primer) and 5'-GGAGTATCGGATGTAGCTGAGT-3' (reverse primer). As an internal control, *HSP90* cDNA was amplified with 5'-GAAATCTGTAGAACCCAAATTTCAA-3' (forward primer) and 5'-TCTTTGGATACCTAATGCGACA-3' (reverse primer). The efficiencies of *ATP5F1E* and *HSP90* primer pairs were 81.2% and 89.3%, respectively.

Each qRT-PCR reaction was set up with 5 ng cDNA, 200 ng/ μ l forward primer, 200 ng/ μ l reverse primer, and 10 μ l EvaGreen qPCR 2 \times Mastermix-ROX (#BEQPCR-R, MIDSCI, St. Louis, MO, USA) in a total volume of 20 μ l. Technical triplicates were set up for each sample. Reactions were performed in the MasterCycler® ep *realplex* 4 Real-Time PCR system (Eppendorf, Hamburg, Germany) using the recommended program for EvaGreen qPCR Mastermix. cDNA was first denatured at 95 °C for 10 min, and then, it underwent 40 cycles of amplification (95 °C for 15 s and 60 °C for 1 min). Threshold cycle (C_t) was calculated by the MasterCycler® ep *realplex* software.

4.2.6 Western blotting

Knockdown efficiencies of *GAPDH*, *ATP5F1E*, and *ATP5PB* siRNAs were also assessed by western blotting.

Reverse transfection and knockdown procedures were the same as those described earlier in section 4.2.5. To harvest cells, spent medium was removed from the 96-well plate before 10 μ l lysis buffer was added to each well. Lysis buffer contained 140 mM Tris (pH 8), 2 mM MgCl₂, 4% sodium dodecyl sulfate (SDS), 50 mM 1,4-dithiothreitol (DTT), 5M urea, and \geq 250 units/ml Benzonase[®] Nuclease (#E1014, Millipore Sigma). To scale up the amount of material, cell lysates of 8 identical wells transfected with the same siRNA were pooled. Samples could be stored at -80 °C if necessary.

Protein concentrations were measured by the Bio-Rad DC Protein Assay Kit (#500-0112, Bio-Rad, Hercules, CA, USA). Briefly, we prepared a set of protein standards, namely 0, 0.1, 0.2, 0.4, and 0.8 mg/ml bovine serum albumin and made three serial dilutions of each cell lysate by 2, 4, and 8-fold. Then, we transferred 5 μ l of sample to each well of a 96-well plate, where technical triplicates were set up for each sample. Every ml of Reagent A was supplemented with 20 μ l Reagent S, and then, 25 μ l mixture was added to each well. After adding 200 μ l Reagent B, the solutions were mixed by pipetting and incubated at room temperature for 15 min. Absorbance reading at 750 nm wavelength was measured in a BMG FLUOstar Omega microplate reader (Ortenberg, Germany). Protein concentration was calculated based on the standard curve and the mean value of technical triplicates for each sample. Using this information, we adjusted all the samples to the same protein concentration in lysis buffer.

For gel electrophoresis, cell lysates were mixed with 5 \times SDS-PAGE sample loading buffer and boiled at 95 °C for 5 min. Then, *GAPDH* knockdown samples were loaded onto Any kD[™] Mini-PROTEAN[®] TGX Stain-Free[™] Protein Gel (#4568124, Bio-Rad), whereas *ATP5F1E* and *ATP5PB* knockdown samples were loaded onto 4-20% Mini-PROTEAN[®] TGX[™] Precast Protein Gel (#4561096, Bio-Rad). Electrophoresis was conducted at 160 V until the protein of interest was expected to reach the middle of the gel.

For *GAPDH* knockdown samples, the Stain-Free[™] gel was photoactivated by UV in the ChemiDoc Imaging System (Bio-Rad), which enabled visualizing the tryptophan fluorescence of total proteins. Then, we used a Tran-Blot Turbo Transfer Pack (#1704156, Bio-Rad) and the Trans-

Blot Turbo Blotting Apparatus (Bio-Rad) to transfer proteins from the gel to the PVDF membrane. An image of successfully transferred proteins was taken, which served as loading control. For *ATP5F1E* and *ATP5PB* knockdown samples, proteins were transferred directly after gel electrophoresis to PVDF membranes in the same way.

Membranes were blocked with 5% non-fat milk dissolved in TBST buffer for 1 h. Then, they were incubated with designated antibodies (prepared in blocking buffer) for the protein of interest. To label GAPDH, an anti-GAPDH antibody (#G9545, Millipore Sigma) was used at 500 ng/ ml, and to label mitochondrial F₀F₁-ATPase ϵ subunit, an anti-ATP5E antibody (A-11) (#sc-393695, Santa Cruz Biotechnology, Inc., Dallas, TX, USA) was used at 5 μ g/ ml. Incubation with primary antibodies was carried out at 4 °C overnight with constant, gentle agitation. Then, primary antibodies were removed, and the membranes were rinsed with TBST buffer for three times.

For the *GAPDH* knockdown samples, the membrane was incubated with 80 ng/ ml Goat anti-Rabbit IgG (H+L) secondary antibody conjugated to horseradish peroxidase (HRP) (#31460, Thermo Fisher Scientific) for 2 h at room temperature. Three TBST washes and two PBS washes were then used to remove unbound antibodies. SuperSignal™ West Pico PLUS Chemiluminescent Substrate (#34580, Thermo Fisher Scientific) was directly applied to the membrane, and chemiluminescence signal was detected by the ChemiDoc Imaging System (Bio-Rad). For the *ATP5F1E* and *ATP5PB* knockdown samples, the membrane was incubated with 67 ng/ ml IRDye® 680LT Goat anti-Mouse secondary antibody (#926-68021, LI-COR Biosciences, Lincoln, NE, USA) for the mitochondrial F₀F₁-ATPase ϵ subunit and 67 ng/ ml IRDye® 800CW Goat anti-Rabbit secondary antibody (#925-32211, LI-COR Biosciences) for GAPDH, the loading control, respectively. Secondary antibodies were prepared in Odyssey® Blocking Buffer (TBS) (#927-50000, LI-COR Biosciences) supplemented with 0.01% SDS and 0.2% Tween 20. The membrane was kept in the dark during the 1 h incubation period, before fluorescence signals were detected using the LI-COR Odyssey® CLx Imaging System (LI-COR Biosciences).

4.2.7 Immunofluorescence labeling and confocal microscopy

We visualized PANK4 and polyP in cisplatin-treated cells with confocal microscopy. Briefly, HeLa cells were seeded at a density of 5×10^4 cells/ well in a 24-well tissue culture plate (#3526, Corning, Inc., Corning, NY, USA) with a piece of coverslip placed at the bottom (#CLS-1760-012, Chemglass Life Sciences, Inc., Vineland, NJ, USA). Cells were cultured at 37 °C with 5% CO₂.

On the next day, cells were treated with 40 μ M cisplatin for 24 h. Fixation, permeabilization, and blocking procedures were the same as those described in section 4.2.4.5, except for volume adjustments for 24-well plate and manual liquid handling using P1000 pipettes (Eppendorf, Hamburg, Germany) instead of Multidrop dispensers. To label PANK4 and polyP, samples were incubated with 4 μ g/ml anti-PANK antibody (#SAB1411043, Sigma-Aldrich) and 10 μ g/ml GFP-*EcPPX_c* (prepared in blocking buffer) at 4 °C overnight, protected from light. To visualize PANK4 signal, a goat anti-rabbit IgG Alexa Fluor[®] 647 secondary antibody (#ab150079, Abcam, Cambridge, United Kingdom) was supplemented to the PBS-washed samples at 1 μ g/ml and incubated at room temperature for 2 h, protected from light. Unbound antibodies were removed by PBS, and samples were stained with 1 μ g/ml DAPI for 5 min. Finally, PBS-washed samples were mounted in Citifluor AF1 mounting medium (#19470, Ted Pella, Inc., Redding, CA, USA) on microscope objective slides. Note that a set of controls for non-specific signals were prepared using GFP and goat anti-rabbit IgG Alexa Fluor[®] 647 alone.

Fluorescence images were acquired by a Leica SP8 laser scanning confocal microscope (Leica GmbH, Mannheim Germany) built on a DMI8 microscope base using LAS X software, 100 \times oil objective (#11506378, Leica GmbH) and a 405 nm diode laser, in addition to a multi-line white light laser, set to 488, 594, and 647 nm excitation wavelengths. Spectral detection using a PMT from 410 to 480 nm was utilized for DAPI, a HyD detector from 493 to 560 nm for GFP and GFP-*EcPPX_c*, and a HyD detector from 653 to 800 nm for Alexa Fluor[®] 647.

4.3 Results

4.3.1 Visualization of polyP accumulation in nutrient shifted bacteria using the mCherry-*EcPPX_c* probe

To test whether mCherry-*EcPPX_c* signal intensities and endogenous polyP levels correlate, we conducted immunofluorescence labeling of polyP in *E. coli*. In this organism, polyP accumulation is stimulated simply by shifting the cells from an nutrient rich environment to a minimal medium, which contains no amino acids and less than 10% of the normal amount of phosphate (5,23,28). Furthermore, it was feasible to genetically manipulate the polyP operon comprised of *ppk* (the gene encoding polyphosphate kinase 1) and *ppx* (the gene encoding exopolyphosphatase) (21,109).

As shown in Fig. 4.1, polyP accumulation phenotype was fully recapitulated by the mCherry-*EcPPX_c* probe. The rod-like shapes of both wild-type and $\Delta ppk\Delta ppx$ strains under normal

conditions changed into a nearly spherical morphology upon nutrient shift, indicative of an efficient growth arrest. Yet, polyP labeling was distinctly different in these strains. Specifically, wild-type cells exhibited a remarkable increase in the mCherry-*EcPPX_c* signal (but not mCherry signal) following nutrient starvation. However, mCherry-*EcPPX_c* fluorescence remained undetectable in nutrient-shifted $\Delta ppk\Delta ppx$ cells, which lacked the polyP synthesizing capacity. These results further supported the conclusion that staining with mCherry-*EcPPX_c* serves as a reliable readout for endogenous polyP.

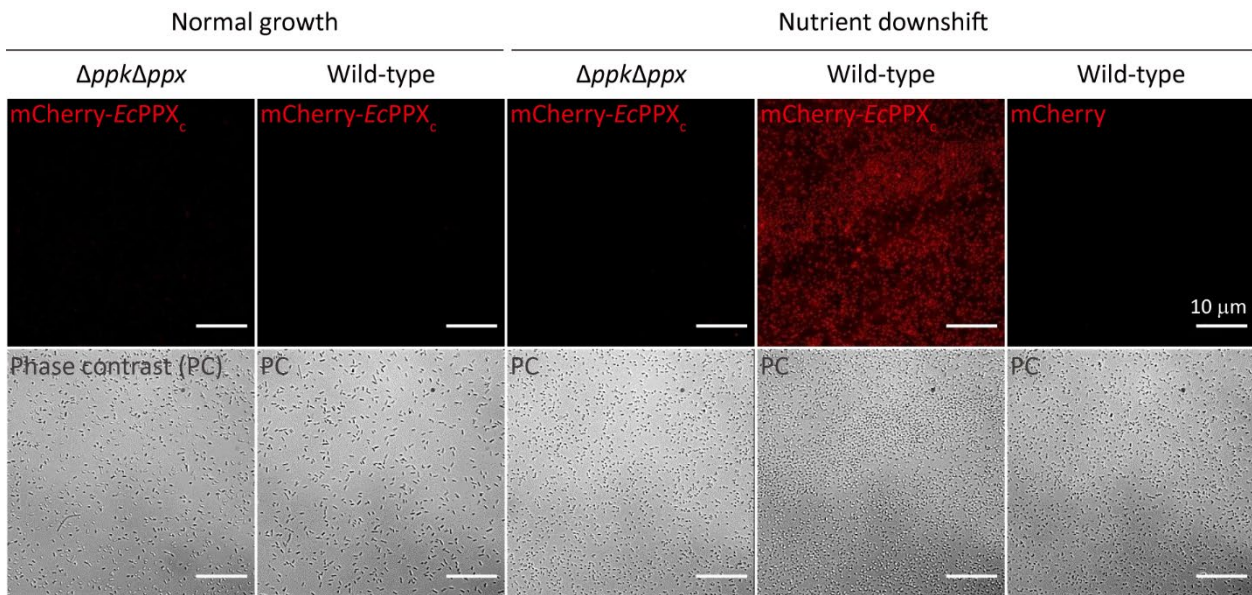


Figure 4.1 Immunofluorescence labeling of polyP by mCherry-*EcPPX_c* in nutrient shifted *E. coli* cells. Wild-type and $\Delta ppk\Delta ppx$ *E. coli* strains were grown either under normal condition or in a nutrient deprived environment. Then, cells were labeled with mCherry-*EcPPX_c* (or the control probe, mCherry) to monitor the levels of polyP. For the immunofluorescence images, brightness and contrast were adjusted on the same scale. The number and the morphology of untreated cells and nutrient starved cells can be visualized in the phase contrast (PC) images at the bottom. Scale bar: 10 μ m.

4.3.2 A genome-wide siRNA screen for polyP regulators in the human genome

Having shown that mCherry-*EcPPX_c* provides a reliable labeling system for endogenous polyP, we set out to establish an unbiased high throughput screening platform for polyP related genes in HeLa cells. This approach exploited the capacity of 384-well plates (laid out in Fig. 4.2A) to batch-process the procedures of HeLa cell culture, siRNA reverse transfection, a three-day knockdown, cisplatin treatment, immunofluorescence labeling with mCherry-*EcPPX_c*, high content imaging, and data analysis (Fig. 4.2B).

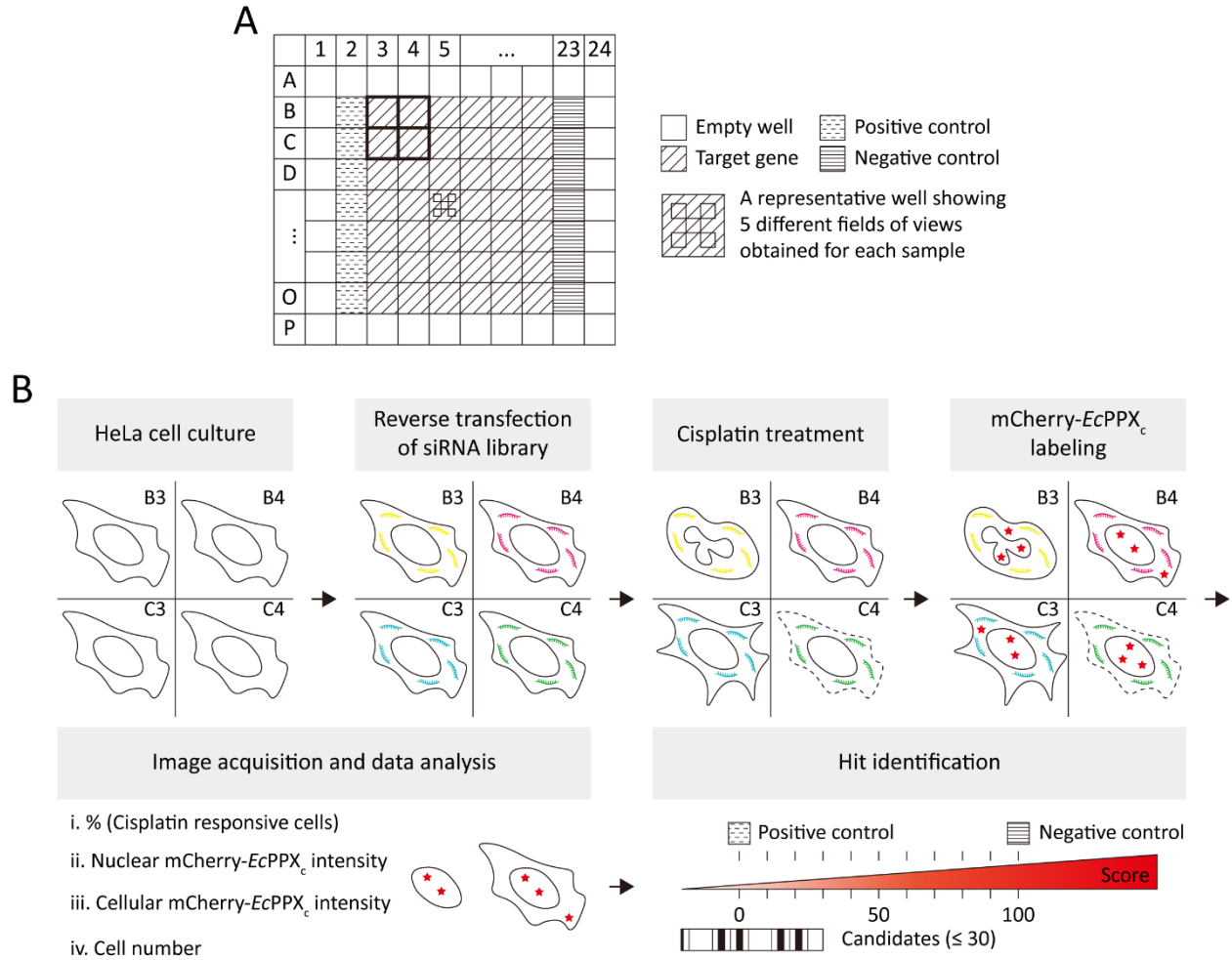


Figure 4.2 Workflow of a genome-wide siRNA screen for mammalian *PPK* genes in cisplatin-treated HeLa cells using mCherry-*EcPPX_c* immunofluorescence labeling. (A) Layout of a typical 384-well plate, which tested 280 different targets (Row B to O and Column 3 to 22) and contained 14 positive controls (Row B to O, column 2), 14 negative controls (Row B to O, column 23), and 76 unlabeled wells to avoid the edge effect of the plate. Positive controls (i.e., without cisplatin treatment and hence no upregulation of polyP) and negative controls (treated with 0.4 mM cisplatin and hence upregulation of polyP) were transfected with non-targeting siRNA. Four wells, B3, B4, C3, and C4 (outlined in bold) were taken as examples to explain the workflow in Fig. 4.2B. Notably, during image acquisition, 5 different fields of view were obtained for each well, and their mean value was reported as the final result. (B) The workflow of the primary screen in HeLa cells involved reverse transfection of a Dharmacon siGENOME SMARTpool[®] siRNA library, a three-day knockdown followed by the exposure of the cells to 0.4 mM cisplatin for 24 h, immunofluorescence labeling of polyP with mCherry-*EcPPX_c*, automated image acquisition, and data analysis. Four different parameters were deduced from the fluorescence images (i-iv), of which the percentage of cisplatin responding cells was used as the primary criterion for hit identification. For each 384-well plate, a range from 0 to 100 was defined using the values of the positive control and the negative control, respectively. Any target, which scored less than 30 in at least two out of three repetitions after cisplatin treatment qualified as candidates for potential *PPK* and/or genes for the upregulation of polyP.

To survey as many genes as possible, we screened a Dharmacon siGENOME siRNA library, which targeted 18,110 loci with four siRNA duplexes (denoted as SMARTpool[®]) for each site to maximize their on-target effect. Knockdown efficiency was assessed by Western blotting analysis of a gene encoding glyceraldehyde-3-phosphate dehydrogenase (GAPDH) (Fig. S4.1A). Quantitation of the GAPDH signals over those of total cell lysates in the siRNA-targeted cells

estimated a knockdown efficiency of 85% to 90%.

Limited by the lack of known polyP regulatory machineries, we devised an arbitrary dynamic range of mCherry-*EcPPX_c* signals. Cells transfected with non-targeting siRNA without cisplatin treatment served as the positive control, that is, cells without an upregulation of polyP. Conversely, cells transfected with non-targeting siRNA and exposed to cisplatin served as the negative control since they fully upregulated polyP levels (Fig. 4.2A).

Quantitative data were extrapolated from the fluorescence images displaying mCherry-*EcPPX_c* fluorescence and analyzed for the following parameters: 1) percentage of cisplatin responsive cells; 2) average mCherry-*EcPPX_c* intensity in the nucleus; 3) average mCherry-*EcPPX_c* intensity in the whole cell; and 4) cell number. Notably, the percentage of cisplatin responsive cells was designated to reflect the reproducible variations in the polyP levels of individual HeLa cells after cisplatin treatment (also discussed in Chapter 2). Only cells accumulating 8 to 12.5-fold more polyP than what was detected at basal level were classified as responsive ones (typically 25-40% of cells of the entire population). Compared to the other two parameters, i.e., average mCherry-*EcPPX_c* intensity in the nucleus or that in the whole cell, which typically varied by 1.5 to 2-fold between the positive and negative controls, the percentage of cisplatin responding cells generated a much wider window from 0% (for the positive control) to up to 40% (for the negative control). Thus, the latter was chosen as the primary parameter for hit identification.

Limited by the number of 384-well plates we could handle in each experiment, we divided the primary screen into 23 independent assays performed on different days. In each assay, we set up technical triplicates on three different plates for every siRNA tested. Therefore, to normalize measurements obtained from different plates (bearing internal positive and negative controls), the value of positive control was set to 0 and that of negative control was set to 100. This value positively correlated with mCherry-*EcPPX_c* fluorescence intensities, hence polyP levels. Any knockdowns scoring no more than 30 in at least two out of three technical replicates were classified as candidates for genes upregulating mammalian polyP levels. This criterion yielded 405 hits in total, however, only 115 of them (listed in Table 4.1) were validated when the siRNAs were retested in the same assay to minimize random noises. This reckoned the final hit rate at 0.64% for the primary screen.

Table 4.1 Candidates for genes upregulating polyP levels in HeLa cells upon cisplatin treatment

Rank ^a	Gene ID	Gene symbol ^b	Name	Score ^c	
				Primary screen	Validation
1	116444	<i>GRIN3B</i>	glutamate ionotropic receptor NMDA type subunit 3B	1.0	4.0
2	9480	<i>ONECUT2</i>	one cut homeobox 2	2.7	2.5
3	146540	<i>ZNF785</i>	zinc finger protein 785	1.1	4.6
4	5031	<i>P2RY6</i>	pyrimidinergic receptor P2Y6	2.5	7.7
5	3208	<i>HPCA</i>	hippocalcin	2.3	11.0
6	120	<i>ADD3</i>	adducin 3	4.7	8.6
7	6757	<i>SSX2</i>	SSX family member 2	10.1	3.7
8	337880	<i>KRTAP11-1</i>	keratin associated protein 11-1	12.2	3.3
9	54496	<i>PRMT7</i>	protein arginine methyltransferase 7	6.5	9.7
10	90167	<i>FRMD7</i>	FERM domain containing 7	10.0	6.5
11	1432	<i>MAPK14</i>	mitogen-activated protein kinase 14	4.9	11.7
12	55806	<i>HR</i>	HR, lysine demethylase and nuclear receptor corepressor	11.4	5.4
13	10809	<i>STARD10</i>	StAR related lipid transfer domain containing 10	10.4	7.5
14	3052	<i>HCCS</i>	holocytochrome c synthase	6.4	12.5
15	442117	<i>GALNTL6</i>	polypeptide N-acetylgalactosaminyltransferase like 6	5.4	14.3
16	57085	<i>AGTRAP</i>	angiotensin II receptor associated protein	9.8	10.3
17	79796	<i>ALG9</i>	ALG9 alpha-1,2-mannosyltransferase	9.4	10.8
18	90187	<i>EMILIN3</i>	elastin microfibril interfacer 3	7.6	12.7
19	29952	<i>DPP7</i>	dipeptidyl peptidase 7	3.6	18.2
20	6358	<i>CCL14</i>	C-C motif chemokine ligand 14	13.7	10.7
21	6001	<i>RGS10</i>	regulator of G protein signaling 10	15.8	9.0
22	5028	<i>P2RY1</i>	purinergic receptor P2Y1	15.4	10.2
23	8452	<i>CUL3</i>	cullin 3	3.4	22.2
24	8851	<i>CDK5R1</i>	cyclin dependent kinase 5 regulatory subunit 1	7.2	19.2
25	514	<i>ATP5F1E</i>	ATP synthase F1 subunit epsilon	22.5	4.1
26	7251	<i>TSG101</i>	tumor susceptibility 101	13.5	13.4
27	84934	<i>RIT1</i>	RBPJ interacting and tubulin associated 1	5.3	22.5
28	2810	<i>SFN</i>	stratifin	2.2	26.6
29	23433	<i>RHOQ</i>	ras homolog family member Q	19.8	9.2
30	9827	<i>RGP1</i>	RGP1 homolog, RAB6A GEF complex partner 1	9.7	19.9
31	286077	<i>FAM83H</i>	family with sequence similarity 83 member H	19.1	10.9
32	5158	<i>PDE6B</i>	phosphodiesterase 6B	7.1	23.1
33	133482	<i>SLCO6A1</i>	solute carrier organic anion transporter family member 6A1	7.0	23.6
34	221938	<i>MMD2</i>	monocyte to macrophage differentiation associated 2	13.0	18.3
35	51506	<i>UFC1</i>	ubiquitin-fold modifier conjugating enzyme 1	9.7	22.1
36	5428	<i>POLG</i>	DNA polymerase gamma, catalytic subunit	16.3	15.8
37	219473	<i>OR8K3</i>	olfactory receptor family 8 subfamily K member 3 (gene/pseudogene)	26.5	6.5
38	10146	<i>G3BP1</i>	G3BP stress granule assembly factor 1	8.0	25.2

^a Candidates are ranked by the average score of the primary screen and the retest (validation) in the order from low to high.

^b Official NCBI gene symbols are listed in this table for those entries with more than one commonly used gene symbols.

^c The mean score of three technical replicates is reported here. Scores are normalized on a scale of 0 to 100 defined by the positive and negative control, respectively.

Rank ^a	Gene ID	Gene symbol ^b	Name	Score ^c	
				Primary screen	Validation
39	7052	<i>TGM2</i>	transglutaminase 2	6.0	27.2
40	55229	<i>PANK4</i>	pantothenate kinase 4	26.8	6.5
41 ^d	100652781	<i>SNX29BP1</i>	sorting nexin 29 pseudogene 1	18.0	15.3
42	4495	<i>MTIG</i>	metallothionein 1G	25.8	7.9
43	339345	<i>NANOS2</i>	nanos C2HC-type zinc finger 2	13.5	21.0
44	85316	<i>BAGE5</i>	BAGE family member 5	7.4	27.4
45	64780	<i>MICAL1</i>	microtubule associated monooxygenase, calponin and LIM domain containing 1	19.3	16.0
46	285527	<i>FRYL</i>	FRY like transcription coactivator	11.1	24.3
47	83695	<i>RHNO1</i>	RAD9-HUS1-RAD1 interacting nuclear orphan 1	8.7	26.8
48	80323	<i>CCDC68</i>	coiled-coil domain containing 68	27.2	8.8
49	652919	<i>RGPD7</i>	RANBP2-like and GRIP domain containing 7	6.5	29.9
50	148870	<i>CCDC27</i>	coiled-coil domain containing 27	6.6	30.3
51	9140	<i>ATG12</i>	autophagy related 12	18.3	19.1
52	9284	<i>NPIPA1</i>	nuclear pore complex interacting protein family member A1	16.0	21.7
53	401994	<i>OR14I1</i>	olfactory receptor family 14 subfamily I member 1	30.9	7.1
54	340351	<i>AGBL3</i>	ATP/GTP binding protein like 3	15.1	23.4
55	222894	<i>FERD3L</i>	Fer3 like bHLH transcription factor	19.3	19.5
56	28970	<i>C11orf54</i>	chromosome 11 open reading frame 54	21.0	18.0
57	391123	<i>VSIG8</i>	V-set and immunoglobulin domain containing 8	23.6	15.9
58	88455	<i>ANKRD13</i>	ankyrin repeat domain 13A	27.0	12.9
59	51239	<i>ANKRD39</i>	ankyrin repeat domain 39	16.9	23.4
60	26261	<i>FBXO24</i>	F-box protein 24	30.3	10.1
61	11047	<i>ADRM1</i>	adhesion regulating molecule 1	23.8	16.7
62	3939	<i>LDHA</i>	lactate dehydrogenase A	24.8	15.7
63	6461	<i>SHB</i>	SH2 domain containing adaptor protein B	22.3	18.8
64	390874	<i>ONECUT3</i>	one cut homeobox 3	29.1	11.5
65	201292	<i>TRIM65</i>	tripartite motif containing 65	13.4	27.2
66	286319	<i>TUSC1</i>	tumor suppressor candidate 1	20.0	21.0
67	441108	<i>IRF1-AS1</i>	IRF1 antisense RNA 1	25.4	16.1
68	9688	<i>NUP93</i>	nucleoporin 93	20.8	20.8
69	3167	<i>HMX2</i>	H6 family homeobox 2	13.9	27.8
70	26985	<i>AP3M1</i>	adaptor related protein complex 3 subunit mu 1	26.5	15.7
71	8883	<i>NAE1</i>	NEDD8 activating enzyme E1 subunit 1	17.4	25.7
72	23151	<i>GRAMD4</i>	GRAM domain containing 4	18.4	25.1
73	56915	<i>EXOSC5</i>	exosome component 5	26.1	17.4
74	91526	<i>ANKRD44</i>	ankyrin repeat domain 44	20.9	22.7
75	8354	<i>HIST1H3I</i>	histone cluster 1 H3 family member i	18.7	25.1
76	131583	<i>FAM43A</i>	family with sequence similarity 43 member A	16.0	28.3
77	2764	<i>GMFB</i>	glia maturation factor beta	18.2	26.3
78	9342	<i>SNAP29</i>	synaptosome associated protein 29	22.9	21.9
79	378832	<i>COL18A1-AS1</i>	COL18A1 antisense RNA 1	20.7	24.2
80	50807	<i>ASAP1</i>	ArfGAP with SH3 domain, ankyrin repeat and PH domain 1	17.5	27.5
81	115201	<i>ATG4A</i>	autophagy related 4A cysteine peptidase	21.1	24.0
82	312	<i>ANXA13</i>	annexin A13	14.8	30.6

^d This entry is the replacement of LOC400509 (Gene ID: 400509) according to NCBI.

Rank ^a	Gene ID	Gene symbol ^b	Name	Score ^c	
				Primary screen	Validation
83	4637	<i>MYL6</i>	myosin light chain 6	29.4	16.1
84	54455	<i>FBXO42</i>	F-box protein 42	18.2	27.6
85	51778	<i>MYOZ2</i>	myozenin 2	29.4	17.9
86	63970	<i>P53AIP1</i>	tumor protein p53 regulated apoptosis inducing protein 1	23.2	24.2
87	4065	<i>LY75</i>	lymphocyte antigen 75	22.1	25.8
88	2700	<i>GJA3</i>	gap junction protein alpha 3	27.3	20.7
89	56891	<i>LGALS14</i>	galectin 14	26.8	21.6
90	10215	<i>OLIG2</i>	oligodendrocyte transcription factor 2	21.0	28.4
91	4131	<i>MAP1B</i>	microtubule associated protein 1B	28.5	20.9
92	440699	<i>LRRCS2</i>	leucine rich repeat containing 52	20.9	30.0
93	154790	<i>CLEC2L</i>	C-type lectin domain family 2 member L	26.1	24.9
94	84924	<i>ZNF566</i>	zinc finger protein 566	24.6	26.6
95	10417	<i>SPON2</i>	spondin 2	21.2	30.2
96	29091	<i>STXBP6</i>	syntaxin binding protein 6	24.2	27.3
97 ^e	221262	<i>CCDC162P</i>	coiled-coil domain containing 162, pseudogene	26.8	25.5
98	55196	<i>RESF1</i>	retroelement silencing factor 1	29.3	23.7
99	440	<i>ASNS</i>	asparagine synthetase (glutamine-hydrolyzing)	26.0	27.1
100	57542	<i>KLHL42</i>	kelch like family member 42	24.0	29.5
101	401265	<i>KLHL31</i>	kelch like family member 31	25.4	28.0
102	84923	<i>FAM104A</i>	family with sequence similarity 104 member A	31.6	21.9
103	148979	<i>GLIS1</i>	GLIS family zinc finger 1	25.7	27.8
104	360023	<i>ZBTB41</i>	zinc finger and BTB domain containing 41	24.1	29.6
105	285440	<i>CYP4V2</i>	cytochrome P450 family 4 subfamily V member 2	21.6	33.3
106	81622	<i>UNC93B1</i>	unc-93 homolog B1, TLR signaling regulator	22.9	32.2
107	7761	<i>ZNF214</i>	zinc finger protein 214	36.6	18.6
108	1836	<i>SLC26A2</i>	solute carrier family 26 member 2	25.3	31.2
109	119032	<i>BORCS7</i>	BLOC-1 related complex subunit 7	27.8	29.5
110	140453	<i>MUC17</i>	mucin 17, cell surface associated	29.1	28.1
111	391189	<i>OR11L1</i>	olfactory receptor family 11 subfamily L member 1	30.4	28.0
112	9927	<i>MFN2</i>	mitofusin 2	32.7	25.9
113	30848	<i>CTAG2</i>	cancer/testis antigen 2	28.5	30.7
114	79990	<i>PLEKHH3</i>	pleckstrin homology, MyTH4 and FERM domain containing H3	29.8	30.3
115	1446	<i>CSN1S1</i>	casein alpha s1	30.5	30.4

To ensure that the above candidates were not skewed by our choice of using cisplatin responsiveness as the chief parameter for hit identification, we ranked the 18,110 targets based on their average mCherry-*EcPPX_c* fluorescence intensities in the nucleus. When the raw measurements were normalized to the positive and negative controls on a scale of 0 to 100, 98 knocked down genes scored 30 or less in at least two technical replicates (Table S4.1). Importantly, 84 of them were scored as hits, based on their proportions of cisplatin responsive cells. In addition

^e This entry is the replacement of FLJ37396 (Gene ID: 285754) according to NCBI.

to giving us more candidate genes (405 vs. 98 before validation), the calculation of cisplatin responsiveness rather than nuclear mCherry-*EcPPX_c* signal was also more consistent judged by the standard deviation values (Table S4.1), further justifying our use of cisplatin responding cells as primary scoring parameter. Nevertheless, we routinely cross-examined different parameters to reach as rigorous conclusions as possible.

In the course of data analysis, we also made an intriguing discovery that RNAi itself might affect the extent of polyP accumulation following cisplatin treatment. This finding became clear once we calculated the average score of all the targets and found it to be 140 and the median to be 146 (Fig. 4.3A). These scores were 40% higher than the score of the negative control, which indicated the amount of polyP found in cisplatin-treated cells exposed to non-targeting siRNA. Consistently, the mean score of mCherry-*EcPPX_c* fluorescence intensity in the nucleus of the whole population also exceeded the negative control by 63% (Fig. 4.3B). However, no such difference existed for cell count, an indirect measurement of cisplatin sensitivity (Fig. 4.3C). Therefore, RNAi might specifically affect polyP regulation rather than cell survival. It is conceivable that the differences in polyP levels emerged from the downstream events of mRNA binding to the antisense strand of the siRNA duplex. Yet, without further experiments, we are unable to ascribe the source of this additional polyP accumulation to an activated RNAi machinery, a general stress response in reply to the loss of a functional protein, or other factors. Nonetheless, this difference in polyP levels rendered our candidates even more significant than previously considered.

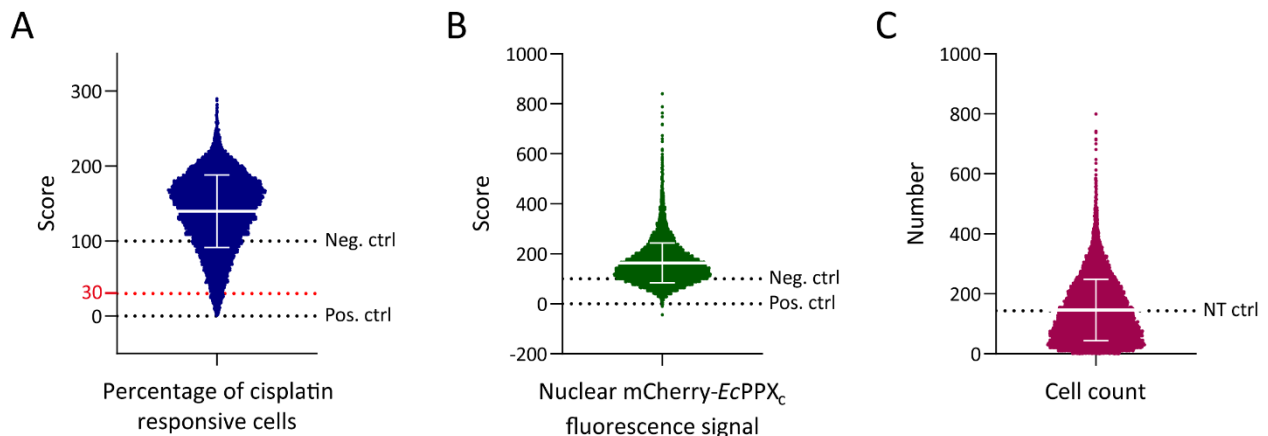


Figure 4.3 Distributions of three major parameters of the primary screen. For each target, (A) the score of the percentage of cisplatin responsive cells, (B) the score of nuclear mCherry-*EcPPX_c* fluorescence intensity, and (C) cell count are shown in violin plots. The percentage of cisplatin responsive cells and the nuclear mCherry-*EcPPX_c* intensity are normalized to the positive control (Pos. ctrl) and the negative control (Neg. ctrl), whose scores were set to 0 and 100, respectively. The hit identification criterion, i.e., scoring below 30 for the percentage of cisplatin responsive cells, is highlighted by a red line in (A). Cell count value for the non-targeting siRNA control (NT ctrl) is indicated by a dashed line in (C). Means and standard deviations are reported in the graphs.

To validate the 115 hits and investigate whether the respective siRNAs also affect the steady state polyP levels, we determined the baseline of polyP content in cells transfected with the 115 siRNAs without cisplatin supplement. Cells containing the non-targeting siRNA were labeled with either mCherry or mCherry-*EcPPX_c* to set a new dynamic range of polyP signals from 0 to 100. Any knockdowns, whose mCherry-*EcPPX_c* brightness scored below 100 were indicative of impaired polyP synthesis compared to the non-targeting siRNA control. Indeed, 98.3% of the candidate siRNAs belonged to this category, and the mean score of the whole group was 71.7, reflecting an average of nearly 30% decrease in basal polyP concentrations (Fig. 4.4A).

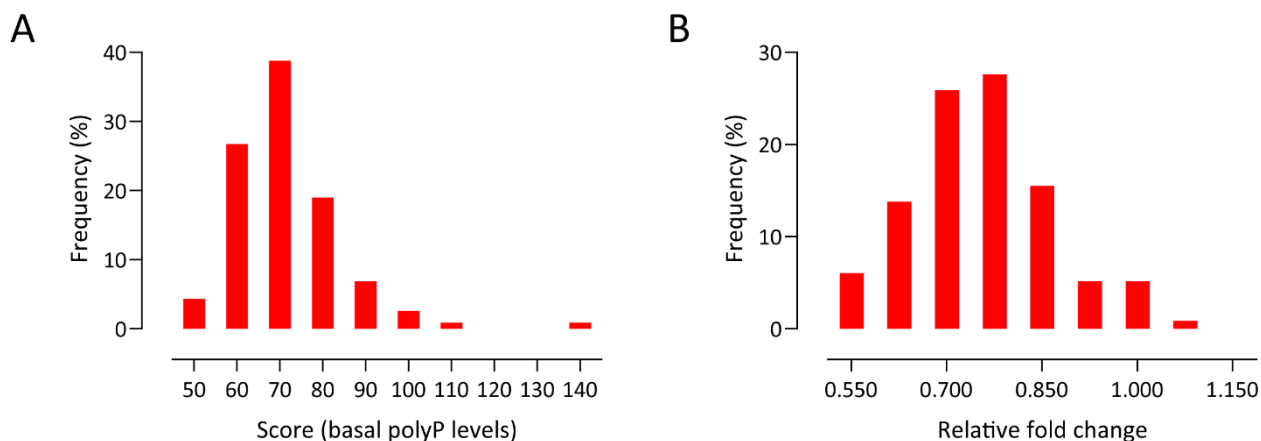


Figure 4.4 Frequency distribution analysis of basal polyP levels and fold increase of polyP concentrations upon cisplatin treatment in the candidates of the primary screen. (A) The scores of basal polyP levels for the 115 candidates clustered below 100. This result indicates lesser amounts of polyP in these samples compared to the non-targeting siRNA control. **(B)** The relative fold change of polyP concentrations before and after cisplatin treatment in cells transfected with 115 candidate siRNAs had an average of 0.76. The fold increase in polyP levels of a knockdown sample was normalized to that of the non-targeting siRNA control, set at 1. Overall, 112 targets, with a relative fold change value below 1, showed lower ability to enrich polyP than the non-targeting siRNA control.

Next, we evaluated the fold change of polyP levels upon cisplatin administration by normalizing the mCherry-*EcPPX_c* fluorescence signals of cisplatin-treated cells to those of untreated cells targeted by the same siRNA sequence. Presumably, this quantitation was more accurate because it took into account the dissimilar basal polyP concentrations due to the knockdown of different targets. When we plotted the frequency distribution of the fold change values of all 115 candidates (relative to the fold change of non-targeting siRNA control, set at 1), we obtained a population with an average of 0.76 (Fig. 4.4B). In fact, only 4 hits (which scored above 1) overtook the non-targeting siRNA control in causing a cisplatin-mediated polyP spike. Taken together, these results testified for the selectivity of our original hit identification parameter for potential *PPK* genes and prompted us to further scrutinize the candidates from the primary screen (Table 4.1).

4.3.3 Validation of *PPK* candidate genes using ON-TARGETplus SMARTpool® siRNAs

An inevitable challenge of RNAi is the potency of off-target effects caused by each siRNA duplex. Besides recognizing its complementary mRNA target, the seed sequence, which refers to the 2nd to the 7th or the 2nd to the 8th positions in the anti-sense strand is inadvertently guided to the 3'UTR of many different mRNA species (214). Due to the promiscuous regulatory functions of the 3'UTR, it is impractical to decipher the mis-targeted sites more often than not. We therefore decided to conduct a secondary screening for selected candidates using an alternative ON-TARGETplus SMARTpool® siRNA library and testing for its effects on cisplatin-induced polyP accumulation.

As an essential premise, we confirmed the knockdown efficiencies of both sets of siRNAs for one representative target, *ATP5F1E*, with qRT-PCR and western blotting analyses. On the mRNA level, 99.4% and 97.2% of the *ATP5F1E* mRNA copies were silenced by *ATP5F1E* specific oligos provided by the ON-TARGETplus and the siGENOME libraries, respectively (Fig. S4.1B). Although three out of four siRNA duplexes differed in sequence between the two SMARTpool® siRNA preparations, their efficacies tied in quadruple biological samples. For a different purpose, we also assessed the influence of *ATP5PB* silencing on the expression levels of *ATP5F1E* gene. Although we found a slight increase in the *ATP5F1E* mRNA level, it was not statistically significant. Therefore, we considered *ATP5PB* siRNA to serve as an additional control to the default non-targeting siRNA. Consistent with the qRT-PCR results, cells transfected with *ATP5F1E* siRNA from either library showed a nearly 75% loss of the mitochondrial ATP synthase ϵ subunit in three independent Western blotting assays (Fig. S4.1C). Although we cannot rule out other potential differences between these two libraries, we regarded the ON-TARGETplus SMARTpool® siRNAs as an adequate substitution for the siGENOME SMARTpool® siRNAs that we used in our primary screen.

In a proof-of-concept study, we then focused on a subset of 36 candidate genes and analyzed their steady-state and cisplatin-induced polyP accumulation upon RNAi using the following parameters: 1) proportion of cisplatin responsive cells (also the chief criterion to be considered for hit validation); 2) fold change of polyP levels before and after cisplatin treatment; 3) polyP levels of cisplatin-treated cells; and 4) basal polyP levels. Results from three to five independent experiments were summarized in Table 4.2 and Table 4.3.

Table 4.2 Percentage of cisplatin responding cells in selected candidates transfected with ON-TARGETplus SMARTpool® siRNAs

Rank	Gene ID	Gene Symbol ^f	Score ^g	SD ^h	Rank	Gene ID	Gene Symbol	Score	SD
1	7251	<i>TSG101</i>	57.25	11.23	19	1432	<i>MAPK14</i>	123.11	18.05
2	133482	<i>SLCO6A1</i>	58.08	16.83	20	337880	<i>KRTAP11-1</i>	124.29	25.21
3	29952	<i>DPP7</i>	59.17	23.01	21	5031	<i>P2RY6</i>	127.78	9.40
4	5428	<i>POLG</i>	65.30	14.69	22	5158	<i>PDE6B</i>	129.41	34.09
5	116444	<i>GRIN3B</i>	70.04	14.49	23	401994	<i>OR14I1</i>	130.08	13.13
6	9480	<i>ONECUT2</i>	71.84	14.54	24	3208	<i>HPCA</i>	135.00	22.96
7	57085	<i>AGTRAP</i>	76.70	23.11	25	64780	<i>MICAL1</i>	135.38	17.38
8	8851	<i>CDK5R1</i>	79.15	28.47	26	90187	<i>EMILIN3</i>	140.38	30.47
9	339345	<i>NANOS2</i>	86.41	8.42	27	6757	<i>SSX2</i>	140.67	7.26
10	9140	<i>ATG12</i>	93.01	15.67	28	79796	<i>ALG9</i>	141.66	22.58
11	55806	<i>HR</i>	93.19	15.55	29	84934	<i>RITAI</i>	145.79	24.92
12	10809	<i>STARD10</i>	100.47	12.80	30	8883	<i>NAE1</i>	148.61	34.61
13	90167	<i>FRMD7</i>	107.17	27.65	31	514	<i>ATP5F1E</i>	151.98	31.90
14	55229	<i>PANK4</i>	108.90	41.79	32	6001	<i>RGS10</i>	161.11	27.28
15	146540	<i>ZNF785</i>	110.99	11.76	33	10146	<i>G3BP1</i>	188.26	25.24
16	5028	<i>P2RY1</i>	114.44	27.84	34	54496	<i>PRMT7</i>	188.60	32.34
17	3052	<i>HCCS</i>	118.06	18.67	35	6358	<i>CCL14</i>	209.59	46.72
18	23433	<i>RHOQ</i>	120.75	20.95	36	120	<i>ADD3</i>	228.36	27.34

To our great surprise, none of the candidates scored 30 or less when their fractions of cisplatin responsive cells were normalized to the corresponding value of the non-targeting siRNA control (which was set to 100) (Table 4.2). Furthermore, the relative fold change of polyP signals before and after cisplatin exposure appeared to make 89% of the hits more proficient at increasing their polyP levels compared to the non-targeting siRNA control (Table 4.3). Ranking these candidates by the fold change of polyP levels was akin to ranking them by cisplatin responsiveness. Based on this analysis, we found that only basal polyP concentrations followed our prediction and scored between 70 and 100 (after normalization) for all the candidates tested (Table 4.3). At a minimum, this observation signified an attenuated polyP synthesizing activity caused by perturbing a candidate gene in an otherwise unstressed cell.

^f Official NCBI gene symbols are listed in this table for those entries with more than one commonly used gene symbols.

^g The mean score of five biological replicates is reported here. Scores are normalized on a scale of 0 to 100 defined by the positive control and the negative control, respectively.

^h SD stands for the standard deviation of the mean for five biological replicates.

Table 4.3 PolyP content before and after cisplatin treatment and the respective fold change in selected candidates targeted by ON-TARGETplus SMARTpool® siRNAs

Rank ⁱ	Gene ID	Gene symbol ^j	Relative fold change		Score (mCherry- <i>Ec</i> PPXc signal in the nucleus after cisplatin treatment)		Score (mCherry- <i>Ec</i> PPXc signal in the nucleus at basal level)	
			Mean	SD ^k	Mean	SD ^l	Mean	SD ^m
1	7251	<i>TSG101</i>	0.90	0.06	68.63	4.69	87.71	10.15
2	9480	<i>ONECUT2</i>	0.91	0.03	82.77	11.61	85.83	8.34
3	29952	<i>DPP7</i>	0.94	0.13	72.89	15.36	77.42	8.97
4	133482	<i>SLCO6A1</i>	0.95	0.13	76.27	8.99	90.83	15.88
5	5428	<i>POLG</i>	1.01	0.08	71.61	10.19	75.38	8.54
6	9140	<i>ATG12</i>	1.05	0.08	92.83	11.65	87.13	18.96
7	116444	<i>GRIN3B</i>	1.06	0.13	89.07	8.61	85.81	6.88
8	90167	<i>FRMD7</i>	1.07	0.02	102.35	12.77	97.70	9.12
9	57085	<i>AGTRAP</i>	1.08	0.02	83.69	12.36	75.15	13.35
10	339345	<i>NANOS2</i>	1.09	0.07	91.45	4.76	80.46	10.74
11	146540	<i>ZNF785</i>	1.09	0.10	105.81	5.66	95.78	6.40
12	55806	<i>HR</i>	1.09	0.04	89.13	10.25	79.53	6.99
13	8851	<i>CDK5R1</i>	1.10	0.16	82.75	13.82	70.55	9.75
14	337880	<i>KRTAP11-1</i>	1.11	0.12	117.67	15.90	92.57	8.94
15	10809	<i>STARD10</i>	1.13	0.12	95.57	5.10	80.93	15.75
16	5028	<i>P2RY1</i>	1.16	0.03	104.03	14.61	84.41	7.99
17	55229	<i>PANK4</i>	1.16	0.15	98.01	24.91	80.18	12.50
18	23433	<i>RHOQ</i>	1.18	0.13	107.23	8.88	86.58	16.05
19	401994	<i>OR14I1</i>	1.19	0.09	117.12	8.82	97.41	9.24
20	5031	<i>P2RY6</i>	1.23	0.14	118.95	7.99	91.93	13.68
21	64780	<i>MICAL1</i>	1.27	0.12	121.07	10.23	82.04	19.11
22	1432	<i>MAPK14</i>	1.28	0.06	117.19	13.66	82.24	14.14
23	3052	<i>HCCS</i>	1.28	0.20	110.57	13.23	75.53	8.39
24	90187	<i>EMILIN3</i>	1.32	0.03	133.23	18.00	84.30	11.32
25	6001	<i>RGS10</i>	1.33	0.13	135.40	16.63	91.29	9.81
26	79796	<i>ALG9</i>	1.34	0.06	126.75	11.93	81.68	13.59
27	5158	<i>PDE6B</i>	1.34	0.12	115.61	16.83	77.02	12.39
28	8883	<i>NAE1</i>	1.37	0.25	136.93	18.54	84.46	12.04
29	6757	<i>SSX2</i>	1.37	0.24	124.37	12.45	74.88	11.31
30	3208	<i>HPCA</i>	1.38	0.10	123.87	14.11	74.26	7.58
31	84934	<i>RITA1</i>	1.39	0.16	137.03	13.29	83.23	11.34
32	514	<i>ATP5E</i>	1.40	0.21	113.33	46.53	84.83	8.88
33	10146	<i>G3BP1</i>	1.57	0.11	163.28	18.16	86.93	7.24
34	54497	<i>PRMT7</i>	1.69	0.18	183.47	32.36	93.69	7.60
35	6358	<i>CCL14</i>	1.85	0.15	190.21	44.04	82.13	13.87
36	120	<i>ADD3</i>	2.04	0.17	208.71	24.88	76.41	10.88

These results suggested that our validation results might be unintentionally skewed by systemic differences between the two libraries. Notably, we only altered the source of target siRNAs but not the non-targeting siRNA. While our intention was to simplify the comparisons between primary

ⁱ Candidates are ranked by their fold change values in an order from low to high.

^j Official NCBI gene symbols were listed in this table for those entries with more than one commonly used gene symbols.

^k SD stands for standard deviation of the mean for three independent measurements of fold change.

^l SD stands for standard deviation of the mean for five independent measurements of nuclear mCherry-*Ec*PPXc fluorescence intensity after cisplatin treatment.

^m SD stands for standard deviation of the mean for four independent measurements of nuclear mCherry-*Ec*PPXc signal at basal level.

and validation screens, we neglected the potential impact of different chemical modifications of siGENOME and ON-TARGETplus siRNAs on the behaviors of endogenous polyP. Presumably, another confounding factor was the effective concentrations of the two siRNA libraries. Although the siGENOME SMARTpool[®] library had been carefully maintained at a core facility, its stability might have been compromised after a few freezing-and-thawing cycles.

4.3.4 Explorations of *ATP5F1E* and *PANK4* siRNAs

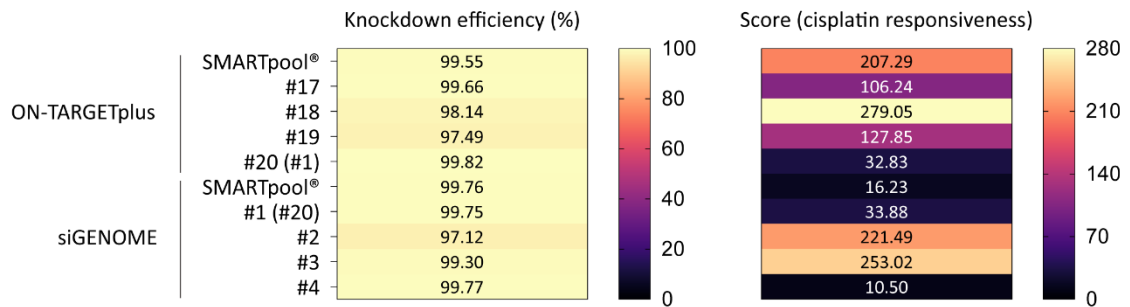
Despite our inability to validate any of the hits with the secondary screen, we nevertheless decided to follow up on a few select targets, which could be relevant players in the cisplatin-triggered polyP reaction. One of these genes was *ATP5F1E*, which encodes the ϵ subunit of the mitochondrial ATP synthase. First and foremost, the ϵ subunit is the only subunit that is unique to the mitochondrial F_oF₁-ATPase (215). This feature implies a novel function and/or regulation of this multicomplex compared to its bacterial and chloroplast equivalents. Coincidentally, mitochondrial F_oF₁-ATPase was recognized for overseeing polyP levels in this organelle, but the underlying mechanism remains unknown to this date (115,116). Provided with the phenotype (from the primary screen) that polyP production was impeded by the knockdown of *ATP5F1E*, we explored whether this gene might serve as the missing link between polyP and mitochondrial F_oF₁-ATPase activity.

To test this hypothesis, we inspected the effect of each individual *ATP5F1E* siRNA derived from the siGENOME SMARTpool[®] collection (#1 to #4) and the ON-TARGETplus SMARTpool[®] collection (#17 to #20) on polyP accumulation in cisplatin-treated cells. Our rationale was that although SMARTpool[®] siRNAs were designed to minimize the off-target effects of each individual component, their combinatory effects might be biased towards a few very potent siRNAs rather than representing the majority of the population.

Using qRT-PCR analysis, we verified the efficacies of all the individual and SMARTpool[®] siRNAs to alter the mRNA levels of *ATP5F1E* (Fig. 4.5A, left panel). Notably, one oligo sequence was shared by the siGENOME collection (#1) and the ON-TARGETplus collection (#20). This would allow us to assess the systematic errors between the two libraries (likely due to differential chemical modifications). It was obvious that all the *ATP5F1E* siRNAs had remarkable and almost identical knockdown efficiencies. Nevertheless, the cells treated with the various *ATP5F1E* siRNAs lowered, maintained or even surpassed the polyP content of the non-targeting siRNA control (Fig. 4.5B). In fact, only two out of seven individual siRNA variants (#1 and #4) were more

potent in disrupting the cisplatin-induced polyP response than the non-targeting siRNA control, whose score was set to 100. Two additional constructs (#17 and #19) resulted in less polyP accumulation than the average of the 18,110 targets, whose mean score approximated to 140. The phenotype of a SMARTpool® siRNA indeed reflected the summed outcomes of all four individual components, especially the ones with the strongest impact. It was likely for this reason that the siGENOME SMARTpool® reagent with two apparent outliers (#2 and #3) was even more robust in lowering polyP levels than the ON-TARGETplus equivalent whose values were dominated by a single siRNA (#18).

A



B

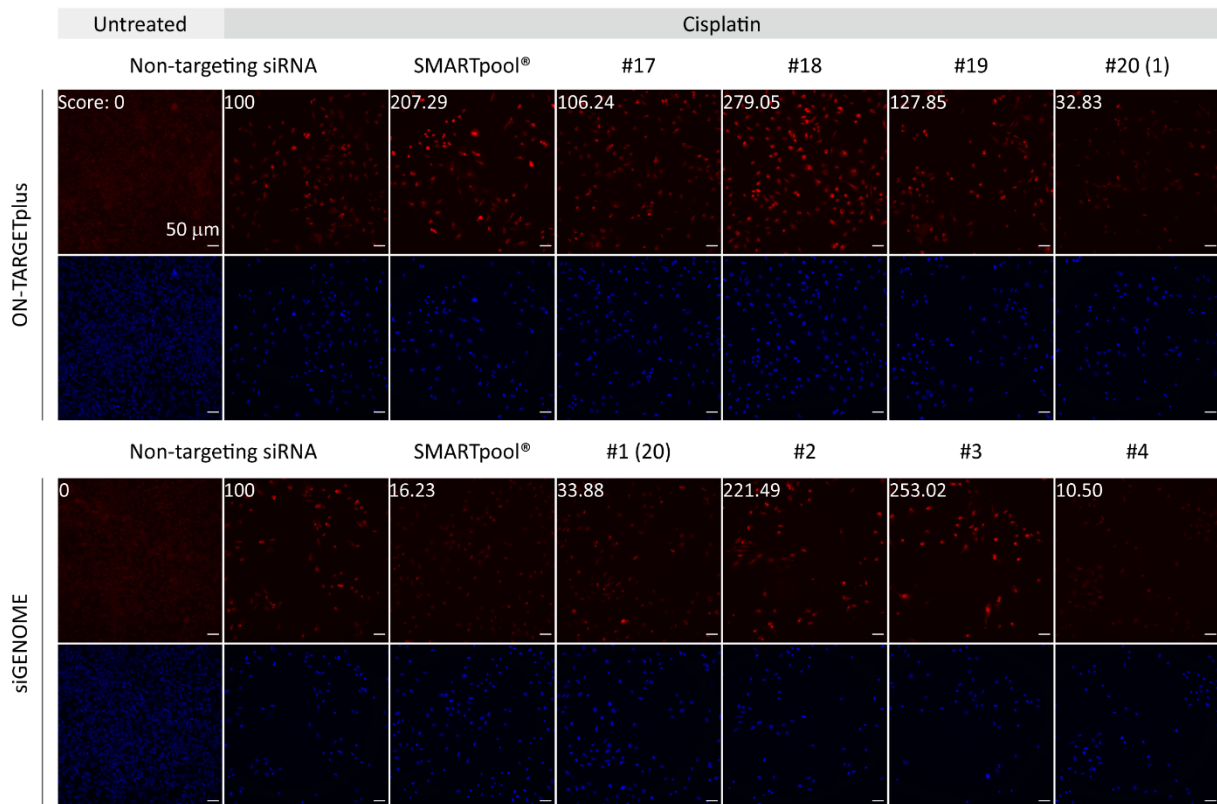


Figure 4.5 Validation of *ATP5F1E* with individual siRNAs from the siGENOME and the ON-TARGETplus libraries. (A) The knockdown efficiencies (left panel) and the scores of cisplatin responsiveness (right panel) of all the individual and SMARTpool® *ATP5F1E* siRNAs are presented in the heatmaps. The expression levels of *ATP5F1E* are almost identical in all the samples, but the extent of polyP accumulation under cisplatin stress is vastly different. siRNA #1 and #20 have the same sequence. (B) Representative images of mCherry-*EcPPXc* labeling (pseudo color: red) and DAPI staining (pseudo color: blue) in cisplatin-treated cells are displayed. Cells were transfected with individual and SMARTpool® *ATP5F1E* siRNAs from either library. Cells transfected with non-targeting siRNA before and after cisplatin exposure served as the positive control and the negative control, respectively. The score of cisplatin responsive cells for each sample is indicated in the image.

These results still did not suffice to conclude that *ATP5F1E* is a candidate for the human PPK gene. Nevertheless, they encouraged us to conduct polyP measurements in knockout models of this non-essential gene in the near future. It is intriguing to figure out whether mitochondrial F₀F₁-ATPase had been reconfigured into a dual functional engine for ATP and polyP synthesis with the ϵ subunit serving as the molecular coordinator of these two functions.

In addition to retesting *ATP5F1E*, this set of experiments also addressed two technical issues concerning the primary and the validation screens using different siRNA libraries. Earlier, we suspected that the unique chemical modifications on the siRNA strands might be the reason for the different effects of the siGENOME and the ON-TARGETplus SMARTpool® siRNAs. However, since we observed a comparable knockdown efficiency as well as polyP content in cisplatin-treated cells harboring either siRNA #1 or #20, we can likely exclude this possibility. Besides, the siGENOME SMARTpool® reagents used in this assay were newly purchased rather than cherry-picked from the core facility, which also circumvented the potential problem of lower effective concentrations of the siGENOME SMARTpool® siRNAs caused by freezing-and-thawing cycles.

In addition to the ϵ subunit of the F₀F₁-ATPase, we also considered pantothenate kinase 4 (PANK4), the one and only kinase on the list, as potential candidate worthy of following up. PANK4 consists of two domains: a putative pantothenate kinase domain at the N terminus and a phosphatase domain at the C terminus. However, ‘PANK4’ is actually a misnomer since this enzyme cannot synthesize 4’-phosphopantothenate from pantothenate due to the lack of the conserved catalytic residues (216). To the best of our knowledge, the specific activity of PANK4 has not been characterized so far.

We therefore decided to monitor the distribution of PANK4 with immunofluorescence labeling in cisplatin-treated cells. Surprisingly, we observed an enhanced signal of PANK4 in cells stressed with 40 μ M cisplatin, which was 10-fold less than what was used in the high throughput screens (Fig. 4.6). However, PANK4 did not appear to co-localize with polyP in either untreated or

cisplatin-treated cells, except for a few very bright foci in the nucleolus (Fig. 4.6, arrows). Based on these preliminary results, we decide to raise cisplatin concentrations and scrutinize the spatial relationship of these two molecules in the follow-up experiments.

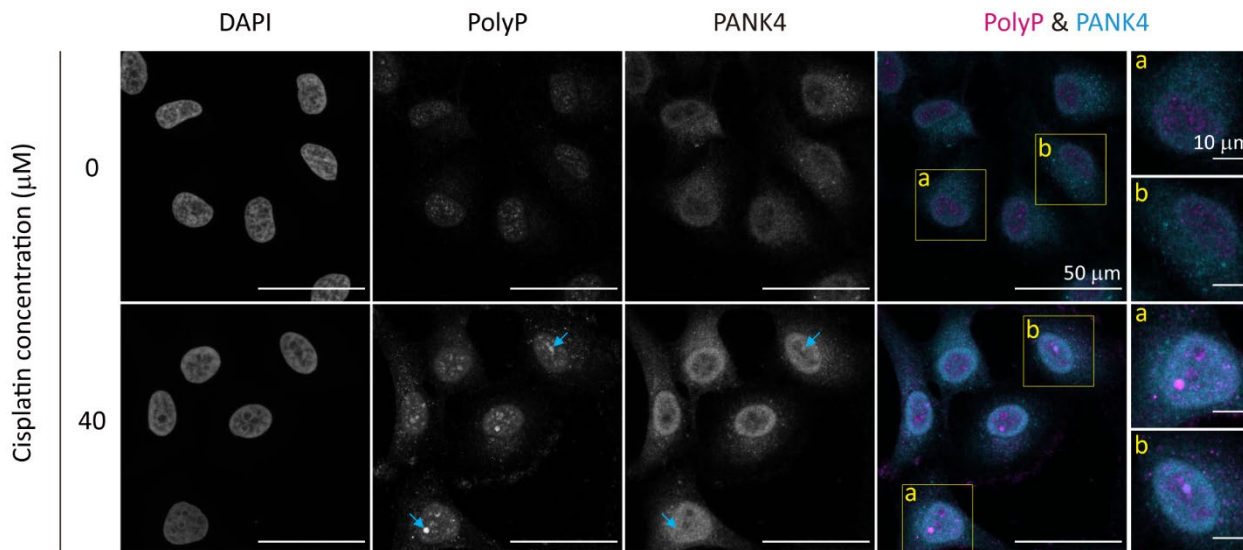


Figure 4.6 PANK4 upregulation in cisplatin-treated cells. Colocalization study of polyP and PANK4 was performed in untreated HeLa cells (top row) and cells treated with 40 μM cisplatin for 24 h (bottom row). Gray scale images from left to right depict the patterns of DNA, polyP (stained with GFP-*EcPPXc*), and PANK4 (labeled with specific primary and secondary antibodies). PolyP (pseudo color: magenta) and PANK4 (pseudo color: cyan) signals are merged to show the partition of the two molecules. Two regions (a and b) are enlarged for more details. Representative images of projected z series are shown on the images. Scale bar information is shown on the images.

4.3.5 Validation of *PPK* candidate genes with individual siGENOME siRNAs

We also applied our validation strategy for *ATP5F1E* to the remaining 35 candidates selected from the primary screen and retested with the ON-TARGET SMARTpool[®] siRNAs as described in section 4.3.3. Here, we targeted each candidate with four individual siRNAs from the siGENOME library and determined how many of them could reduce the polyP accumulation mediated by cisplatin.

Similar to what we observed for *ATP5F1E*, not every siRNA affected the polyP-related phenotypes to the same extent (Fig. 4.7). When we analyzed the proportion of cisplatin responsive cells, we classified the 35 candidates into five groups (I to V) based on the number of siRNAs which scored below the mean of the entire 18,110 targets in the primary screening, i.e., 140. This analysis put *RIT1* and *KRTAP11-1* at the top of the list with all 4 siRNAs qualified for this criterion (group I). The majority of the candidates clustered in groups II and III with one and two siRNA outliers, respectively. Both *ATP5F1E* and *PANK4* belonged to this population. For those genes in categories

IV and V, it was much more perplexing to interpret the inverse outcomes of the siGENOME individual siRNAs and the corresponding siGENOME SMARTpool® form. It was likely that those hits suffered from stronger off-target effects and therefore ought to be considered with more caution.

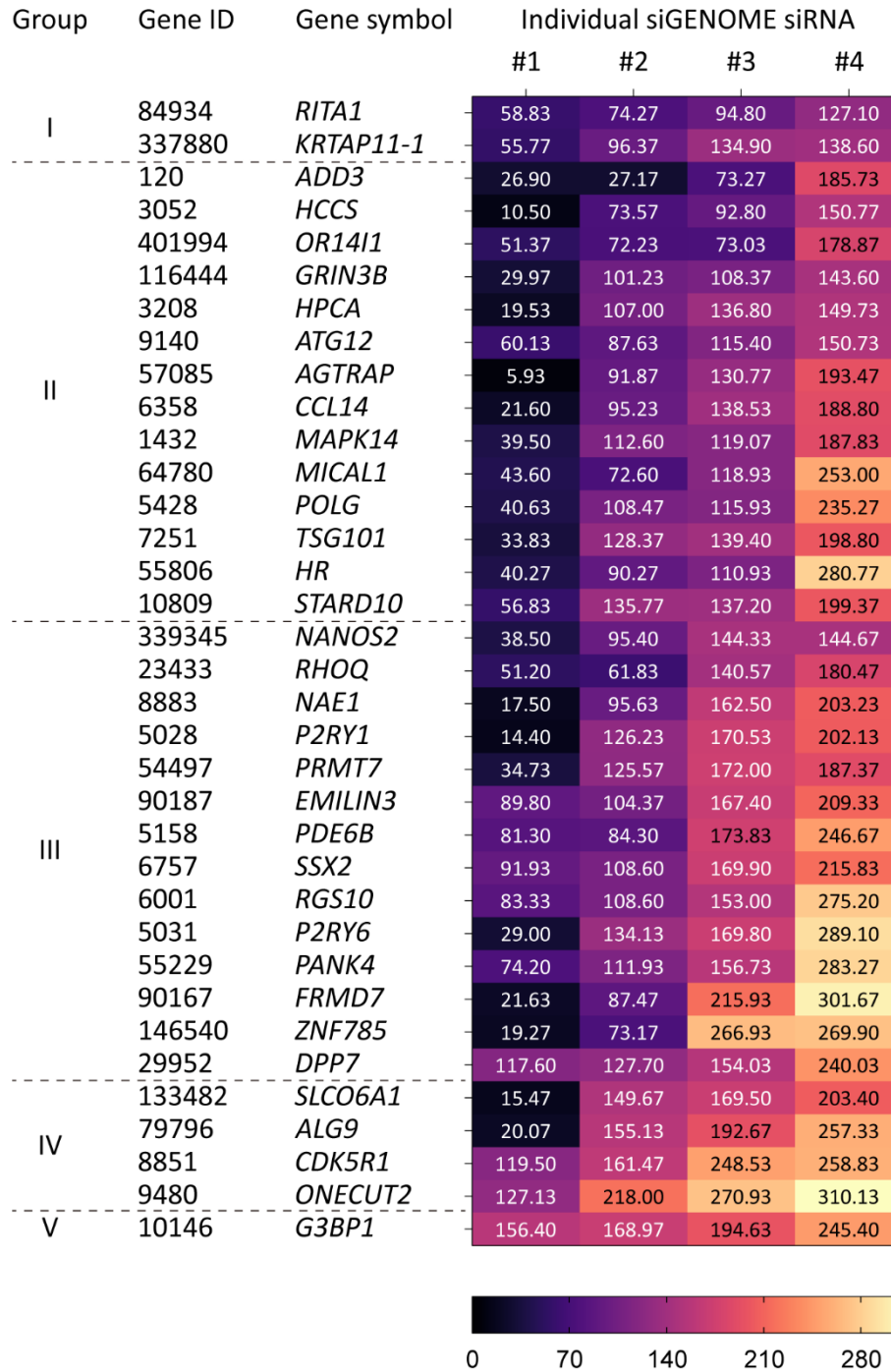


Figure 4.7 Effects of individual siGENOME siRNAs on the polyP content of selected candidates after cisplatin treatment. Each candidate was targeted by four individual siRNAs (#1 to #4) from the siGENOME collection. The scores of cisplatin responsiveness are presented in a heatmap. Overall, these candidates can be classified into five groups (I to V) based on the number of siRNAs that scored below 140 (the mean value of all the targets from the primary screening). Within each group, hits are ranked by the average scores of the four individual siRNAs.

4.3.6 Potential candidates for genes that downregulate polyP

Apart from revealing potential human *PPK* and other genes involved in polyP upregulation, our screening also shed light on the mechanisms by which polyP may be downregulated in mammalian cells. Focusing on the mCherry-*EcPPX_c* signal in the nucleus, we identified 79 knockdown samples which accumulated at least three times as much polyP as the mean of the entire library, or nearly five times as much as the non-targeting siRNA control (Table 4.4). Notably, we ranked the targets by their scores of nuclear mCherry-*EcPPX_c* fluorescence intensities rather than the scores of cisplatin responding cells because the former parameter showed a much wider dynamic range for targets with substantially elevated scores (Fig. 4.3, A and B). Nevertheless, we observed an average of a 2.2-fold increase in the percentage of cisplatin responsive cells in this subset of candidates compared to the non-targeting siRNA control, or a 1.6-fold increase compared to the mean of the 18,110 targets in total (Table 4.4).

Table 4.4 Potential candidates for genes responsible for polyP downregulation

Rank ^a	Gene ID	Gene Symbol ^o	Score (Nuclear mCherry- <i>EcPPX_c</i> signal)	Score (% of cisplatin responsive cells)	Rank	Gene ID	Gene Symbol	Score (Nuclear mCherry- <i>EcPPX_c</i> signal)	Score (% of cisplatin responsive cells)
1	90231	<i>KIAA2013</i>	840.2	243.5	41	81602	<i>CDADC1</i>	539.4	235.8
2	2560	<i>GABRB1</i>	788.6	227.3	42	6755	<i>SSTR5</i>	538.4	244.5
3	53827	<i>FXYS5</i>	763.5	226.1	43	6794	<i>STK11</i>	536.5	221.2
4	56604	<i>TUBB7P</i>	748.6	191.2	44	344905	<i>ATP13A5</i>	531.7	219.0
5	79883	<i>PODNL1</i>	722.8	243.8	45	7755	<i>ZNF205</i>	531.2	206.8
6	491	<i>ATP2B2</i>	718.6	207.1	46	4293	<i>MAP3K9</i>	530.8	220.6
7	9651	<i>PLCH2</i>	716.8	226.1	47	160857	<i>CCDC122</i>	527.0	224.7
8	260425	<i>MAGI3</i>	673.6	217.3	48	84445	<i>LZTS2</i>	525.5	232.9
9	5429	<i>POLH</i>	662.1	180.4	49	1742	<i>DLG4</i>	525.0	248.5
10	8464	<i>SUPT3H</i>	660.6	184.2	50	3791	<i>KDR</i>	524.2	213.9
11	6667	<i>SP1</i>	651.9	224.0	51	1118	<i>CHIT1</i>	523.8	239.1
12	138639	<i>PTPDC1</i>	649.2	226.4	52	26240	<i>FAM50B</i>	522.4	287.6
13	4908	<i>NTF3</i>	618.4	178.8	53	862	<i>RUNX1T1</i>	522.3	190.6
14	9928	<i>KIF14</i>	613.8	224.6	54	11113	<i>CIT</i>	521.6	212.1
15	64419	<i>MTMR14</i>	602.1	222.0	55	5529	<i>PPP2R5E</i>	521.0	219.9
16	158055	<i>C9orf163</i>	598.2	99.5	56	2203	<i>FBP1</i>	519.9	219.3
17	11318	<i>GPR182</i>	587.4	246.7	57	10753	<i>CAPN9</i>	519.3	223.4
18	773	<i>CACNA1A</i>	585.7	232.6	58	1945	<i>EFNA4</i>	519.0	241.6
19	1198	<i>CLK3</i>	582.5	220.7	59	1340	<i>COX6B1</i>	518.2	201.9

^a The candidates are ranked by their scores of nuclear mCherry-*EcPPX_c* fluorescence intensities in an order from high to low.

^o Official NCBI gene symbols are listed in this table for those entries with more than one commonly used gene symbols.

Rank "	Gene ID	Gene Symbol ^o	Score (Nuclear mCherry- EcPPX _c signal)	Score (% of cisplatin responsive cells)	Rank	Gene ID	Gene Symbol	Score (Nuclear mCherry- EcPPX _c signal)	Score (% of cisplatin responsive cells)
20	1850	<i>DUSP8</i>	577.7	225.8	60	2532	<i>ACKR1</i>	517.7	245.6
21	843	<i>CASP10</i>	573.5	230.1	61	53	<i>ACP2</i>	513.3	217.6
22	3631	<i>INPP4A</i>	565.3	223.7	62	1580	<i>CYP4B1</i>	512.5	204.3
23	5347	<i>PLK1</i>	565.1	175.8	63	1601	<i>DAB2</i>	512.1	216.6
24	8844	<i>KSRI</i>	564.8	239.6	64	5159	<i>PDGFRB</i>	510.9	211.5
25	7031	<i>TFE1</i>	561.2	186.3	65	51305	<i>KCNK9</i>	510.7	229.4
26	165829	<i>GPR156</i>	559.5	226.5	66	95681	<i>CEP41</i>	508.6	166.9
27	1437	<i>CSF2</i>	556.9	184.2	67	403313	<i>PLPP6</i>	505.0	230.2
28	4161	<i>MC5R</i>	556.5	250.3	68	23636	<i>NUP62</i>	504.6	199.6
29	56623	<i>INPP5E</i>	555.5	218.8	69	766	<i>CA7</i>	504.6	220.6
30	1314	<i>COPA</i>	555.0	211.2	70	1847	<i>DUSP5</i>	503.6	228.9
31	2268	<i>FGFR</i>	553.4	216.7	71	5747	<i>PTK2</i>	502.1	243.4
32	4356	<i>MPP3</i>	553.3	212.2	72	8031	<i>NCOA4</i>	500.7	203.2
33	9973	<i>CCS</i>	551.3	210.5	73	6790	<i>AURKA</i>	500.3	207.9
34	659	<i>BMP2</i>	548.9	199.8	74	4923	<i>NTSR1</i>	497.5	248.4
35	4140	<i>MARK3</i>	548.6	230.6	75	10434	<i>LYPLAI</i>	497.1	236.4
36	5297	<i>PI4KA</i>	547.2	241.2	76	54826	<i>GIN1</i>	495.2	203.3
37	92370	<i>PXYLP1</i>	546.6	219.7	77	8560	<i>DEGS1</i>	494.4	204.4
38	6204	<i>RPS10</i>	544.0	178.3	78	5901	<i>RAN</i>	493.2	238.2
39	2538	<i>G6PC</i>	543.7	212	79	23414	<i>ZFPM2</i>	492.0	200.8
40	118471	<i>PRAP1</i>	542.1	196.9					

To further understand the biological meanings behind these candidates, we ran a gene ontology enrichment analysis (<http://geneontology.org/>) to decipher the biological processes that were significantly overrepresented by these genes. In the end, we revealed ten such biological processes (not including the ones with higher hierarchies in the gene ontology structure; e.g., positive regulation of cytokinesis (GO:0032467) is a branch of regulation of cytokinesis (GO:0032465), which was also significantly overrepresented but not included in this figure) (Fig. 4.8). Strikingly, three biological processes were related to inositol phosphate and phosphatidylinositol. In particular, several enzymes directly involved in the phosphorylation and dephosphorylation of the inositol moiety were now proposed to negatively influence polyP levels in response to cisplatin. These enzymes included 1-phosphatidylinositol 4,5-bisphosphate phosphodiesterase eta-2 (PLCH2), inositol polyphosphate 4-phosphatase type I A (INPP4A), phosphatidylinositol polyphosphate 5-phosphatase type IV (INPP5E), and phosphatidylinositol 4-kinase alpha (PI4KA). At this point, we cannot rule out the possibility that polyP is a previously uncharacterized substrate of certain phosphatidylinositol phosphatases. However, it appears more likely to us that polyP regulation is partially entwined with phosphatidylinositol and inositol phosphate metabolism. This notion is consistent with previous findings that loss of inositol hexakisphosphate kinase 1 (IP6K1) activity in several model organisms, including yeast, *Trypanosoma*, and mice, led to a 50-100% inhibition

of polyP synthesis (120-123). Yet, it is Vtc4 – not Ip6k1 – that catalyzes the polyP elongation reaction in the unicellular eukaryotes, and we did not identify *IP6K1* as a candidate for human *PPK* genes in our screens either. As for other biological processes, such as the positive regulation of cytokinesis and the MAPK cascade, they might be crucial to sensing and signaling cisplatin stress, which acts on the upstream of polyP synthesis.

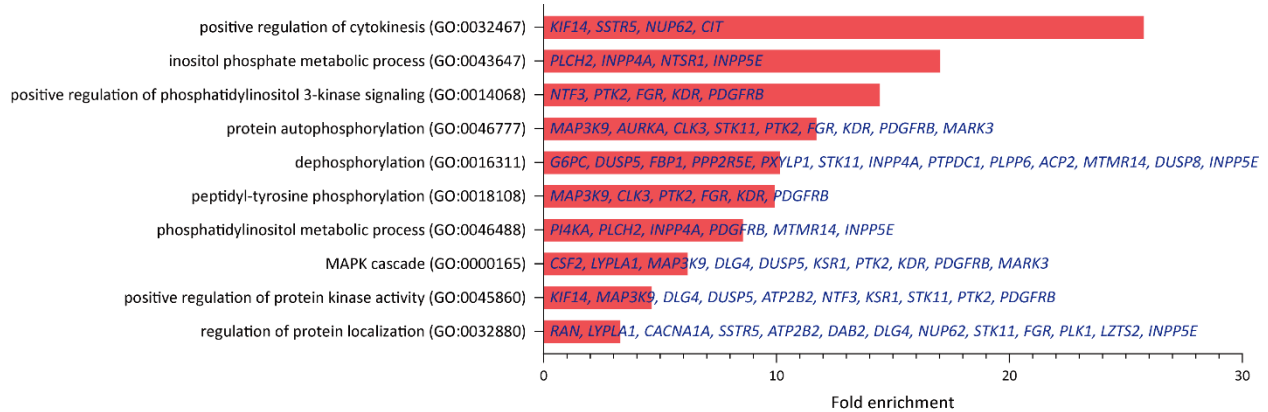


Figure 4.8 Biological processes overrepresented by the potential candidates that downregulate polyP. A PANTHER Overrepresentation Test using the GO biological process complete annotation dataset revealed ten biological processes to be significantly overrepresented by the 79 candidate genes for polyP downregulation. Fold enrichment of each biological process was shown in the graph, and the genes in each category were listed in the corresponding column.

4.3.7 Potential candidates for the regulation of cisplatin sensitivity in HeLa cells

In the previous sections, we focused exclusively on the polyP-related phenotypes in the primary screen. However, another important aspect of this study concerned the cisplatin sensitivities of the 18,110 targets. We decided to use cell count as a rough estimation of cisplatin toxicity. For the non-targeting siRNA control, we observed an 88% cell loss (from 1170.9 cells to 143.8 cells) after 24 hours of cisplatin treatment. In parallel, the cell numbers of cisplatin-treated knockdown samples varied from 0.1 to 799.4 with an average of 146.0 (Fig. 4.3C). This value was almost identical to that of the non-targeting siRNA control, which led us to believe that the non-targeting siRNA serve as an appropriate reference in this case.

In the initial experimental setup, we did not determine the cell count or polyP levels before cisplatin treatment. Hence, we decided to sort the targets by their absolute cell numbers after cisplatin exposure and focused on the 108 targets with 1/30 or fewer cells than the non-targeting siRNA control.

Table 4.5 Potential candidates for the regulation of cisplatin toxicity

Rank	Gene ID	Gene Symbol	Cell count	Rank	Gene ID	Gene Symbol	Cell count
1	7884	<i>SLBP</i>	0.1	55	7415	<i>VCP</i>	3.2
2	5430	<i>POLR2A</i>	0.5	56	1308	<i>COL17A1</i>	3.2
3	93611	<i>FBXO44</i>	0.5	57	3084	<i>NRG1</i>	3.2
4	79624	<i>ARMT1</i>	0.7	58	200159	<i>C1orf100</i>	3.2
5	6651	<i>SON</i>	0.9	59	6272	<i>SORT1</i>	3.3
6	389118	<i>CDHR4</i>	1.1	60	401665	<i>OR51T1</i>	3.3
7	2519	<i>FUCA2</i>	1.1	61	7844	<i>RNF103</i>	3.4
8	10482	<i>NXFI</i>	1.1	62	2567	<i>GABRG3</i>	3.4
9	7314	<i>UBB</i>	1.2	63	3765	<i>KCNJ9</i>	3.5
10	1212	<i>CLTB</i>	1.3	64	23263	<i>MCF2L</i>	3.5
11	84448	<i>ABLIM2</i>	1.3	65	55362	<i>C6ORF110</i>	3.5
12	5683	<i>PSMA2</i>	1.4	66	336	<i>APOA2</i>	3.5
13	51676	<i>ASB2</i>	1.4	67	1622	<i>DBI</i>	3.5
14	157574	<i>FBXO16</i>	1.5	68	7364	<i>UGT2B7</i>	3.5
15	11269	<i>DDX19</i>	1.6	69	1654	<i>DDX3X</i>	3.5
16	22974	<i>TPX2</i>	1.6	70	3249	<i>HPN</i>	3.6
17	80852	<i>GRIP2</i>	1.8	71	9861	<i>PSMD6</i>	3.6
18	151648	<i>SGO1</i>	1.8	72	91074	<i>ANKRD30A</i>	3.7
19	255488	<i>IBRDC2</i>	1.8	73	130814	<i>C2ORF22</i>	3.7
20	342357	<i>ZKSCAN2</i>	1.9	74	64326	<i>COPI</i>	3.7
21	57621	<i>ZBTB2</i>	1.9	75	160857	<i>CCDC122</i>	3.7
22	5768	<i>QSOX1</i>	1.9	76	3782	<i>KCNN3</i>	3.9
23	4605	<i>MYBL2</i>	1.9	77	84304	<i>NUDT22</i>	3.9
24	10155	<i>TRIM28</i>	2.0	78	9348	<i>NDST3</i>	3.9
25	2629	<i>GBA</i>	2.1	79	390212	<i>GPR152</i>	3.9
26	123879	<i>DCUN1D3</i>	2.1	80	5149	<i>PDE6H</i>	3.9
27	891	<i>CCNB1</i>	2.1	81	9640	<i>ZNF592</i>	3.9
28	56891	<i>LGALS14</i>	2.2	82	1278	<i>COL1A2</i>	4.1
29	5435	<i>POLR2F</i>	2.2	83	7515	<i>XRCC1</i>	4.1
30	4702	<i>NDUFA8</i>	2.2	84	6299	<i>SALL1</i>	4.1
31	159296	<i>NKX2-3</i>	2.3	85	81853	<i>TMEM14B</i>	4.1
32	23450	<i>SF3B3</i>	2.3	86	387	<i>RHOA</i>	4.1
33	3744	<i>KCNA10</i>	2.4	87	9034	<i>CCRL2</i>	4.1
34	5347	<i>PLK1</i>	2.4	88	139793	<i>PAGE3</i>	4.2
35	5901	<i>RAN</i>	2.5	89	26539	<i>OR10H1</i>	4.2
36	30837	<i>SOCS7</i>	2.5	90	5053	<i>PAH</i>	4.3
37	131669	<i>UROCI</i>	2.5	91	55790	<i>CHGN</i>	4.3
38	55734	<i>ZFP64</i>	2.5	92	401190	<i>RGS7BP</i>	4.3
39	3118	<i>HLA-DQA2</i>	2.5	93	8988	<i>HSPB3</i>	4.3
40	10741	<i>RBBP9</i>	2.5	94	245812	<i>CNPY4</i>	4.4
41	11073	<i>TOPBP1</i>	2.5	95	7423	<i>VEGFB</i>	4.5
42	1192	<i>CLIC1</i>	2.6	96	3992	<i>FADS1</i>	4.5
43	27246	<i>RNF115</i>	2.7	97	374877	<i>TEX45</i>	4.5
44	11331	<i>PHB2</i>	2.7	98	442867	<i>BPY2B</i>	4.5
45	3183	<i>HNRPC</i>	2.8	99	2561	<i>GABRB2</i>	4.5
46	91544	<i>UBXN11</i>	2.8	100	643365	<i>LINC00452</i>	4.5
47	6693	<i>SPN</i>	2.8	101	5087	<i>PBX1</i>	4.5
48	10204	<i>NUTF2</i>	2.9	102	2206	<i>MS4A2</i>	4.5
49	1161	<i>CKNI</i>	2.9	103	79883	<i>PODNL1</i>	4.5
50	140625	<i>ARPM2</i>	2.9	104	84056	<i>KATNAL1</i>	4.5
51	158055	<i>C9orf163</i>	2.9	105	1981	<i>EIF4G1</i>	4.6
52	10720	<i>UGT2B11</i>	3.1	106	7458	<i>WBSR1</i>	4.7
53	203076	<i>C8orf74</i>	3.1	107	25832	<i>NBPF14</i>	4.7
54	57582	<i>KCNT1</i>	3.1	108	147381	<i>CBLN2</i>	4.7

Through a gene ontology enrichment analysis, we identified several biological processes to be significantly overrepresented by this subset of genes (Fig. 4.9). In particular, we found transcription-coupled nucleotide-excision repair, proteasomal ubiquitin-dependent protein catabolism, and mitotic cell cycle phase transitions to be highly enriched (>11.5-fold). These results were fully consistent with the notion that cisplatin toxicity is largely incurred by DNA damage, and that cell survival likely requires a cell cycle arrest for DNA damage repair. In the meantime, genes responsible for ubiquitination and proteasomal degradation were also significantly overrepresented, which indicates severe protein damage caused by cisplatin. We postulate that all these processes have come into play to minimize the detrimental consequences of cisplatin on the cells.

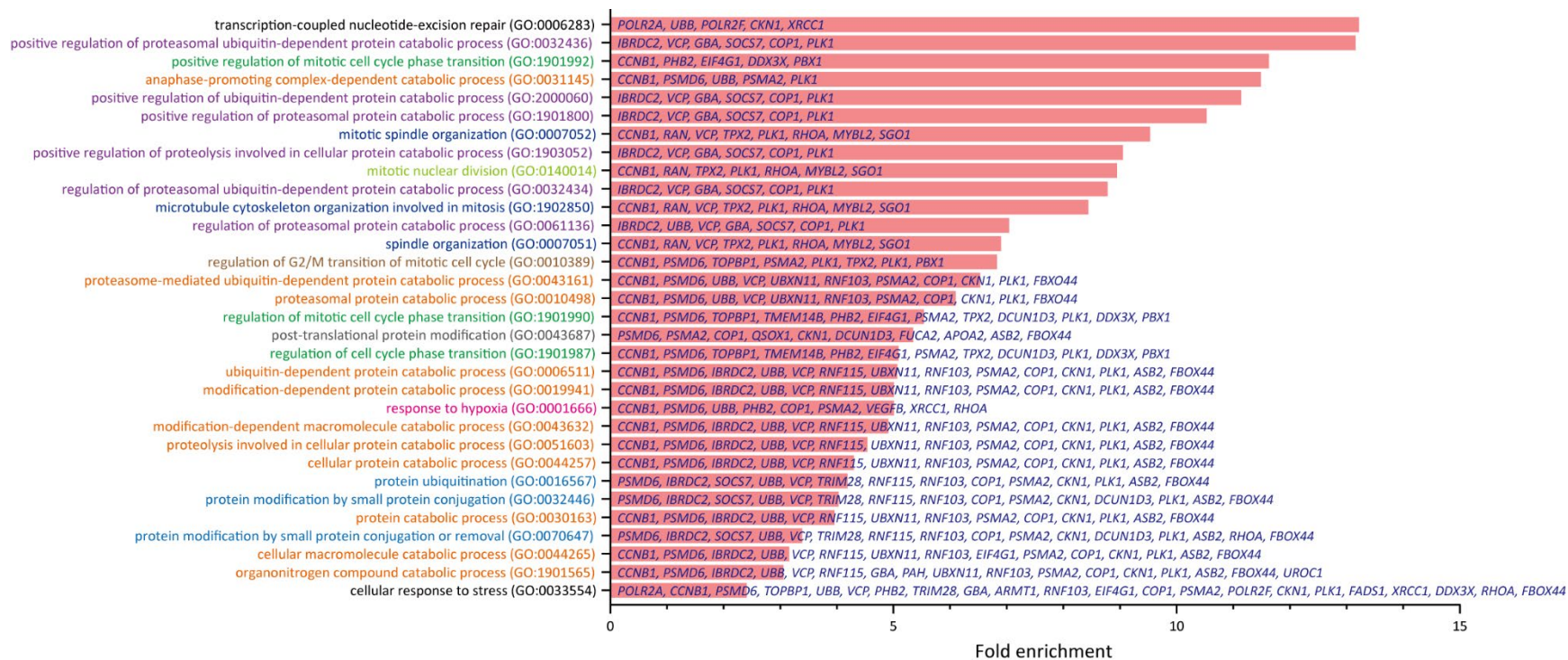


Figure 4.9 A gene ontology enrichment analysis of targets involved in the regulation of cisplatin sensitivity. 108 knockdown samples were selected from the primary screen for having fewer than 4.8 cells (i.e., 1/30 of the number of cells in the non-targeting siRNA control) after cisplatin treatment. They were subject to a PANTHER Overrepresentation Test using the GO biological process complete annotation dataset. Listed here are all the significantly overrepresented categories and their respective fold changes. Terms with the same color belong to the same branch of the hierarchical gene ontology structure. Specific genes identified for each category are listed in the designated column.

4.4 Discussion

4.4.1 An siRNA screen designed for identifying human *PPK* genes

The most important purpose of this study was to identify the potential regulators of polyP levels in humans, especially the polyphosphate kinase(s). To achieve this goal, we used an siGENOME SMARTpool[®] siRNA library to target 18,110 mRNAs in the transcriptome of HeLa cells and monitored the cisplatin-induced polyP response with mCherry-*EcPPX_c* fluorescence.

For data analysis, we designed four parameters to describe the phenotypes we observed: 1) percentage of cisplatin responsive cells; 2) polyP concentration in the nucleus; 3) polyP concentration in the whole cell; and 4) cell count. All the measurements, except cell numbers, were normalized on a scale of 0 to 100, defined by the positive control and the negative control, respectively. The proportion of cisplatin responsive cells was chosen as the chief parameter for hit identification because the widest dynamic range could be attained from this measurement. Consistently, calculations of cisplatin responsiveness and nuclear mCherry-*EcPPX_c* fluorescence yielded a similar subset of hits (Table 4.1 and Table S4.1).

After the primary screen, we analyzed the overall distributions of polyP-related phenotypes and cell count for all the 18,110 targets (Fig. 4.3). As it turns out, the mean scores of cisplatin responsiveness as well as nuclear mCherry-*EcPPX_c* signal for the 18,110 targets exceeded those of the non-targeting siRNA control. This observation raised an intriguing possibility that polyP levels might increase in response to the execution of RNAi by the RNA-induced silencing complex (RISC). At this point, we are unable to establish a direct interaction between polyP and RISC. However, there are several mechanisms which might explain our observation. RISC and exogenous siRNA oligos are sequestered in the cytoplasmic GW bodies (or processing bodies, P-bodies), and the structural integrity of GW bodies is an important premise for the efficiency of RNAi (217). GW bodies are formed by phase-phase separation just like the nucleoli. In a previous study, we characterized polyP as a nucleolar component, which appeared highly dynamic under rRNA synthesis stress (127). Therefore, we wonder whether polyP is also enriched in the GW bodies and partakes in RNAi. Alternatively, polyP upregulation might be a general stress response to the perturbation of a functional protein by RNAi. After all, polyP is considered as a cytoprotective agent under many stressful conditions (1). In either case, a 40% difference in the mean polyP content of the knockdown samples and that of the non-targeting siRNA control

prompted us to reestablish proper reference values for the polyP-related phenotypes. Notably, this adjustment was not necessary for the cell count parameter, suggesting that cisplatin sensitivity was not altered by RNAi per se.

To generate a list of potential candidates for human *PPK* genes, we set an arbitrary cutoff at the score of 30 for the measurement of cisplatin responding cells. When we took into consideration the mean score of the whole siRNA library, this criterion only selected those candidates with less than 21.4% of the ability to enrich polyP after cisplatin treatment. We were able to identify 405 hits after screening 201 plates in 23 independent assays. However, only 115 of them were validated with the same siRNA and the same experimental setup in an assay combining all the hits together (Table 4.1). This outcome informed us of substantial variations from experiment to experiment. We would ascribe this result to the random noises of cell conditions, effective cisplatin concentrations, transfection efficiencies, and/or immunofluorescence labeling.

Focusing on the 115 candidates, we evaluated their basal polyP levels and the fold changes of nuclear mCherry-*EcPPX_c* signals upon cisplatin treatment (Fig 4.4). Overall, these candidates had 28.3% less polyP than the non-targeting siRNA control under normal growth condition (Fig. 4.4A). Due to the limitation of our experimental setup, we could not calculate the mean score of basal polyP levels for all the targets involved in the primary screening. Hence, we could not estimate the relative change of this parameter for the 115 candidates against the entire library. Still, our results supported a role of the corresponding genes in making ample polyP to sustain the most fundamental cellular activities. Furthermore, this subset of candidates also exhibited a reduced fold increase in the mCherry-*EcPPX_c* fluorescence intensity following cisplatin supplement (Fig. 4.4B). The ratiometric measurement of polyP signals with and without cisplatin seemed to be dominated by the post-cisplatin measurements. This might be due to an individualized response of each knockdown sample to cisplatin, which greatly expanded the dynamic range of this parameter. In summary, analyses of basal polyP levels as well as the amplitude of cisplatin-mediated polyP response confirmed a severe impairment of polyP regulation in this subset of candidates.

4.4.2 Validation of the potential candidates for human *PPK* genes

RNAi remains a powerful tool to study gene expression, yet, its outcome is often confounded by inadvertent off-target effects. Therefore, we decided to further scrutinize our candidates with 1) ON-TARGETplus SMARTpool[®] siRNAs and 2) individual siRNAs derived from the siGENOME

SMARTpool[®] library. The former aimed at discriminating the on-target and off-target effects by modifying siRNA sequences, while the latter took advantage of numbers to tell the major (on-target) and minor (off-target) effects apart.

The results of the validation screens were quite perplexing. First and foremost, we could not reproduce the > 70% reduction of cisplatin responding cells for any of the 36 targets tested in a pioneer study using ON-TARGETplus SMARTpool[®] siRNAs (Table 4.2). This issue was not due to insufficient knockdown efficiencies (Fig. S4.1) or systematic errors between the siGENOME and ON-TARGETplus libraries (Fig. 4.5, *ATP5F1E* siRNA #1 and #20). In the worst-case scenario, this meant a 100% false positive rate for this subset of hits, raising doubts about the validity of the primary screen. However, it is also possible that the combinatory effect of ON-TARGETplus SMARTpool[®] siRNAs might be skewed by a few individual components with very potent phenotypes. At a minimum, this was the case for *ATP5F1E*, where a single siRNA (#18) with a surge of polyP dominated all three others with varying degrees of polyP reduction (in relative to the mean score of the 18,110 targets) (Fig. 4.5). We are fully aware that these results are inadequate to verify the role of *ATP5F1E* in polyP synthesis. Still, it encourages us to follow up on a few top hits in this pioneer study and determine the consequence of knocking down the corresponding genes with individual ON-TARGETplus siRNAs.

Along the same line, we compared individual siRNAs from the siGENOME library to their corresponding SMARTpool[®] formats. Again, using the average score of the whole population as a reference, we classified the majority of the 36 candidates into groups with two, three, and four individual siRNAs qualified for a polyP reduction (Fig. 4.7). Assuming that the majority of individual siRNAs were guided to their specific mRNA targets, and that mistargeting events were only sporadic, our results tend to suggest that many of these genes are promising candidates for the upregulation of polyP in mammalian cells.

4.4.3 Evaluation of the candidates for human *PPK* genes

To prioritize the most promising candidates, we considered the three types of screens that we conducted for the subset of 36 targets: 1) a genome-wide screen with siGENOME SMARTpool[®] siRNAs and a validation screen with the same reagent; 2) a validation screen with ON-TARGETplus SMARTpool[®] siRNAs; and 3) a validation screen with individual siGENOME siRNAs. The rankings of the hits differed, sometimes dramatically, from one screen to another

(Table 4.1, Table 4.2, Fig. 4.7), and it was not trivial to weigh the reliability of each approach given their respective strengths and drawbacks.

Yet, simply considering all the screens equally, we noticed *GRIN3B* at the top of each list. This gene encodes GluN3B, a subunit of the unconventional *N*-methyl-D-aspartate (NMDA) type glutamate receptor, which can be excited by glycine alone and is relatively impermeable to Ca^{2+} (218). The spatial and temporal expression patterns of this protein have been characterized in the brain, and its malfunction is a risk factor for schizophrenia (218-221). Intriguingly, polyP has been shown to modulate NMDA receptors, presumably those with low Ca^{2+} permeability in the dentate gyrus of the hippocampus (222). This finding now creates a biologically relevant context for our hypothesis that GluN3B might in turn control polyP metabolism in a yet unknown manner. Furthermore, our discovery reminded us of a dormant notion in the field that “*because polyP synthesis from Pi in the medium bypasses intracellular Pi and ATP pools, a direct involvement of energy sources in cell membranes...should be considered*” (202). Given our limited understanding of GluN3B and polyP, we cannot conceive a model of polyP synthesis by GluN3B directly. However, this protein indicates the potential importance of plasma membrane proteins in the regulation and/or synthesis of polyP.

Apart from referencing the hit rankings, we also conducted extensive literature searches to seek polyP-related information for the hits. Indeed, we were able to establish at least tangential connections between polyP and a handful of candidates. Such examples included *P2RY1*, which encodes the best characterized polyP receptor in the astrocytes and endothelial cells (42,77), and *P2RY6*, which belongs to the same family of purinergic receptors. In fact, much of polyP’s signaling properties depend on P2Y1. Either a genetic or a pharmacologic perturbation of this receptor dampens polyP-mediated signaling cascades (42,77,222). Notably, P2Y1 underpins the cytoprotective function of polyP against mitochondrial membrane depolarization incurred by an overflow of glutamate in the cortical neurons (222). Therefore, a connection between *GRIN3B* and *P2RY1* appears likely. Another intriguing candidate, *AP3MI* (ranked 70th in the primary screen) encodes the mu-1 subunit of the adaptor-related protein complex 3 (AP-3). Previous studies in *Trypanosoma* and *Leishmania* have established the critical importance of the AP-3 complex in the enrichment of polyP in the acidocalcisomes, presumably by overseeing the protein trafficking to this organelle (223,224). Genetic mutations in several subunits of the AP-3 complex lead to Hermansky-Pudlak syndrome (225,226) in humans, a rare disease associated with the lack of

platelet dense granules – the most prominent intracellular polyP storage. These findings suggest that *AP3MI* might be a novel member of the acidocalcisome-related polyP machinery.

From the perspective of polyP synthesis, we were most excited about identifying *ATP5F1E*, which encodes the ϵ subunit of mitochondrial F_0F_1 -ATPase. This small protein (7 kDa) in the central stalk of the F_1 catalytic domain has no structural equivalent in the bacterial or chloroplast ATP synthases (215). Moreover, previous studies recording polyP-DAPI fluorescence in either intact cells or isolated mitochondria have alluded to a causal relation between the activity of F_0F_1 -ATPase and the concentration of mitochondrial polyP (115,116). Joint together, these findings created a perfect niche for our hypothesis that the ϵ subunit adapts the mitochondrial F_0F_1 -ATPase into a dual functional engine for both ATP and polyP synthesis. As a consequence, we performed the most extensive validation experiments for this candidate. To summarize, we were able to achieve varying degrees of polyP depletion by targeting this gene with four out of seven uniquely designed siRNAs (with #1 and #20 sharing the same sequence) (Fig. 4.5). And the outcomes of the siGENOME SMARTpool[®] and the ON-TARGETplus SMARTpool[®] collections hinged on their respective siRNA compositions (Fig. 4.5). Contrary to our expectation, we were unable to conclude that *ATP5F1E* is a true candidate for human *PPK* genes. But we will now attempt to recapitulate the phenotype of *ATP5F1E* knockdown with a complete gene knockout.

Prompted by the notion that ATP is the universal substrate for all polyP synthesizing machineries known to date, we paid attention to another candidate, *PANK4*, which encodes the only kinase on the list. *PANK4* appealed to us for several reasons. Primarily, both *PANK4* and polyP were upregulated by a low dose of cisplatin (40 μ M) (Fig. 4.6), and *PANK4* knockdown obstructed polyP accumulation in cisplatin-treated cells. Moreover, this protein harbors a kinase domain and a phosphatase domain whose enzymatic activities remain yet uncharacterized. For follow-up experiments, we will test a higher dose of cisplatin for recruiting *PANK4* and polyP to colocalize in the same hotspots, and we will corroborate the phenotype of *PANK4* knockdown cells with either an siRNA-resistant *PANK4* variant or a *PANK4* knockout model. Even in the worst-case scenario that *PANK4* and polyP are completely irrelevant, our discovery that *PANK4* is part of the cisplatin response might still shed light on the function of this protein.

Our experimental design does not allow us to distinguish polyP synthesizing machines from cisplatin sensors. Instead, any impairment in the transmission of cisplatin signal from outside the

cell to the PPK enzyme will manifest a similar phenotype as an impairment in the enzyme itself. For example, one of the top hits, tumor susceptibility gene 101 (*TSG101*) encodes a component of the endosomal sorting complexes required for transport-I (ESCRT-I) machinery. While this protein is largely recognized for multivesicular body formation, membrane abscission, and budding of viral particles (227), it is also proclaimed to be an essential gene for cell proliferation and prognostic marker for certain types of cancers (228). Other candidates, such as *MAPK14*, *P53AIP1*, *MTIG* might also be more closely related to cisplatin rather than polyP (Table 4.1).

4.4.4 Potential candidates for the downregulation of polyP

Conceivably, not only polyP synthesis but also polyP degradation is critical to maintaining the homeostasis of such an energetic and multifunctional polymer. Therefore, we also focused on genes whose knockdowns led to an enormous accumulation of polyP in cisplatin-treated cells. As it turns out, 79 candidates had more than three times the mean polyP level of the whole library or five times the value of the non-targeting siRNA control (Table 4.4). Many of them participated in distinct biological processes revealed by gene ontology enrichment analysis (Fig. 4.8). Three out of ten such biological processes raised our attention: 1) inositol phosphate metabolism (with a 17-fold enrichment); 2) positive regulation of phosphatidylinositol 3-kinase signaling (with a 14-fold enrichment); and 3) phosphatidylinositol metabolism (with a more than 8-fold enrichment). In our opinion, these results strongly suggest the roles of inositol phosphates in controlling polyP production and/or utilization. In fact, IP6K1, which catalyzes the formation of highly phosphorylated inositol phosphate species (including IP₇ and IP₈) from IP₆, has been found to maintain the steady-state polyP levels in yeast, *Trypanosoma*, and mice (120-123). In yeast cells, IP₆, IP₇, and IP₈ are novel binding partners of the SPX domain of Vtc4 (124,125), the bona fide polyP synthesizing machinery. Association of inositol phosphates with the SPX domain enhances Vtc4 enzymatic activity, with IP₈ and IP₇ being significantly more potent than IP₆. Therefore, this model explains how IP6K1 might influence intracellular polyP concentrations without mediating polyP elongation per se. Given that no *VTC4* homologue exists in the mouse genome, it is intriguing how IP6K1 could elicit a similar effect on polyP production in vertebrates. It is tempting to speculate that mammalian PPK enzyme(s) might also harbor an inositol phosphate-sensitive domain which confer the regulatory effects of different inositol phosphate species. Along the same line, we propose that several candidates for the downregulation of polyP, such as PLCH2, INPP4A and INPP5E, might not catalyze the depolymerization of polyP chains, but rather modify the

cellular inositol phosphate levels and compositions, which causes an alteration of polyP abundance in the cell.

4.4.5 Potential mechanisms for the regulation of cisplatin sensitivity

Since our screens exploited the power of cisplatin to mobilize polyP, we also expected to find genes responsible for sensing and combatting cisplatin stress. Here, we utilized the number of remaining cells after drug treatment (and immunofluorescence labeling) as a rough estimation of cisplatin resistance. Certainly, this parameter was oversimplified in more than one aspect. In essence, it measured the combined cytotoxicity of abnormal gene expression (as a result of RNAi) and cisplatin-related cellular damages. This factor became important for those genes either beneficial or harmful to cell growth and proliferation. Moreover, we could not ascertain the fate of the remaining cells without a sophisticated analysis of different cell death markers. It was inconceivable that any cells could have survived such a high dose of cisplatin (0.4 mM) for 24 h. However, different samples might have followed different cell death pathways, leaving the remaining cells in a broad spectrum of different numbers and morphologies.

Taking into consideration the abovementioned caveats, we decided to focus on the targets with the least number of cells, namely fewer than 4.8 (or 1/30 of the number for the non-targeting siRNA control). This criterion yielded 108 candidates (Table 4.5) with a clear pattern of gene ontology enrichment (Fig. 4.9).

The transcription-associated nucleotide excision repair mechanism (represented by *POLR2A*, *UBB*, *POLR2F*, *CKNI*, and *XRCCI*) was most overrepresented due to the formation of DNA-cisplatin adducts. It is conceivable that cells become sensitized to cisplatin when DNA damages remain unrepaired. This result also inferred that DNA remains the most vulnerable target when the drug was administered at high concentrations. Meanwhile, it was also likely that deletion of *POLR2A* and *POLR2F* may disrupt cellular homeostasis independently of cisplatin. The former gene encodes RPB1, the largest subunit of RNA polymerase II (Pol II), and the latter encodes RPABC2, a universal component of Pol I, Pol II, and Pol III. Hence, *POLR2A* and *POLR2F* knockdowns might alter the gene expression landscape of the cell, and it is crucial to determine the toxicity of this aspect alone. In a highly speculative way, this finding also reminded us of our previous finding on polyP and Pol I during cisplatin-mediated apoptosis (127). Given that polyP and Pol I are sequestered in the vicinity of each other under cisplatin stress, it is intriguing whether a similar

spatial (and maybe functional) relation exists among polyP and other RNA polymerases. After all, polyP and bacterial RNA polymerase are binding partners of each other (32).

Another distinct biological process overrepresented by this subset of genes was the positive regulation of proteasomal ubiquitin-dependent protein catabolism. As part of the protein quality control network, the ubiquitin-proteasome system mitigates the burden of misfolded proteins by rapidly decomposing its substrates with the energy of ATP. Interestingly, the expression of proteasome subunits is stimulated by cisplatin, possibly to compensate for the inhibition of proteasomal activities by the same drug (229,230). In fact, synergistic effects of cisplatin and proteasome inhibitors have been observed in HeLa cells and bladder cancer cells, where these drugs amplify apoptotic signals by altering the concentrations of pro- and anti-apoptotic proteins (231,232). These findings support our observation that proteasomal perturbation by RNAi renders HeLa cells more susceptible to cisplatin. And we believe that our screens have likely provided valuable targets for understanding as well as optimizing the current platinum-based cancer therapies.

As expected, cell cycle progression was another prominent biological process overrepresented by this subset of candidates. We attributed this phenomenon to the overwhelming DNA damages which likely activated the corresponding cell cycle checkpoints.

In summary, although our approach to estimate cisplatin resistance by the number of remaining cells was far from perfect, it shed light on the mechanisms of cisplatin toxicity with coherent evidence from the literature. For those hits of interest, we strongly suggest reassessing their cisplatin sensitivities by detecting classic cell death markers before and after cisplatin treatment. Then, either a genetic or a pharmaceutical intervention of the selected gene can be tested for triggering cancer cell death synergistically with cisplatin. Furthermore, encouraged by our findings on the potential sensitizers of cisplatin toxicity, we are now confident to explore the other extreme – knockdown samples conferring remarkable cisplatin resistance. We believe that these endeavors are equally important to our study as finding the human polyP regulators.

4.5 Outlook

In this study, we completed a genome-wide siRNA screen for polyP regulatory genes in humans. After a pioneer validation experiment, we sorted out a few candidates of interest: *GRIN3B*, *P2RY1*, *ATP5F1E*, *PANK4*, and *AP3MI* for upregulating polyP levels. Meanwhile, we proposed a tight

connection between inositol phosphate metabolism and polyP regulation. In the follow-up experiments, we plan to use CRISPR to genetically manipulate these genes of interest and reexamine their cisplatin-induced polyP accumulation phenotypes. We believe that this work is of great importance because the discovery of genuine polyP regulators in humans will create unprecedented opportunities for characterizing the physiological functions of this polymer.

In parallel, we appreciated the potential of our screens to uncover the intracellular targets and effectors of cisplatin. Focusing on the cisplatin sensitizers, we identified a list of knockdown samples involved in nucleotide excision repair, the ubiquitin-proteasome system, and cell cycle progression. Since the current platinum-based chemotherapies are challenged by two outstanding problems: side effects and drug resistance, it might be fruitful to explore the synergistic effects of cisplatin and a cellular target to trigger cancer cell death more effectively.

4.6 Supplemental information

Supplementary Table 4.1 Candidates for genes upregulating polyP levels based on the average fluorescence intensities of mCherry-*EcPPX_c* in the nucleus

Rank ^a	Gene ID	Gene symbol ^b	Score		Score	
			(mCherry- <i>EcPPX_c</i> fluorescence intensity in the nucleus)		(Percentage of cisplatin responsive cells)	
			Mean	SD	Mean	SD
1	7884	<i>SLBP</i>	-43.43	35.38	17.67	24.84
2	50508	<i>NOX3</i>	-9.20	3.02	20.63	3.22
3	90187	<i>EMILIN3</i>	-2.03	2.10	7.63	0.82
4	1233 ^c	<i>CCR4</i>	1.70	14.12	31.57	4.59
5	51700	<i>CYB5R2</i>	1.87	9.76	21.03	3.07
6	9344	<i>TAOK2</i>	3.77	19.49	17.77	7.41
7	29952	<i>DPP7</i>	3.80	2.86	3.60	0.28
8	10215	<i>OLIG2</i>	4.80	15.61	20.97	10.67
9	6358	<i>CCL14</i>	6.83	4.24	13.67	1.37
10	146540	<i>ZNF785</i>	8.27	4.22	1.07	0.19
11	3052	<i>HCCS</i>	8.90	1.70	6.37	1.88
12	1432	<i>MAPK14</i>	9.27	7.72	4.90	3.21
13	55561	<i>CDC42BPG</i>	9.30	9.84	39.00	6.19
14	8569	<i>MKNK1</i>	10.03	9.23	15.87	6.49
15	5031	<i>P2RY6</i>	10.57	12.74	2.47	2.87
16	2296	<i>FOXC1</i>	11.67	2.82	5.30	2.08
17	646	<i>BNCI</i>	11.77	10.36	6.23	2.15
18	8452	<i>CUL3</i>	12.03	4.15	3.43	0.56
19	116444	<i>GRIN3B</i>	13.03	3.52	0.97	0.46
20	2016	<i>EMX1</i>	13.80	37.76	15.03	6.14
21	5188	<i>GATB</i>	13.90	14.37	12.00	12.16
22	10941	<i>UGT2A1</i>	14.30	3.42	5.93	3.09

^a Candidates are ranked based on the score of mCherry-*EcPPX_c* fluorescence intensity in the nucleus.

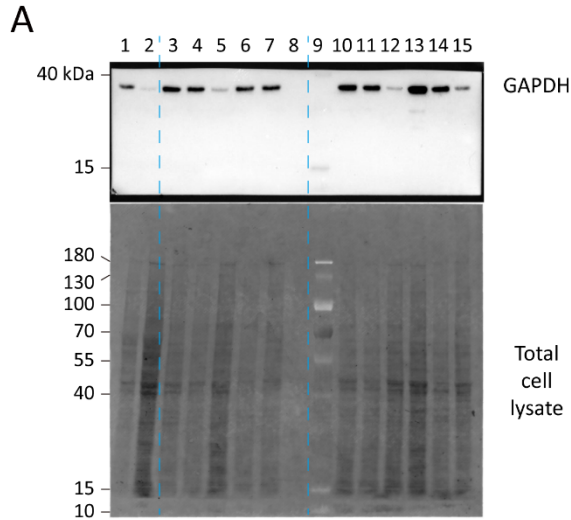
^b Official NCBI gene symbols are listed in this table for those entries with more than one commonly used gene symbols

^c Entries shadowed in gray are assigned as candidates based on their average mCherry-*EcPPX_c* fluorescence intensities in the nuclei but not the percentage of cisplatin responding cells.

Rank ^a	Gene ID	Gene symbol ^b	Score (mCherry- <i>EcPPX_c</i> fluorescence intensity in the nucleus)		Score (Percentage of cisplatin responsive cells)	
			Mean	SD	Mean	SD
23	9655	<i>SOCS5</i>	14.43	3.29	5.13	3.08
24	3617	<i>IMPG1</i>	15.27	1.39	3.67	1.27
25	22998	<i>LIMCH1</i>	15.40	7.38	5.33	1.87
26	79796	<i>ALG9</i>	15.50	1.53	9.43	6.18
27	7251	<i>TSG101</i>	16.03	6.17	13.53	0.82
28	9140	<i>ATG12</i>	16.67	4.65	18.27	4.37
29	25819	<i>NOCT</i>	17.13	3.95	3.97	1.33
30	100506658 ^d	<i>OCLN</i>	17.47	9.52	23.73	6.74
31	378832	<i>COL18A1-AS1</i>	18.23	16.31	20.70	5.20
32	337880	<i>KRTAP11-1</i>	18.37	2.22	12.20	1.77
33	7067	<i>THRA</i>	18.53	2.58	2.90	1.92
34	3761	<i>KCNJ4</i>	20.10	2.70	3.33	0.39
35	84844	<i>PHF5A</i>	20.20	6.93	12.77	5.92
36	9480	<i>ONECUT2</i>	20.33	0.94	2.70	1.31
37	2515	<i>ADAM2</i>	20.40	3.40	9.27	2.11
38	27199	<i>OXGR1</i>	20.67	3.40	14.63	1.16
39	56140	<i>PCDHA8</i>	20.70	2.50	7.97	0.74
40	57639	<i>CCDC146</i>	22.00	2.41	3.43	1.04
41	1743	<i>DLST</i>	22.43	3.07	2.17	0.78
42	55806	<i>HR</i>	22.80	4.92	11.37	1.76
43	8851	<i>CDK5R1</i>	22.90	17.26	7.17	1.07
44	2302	<i>FOXJ1</i>	23.10	1.31	9.10	1.82
45	3479	<i>IGF1</i>	23.30	2.46	7.20	4.63
46	157574	<i>FBXO16</i>	23.37	21.00	49.33	20.02
47	11185	<i>INMT</i>	23.43	3.48	4.33	1.39
48	120	<i>ADD3</i>	23.63	3.03	4.73	3.82
49	8883	<i>NAE1</i>	24.00	2.78	17.37	3.11
50	9361	<i>LONP1</i>	24.60	3.76	6.97	3.07
51	153579	<i>BTNL9</i>	24.83	3.58	16.50	4.73
52	3249	<i>HPN</i>	25.00	18.08	11.67	9.59
53	11094	<i>CACFD1</i>	25.00	3.47	11.80	3.37
54	54708	<i>MARCHF5</i>	25.03	4.29	8.17	5.76
55	1660	<i>DHX9</i>	25.20	3.98	18.07	5.38
56	6757	<i>SSX2</i>	25.30	2.57	10.10	2.12
57	81603	<i>TRIM8</i>	25.37	8.10	25.53	4.72
58	11216	<i>AKAP10</i>	25.67	7.55	50.43	7.86
59	85316	<i>BAGE5</i>	26.43	1.82	7.37	0.17
60	54496	<i>PRMT7</i>	26.57	4.11	6.50	4.82
61	5158	<i>PDE6B</i>	26.77	5.20	7.07	2.28
62	7743	<i>ZNF189</i>	26.93	2.60	16.23	1.35
63	222546	<i>RFX6</i>	27.07	3.36	20.17	6.50
64	23492	<i>CBX7</i>	27.30	9.18	55.30	24.39
65	4825	<i>NKX6-1</i>	27.43	2.71	15.33	1.73
66	2862	<i>MLNR</i>	27.73	1.05	34.90	1.43
67	339345	<i>NANOS2</i>	27.77	4.64	13.50	2.99
68	151306	<i>GPBAR1</i>	28.13	12.21	24.37	8.78
69	4879	<i>NPPB</i>	28.27	8.68	29.97	1.23
70	3748	<i>KCNC3</i>	28.43	2.53	9.23	2.95
71	7706	<i>TRIM25</i>	28.53	2.29	10.63	3.84
72	1024	<i>CDK8</i>	28.60	12.14	26.70	3.14
73	2564	<i>GABRE</i>	28.60	2.30	14.73	3.09
74	56891	<i>LGALS14</i>	28.87	18.57	26.83	25.14

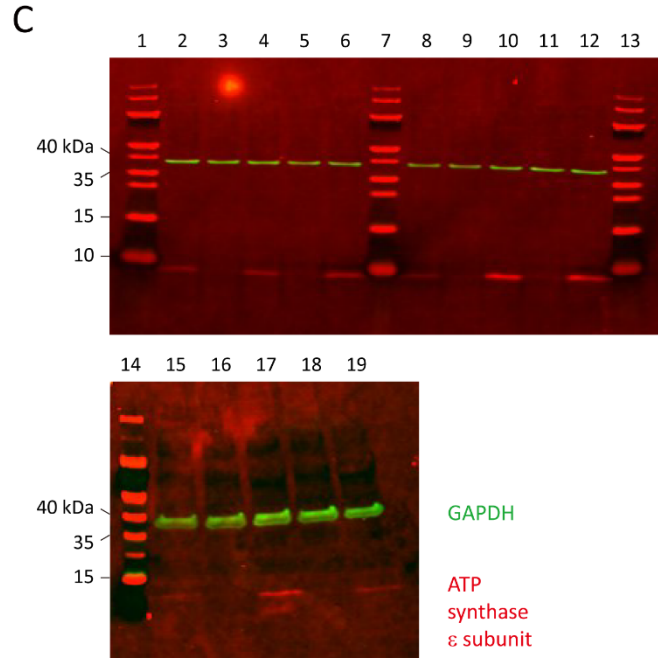
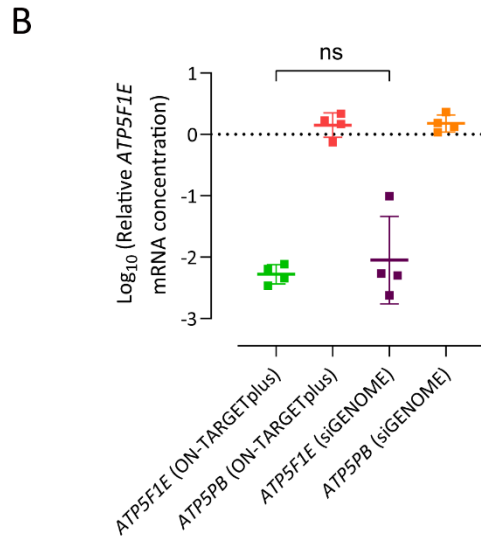
^d This entry is the replacement of *OCLN* (Gene ID: 4950) according to NCBI.

Rank ^a	Gene ID	Gene symbol ^b	Score (mCherry- <i>EcPPX_c</i> fluorescence intensity in the nucleus)		Score (Percentage of cisplatin responsive cells)	
			Mean	SD	Mean	SD
75	91683	<i>SYT12</i>	28.97	1.44	5.53	1.30
76	84073	<i>MYCBPAP</i>	29.00	3.51	15.47	0.94
77	115708	<i>TRMT61A</i>	30.07	5.12	21.60	0.73
78	64780	<i>MICAL1</i>	30.43	11.31	19.33	1.44
79	201255	<i>LRRC45</i>	30.53	1.96	163.33	7.36
80	133482	<i>SLCO6A1</i>	30.57	5.47	7.00	2.63
81	2810	<i>SFN</i>	30.67	2.66	2.23	0.74
82	84934	<i>RIT1</i>	30.77	2.35	5.30	0.86
83	285527	<i>FRYL</i>	31.17	4.91	11.07	5.86
84	390598	<i>SKOR1</i>	31.67	8.49	130.23	4.11
85	81622	<i>UNC93B1</i>	31.70	11.03	22.93	3.50
86	5973	<i>REBP</i>	31.87	14.87	16.43	10.15
87	6001	<i>RGS10</i>	32.53	4.46	15.83	6.80
88	154881	<i>KCTD7</i>	32.67	5.38	12.10	2.45
89	114789	<i>SLC25A25</i>	33.20	24.78	39.73	21.74
90	159296	<i>NKX2-3</i>	33.60	25.10	69.07	36.39
91	8520	<i>HAT1</i>	35.53	15.05	37.00	8.77
92	1612	<i>DAPK1</i>	36.23	51.09	24.90	7.86
93	5683	<i>PSMA2</i>	38.73	104.14	46.07	52.86
94	123879	<i>DCUNID3</i>	40.73	28.97	48.33	17.35
95	3705	<i>ITPK1</i>	41.40	56.80	94.33	22.08
96	143471	<i>PSMA8</i>	53.10	42.36	14.97	6.34
97	472	<i>ATM</i>	59.00	57.81	26.93	6.66
98	389118	<i>CDHR4</i>	64.40	75.12	77.43	58.67



Annotations:

- 1 - Biological replicate (A), non-targeting siRNA, 30 nM
- 2 - Biological replicate (A), *GAPDH* siRNA, 30 nM
- 3 - Biological replicate (B), siRNA buffer
- 4 - Biological replicate (B), non-targeting siRNA, 30 nM
- 5 - Biological replicate (B), *GAPDH* siRNA, 30 nM
- 6 - Biological replicate (B), siRNA buffer
- 7 - Biological replicate (B), non-targeting siRNA, 15 nM
- 8 - Biological replicate (B), *GAPDH* siRNA, 15 nM
- 9 - Protein ladder
- 10 - Biological replicate (C), siRNA buffer
- 11 - Biological replicate (C), non-targeting siRNA, 30 nM
- 12 - Biological replicate (C), *GAPDH* siRNA, 30 nM
- 13 - Biological replicate (C), siRNA buffer
- 14 - Biological replicate (C), non-targeting siRNA, 15 nM
- 15 - Biological replicate (C), *GAPDH* siRNA, 15 nM



Annotations:

- 1 - Protein ladder
- 2 - Biological replicate (A), non-targeting siRNA
- 3 - Biological replicate (A), ON-TARGETplus *ATP5F1E* siRNA
- 4 - Biological replicate (A), ON-TARGETplus *ATP5PB* siRNA
- 5 - Biological replicate (A), siGENOME *ATP5F1E* siRNA
- 6 - Biological replicate (A), siGENOME *ATP5PB* siRNA
- 7 - Protein ladder
- 8 - Biological replicate (B), non-targeting siRNA
- 9 - Biological replicate (B), ON-TARGETplus *ATP5F1E* siRNA
- 10 - Biological replicate (B), ON-TARGETplus *ATP5PB* siRNA
- 11 - Biological replicate (B), siGENOME *ATP5F1E* siRNA
- 12 - Biological replicate (B), siGENOME *ATP5PB* siRNA
- 13 - Protein ladder
- 14 - Protein ladder
- 15 - Biological replicate (C), non-targeting siRNA
- 16 - Biological replicate (C), ON-TARGETplus *ATP5F1E* siRNA
- 17 - Biological replicate (C), ON-TARGETplus *ATP5PB* siRNA
- 18 - Biological replicate (C), siGENOME *ATP5F1E* siRNA
- 19 - Biological replicate (C), siGENOME *ATP5PB* siRNA

Supplementary Figure 4.1 Assessment of the knockdown efficiencies of siGENOME and ON-TARGETplus SMARTpool® siRNAs by qRT-PCR and Western blotting analyses. (A) A dose-dependent reduction of GAPDH protein levels in HeLa cells was caused by reverse transfection with 15 and 30 nM *GAPDH* specific siRNAs but not the non-targeting siRNAs from the siGENOME SMARTpool® library. Results from three biological replicates (separated by blue dashed lines) are shown. The top panel is an overlay of the chemiluminescence signals of GAPDH antibodies and the colorimetric signals of the protein ladder. GAPDH has a molecular weight of 36 kDa. The bottom panel is a visualization of the enhanced tryptophan fluorescence of the total cell lysate. **(B)** Quantitation of *ATP5F1E* mRNA levels by qRT-PCR reported a knockdown efficiency of 99.4% and 97.2% for *ATP5F1E* specific siRNAs from the ON-TARGETplus and the siGENOME SMARTpool® libraries, respectively. In contrast, siRNAs designated for the *ATP5PB* gene which encodes subunit b of the F₀F₁-ATPase slightly increased the expression level of *ATP5F1E*. All the measurements were normalized to the *ATP5F1E* mRNA concentrations in cells treated with non-targeting siRNA. Statistical analysis of four biological replicates was performed using repeated-measures one-way ANOVA and Sidak's multiple comparisons test, which rendered the differences between the two types of *ATP5F1E* siRNAs not significant. **(C)** An efficient knockdown of the mitochondrial ATP synthase ϵ subunit was achieved by siGENOME and ON-TARGETplus SMARTpool® siRNAs targeting the *ATP5F1E* gene. Non-targeting siRNAs and *ATP5PB* siRNAs retained and slightly increased the expression levels of the ϵ subunit, respectively. These observations are consistent among three biological replicates. The ϵ subunit (7 kDa) and GAPDH (36 kDa) were detected with designated primary antibodies and secondary antibodies conjugated with IRDye® 680LT (for the ϵ subunit) and IRDye® 800CW (for GAPDH). GAPDH served as a loading control.

Bibliography

1. Xie, L. H., and Jakob, U. (2019) Inorganic polyphosphate, a multifunctional polyanionic protein scaffold. *J Biol Chem* **294**, 2180-2190
2. Brown, M. R., and Kornberg, A. (2004) Inorganic polyphosphate in the origin and survival of species. *Proc Natl Acad Sci U S A* **101**, 16085-16087
3. Widra, A. (1959) Metachromatic granules of microorganisms. *J Bacteriol* **78**, 664-670
4. Kornberg, A. (1995) Inorganic polyphosphate: toward making a forgotten polymer unforgettable. *J Bacteriol* **177**, 491-496
5. Ault-Riche, D., Fraley, C. D., Tzeng, C. M., and Kornberg, A. (1998) Novel assay reveals multiple pathways regulating stress-induced accumulations of inorganic polyphosphate in *Escherichia coli*. *Journal of Bacteriology* **180**, 1841-1847
6. Rao, N. N., Liu, S. J., and Kornberg, A. (1998) Inorganic polyphosphate in *Escherichia coli*: the phosphate regulon and the stringent response. *Journal of Bacteriology* **180**, 2186-2193
7. Ahn, K. H., and Kornberg, A. (1990) Polyphosphate Kinase from *Escherichia-Coli* - Purification and Demonstration of a Phosphoenzyme Intermediate. *J Biol Chem* **265**, 11734-11739
8. Zhang, H. Y., Ishige, K., and Kornberg, A. (2002) A polyphosphate kinase (PPK2) widely conserved in bacteria. *P Natl Acad Sci USA* **99**, 16678-16683
9. Kim, K. S., Rao, N. N., Fraley, C. D., and Kornberg, A. (2002) Inorganic polyphosphate is essential for long-term survival and virulence factors in *Shigella* and *Salmonella* spp. *P Natl Acad Sci USA* **99**, 7675-7680
10. Rao, N. N., and Kornberg, A. (1996) Polyphosphate supports resistance and survival of stationary-phase *Escherichia coli*. *Journal of Bacteriology* **178**, 1394-1400
11. Rashid, M. H., and Kornberg, A. (2000) Inorganic polyphosphate is needed for swimming, swarming, and twitching motilities of *Pseudomonas aeruginosa*. *P Natl Acad Sci USA* **97**, 4885-4890
12. Rashid, M. H., Rao, N. N., and Kornberg, A. (2000) Inorganic polyphosphate is required for motility of bacterial pathogens. *Journal of Bacteriology* **182**, 225-227
13. Rashid, M. H., Rumbaugh, K., Passador, L., Davies, D. G., Hamood, A. N., Iglewski, B. H., and Kornberg, A. (2000) Polyphosphate kinase is essential for biofilm development, quorum sensing, and virulence of *Pseudomonas aeruginosa*. *P Natl Acad Sci USA* **97**, 9636-9641
14. Shi, X. B., Rao, N. N., and Kornberg, A. (2004) Inorganic polyphosphate in *Bacillus cereus*: Motility, biofilm formation, and sporulation. *P Natl Acad Sci USA* **101**, 17061-17065
15. Abramov, A. Y., Fraley, C., Diao, C. T., Winkfein, R., Colicos, M. A., Duchon, M. R.,

- French, R. J., and Pavlov, E. (2007) Targeted polyphosphatase expression alters mitochondrial metabolism and inhibits calcium-dependent cell death. *P Natl Acad Sci USA* **104**, 18091-18096
16. Muller, F., Mutch, N. J., Schenk, W. A., Smith, S. A., Esterl, L., Spronk, H. M., Schmidbauer, S., Gahl, W. A., Morrissey, J. H., and Renne, T. (2009) Platelet Polyphosphates Are Proinflammatory and Procoagulant Mediators In Vivo. *Cell* **139**, 1143-1156
 17. Omelon, S., Georgiou, J., Henneman, Z. J., Wise, L. M., Sukhu, B., Hunt, T., Wynnyckyj, C., Holmyard, D., Bielecki, R., and Grynblas, M. D. (2009) Control of Vertebrate Skeletal Mineralization by Polyphosphates. *Plos One* **4**
 18. Wang, L. H., Fraley, C. D., Faridi, J., Kornberg, A., and Roth, R. A. (2003) Inorganic polyphosphate stimulates mammalian TOR, a kinase involved in the proliferation of mammary cancer cells. *P Natl Acad Sci USA* **100**, 11249-11254
 19. Ishige, K., Zhang, H. Y., and Arthur, K. (2002) Polyphosphate kinase (PPK2), a potent, polyphosphate-driven generator of GTP. *P Natl Acad Sci USA* **99**, 16684-16688
 20. Nocek, B., Kochinyan, S., Proudfoot, M., Brown, G., Evcokimova, E., Osipiuk, J., Edwards, A. M., Savchenko, A., Joachimiak, A., and Yakunin, A. F. (2008) Polyphosphate-dependent synthesis of ATP and ADP by the family-2 polyphosphate kinases in bacteria. *P Natl Acad Sci USA* **105**, 17730-17735
 21. Akiyama, M., Crooke, E., and Kornberg, A. (1993) An Exopolyphosphatase of Escherichia-Coli - the Enzyme and Its Ppx Gene in a Polyphosphate Operon. *J Biol Chem* **268**, 633-639
 22. Rudat, A. K., Pokhrel, A., Green, T. J., and Gray, M. J. (2018) Mutations in Escherichia coli Polyphosphate Kinase That Lead to Dramatically Increased In Vivo Polyphosphate Levels. *Journal of Bacteriology* **200**
 23. Shiba, T., Tsutsumi, K., Yano, H., Ihara, Y., Kameda, A., Tanaka, K., Takahashi, H., Munekata, M., Rao, N. N., and Kornberg, A. (1997) Inorganic polyphosphate and the induction of rpoS expression. *P Natl Acad Sci USA* **94**, 11210-11215
 24. Mullan, A., Quinn, J. P., and McGrath, J. W. (2002) Enhanced phosphate uptake and polyphosphate accumulation in Burkholderia cepacia grown under low-pH conditions. *Microb Ecol* **44**, 69-77
 25. Gray, M. J., Wholey, W. Y., Wagner, N. O., Cremers, C. M., Mueller-Schickert, A., Hock, N. T., Krieger, A. G., Smith, E. M., Bender, R. A., Bardwell, J. C. A., and Jakob, U. (2014) Polyphosphate Is a Primordial Chaperone. *Mol Cell* **53**, 689-699
 26. Yoo, N. G., Dogra, S., Meinen, B. A., Tse, E., Haefliger, J., Southworth, D. R., Gray, M. J., Dahl, J. U., and Jakob, U. (2018) Polyphosphate Stabilizes Protein Unfolding Intermediates as Soluble Amyloid-like Oligomers. *J Mol Biol* **430**, 4195-4208
 27. Crooke, E., Akiyama, M., Rao, N. N., and Kornberg, A. (1994) Genetically Altered Levels of Inorganic Polyphosphate in Escherichia-Coli. *J Biol Chem* **269**, 6290-6295
 28. Dahl, J. U., Gray, M. J., Bazopoulou, D., Beaufay, F., Lempart, J., Koenigsnecht, M. J., Wang, Y., Baker, J. R., Hasler, W. L., Young, V. B., Sun, D. X., and Jakob, U. (2017) The

- anti-inflammatory drug mesalamine targets bacterial polyphosphate accumulation. *Nat Microbiol* **2**
29. Groitl, B., Dahl, J. U., Schroeder, J. W., and Jakob, U. (2017) *Pseudomonas aeruginosa* defense systems against microbicidal oxidants. *Mol Microbiol* **106**, 335-350
 30. Fraley, C. D., Rashid, M. H., Lee, S. S. K., Gottschalk, R., Harrison, J., Wood, P. J., Brown, M. R. W., and Kornberg, A. (2007) A polyphosphate kinase 1 (ppk1) mutant of *Pseudomonas aeruginosa* exhibits multiple ultrastructural and functional defects. *P Natl Acad Sci USA* **104**, 3526-3531
 31. Maciag, A., Peano, C., Pietrelli, A., Egli, T., De Bellis, G., and Landini, P. (2011) In vitro transcription profiling of the Sigma(S) subunit of bacterial RNA polymerase: re-definition of the Sigma(S) regulon and identification of Sigma(S)-specific promoter sequence elements. *Nucleic Acids Res* **39**, 5338-5355
 32. Kusano, S., and Ishihama, A. (1997) Functional interaction of *Escherichia coli* RNA polymerase with inorganic polyphosphate. *Genes Cells* **2**, 433-441
 33. Silby, M. W., Nicoll, J. S., and Levy, S. B. (2012) Regulation of Polyphosphate Kinase Production by Antisense RNA in *Pseudomonas fluorescens* Pf0-1. *Appl Environ Microb* **78**, 4533-4537
 34. Gray, M. J., Wholey, W. Y., Parker, B. W., Kim, M., and Jakob, U. (2013) NemR Is a Bleach-sensing Transcription Factor. *J Biol Chem* **288**, 13789-13798
 35. Wang, S. Y., Deng, K. P., Zaremba, S., Deng, X. Y., Lin, C. H., Wang, Q., Tortorello, M. L., and Zhang, W. (2009) Transcriptomic Response of *Escherichia coli* O157:H7 to Oxidative Stress. *Appl Environ Microb* **75**, 6110-6123
 36. Kumble, K. D., and Kornberg, A. (1995) Inorganic Polyphosphate in Mammalian-Cells and Tissues. *J Biol Chem* **270**, 5818-5822
 37. Aschar-Sobbi, R., Abramov, A. Y., Diao, C., Kargacin, M. E., Kargacin, G. J., French, R. J., and Pavlov, E. (2008) High sensitivity, quantitative measurements of polyphosphate using a new DAPI-Based approach. *J Fluoresc* **18**, 859-866
 38. Jimenez-Nunez, M. D., Moreno-Sanchez, D., Hernandez-Ruiz, L., Benitez-Rondan, A., Ramos-Amaya, A., Rodriguez-Bayona, B., Medina, F., Brieva, J. A., and Ruiz, F. A. (2012) Myeloma cells contain high levels of inorganic polyphosphate which is associated with nucleolar transcription. *Haematol-Hematol J* **97**, 1264-1271
 39. Moreno-Sanchez, D., Hernandez-Ruiz, L., Ruiz, F. A., and Docampo, R. (2012) Polyphosphate Is a Novel Pro-inflammatory Regulator of Mast Cells and Is Located in Acidocalcisomes. *J Biol Chem* **287**, 28435-28444
 40. Angelova, P. R., Agrawalla, B. K., Elustondo, P. A., Gordon, J., Shiba, T., Abramov, A. Y., Chang, Y. T., and Pavlov, E. V. (2014) In Situ Investigation of Mammalian Inorganic Polyphosphate Localization Using Novel Selective Fluorescent Probes JC-D7 and JC-D8. *Acs Chem Biol* **9**, 2101-2110
 41. Angelova, P. R., Iversen, K. Z., Teschemacher, A. G., Kasparov, S., Gourine, A. V., and Abramov, A. Y. (2018) Signal transduction in astrocytes: Localization and release of inorganic polyphosphate. *Glia* **66**, 2126-2136

42. Holmstrom, K. M., Marina, N., Baev, A. Y., Wood, N. W., Gourine, A. V., and Abramov, A. Y. (2013) Signalling properties of inorganic polyphosphate in the mammalian brain. *Nat Commun* **4**
43. Belozersky, A. N., and Kulaev, I. S. (1970) The polyphosphate-ribonucleic acid complexes in yeasts (in Russian). *Biokhimiya i Fiziologiya Bol'nogo i Z.dorovogo Rasteniya (The Biochemistry and Physiology of Diseased and Healthy Plants)*, Izdatelstvo, MGU, Moscow, p.42
44. Stahl, A. J. C., and Ebel, J. P. (1963) Etude des complexes entre acides ribonucleiques el polyphosphates inorganiques dans le levure. III. Role des cations divalents dans la formation des complexes. *Bull. Soc. Chim. Biol.*, 887-1001
45. Blum, E., Py, B., Carpousis, A. J., and Higgins, C. F. (1997) Polyphosphate kinase is a component of the Escherichia coli RNA degradosome. *Mol Microbiol* **26**, 387-398
46. Vaillancourt, S., Beaucheminnewhouse, N., and Cedergren, R. J. (1978) Polyphosphate-Deficient Mutants of Anacystis-Nidulans. *Can J Microbiol* **24**, 112-116
47. Azevedo, C., Livermore, T., and Saiardi, A. (2015) Protein Polyphosphorylation of Lysine Residues by Inorganic Polyphosphate. *Mol Cell* **58**, 71-82
48. Bentley-DeSousa, A., Holinier, C., Moteshareie, H., Tseng, Y. C., Kajjo, S., Nwosu, C., Amodeo, G. F., Bondy-Chorney, E., Sai, Y., Rudner, A., Golshani, A., Davey, N. E., and Downey, M. (2018) A Screen for Candidate Targets of Lysine Polyphosphorylation Uncovers a Conserved Network Implicated in Ribosome Biogenesis. *Cell Rep* **22**, 3427-3439
49. Lorenzo-Orts, L., Hohmann, U., Zhu, J. S., and Hothorn, M. (2019) Molecular characterization of CHAD domains as inorganic polyphosphate-binding modules. *Life Sci Alliance* **2**
50. Negreiros, R. S., Lander, N., Huang, G. Z., Cordeiro, C. D., Smith, S. A., Morrissey, J. H., and Docampo, R. (2018) Inorganic polyphosphate interacts with nucleolar and glycosomal proteins in trypanosomatids. *Mol Microbiol* **110**, 973-994
51. Reusch, R. N., and Sadoff, H. L. (1988) Putative Structure and Functions of a Poly-Beta-Hydroxybutyrate Calcium Polyphosphate Channel in Bacterial Plasma-Membranes. *P Natl Acad Sci USA* **85**, 4176-4180
52. Reusch, R. N. (1999) Streptomyces lividans potassium channel contains poly-(R)-3-hydroxybutyrate and inorganic polyphosphate. *Biochemistry* **38**, 15666-15672
53. Zakharian, E., Thyagarajan, B., French, R. J., Pavlov, E., and Rohacs, T. (2009) Inorganic Polyphosphate Modulates TRPM8 Channels. *Plos One* **4**
54. Reusch, R. N., Huang, R. P., and KoskKosicka, D. (1997) Novel components and enzymatic activities of the human erythrocyte plasma membrane calcium pump. *Febs Lett* **412**, 592-596
55. Pavlov, E., Zakharian, E., Bladen, C., Diao, C. T. M., Grimbly, C., Reusch, R. N., and French, R. J. (2005) A large, voltage-dependent channel, isolated from mitochondria by water- free chloroform extraction. *Biophys J* **88**, 2614-2625

56. Reusch, R. N. (1989) Poly-Beta-Hydroxybutyrate Calcium Polyphosphate Complexes in Eukaryotic Membranes. *P Soc Exp Biol Med* **191**, 377-381
57. Alavian, K. N., Beutner, G., Lazrove, E., Sacchetti, S., Park, H. A., Licznanski, P., Li, H. M., Nabili, P., Hockensmith, K., Graham, M., Porter, G. A., and Jonas, E. A. (2014) An uncoupling channel within the c-subunit ring of the F1FO ATP synthase is the mitochondrial permeability transition pore. *P Natl Acad Sci USA* **111**, 10580-10585
58. Bonora, M., Bononi, A., De Marchi, E., Giorgi, C., Lebiedzinska, M., Marchi, S., Patergnani, S., Rimessi, A., Suski, J. M., Wojtala, A., Wieckowski, M. R., Kroemer, G., Galluzzi, L., and Pinton, P. (2013) Role of the c subunit of the F-O ATP synthase in mitochondrial permeability transition. *Cell Cycle* **12**, 674-683
59. Giorgio, V., von Stockum, S., Antoniel, M., Fabbro, A., Fogolari, F., Forte, M., Glick, G. D., Petronilli, V., Zoratti, M., Szabo, I., Lippe, G., and Bernardi, P. (2013) Dimers of mitochondrial ATP synthase form the permeability transition pore. *P Natl Acad Sci USA* **110**, 5887-5892
60. Seidlmayer, L. K., Gomez-Garcia, M. R., Blatter, L. A., Pavlov, E., and Dedkova, E. N. (2012) Inorganic polyphosphate is a potent activator of the mitochondrial permeability transition pore in cardiac myocytes. *J Gen Physiol* **139**, 321-331
61. Solesio, M. E., Xie, L., Ellenberger, M., Mitaishvili, E., Bhadra-Lobo, S., Bettcher, L. F., Bazil, J. N., Raftery, D., Jakob, U., and Pavlov, E. (2020) Depletion of mitochondrial inorganic polyphosphate causes metabolic shift from OXPHOS to glycolysis. *Manuscript submitted for publication*
62. Ogawa, N., DeRisi, J., and Brown, P. O. (2000) New components of a system for phosphate accumulation and polyphosphate metabolism in *Saccharomyces cerevisiae* revealed by genomic expression analysis. *Mol Biol Cell* **11**, 4309-4321
63. Hothorn, M., Neumann, H., Lenherr, E. D., Wehner, M., Rybin, V., Hassa, P. O., Uttenweiler, A., Reinhardt, M., Schmidt, A., Seiler, J., Ladurner, A. G., Herrmann, C., Scheffzek, K., and Mayer, A. (2009) Catalytic Core of a Membrane-Associated Eukaryotic Polyphosphate Polymerase. *Science* **324**, 513-516
64. Bru, S., Martinez-Lainez, J. M., Hernandez-Ortega, S., Quandt, E., Torres-Torronteras, J., Marti, R., Canadell, D., Arino, J., Sharma, S., Jimenez, J., and Clotet, J. (2016) Polyphosphate is involved in cell cycle progression and genomic stability in *Saccharomyces cerevisiae*. *Mol Microbiol* **101**, 367-380
65. Andreeva, N., Ryazanova, L., Dmitriev, V., Kulakovskaya, T., and Kulaev, I. (2013) Adaptation of *Saccharomyces cerevisiae* to toxic manganese concentration triggers changes in inorganic polyphosphates. *Fems Yeast Res* **13**, 463-470
66. Trilisenko, L., Kulakovskaya, E., and Kulakovskaya, T. (2017) The cadmium tolerance in *Saccharomyces cerevisiae* depends on inorganic polyphosphate. *J Basic Microb* **57**, 982-986
67. Durr, M., Urech, K., Boller, T., Wiemken, A., Schwencke, J., and Nagy, M. (1979) Sequestration of Arginine by Polyphosphate in Vacuoles of Yeast (*Saccharomyces Cerevisiae*). *Arch Microbiol* **121**, 169-175

68. Gerasimaite, R., Sharma, S., Desfougeres, Y., Schmidt, A., and Mayer, A. (2014) Coupled synthesis and translocation restrains polyphosphate to acidocalcisome-like vacuoles and prevents its toxicity. *J Cell Sci* **127**, 5093-5104
69. Pisoni, R. L., and Lindley, E. R. (1992) Incorporation of [P-32] Orthophosphate into Long Chains of Inorganic Polyphosphate within Lysosomes of Human Fibroblasts. *J Biol Chem* **267**, 3626-3631
70. Gomes, F. M., Carvalho, D. B., Peron, A. C., Saito, K., Miranda, K., and Machado, E. A. (2012) Inorganic polyphosphates are stored in spherites within the midgut of *Anticarsia gemmatalis* and play a role in copper detoxification. *J Insect Physiol* **58**, 211-219
71. Ruiz, F. A., Lea, C. R., Oldfield, E., and Docampo, R. (2004) Human platelet dense granules contain polyphosphate and are similar to acidocalcisomes of bacteria and unicellular eukaryotes. *J Biol Chem* **279**, 44250-44257
72. Vickerman, K., and Tetley, L. (1977) Recent Ultrastructural Studies on Trypanosomes. *Ann Soc Belg Med Tr* **57**, 441-457
73. Docampo, R., de Souza, W., Miranda, K., Rohloff, P., and Moreno, S. N. J. (2005) Acidocalcisomes - Conserved from bacteria to man. *Nat Rev Microbiol* **3**, 251-261
74. Vercesi, A. E., Moreno, S. N. J., and Docampo, R. (1994) Ca²⁺/H⁺ Exchange in Acidic Vacuoles of *Trypanosoma-Brucei*. *Biochem J* **304**, 227-233
75. Scott, D. A., Docampo, R., Dvorak, J. A., Shi, S. L., and Leapman, R. D. (1997) In situ compositional analysis of acidocalcisomes in *Trypanosoma cruzi*. *J Biol Chem* **272**, 28020-28029
76. Bae, J. S., Lee, W., and Rezaie, A. R. (2012) Polyphosphate elicits pro-inflammatory responses that are counteracted by activated protein C in both cellular and animal models. *J Thromb Haemost* **10**, 1145-1151
77. Dinarvand, P., Hassanian, S. M., Qureshi, S. H., Manithody, C., Eissenberg, J. C., Yang, L. K., and Rezaie, A. R. (2014) Polyphosphate amplifies proinflammatory responses of nuclear proteins through interaction with receptor for advanced glycation end products and P2Y(1) purinergic receptor. *Blood* **123**, 935-945
78. Hassanian, S. M., Dinarvand, P., Smith, S. A., and Rezaie, A. R. (2015) Inorganic polyphosphate elicits pro-inflammatory responses through activation of the mammalian target of rapamycin complexes 1 and 2 in vascular endothelial cells. *J Thromb Haemost* **13**, 860-871
79. Smith, S. A., Choi, S. H., Davis-Harrison, R., Huyck, J., Boettcher, J., Reinstra, C. M., and Morrissey, J. H. (2010) Polyphosphate exerts differential effects on blood clotting, depending on polymer size. *Blood* **116**, 4353-4359
80. Stotz, S. C., Scott, L. O. M., Drummond-Main, C., Avchalumov, Y., Giroto, F., Davidsen, J., Gomez-Garcia, M. R., Rho, J. M., Pavlov, E. V., and Colicos, M. A. (2014) Inorganic polyphosphate regulates neuronal excitability through modulation of voltage-gated channels. *Mol Brain* **7**
81. Li, L. N., Khong, M. L., Lui, E. L. H., Mebarek, S., Magne, D., Buchet, R., and Tanner, J. A. (2019) Long-chain polyphosphate in osteoblast matrix vesicles: Enrichment and

- inhibition of mineralization. *Bba-Gen Subjects* **1863**, 199-209
82. Muller, W. E. G., Wang, X. H., Diehl-Seifert, B., Kropf, K., Schlossmacher, U., Lieberwirth, I., Glasser, G., Wiens, M., and Schroder, H. C. (2011) Inorganic polymeric phosphate/polyphosphate as an inducer of alkaline phosphatase and a modulator of intracellular Ca²⁺ level in osteoblasts (SaOS-2 cells) in vitro. *Acta Biomater* **7**, 2661-2671
 83. Keasling, J. D., and Hupf, G. A. (1996) Genetic manipulation of polyphosphate metabolism affects cadmium tolerance in Escherichia coli. *Appl Environ Microb* **62**, 743-746
 84. Cremers, C. M., Knoefler, D., Gates, S., Martin, N., Dahl, J. U., Lempart, J., Xie, L. H., Chapman, M. R., Galvan, V., Southworth, D. R., and Jakob, U. (2016) Polyphosphate: A Conserved Modifier of Amyloidogenic Processes. *Mol Cell* **63**, 768-780
 85. Harms, A., Fino, C., Sorensen, M. A., Semsey, S., and Gerdes, K. (2017) Prophages and Growth Dynamics Confound Experimental Results with Antibiotic-Tolerant Persister Cells. *Mbio* **8**
 86. McInerney, P., Mizutani, T., and Shiba, T. (2006) Inorganic polyphosphate interacts with ribosomes and promotes translation fidelity in vitro and in vivo. *Mol Microbiol* **60**, 438-447
 87. Pavlov, E., Grimbley, C., Diao, C. T. M., and French, R. J. (2005) A high-conductance mode of a poly-3-hydroxybutyrate/calcium/polyphosphate channel isolated from competent Escherichia coli cells. *Febs Lett* **579**, 5187-5192
 88. Bru, S., Samper-Martin, B., Quandt, E., Hernandez-Ortega, S., Martinez-Lainez, J. M., Gari, E., Rafel, M., Torres-Torronteras, J., Marti, R., Ribeiro, M. P. C., Jimenez, J., and Clotet, J. (2017) Polyphosphate is a key factor for cell survival after DNA damage in eukaryotic cells. *DNA Repair* **57**, 171-178
 89. Livermore, T. M., Chubb, J. R., and Saiardi, A. (2016) Developmental accumulation of inorganic polyphosphate affects germination and energetic metabolism in Dictyostelium discoideum. *P Natl Acad Sci USA* **113**, 996-1001
 90. Zhang, H. Y., Gomez-Garcia, M. R., Brown, M. R. W., and Kornberg, A. (2005) Inorganic polyphosphate in Dictyostelium discoideum: Influence on development, sporulation, and predation. *P Natl Acad Sci USA* **102**, 2731-2735
 91. Zhang, H. Y., Gomez-Garcia, M. R., Shi, X. B., Rao, N. N., and Kornberg, A. (2007) Polyphosphate kinase 1, a conserved bacterial enzyme, in a eukaryote, Dictyostelium discoideum with a role in cytokinesis. *P Natl Acad Sci USA* **104**, 16486-16491
 92. Fang, J. M., Rohloff, P., Miranda, K., and Docampo, R. (2007) Ablation of a small transmembrane protein of Trypanosoma brucei (TbVTC1) involved in the synthesis of polyphosphate alters acidocalcisome biogenesis and function, and leads to a cytokinesis defect. *Biochem J* **407**, 161-170
 93. Galizzi, M., Bustamante, J. M., Fang, J. M., Miranda, K., Medeiros, L. C. S., Tarleton, R. L., and Docampo, R. (2013) Evidence for the role of vacuolar soluble pyrophosphatase and inorganic polyphosphate in Trypanosoma cruzi persistence. *Mol Microbiol* **90**, 699-715
 94. Ruiz, F. A., Rodrigues, C. O., and Docampo, R. (2001) Rapid changes in polyphosphate content within acidocalcisomes in response to cell growth, differentiation, and

- environmental stress in *Trypanosoma cruzi*. *J Biol Chem* **276**, 26114-26121
95. Lander, N., Ulrich, P. N., and Docampo, R. (2013) *Trypanosoma brucei* Vacuolar Transporter Chaperone 4 (TbVtc4) Is an Acidocalcisome Polyphosphate Kinase Required for in Vivo Infection. *J Biol Chem* **288**, 34205-34216
 96. Kim, D., and Cavanaugh, E. J. (2007) Requirement of a soluble intracellular factor for activation of transient receptor potential A1 by pungent chemicals: Role of inorganic polyphosphates. *J Neurosci* **27**, 6500-6509
 97. Segawa, S., Fujiya, M., Konishi, H., Ueno, N., Kobayashi, N., Shigyo, T., and Kohgo, Y. (2011) Probiotic-Derived Polyphosphate Enhances the Epithelial Barrier Function and Maintains Intestinal Homeostasis through Integrin-p38 MAPK Pathway. *Plos One* **6**
 98. Shiba, T., Nishimura, D., Kawazoe, Y., Onodera, Y., Tsutsumi, K., Nakamura, R., and Ohshiro, M. (2003) Modulation of mitogenic activity of fibroblast growth factors by inorganic polyphosphate. *J Biol Chem* **278**, 26788-26792
 99. Gabel, N. W., and Thomas, V. (1971) Evidence for the occurrence and distribution of inorganic polyphosphates in vertebrate tissues. *J Neurochem* **18**, 1229-1242
 100. Lorenz, B., Munkner, J., Oliveira, M. P., Kuusksalu, A., Leitao, J. M., Muller, W. E. G., and Schroder, H. C. (1997) Changes in metabolism of inorganic polyphosphate in rat tissues and human cells during development and apoptosis. *Bba-Gen Subjects* **1335**, 51-60
 101. Baker, C. J., Smith, S. A., and Morrissey, J. H. (2019) Polyphosphate in thrombosis, hemostasis, and inflammation. *Res Pract Thromb Hae* **3**, 18-25
 102. Gray, M. J., and Jakob, U. (2015) Oxidative stress protection by polyphosphate - new roles for an old player. *Curr Opin Microbiol* **24**, 1-6
 103. Kulakovskaya, E. V., Zemskova, M. Y., and Kulakovskaya, T. V. (2018) Inorganic Polyphosphate and Cancer. *Biochemistry-Moscow+* **83**, 961-968
 104. Lempart, J., and Jakob, U. (2019) Role of Polyphosphate in Amyloidogenic Processes. *Csh Perspect Biol* **11**
 105. Rao, N. N., Gomez-Garcia, M. R., and Kornberg, A. (2009) Inorganic Polyphosphate: Essential for Growth and Survival. *Annu Rev Biochem* **78**, 605-647
 106. Lempart, J., Tse, E., Lauer, J. A., Ivanova, M. I., Sutter, A., Yoo, N., Huettemann, P., Southworth, D., and Jakob, U. (2019) Mechanistic insights into the protective roles of polyphosphate against amyloid cytotoxicity. *Life Sci Alliance* **2**
 107. Wickramasinghe, S. P., Lempart, J., Merens, H. E., Murphy, J., Huettemann, P., Jakob, U., and Rhoades, E. (2019) Polyphosphate Initiates Tau Aggregation through Intra- and Intermolecular Scaffolding. *Biophys J* **117**, 717-728
 108. Wang, L., Yan, J. W., Wise, M. J., Liu, Q. H., Asenso, J., Huang, Y., Dai, S. Y., Liu, Z. Z., Du, Y., and Tang, D. Q. (2018) Distribution Patterns of Polyphosphate Metabolism Pathway and Its Relationships With Bacterial Durability and Virulence. *Front Microbiol* **9**
 109. Akiyama, M., Crooke, E., and Kornberg, A. (1992) The polyphosphate kinase gene of *Escherichia coli*. Isolation and sequence of the ppk gene and membrane location of the protein. *J Biol Chem* **267**, 22556-22561

110. Whitehead, M. P., Eagles, L., Hooley, P., and Brown, M. R. W. (2014) Most bacteria synthesize polyphosphate by unknown mechanisms. *Microbiol-Sgm* **160**, 829-831
111. Whitehead, M. P., Hooley, P., and MR, W. B. (2013) Horizontal transfer of bacterial polyphosphate kinases to eukaryotes: implications for the ice age and land colonisation. *BMC Res Notes* **6**, 221
112. Zhu, Y., Huang, W. J., Lee, S. S. K., and Xu, W. Q. (2005) Crystal structure of a polyphosphate kinase and its implications for polyphosphate synthesis. *Embo Rep* **6**, 681-687
113. Jenkins, G. M., and Frohman, M. A. (2005) Phospholipase D: a lipid centric review. *Cell Mol Life Sci* **62**, 2305-2316
114. Gomez-Garcia, M. R., and Kornberg, A. (2004) Formation of an actin-like filament concurrent with the enzymatic synthesis of inorganic polyphosphate. *P Natl Acad Sci USA* **101**, 15876-15880
115. Pavlov, E., Aschar-Sobbi, R., Campanella, M., Turner, R. J., Gomez-Garcia, M. R., and Abramov, A. Y. (2010) Inorganic Polyphosphate and Energy Metabolism in Mammalian Cells. *J Biol Chem* **285**, 9420-9428
116. Baev, A. Y., Angelova, P. R., and Abramov, A. Y. (2020) Inorganic polyphosphate is produced and hydrolyzed in F0F1-ATP synthase of mammalian mitochondria. *Biochem J* **477**, 1515-1524
117. Draskovic, P., Saiardi, A., Bhandari, R., Burton, A., Ilc, G., Kovacevic, M., Snyder, S. H., and Podobnik, M. (2008) Inositol hexakisphosphate kinase products contain diphosphate and triphosphate groups. *Chem Biol* **15**, 274-286
118. Fridy, P. C., Otto, J. C., Dollins, D. E., and York, J. D. (2007) Cloning and characterization of two human VIP1-like inositol hexakisphosphate and diphosphoinositol pentakisphosphate kinases. *J Biol Chem* **282**, 30754-30762
119. Chakraborty, A. (2018) The inositol pyrophosphate pathway in health and diseases. *Biol Rev* **93**, 1203-1227
120. Cordeiro, C. D., Saiardi, A., and Docampo, R. (2017) The inositol pyrophosphate synthesis pathway in *Trypanosoma brucei* is linked to polyphosphate synthesis in acidocalcisomes. *Mol Microbiol* **106**, 319-333
121. Ghosh, S., Shukla, D., Suman, K., Lakshmi, B. J., Manorama, R., Kumar, S., and Bhandari, R. (2013) Inositol hexakisphosphate kinase 1 maintains hemostasis in mice by regulating platelet polyphosphate levels. *Blood* **122**, 1478-1486
122. Hou, Q. M., Liu, F., Chakraborty, A., Jia, Y. H., Prasad, A., Yu, H. B., Zhao, L., Ye, K. Q., Snyder, S. H., Xu, Y. F., and Luo, H. B. R. (2018) Inhibition of IP6K1 suppresses neutrophil-mediated pulmonary damage in bacterial pneumonia. *Sci Transl Med* **10**
123. Lonetti, A., Szijgyarto, Z., Bosch, D., Loss, O., Azevedo, C., and Saiardi, A. (2011) Identification of an Evolutionarily Conserved Family of Inorganic Polyphosphate Endopolyphosphatases. *J Biol Chem* **286**, 31966-31974
124. Gerasimaite, R., Pavlovic, I., Capolicchio, S., Hofer, A., Schmidt, A., Jessen, H. J., and

- Mayer, A. (2017) Inositol Pyrophosphate Specificity of the SPX-Dependent Polyphosphate Polymerase VTC. *Acs Chem Biol* **12**, 648-653
125. Wild, R., Gerasimaite, R., Jung, J. Y., Truffault, V., Pavlovic, I., Schmidt, A., Saiardi, A., Jessen, H. J., Poirier, Y., Hothorn, M., and Mayer, A. (2016) Control of eukaryotic phosphate homeostasis by inositol polyphosphate sensor domains. *Science* **352**, 986-990
 126. Kulaev, I. S. (1994) Inorganic Polyphosphate Functions at Various Stages of Cell Evolution. *J Biol Phys* **20**, 255-273
 127. Xie, L. H., Rajpurkar, A., Quarles, E., Taube, N., Rai, A. S., Erba, J., Sliwinski, B., Markowitz, M., Jakob, U., and Knoefler, D. (2019) Accumulation of Nucleolar Inorganic Polyphosphate Is a Cellular Response to Cisplatin-Induced Apoptosis. *Front Oncol* **9**
 128. Siegel, R. L., Miller, K. D., and Jemal, A. (2018) Cancer statistics, 2018. *CA Cancer J Clin* **68**, 7-30
 129. Dasari, S., and Tchounwou, P. B. (2014) Cisplatin in cancer therapy: molecular mechanisms of action. *Eur J Pharmacol* **740**, 364-378
 130. Travis, L. B., Fossa, S. D., Sesso, H. D., Frisina, R. D., Herrmann, D. N., Beard, C. J., Feldman, D. R., Pagliaro, L. C., Miller, R. C., Vaughn, D. J., Einhorn, L. H., Cox, N. J., Dolan, M. E., and Platinum Study, G. (2014) Chemotherapy-induced peripheral neurotoxicity and ototoxicity: new paradigms for translational genomics. *J Natl Cancer Inst* **106**
 131. Galluzzi, L., Senovilla, L., Vitale, I., Michels, J., Martins, I., Kepp, O., Castedo, M., and Kroemer, G. (2012) Molecular mechanisms of cisplatin resistance. *Oncogene* **31**, 1869-1883
 132. Prestayko, A. W., D'Aoust, J. C., Issell, B. F., and Crooke, S. T. (1979) Cisplatin (cis-diamminedichloroplatinum II). *Cancer Treat Rev* **6**, 17-39
 133. Perez, R. P. (1998) Cellular and molecular determinants of cisplatin resistance. *Eur J Cancer* **34**, 1535-1542
 134. Reedijk, J., and Lohman, P. H. (1985) Cisplatin: synthesis, antitumour activity and mechanism of action. *Pharm Weekbl Sci* **7**, 173-180
 135. Siddik, Z. H. (2003) Cisplatin: mode of cytotoxic action and molecular basis of resistance. *Oncogene* **22**, 7265-7279
 136. Mandic, A., Hansson, J., Linder, S., and Shoshan, M. C. (2003) Cisplatin induces endoplasmic reticulum stress and nucleus-independent apoptotic signaling. *J Biol Chem* **278**, 9100-9106
 137. Marullo, R., Werner, E., Degtyareva, N., Moore, B., Altavilla, G., Ramalingam, S. S., and Doetsch, P. W. (2013) Cisplatin Induces a Mitochondrial-ROS Response That Contributes to Cytotoxicity Depending on Mitochondrial Redox Status and Bioenergetic Functions. *Plos One* **8**
 138. Messori, L., and Merlino, A. (2016) Cisplatin binding to proteins: A structural perspective. *Coordin Chem Rev* **315**, 67-89
 139. Shoeib, T., and Sharp, B. L. (2013) Monomeric cisplatin complexes with glutathione:

- Coordination modes and binding affinities. *Inorg Chim Acta* **405**, 258-264
140. Yang, Z. J., Schumaker, L. M., Egorin, M. J., Zuhowski, E. G., Guo, Z. M., and Cullen, K. J. (2006) Cisplatin preferentially binds mitochondrial DNA and voltage-dependent anion channel protein in the mitochondrial membrane of head and neck squamous cell carcinoma: Possible role in apoptosis. *Clin Cancer Res* **12**, 5817-5825
 141. Han, K. Y., Hong, B. S., Yoon, Y. J., Yoon, C. M., Kim, Y. K., Kwon, Y. G., and Gho, Y. S. (2007) Polyphosphate blocks tumour metastasis via anti-angiogenic activity. *Biochem J* **406**, 49-55
 142. Hernandez-Ruiz, L., Gonzalez-Garcia, I., Castro, C., Brieva, J. A., and Ruiz, F. A. (2006) Inorganic polyphosphate and specific induction of apoptosis in human plasma cells. *Haematologica* **91**, 1180-1186
 143. Tammenkoski, M., Koivula, K., Cusanelli, E., Zollo, M., Steegborn, C., Baykov, A. A., and Lahti, R. (2008) Human metastasis regulator protein H-prune is a short-chain exopolyphosphatase. *Biochemistry* **47**, 9707-9713
 144. Werner, T. P., Amrhein, N., and Freimoser, F. M. (2007) Specific localization of inorganic polyphosphate (poly P) in fungal cell walls by selective extraction and immunohistochemistry. *Fungal Genet Biol* **44**, 845-852
 145. Weidenfeld, I., Gossen, M., Low, R., Kentner, D., Berger, S., Gorlich, D., Bartsch, D., Bujard, H., and Schoinig, K. (2009) Inducible expression of coding and inhibitory RNAs from retargetable genomic loci. *Nucleic Acids Res* **37**
 146. Oleson, B. J., Broniowska, K. A., Naatz, A., Hogg, N., Tarakanova, V. L., and Corbett, J. A. (2016) Nitric Oxide Suppresses beta-Cell Apoptosis by Inhibiting the DNA Damage Response. *Mol Cell Biol* **36**, 2067-2077
 147. Saito, K., Ohtomo, R., Kuga-Uetake, Y., Aono, T., and Saito, M. (2005) Direct labeling of polyphosphate at the ultrastructural level in *Saccharomyces cerevisiae* by using the affinity of the polyphosphate binding domain of *Escherichia coli* exopolyphosphatase. *Appl Environ Microb* **71**, 5692-5701
 148. Boulon, S., Westman, B. J., Hutten, S., Boisvert, F. M., and Lamond, A. I. (2010) The Nucleolus under Stress. *Mol Cell* **40**, 216-227
 149. Lam, Y. W., Trinkle-Mulcahy, L., and Lamond, A. I. (2005) The nucleolus. *J Cell Sci* **118**, 1335-1337
 150. Burger, K., Muhl, B., Harasim, T., Rohrmoser, M., Malamoussi, A., Orban, M., Kellner, M., Gruber-Eber, A., Kremmer, E., Holzner, M., and Eick, D. (2010) Chemotherapeutic Drugs Inhibit Ribosome Biogenesis at Various Levels. *J Biol Chem* **285**, 12416-12425
 151. Johnson, S. W., Laub, P. B., Beesley, J. S., Ozols, R. F., and Hamilton, T. C. (1997) Increased platinum-DNA damage tolerance is associated with cisplatin resistance and cross-resistance to various chemotherapeutic agents in unrelated human ovarian cancer cell lines. *Cancer Res* **57**, 850-856
 152. Kim, M. K., Caplen, N., Chakka, S., Hernandez, L., House, C., Pongas, G., Jordan, E., and Annunziata, C. M. (2016) Identification of therapeutic targets applicable to clinical strategies in ovarian cancer. *Bmc Cancer* **16**

153. Boisvert, F. M., van Koningsbruggen, S., Navascues, J., and Lamond, A. I. (2007) The multifunctional nucleolus. *Nat Rev Mol Cell Bio* **8**, 574-585
154. Jordan, P., and Carmo-Fonseca, M. (1998) Cisplatin inhibits synthesis of ribosomal RNA in vivo. *Nucleic Acids Res* **26**, 2831-2836
155. Bywater, M. J., Poortinga, G., Sanij, E., Hein, N., Peck, A., Cullinane, C., Wall, M., Cluse, L., Drygin, D., Anderes, K., Huser, N., Proffitt, C., Bliesath, J., Haddach, M., Schwaebe, M. K., Ryckman, D. M., Rice, W. G., Schmitt, C., Lowe, S. W., Johnstone, R. W., Pearson, R. B., McArthur, G. A., and Hannan, R. D. (2012) Inhibition of RNA Polymerase I as a Therapeutic Strategy to Promote Cancer-Specific Activation of p53. *Cancer Cell* **22**, 51-65
156. Sakatani, A., Fujiya, M., Ueno, N., Kashima, S., Sasajima, J., Moriichi, K., Ikuta, K., Tanabe, H., and Kohgo, Y. (2016) Polyphosphate Derived from *Lactobacillus brevis* Inhibits Colon Cancer Progression Through Induction of Cell Apoptosis. *Anticancer Res* **36**, 591-598
157. Horoky, M., Kotala, V., Anton, M., and Wesierska-Gadek, J. (2002) Nucleolus and apoptosis. *Ann Ny Acad Sci* **973**, 258-264
158. Horoky, M., Wurzer, G., Kotala, V., Anton, M., Vojtesek, B., Vacha, J., and Wesierska-Gadek, J. (2001) Segregation of nucleolar components coincides with caspase-3 activation in cisplatin-treated HeLa cells. *J Cell Sci* **114**, 663-670
159. Samejima, K., Svingen, P. A., Basi, G. S., Kottke, T., Mesner, P. W., Stewart, L., Durrieu, F., Poirier, G. G., Alnemri, E. S., Champoux, J. J., Kaufmann, S. H., and Earnshaw, W. C. (1999) Caspase-mediated cleavage of DNA topoisomerase I at unconventional sites during apoptosis. *J Biol Chem* **274**, 4335-4340
160. Saiardi, A. (2012) How inositol pyrophosphates control cellular phosphate homeostasis? *Adv Biol Regul* **52**, 351-359
161. Tsutsumi, K., Matsuya, Y., Sugahara, T., Tamura, M., Sawada, S., Fukura, S., Nakano, H., and Date, H. (2017) Inorganic polyphosphate enhances radio-sensitivity in a human non-small cell lung cancer cell line, H1299. *Tumour Biol* **39**, 1010428317705033
162. Carotenuto, M., De Antonellis, P., Liguori, L., Benvenuto, G., Magliulo, D., Alonzi, A., Turino, C., Attanasio, C., Damiani, V., Bello, A. M., Vitiello, F., Pasquinelli, R., Terracciano, L., Federico, A., Fusco, A., Freeman, J., Dale, T. C., Decraene, C., Chiappetta, G., Piantedosi, F., Calabrese, C., and Zollo, M. (2014) H-Prune through GSK-3 beta interaction sustains canonical WNT/beta-catenin signaling enhancing cancer progression in NSCLC. *Oncotarget* **5**, 5736-5749
163. Plooy, A. C. M., Vandijk, M., and Lohman, P. H. M. (1984) Induction and Repair of DNA Cross-Links in Chinese-Hamster Ovary Cells Treated with Various Platinum Coordination-Compounds in Relation to Platinum Binding to DNA, Cyto-Toxicity, Mutagenicity, and Antitumor-Activity. *Cancer Res* **44**, 2043-2051
164. Messori, L., and Merlino, A. (2014) Cisplatin Binding to Proteins: Molecular Structure of the Ribonuclease A Adduct. *Inorg Chem* **53**, 3929-3931
165. Beaufay, F., Quarles, E., Franz, A., Katamanin, O., Wholey, W. Y., and Jakob, U. (2020)

Polyphosphate Functions In Vivo as an Iron Chelator and Fenton Reaction Inhibitor. *Mbio* **11**

166. Andersen, J. S., Lam, Y. W., Leung, A. K. L., Ong, S. E., Lyon, C. E., Lamond, A. I., and Mann, M. (2005) Nucleolar proteome dynamics. *Nature* **433**, 77-83
167. Cooper, G. (2000) The Nucleolus. in *The Cell: A Molecular Approach. 2nd eddition.*, Sunderland (MA): Sinauer Associates. pp
168. Feric, M., Vaidya, N., Harmon, T. S., Mitrea, D. M., Zhu, L., Richardson, T. M., Kriwacki, R. W., Pappu, R. V., and Brangwynne, C. P. (2016) Coexisting Liquid Phases Underlie Nucleolar Subcompartments. *Cell* **165**, 1686-1697
169. Banani, S. F., Lee, H. O., Hyman, A. A., and Rosen, M. K. (2017) Biomolecular condensates: organizers of cellular biochemistry. *Nat Rev Mol Cell Bio* **18**, 285-298
170. Latonen, L. (2019) Phase-to-Phase With Nucleoli - Stress Responses, Protein Aggregation and Novel Roles of RNA. *Front Cell Neurosci* **13**
171. Shav-Tal, Y., Blechman, J., Darzacq, X., Montagna, C., Dye, B. T., Patton, J. G., Singer, R. H., and Zipori, D. (2005) Dynamic sorting of nuclear components into distinct nucleolar caps during transcriptional inhibition. *Mol Biol Cell* **16**, 2395-2413
172. Gilder, A. S., Do, P. M., Carrero, Z. I., Cosman, A. M., Broome, H. J., Velma, V., Martinez, L. A., and Hebert, M. D. (2011) Coilin participates in the suppression of RNA polymerase I in response to cisplatin-induced DNA damage. *Mol Biol Cell* **22**, 1070-1079
173. Louvet, E., Junera, H. R., Le Panse, S., and Hernandez-Verdun, D. (2005) Dynamics and compartmentation of the nucleolar processing machinery. *Exp Cell Res* **304**, 457-470
174. Marshall, N. F., and Price, D. H. (1995) Purification of P-Tefb, a Transcription Factor Required for the Transition into Productive Elongation. *J Biol Chem* **270**, 12335-12338
175. Zandomeni, R., Zandomeni, M. C., Shugar, D., and Weinmann, R. (1986) Casein Kinase Type-Ii Is Involved in the Inhibition by 5,6-Dichloro-1-Beta-D-Ribofuranosylbenzimidazole of Specific Rna Polymerase-Ii Transcription. *J Biol Chem* **261**, 3414-3419
176. Azkanaz, M., Lopez, A. R., de Boer, B., Huiting, W., Angrand, P. O., Vellenga, E., Kampinga, H. H., Bergink, S., Martens, J. H. A., Schuringa, J. J., and van den Boom, V. (2019) Protein quality control in the nucleolus safeguards recovery of epigenetic regulators after heat shock. *Elife* **8**
177. Frottin, F., Schueder, F., Tiwary, S., Gupta, R., Korner, R., Schlichthaerle, T., Cox, J., Jungmann, R., Hartl, F. U., and Hipp, M. S. (2019) The nucleolus functions as a phase-separated protein quality control compartment. *Science* **365**, 342-+
178. Latonen, L., Moore, H. M., Bai, B., Jaamaa, S., and Laiho, M. (2011) Proteasome inhibitors induce nucleolar aggregation of proteasome target proteins and polyadenylated RNA by altering ubiquitin availability. *Oncogene* **30**, 790-805
179. Latonen, L. (2011) Nucleolar aggresomes as counterparts of cytoplasmic aggresomes in proteotoxic stress Proteasome inhibitors induce nuclear ribonucleoprotein inclusions that accumulate several key factors of neurodegenerative diseases and cancer. *Bioessays* **33**,

180. Mishra, A., Godavarthi, S. K., Maheshwari, M., Goswami, A., and Jana, N. R. (2009) The Ubiquitin Ligase E6-AP Is Induced and Recruited to Aggresomes in Response to Proteasome Inhibition and May Be Involved in the Ubiquitination of Hsp70-bound Misfolded Proteins. *J Biol Chem* **284**, 10537-10545
181. Patel, A., Lee, H. O., Jawerth, L., Maharana, S., Jahnel, M., Hein, M. Y., Stoykov, S., Mahamid, J., Saha, S., Franzmann, T. M., Pozniakovski, A., Poser, I., Maghelli, N., Royer, L. A., Weigert, M., Myers, E. W., Grill, S., Drechsel, D., Hyman, A. A., and Alberti, S. (2015) A Liquid-to-Solid Phase Transition of the ALS Protein FUS Accelerated by Disease Mutation. *Cell* **162**, 1066-1077
182. Isaac, C., Yang, Y. F., and Meier, U. T. (1998) Nopp140 functions as a molecular link between the nucleolus and the coiled bodies. *J Cell Biol* **142**, 319-329
183. Chen, H. K., Pai, C. Y., Huang, J. Y., and Yeh, N. H. (1999) Human Nopp140, which interacts with RNA polymerase I: Implications for rRNA gene transcription and nucleolar structural organization. *Mol Cell Biol* **19**, 8536-8546
184. Rogakou, E. P., Pilch, D. R., Orr, A. H., Ivanova, V. S., and Bonner, W. M. (1998) DNA double-stranded breaks induce histone H2AX phosphorylation on serine 139. *J Biol Chem* **273**, 5858-5868
185. He, S. D., Wang, L., Miao, L., Wang, T., Du, F. H., Zhao, L. P., and Wang, X. D. (2009) Receptor Interacting Protein Kinase-3 Determines Cellular Necrotic Response to TNF-alpha. *Cell* **137**, 1100-1111
186. Bensaude, O. (2011) Inhibiting eukaryotic transcription: Which compound to choose? How to evaluate its activity? *Transcription* **2**, 103-108
187. Hayes, M. H., Peuchen, E. H., Dovichi, N. J., and Weeks, D. L. (2018) Dual roles for ATP in the regulation of phase separated protein aggregates in *Xenopus* oocyte nucleoli. *Elife* **7**
188. Langdon, E. M., Qiu, Y. P., Niaki, A. G., McLaughlin, G. A., Weidmann, C. A., Gerbich, T. M., Smith, J. A., Crutchley, J. M., Termini, C. M., Weeks, K. M., Myong, S., and Gladfelter, A. S. (2018) mRNA structure determines specificity of a polyQ-driven phase separation. *Science* **360**, 922-927
189. Maharana, S., Wang, J., Papadopoulos, D. K., Richter, D., Pozniakovsky, A., Poser, I., Bickle, M., Rizk, S., Guillen-Boixet, J., Franzmann, T. M., Jahnel, M., Marrone, L., Chang, Y. T., Sternecker, J., Tomancak, P., Hyman, A. A., and Alberti, S. (2018) RNA buffers the phase separation behavior of prion-like RNA binding proteins. *Science* **360**, 918-921
190. Patel, A., Malinowska, L., Saha, S., Wang, J., Alberti, S., Krishnan, Y., and Hyman, A. A. (2017) ATP as a biological hydrotrope. *Science* **356**, 753-756
191. Tourriere, H., Chebli, K., Zekri, L., Courselaud, B., Blanchard, J. M., Bertrand, E., and Tazi, J. (2003) The RasGAP-associated endoribonuclease G3BP assembles stress granules. *J Cell Biol* **160**, 823-831
192. Pai, C. Y., Chen, H. K., Sheu, H. L., and Yeh, N. H. (1995) Cell-cycle-dependent alterations of a highly phosphorylated nucleolar protein p130 are associated with nucleologenesis. *J Cell Sci* **108 (Pt 5)**, 1911-1920

193. Tantos, A., Szrnka, K., Szabo, B., Bokor, M., Kamasa, P., Matus, P., Bekesi, A., Tompa, K., Han, K. H., and Tompa, P. (2013) Structural disorder and local order of hNopp140. *Bba-Proteins Proteom* **1834**, 342-350
194. Meier, U. T. (1996) Comparison of the rat nucleolar protein Nopp140 with its yeast homolog SRP40 - Differential phosphorylation in vertebrates and yeast. *J Biol Chem* **271**, 19376-19384
195. Frege, T., and Uversky, V. N. (2015) Intrinsically disordered proteins in the nucleus of human cells. *Biochem Biophys Rep* **1**, 33-51
196. Makarov, V., Rakitina, D., Protopopova, A., Yaminsky, I., Arutiunian, A., Love, A. J., Taliansky, M., and Kalinina, N. (2013) Plant Coilin: Structural Characteristics and RNA-Binding Properties. *Plos One* **8**
197. Sobell, H. M., Jain, S. C., Sakore, T. D., and Nordman, C. E. (1971) Stereochemistry of actinomycin--DNA binding. *Nat New Biol* **231**, 200-205
198. Stone, P. J., Kelman, A. D., and Sinex, F. M. (1974) Specific Binding of Antitumor Drug Cis-Pt(Nh3)2cl2 to DNA Rich in Guanine and Cytosine. *Nature* **251**, 736-737
199. Kwon, H., and Green, M. R. (1994) The Rna-Polymerase-I Transcription Factor, Upstream Binding-Factor, Interacts Directly with the Tata Box-Binding Protein. *J Biol Chem* **269**, 30140-30146
200. Wang, X., Shi, C. K., Mo, J. B., Xu, Y., Wei, W., and Zhao, J. (2020) An Inorganic Biopolymer Polyphosphate Controls Positively Charged Protein Phase Transitions. *Angew Chem Int Edit* **59**, 2679-2683
201. Kornberg, A., Kornberg, S. R., and Simms, E. S. (1956) Metaphosphate synthesis by an enzyme from Escherichia coli. *Biochim Biophys Acta* **20**, 215-227
202. Kornberg, A., Rao, N. N., and Ault-Riche, D. (1999) Inorganic polyphosphate: A molecule of many functions. *Annu Rev Biochem* **68**, 89-125
203. Bru, S., Jimenez, J., Canadell, D., Arino, J., and Clotet, J. (2016) Improvement of biochemical methods of polyP quantification. *Microb Cell* **4**, 6-15
204. Smith, S. A., and Morrissey, J. H. (2007) Sensitive fluorescence detection of polyphosphate in polyacrylamide gels using 4',6-diamidino-2-phenylindol. *Electrophoresis* **28**, 3461-3465
205. Losito, O., Sziogyarto, Z., Resnick, A. C., and Saiardi, A. (2009) Inositol pyrophosphates and their unique metabolic complexity: analysis by gel electrophoresis. *Plos One* **4**, e5580
206. Kolozsvari, B., Parisi, F., and Saiardi, A. (2014) Inositol phosphates induce DAPI fluorescence shift. *Biochem J* **460**, 377-385
207. Martin, P., and Van Mooy, B. A. (2013) Fluorometric quantification of polyphosphate in environmental plankton samples: extraction protocols, matrix effects, and nucleic acid interference. *Appl Environ Microbiol* **79**, 273-281
208. Zhu, J., Loubery, S., Broger, L., Zhang, Y., Lorenzo-Orts, L., Utz-Pugin, A., Fernie, A. R., Young-Tae, C., and Hothorn, M. (2020) A genetically validated approach for detecting inorganic polyphosphates in plants. *Plant J* **102**, 507-516
209. Werner, T. P., Amrhein, N., and Freimoser, F. M. (2007) Inorganic polyphosphate occurs in

- the cell wall of *Chlamydomonas reinhardtii* and accumulates during cytokinesis. *BMC Plant Biol* **7**, 51
210. Ramos, I., Gomes, F., Koeller, C. M., Saito, K., Heise, N., Masuda, H., Docampo, R., de Souza, W., Machado, E. A., and Miranda, K. (2011) Acidocalcisomes as calcium- and polyphosphate-storage compartments during embryogenesis of the insect *Rhodnius prolixus* Stahl. *Plos One* **6**, e27276
 211. Ramos, I. B., Miranda, K., Pace, D. A., Verbist, K. C., Lin, F. Y., Zhang, Y., Oldfield, E., Machado, E. A., De Souza, W., and Docampo, R. (2010) Calcium- and polyphosphate-containing acidic granules of sea urchin eggs are similar to acidocalcisomes, but are not the targets for NAADP. *Biochem J* **429**, 485-495
 212. Kuroda, A., Tanaka, S., Ikeda, T., Kato, J., Takiguchi, N., and Ohtake, H. (1999) Inorganic polyphosphate kinase is required to stimulate protein degradation and for adaptation to amino acid starvation in *Escherichia coli*. *Proc Natl Acad Sci U S A* **96**, 14264-14269
 213. Jacob, R. T., Larsen, M. J., Larsen, S. D., Kirchoff, P. D., Sherman, D. H., and Neubig, R. R. (2012) MScreen: An Integrated Compound Management and High-Throughput Screening Data Storage and Analysis System. *J Biomol Screen* **17**, 1080-1087
 214. Birmingham, A., Anderson, E. M., Reynolds, A., Ilsley-Tyree, D., Leake, D., Fedorov, Y., Baskerville, S., Maksimova, E., Robinson, K., Karpilow, J., Marshall, W. S., and Khvorova, A. (2006) 3' UTR seed matches, but not overall identity, are associated with RNAi off-targets. *Nat Methods* **3**, 199-204
 215. Havlickova, V., Kaplanova, V., Nuskova, H., Drahota, Z., and Houstek, J. (2010) Knockdown of F-1 epsilon subunit decreases mitochondrial content of ATP synthase and leads to accumulation of subunit c. *Bba-Bioenergetics* **1797**, 1124-1129
 216. Yao, J. W., Subramanian, C., Rock, C. O., and Jackowski, S. (2019) Human pantothenate kinase 4 is a pseudo-pantothenate kinase. *Protein Sci* **28**, 1031-1047
 217. Jakymiw, A., Lian, S. L., Eystathioy, T., Li, S. Q., Satoh, M., Hamel, J. C., Fritzler, M. J., and Chan, E. K. L. (2005) Disruption of GW bodies impairs mammalian RNA interference. *Nat Cell Biol* **7**, 1267-1274
 218. Chatterton, J. E., Awobuluyi, M., Premkumar, L. S., Takahashi, H., Talantova, M., Shin, Y., Cui, J. K., Tu, S. C., Kevin, A. S. K., Nakanishi, N., Tong, G., Lipton, S. A., and Zhang, D. X. (2002) Excitatory glycine receptors containing the NR3 family of NMDA receptor subunits. *Nature* **415**, 793-798
 219. Matsuno, H., Ohi, K., Hashimoto, R., Yamamori, H., Yasuda, Y., Fujimoto, M., Yano-Umeda, S., Saneyoshi, T., Takeda, M., and Hayashi, Y. (2015) A Naturally Occurring Null Variant of the NMDA Type Glutamate Receptor NR3B Subunit Is a Risk Factor of Schizophrenia. *Plos One* **10**
 220. Wee, K. S. L., Tan, F. C. K., Cheong, Y. P., Khanna, S., and Low, C. M. (2016) Ontogenic Profile and Synaptic Distribution of GluN3 Proteins in the Rat Brain and Hippocampal Neurons. *Neurochem Res* **41**, 290-297
 221. Wee, K. S. L., Zhang, Y. B., Khanna, S., and Low, C. M. (2008) Immunolocalization of NMDA receptor subunit NR3B in selected structures in the rat forebrain, cerebellum, and

- lumbar spinal cord. *J Comp Neurol* **509**, 118-135
222. Maiolino, M., O'Neill, N., Lariccia, V., Amoroso, S., Sylantyev, S., Angelova, P. R., and Abramov, A. Y. (2019) Inorganic Polyphosphate Regulates AMPA and NMDA Receptors and Protects Against Glutamate Excitotoxicity via Activation of P2Y Receptors. *J Neurosci* **39**, 6038-6048
223. Besteiro, S., Tonn, D., Tetley, L., Coombs, G. H., and Mottram, J. C. (2008) The AP3 adaptor is involved in the transport of membrane proteins to acidocalcisomes of *Leishmania*. *J Cell Sci* **121**, 561-570
224. Huang, G. Z., Fang, J. M., Sant'Anna, C., Li, Z. H., Wellems, D. L., Rohloff, P., and Docampo, R. (2011) Adaptor Protein-3 (AP-3) Complex Mediates the Biogenesis of Acidocalcisomes and Is Essential for Growth and Virulence of *Trypanosoma brucei*. *J Biol Chem* **286**, 36619-36630
225. Dell'Angelica, E. C., Shotelersuk, V., Aguilar, R. C., Gahl, W. A., and Bonifacino, J. S. (1999) Altered trafficking of lysosomal proteins in Hermansky-Pudlak syndrome due to mutations in the beta 3A subunit of the AP-3 adaptor. *Mol Cell* **3**, 11-21
226. Kantheti, P., Qiao, X. X., Diaz, M. E., Peden, A. A., Meyer, G. E., Carskadon, S. L., Kapfhamer, D., Sufalko, D., Robinson, M. S., Noebels, J. L., and Burmeister, M. (1998) Mutation in AP-3 delta in the mocha mouse links endosomal transport to storage deficiency in platelets, melanosomes, and synaptic vesicles. *Neuron* **21**, 111-122
227. Vietri, M., Radulovic, M., and Stenmark, H. (2020) The many functions of ESCRTs. *Nat Rev Mol Cell Bio* **21**, 25-42
228. Ferraiuolo, R. M., Manthey, K. C., Stanton, M. J., Triplett, A. A., and Wagner, K. U. (2020) The Multifaceted Roles of the Tumor Susceptibility Gene 101 (TSG101) in Normal Development and Disease. *Cancers* **12**
229. Tundo, G. R., Sbardella, D., Ciaccio, C., De Pascali, S., Campanella, V., Cozza, P., Tarantino, U., Coletta, M., Fanizzi, F. P., and Marini, S. (2015) Effect of cisplatin on proteasome activity. *J Inorg Biochem* **153**, 253-258
230. Gatti, L., Chen, D., Beretta, G. L., Rustici, G., Carenini, N., Corna, E., Colangelo, D., Zunino, F., Bahler, J., and Perego, P. (2004) Global gene expression of fission yeast in response to cisplatin. *Cell Mol Life Sci* **61**, 2253-2263
231. Konac, E., Varol, N., Kiliccioglu, I., and Bilen, C. Y. (2015) Synergistic effects of cisplatin and proteasome inhibitor bortezomib on human bladder cancer cells. *Oncol Lett* **10**, 560-564
232. Xu, Y., Li, D., Zeng, L. C., Wang, C. Y., Zhang, L. L., Wang, Y., Yu, Y., Liu, S. B., and Li, Z. X. (2015) Proteasome inhibitor lactacystin enhances cisplatin cytotoxicity by increasing endoplasmic reticulum stress-associated apoptosis in HeLa cells. *Mol Med Rep* **11**, 189-195